



National Library
of Canada

Bibliothèque nationale
du Canada

Canadian Theses Service

Services des thèses canadiennes

Ottawa, Canada
K1A 0N4

CANADIAN THESES

THÈSES CANADIENNES

NOTICE

The quality of this microfiche is heavily dependent upon the quality of the original thesis submitted for microfilming. Every effort has been made to ensure the highest quality of reproduction possible.

If pages are missing, contact the university which granted the degree.

Some pages may have indistinct print especially if the original pages were typed with a poor typewriter ribbon or if the university sent us an inferior photocopy.

Previously copyrighted materials (journal articles, published tests, etc.) are not filmed.

Reproduction in full or in part of this film is governed by the Canadian Copyright Act, R.S.C. 1970, c. C-30.

**THIS DISSERTATION
HAS BEEN MICROFILMED
EXACTLY AS RECEIVED**

AVIS

La qualité de cette microfiche dépend grandement de la qualité de la thèse soumise au microfilmage. Nous avons tout fait pour assurer une qualité supérieure de reproduction.

S'il manque des pages, veuillez communiquer avec l'université qui a conféré le grade.

La qualité d'impression de certaines pages peut laisser à désirer, surtout si les pages originales ont été dactylographiées à l'aide d'un ruban usé ou si l'université nous a fait parvenir une photocopie de qualité inférieure.

Les documents qui font déjà l'objet d'un droit d'auteur (articles de revue, examens publiés, etc.) ne sont pas microfilmés.

La reproduction, même partielle, de ce microfilm est soumise à la Loi canadienne sur le droit d'auteur, SRC 1970, c. C-30.

**LA THÈSE A ÉTÉ
MICROFILMÉE TELLE QUE
NOUS L'AVONS REÇUE**

THE UNIVERSITY OF ALBERTA

THE GEOCHRONOLOGY AND PETROGENESIS OF THE
'BIG SPRUCE LAKE ALKALINE COMPLEX'

by

PATRICIA ANNE CAVELL

A THESIS

SUBMITTED TO THE FACULTY OF GRADUATE STUDIES AND RESEARCH
IN PARTIAL FULFILMENT OF THE REQUIREMENTS FOR THE DEGREE

OF

DOCTOR OF PHILOSOPHY

DEPARTMENT OF GEOLOGY

EDMONTON, ALBERTA

SPRING 1986

Permission has been granted to the National Library of Canada to microfilm this thesis and to lend or sell copies of the film.

The author (copyright owner) has reserved other publication rights, and neither the thesis nor extensive extracts from it may be printed or otherwise reproduced without his/her written permission.

L'autorisation a été accordée à la Bibliothèque nationale du Canada, de microfilmer cette thèse et de prêter ou de vendre des exemplaires du film.

L'auteur (titulaire du droit d'auteur) se réserve les autres droits de publication; ni la thèse ni de longs extraits de celle-ci ne doivent être imprimés ou autrement reproduits sans son autorisation écrite.

ISBN 0-315-30180-5



University of Alberta
Edmonton

Department of Geology

Canada T6G 2E3

158 Earth Sciences Building, Telephone (403) 432-3265

07 February 1986

To whom it may concern:

I hereby give such permission as is necessary to Patricia
A. Cavell to include a copy of the paper entitled,

Geochronology of the Big Spruce Lake
Alkaline Intrusion

by P.A. Cavell and H. Baadsgaard in the appendix of her Ph.D.
thesis

Sincerely,

H. Baadsgaard

HB/ih

T H E U N I V E R S I T Y O F A L B E R T A

RELEASE FORM

NAME OF AUTHOR PATRICIA ANNE CAVELL
TITLE OF THESIS THE GEOCHRONOLOGY AND PETROGENESIS OF THE
BIG SPRUCE LAKE ALKALINE COMPLEX
DEGREE FOR WHICH THESIS WAS PRESENTED Ph.D.
YEAR THIS DEGREE GRANTED 1986

Permission is hereby granted to THE UNIVERSITY OF ALBERTA LIBRARY to reproduce single copies of this thesis and to lend or sell such copies for private, scholarly or scientific research purposes only.

The author reserves other publication rights, and neither the thesis nor extensive extracts from it may be printed or otherwise reproduced without the author's written permission.

(Signed)

Patricia A. Cavell

PERMANENT ADDRESS:

12420 - 47 Avenue
Edmonton, Alberta
T6H 0B4

DATED

February 10

1986

THE UNIVERSITY OF ALBERTA

FACULTY OF GRADUATE STUDIES AND RESEARCH

The undersigned certify that they have read, and recommend to the Faculty of Graduate Studies and Research, for acceptance, a thesis entitled THE GEOCHRONOLOGY AND PETROGENESIS OF THE BIG SPRUCE LAKE ALKALINE COMPLEX submitted by PATRICIA A. CAVELL in partial fulfilment of the requirements for the degree of DOCTOR OF PHILOSOPHY

H. Baadsgaard

Supervisor

G. C. Murray

R. S. J. Lambert

P. J. L. Taylor

K. W. W. ...

R. A. Burnett

[Signature]

External Examiner

DATE

January 6, 1986

To R.G.C.

ABSTRACT

A revised geological map of the Big Spruce Lake alkaline complex, N.W.T. (63° 33' N, 115° 55' W) has been prepared. Field evidence and element abundances and ratios (37 elements determined) in WR samples from each of five intrusive centres have been used to elucidate petrogenetic relationships. The silica-saturated gabbro-syenite suite (Centres 1 and 2) forms a single differentiation trend. Minor gneissic contamination, multiple magma pulses and highly localised post-intrusive disturbance contribute to data scatter. Magnetite pyroxenites are an early cumulate phase of the gabbro-syenite series. The sodic alkali basalt parent melt of Centres 1 and 2 was LILE-enriched and highly LILE-fractionated. Compositions of the silica-undersaturated foyaite-ijolite suite (Centre 3) indicate a cumulate character. General enrichment of LILE (REE, Y, Zr, Hf, Nb, Ta, U, Th) in more mafic members may result from differential accumulation or, in some cases, from crystallisation of enriched mafic liquid. Chilled margins (melt compositions) are highly sodic and leucocratic, LILE-enriched and LILE-fractionated, with low Al/alkali, low Si/alkali and low Fe^{2+}/Fe^{3+} . Individual carbonatite bodies (Centre 4) may be derived from a carbonated foyaite-ijolite series by separate carbonate/silicate melt

immiscibility events. Gneissic contamination of two carbonatites is discernible from trace element data. Compositional variation in mafic K-rich rocks (Centre 5 - satellite intrusion) is dominated by modal variations. LILE-enrichment and LILE-fractionation preclude gneissic assimilation by basaltic melt as a source for these rocks.

A zircon age of $2188 \pm 16/-10$ Ma has been determined for syenites of Centre 2. A WR Pb-Pb age of $2165 \pm 21/-22$ Ma was obtained for foyaites and ijolites of Centre 3, and 2155 ± 16 Ma for the complex as a whole. The Sm-Nd WR data yield an age of 2183 ± 75 Ma for the complex as a whole. Weighting the ages by the inverse square of the standard deviations, an average age for the complex of 2174 ± 20 Ma is determined. However, it is felt the zircon age is the most reliable for the time of crystallisation of the complex. Minor contamination by country rock (Sm-Nd model ages of 2467 to 2595 Ma) and metasomatism contribute to scattered data points and large errors in the ages obtained for the five individual centres. The Pb-Pb data enable a limiting estimate of about 50 Ma for the maximum time span for the intrusion of Centres 1 to 4.

All parent melts were mainly mantle-derived. No isotopically discrete mantle sources can be distinguished for any of the five separate centres. The common mantle

source region had been LILE-depleted prior to 2188 Ma to create $\epsilon_{Nd} = +3$, $\epsilon_{Sr} = -10$ and $\mu = 9.2$ to 9.4 at the time of magma formation.

A model of mantle diapiric uprise related to activity on the Snare Fault and involving deep mantle volatiles could account for the wide range of rock types and reconcile the LILE-enrichment of magmas with the prior LILE-depletion of the source region.

ACKNOWLEDGEMENTS

This work was carried out during the tenure of an NSERC scholarship and a Steinhauer (Alberta Heritage Scholarship Fund) award. Field work was facilitated by aid from the Yellowknife office (Bill Padgham) of the Department of Indian and Northern Affairs (Canada) and by a grant from the Boreal Institute for Northern Studies. Northern Canada Power Commission personnel at Yellowknife and at the Snare Rapids damsite (A.S. Littlejohn and J. Woodman) greatly facilitated sample collection and transportation. Giant Yellowknife Mines Ltd. made their files on the Big Spruce Lake complex available to the author. John Samson of the Department of Physics, University of Alberta aided in re-evaluation of aeromagnetic data.

The author would like to thank John Duke, Dennis Ng and the rest of the staff at the University of Alberta Slowpoke facility for their help and advice, Takeru Yanagi and Richard Lambert for stimulating discussions, Dorian Smith for bringing the Big Spruce Lake complex to my attention and helping in the early stages of the project, Dragan Krstic, and the fellows in the mass spectrometry lab for ever-present back-up, Wayne Day, Alex Stelmach and Dave Tomlinson for general technical support.

A special thank you is owed to Bud Baadsgaard for his unflinching support and encouragement.

TABLE OF CONTENTS

CHAPTER	PAGE
1. INTRODUCTION.....	1
2. GEOLOGY	6
A. Introduction and General Geology.....	6
B. Intrusive Centre 1 - Diorites, Gabbros and Pyroxenites.....	12
1. Diorite.....	12
2. Gabbro Series.....	14
3. Magnetite clinopyroxenite.....	17
C. Intrusive Centre 2 - Syenites.....	19
D. Intrusive Centre 3 - Silica-undersaturated Suite.....	26
E. Intrusive Centre 4 - Carbonatites.....	33
F. Intrusive Centre 5 - Satellite Intrusion at Moose Island.....	37
3. ELEMENT GEOCHEMISTRY.....	44
A. Introduction.....	44
B. Analytical Methods.....	50
C. General Geochemical Results.....	51
D. Intrusive Centres 1 and 2 - Gabbros, Diorites, Syenites and Pyroxenites.....	57
1. Characterisation of Individual Units.....	57
2. Differentiation Trend.....	63

CHAPTER	PAGE
3. Trace Element Variations.....	68
4. Granodioritic Country Rock.....	102
5. Evaluation of Effects of Contamination, Open System Crystallisation and Cumulate Formation on Trace Elements.....	106
6. Magnetite Pyroxenites.....	116
7. Parent Magma.....	132
8. Summary and Discussion.....	140
E. Intrusive Centre 3 - Silica-Undersaturated Suite.....	146
1. Major and Minor Element Results.....	147
2. Trace Element Results.....	164
3. Melt Composition.....	184
4. Summary and Discussion.....	188
F. Carbonatites.....	196
1. Major and Trace Element Results.....	196
2. Discussion.....	206
G. Intrusive Centre 5 - Satellite Intrusion.....	213
1. Compositional Variations.....	215
2. Parent Magma.....	232
3. Summary and Discussion.....	235
4. ISOTOPE GEOCHEMISTRY.....	238
A. Introduction.....	238
B. Samples and Analytical Methods.....	240

CHAPTER	PAGE
C. Geochronology of the Complex.....	240
D. Rb-Sr Systematics.....	242
E. Sm-Nd Systematics.....	260
F. U-Th-Pb Systematics.....	281
G. Summary and Conclusions.....	300
5. PETROGENETIC RELATIONSHIPS: SUMMARY AND CONCLUSIONS.....	305
A. Relationship to the Surrounding Area.....	305
B. Magma Types and Sources.....	312
C. Generalised Model.....	320

REFERENCES.....	325
APPENDIX 1. SAMPLE LOCATIONS AND DESCRIPTIONS.....	352
APPENDIX 2. ANALYTICAL METHODS.....	377
APPENDIX 3. DETAILED ANALYTICAL RESULTS FOR WHOLE ROCK SAMPLES.....	396
APPENDIX 4. GEOCHRONOLOGY OF THE BIG SPRUCE LAKE ALKALINE INTRUSION.....	408

LIST OF TABLES

TABLE	PAGE
1. List of analysed samples.....	46
2. Rare earth element data for intrusive Centres 1 and 2.....	73
3. LILE "primordial mantle" abundances.....	86
4. Rare earth element data for granodiorites.....	105
5. Calculated REE composition of magnetite pyroxenite parent liquids.....	125
6. Relative abundances of incompatible elements in a possible parent melt for Centres 1 and 2....	137
7. CIPW normative compositions of foyaïtes, ijolites and melteigites analysed in this study..	149
8. Volatile content of foyaïtes and melteigite.....	150
9. CIPW normative compositions for samples from Martineau (1970).....	153
10. Rare earth element data for intrusive Centre 3...	179
11. Compositions of foyaïte chilled margins reported by Martineau (1970).....	185
12. Minor and trace element compositions of foyaïte chilled margins compared to those of mafic and quartz syenites of Centre 2.....	186

TABLE	PAGE
13. Range of compositions of carbonatites from the Big Spruce Lake intrusion.....	199
14. Rare earth element data for carbonatites.....	204
15. CIPW normative compositions of samples from the satellite intrusion.....	215
16. Rare earth element data for Centres 1 and 2.....	224
17. Relative abundances of incompatible elements in parent liquid of the satellite intrusion.....	234
18. Rb-Sr analytical results for silicates from the Big Spruce Lake intrusion.....	244
19. Rb-Sr geochronological results.....	245
20. Rb-Sr analytical results for carbonatites.....	248
21. Rb-Sr analytical results for gneissic host rock..	254
22. ϵ_{Nd} and ϵ_{Sr} for individual samples.....	265
23. Whole rock lead analytical data for gneisses.....	282
24. Pb isotopic composition of leachable and residual Pb in carbonatites.....	289
25. US-GS standards analysed by XRF.....	380
26. γ -energies and irradiation schemes for INAA.....	383
27. Analytical results: Centre 1 - gabbros and diorites.....	397
28. Analytical results: Centre 2 - quartz-free syenites.....	398
29. Analytical results: Centre 2 - quartz syenites..	399

TABLE	PAGE
30. Analytical results: gneisses.....	400
31. Analytical results: Centre 1 - pyroxenites.....	401
32. Analytical results: Centre 3 - foyaites.....	402
33. Analytical results: Centre 3 - ijolites and melteigites.....	403
34. Analytical results: Centre 4 - carbonatites(a)..	404
35. Analytical results: Centre 4 - carbonatites(b)..	405
36. Analytical results: Centre 5 - shonkinites and biotite pyroxenites.....	406
37. Analytical results: Centre 5 - by XRF only.....	407
38. Whole rock lead analytical data.....	417
207Pb vs 206Pb regression and slope age results..	424
40. U-Pb analytical data for syenite zircons.....	429
41. Sm/Nd whole rock analytical data.....	435
42. Sm/Nd analytical data and model ages for granodioritic country rock.....	436
43. Sm/Nd whole rock regression and age results.....	437

LIST OF FIGURES

FIGURE	PAGE
1. Outline map of the Big Spruce Lake alkaline complex.....	7
2. Sketch of quartz syenite-mafic foyaite contact zone.....	29
3. Outline map of the satellite intrusion.....	38
4. Alkali vs silica classification diagram for rocks from intrusive Centres 1-2 and 5.....	52
5. Agpaitic index vs silica diagram for silicate rocks.....	54
6. Alkali vs silica diagram for silica-under-saturated rocks of intrusive Centre 3.....	56
7. Plot of $Na_2O + K_2O$ vs SiO_2 showing individual samples of the gabbro-syenite series.....	59
8. Location map of reclassified quartz syenite body.....	61
9. Trace element plots correlating the reclassified composition of the syenite with those of quartz syenite.....	62
10. REE distribution plots of reclassified syenite and ring syenite.....	64
11. Y vs CaO in the gabbro-syenite series.....	67

FIGURE	PAGE
12. REE distribution plots for gabbros and diorites.....	69
13. REE distribution plots for mafic and ring syenite.....	70
14. REE distribution plots for inner and reclassified quartz syenites.....	71
15. REE distribution plots for outer quartz syenites.....	72
16. Distribution coefficients for REE in rock-forming minerals.....	75
17. Ce/Yb vs Ce for the gabbro-syenite series.....	76
18. Distribution coefficients for REE in accessory minerals.....	79
19. P ₂ O ₅ vs ΣREE for the gabbro-syenite series.....	81
20. Mantle-normalised LILE distribution plots for gabbros.....	88
21. Mantle-normalised LILE distribution plots for diorites.....	89
22. Mantle-normalised LILE distribution plots for mafic and ring syenites.....	90
23. Mantle-normalised LILE distribution plots for outer quartz syenites.....	91
24. Mantle-normalised LILE distribution plots for inner and reclassified quartz syenites.....	92

FIGURE	PAGE
25. Eu/Eu* vs Sr/Sr* in rocks of the gabbro-syenite series.....	96
26. REE distribution plots for granodiorites,.....	103
27. Mantle-normalised LILE distribution plots for granodiorites.....	104
28. Nb vs Ta and Zr vs Hf for the gabbro-syenite series.....	108
29. Σ REE vs Y and vs Zr for the gabbro syenite series.....	109
30. Σ REE vs Nb and vs Rb for the gabbro-syenite series.....	110
31. Na ₂ O + K ₂ O vs Nb, Zr and Rb for the gabbro-syenite series showing petrologic control of compositions.....	112
32. Harker diagrams of Sc, Th, Rb and Zr for the gabbro-syenite series indicating possible ring syenite contamination.....	114
33. REE distribution plots for magnetite pyroxenites.....	118
34. REE distribution plots for whole rock magnetite pyroxenite, pyroxene separate and calculated parent liquid compositions.....	120
35. Mineral/melt partition coefficients for olivine, magnetite and clinopyroxene.....	122

FIGURE	PAGE
36. Big Spruce Lake magnetite pyroxenite compositions in the ol-di-spinel system from Martineau (1970).....	127
37. Plots of Zr vs Hf, Ta, Nb and Y in the early gabbro-syenite trend from which relative abundances in parent melt can be extrapolated....	134
38. Plots of Zr vs La, Tb, Ce and Rb in the early gabbro-syenite trend from which relative abundances in parent melt can be extrapolated....	135
39. Compositions of analysed foyaites and ijolites in the residua system.....	152
40. Phase relationships in the system Ne-Ab-(Ac+Di) at $P_{H_2O} = 1000 \text{ kg/cm}^2$	160
41. Compositions of analysed foyaites and ijolites in the system (Ne+Ks)-(Ab+Or)-(Ac+Di).....	162
42. Co and Sc variation with mafic content of the foyaites-ijolite suite.....	165
43. Σ REE, Y, Zr and Th variation with mafic content of the foyaites-ijolite suite.....	167
44. U and Nb variation with mafic content of the foyaites-ijolite suite.....	168
45. Mantle-normalised LILE distribution plots for southern foyaites from the Big Spruce Lake intrusion.....	169

FIGURE	PAGE
46. Mantle-normalised LILE distribution plots for northern foyaites from the Big Spruce Lake intrusion.....	170
47. Mantle-normalised LILE distribution plots for ijolites from the Big Spruce Lake intrusion.....	171
48. Mantle-normalised LILE distribution plots for melteigites from the Big Spruce Lake intrusion...	172
49. Plots of Ta vs Nb and Hf vs Zr in rocks of the foyaite-ijolite suite.....	175
50. REE distribution plots for foyaites.....	177
51. REE distribution plots for ijolites and melteigites.....	178
52. Ce vs Ce/Yb for rocks of the foyaite-ijolite suite.....	181
53. Σ REE vs Y in rocks of the foyaite-ijolite suite.....	187
54. Carbonatite classification diagram.....	197
55. REE distribution patterns for sövite dykes.....	201
56. REE distribution patterns for three grey laminated sövite dykes.....	202
57. REE distribution patterns for magnetite dolomite carbonatites.....	203
58. Trace element abundances in carbonatites and associated foyaites-ijolites.....	209

FIGURE	PAGE
59. Silica vs CaO, Al ₂ O ₃ , K ₂ O and Na ₂ O in shonkinites and biotite pyroxenites.....	217
60. Silica vs MgO, ΣFe ₂ O ₃ , TiO ₂ and MnO in shonkinites and biotite pyroxenites.....	218
61. Silica vs Nb, Ba, Zr and Rb in shonkinites and biotite pyroxenites.....	220
62. Rb vs K ₂ O in biotite pyroxenites and shonkinites.....	222
63. REE distribution patterns for shonkinites and biotite pyroxenites.....	223
64. Mantle-normalised LILE distribution plots for Ba-enriched shonkinite and biotite pyroxenite....	228
65. Mantle-normalised LILE distribution plots for biotite pyroxenites and shonkinites.....	229
66. Zr vs Rb and Cs, and Cs vs K ₂ O and Rb in rocks of the satellite intrusion and in granodiorite.....	231
67. Plots of Zr vs U, Th, Nb and Hf in rocks of the satellite intrusion, from which relative abundances in parent melt can be extrapolated....	233
68. Abstract of "Geochronology of the Big Spruce Lake Alkaline Intrusion".....	241
69. Rb-Sr results for samples from a) Centre 2, b) Centres 1 and 3.....	243

FIGURE	PAGE
70. Rb-Sr results for samples from the satellite intrusion.....	246
71. Model initial $^{87}\text{Sr}/^{86}\text{Sr}$ ratios vs ppm Sr for WR samples.....	256
72. Initial Sr ratio vs age for carbonatites of the Canadian Shield (from Bell <u>et al</u> , 1982).....	259
73. Sm-Nd results for all samples.....	263
74. Histogram of individual ϵ_{Nd} values.....	266
75. ϵ_{Sr} vs ϵ_{Nd} for analysed samples.....	272
76. $^{207}\text{Pb}/^{204}\text{Pb}$ vs $^{206}\text{Pb}/^{204}\text{Pb}$ for whole rock samples from all intrusive centres.....	284
77. Isotopic compositions of leachable and residual Pb in low-U sövites.....	290
78. Isotopic compositions of leachable and residual Pb in dolomite carbonatites and a U-rich sövite.....	291
79. Effects of a) recent Pb movement on measured Pb-isotopic compositions, b) old Pb and U movement on measured Pb-isotopic compositions....	295
80. Composite Landsat photograph of the area around the Big Spruce Lake intrusion.....	307
81. Structures in the area around the Big Spruce Lake intrusion (Marfinau, 1970).....	309
82. Sketch of diapiric model for Big Spruce Lake.....	323

FIGURE	PAGE
83. Whole rock lead isotope ratios for samples from Centres 1 and 2.....	420
84. Whole rock lead isotope ratios for samples from Centre 3.....	421
85. Whole rock lead isotope ratios for samples from Centre 4.....	422
86. Whole rock lead isotope ratios for samples from the satellite intrusion, Centre 5.....	423
87. U-Pb results for zircons from syenites.....	431
88. Sm-Nd results for whole rock samples from all centres of the intrusion.....	433

GLOSSARY OF ACRONYMS

BABI	Basaltic achondrite best initial
BFG	Big Feldspar Gabbro
CHUR	chondritic uniform reservoir
CN	chondrite-normalised
D value	mineral/melt distribution coefficient
DM	depleted mantle
DNC	delayed neutron counting
HREE	heavy rare earth elements
LILE	large ion lithophile element
LLG	Leucocratic Laminated Gabbro
LREE	light rare earth element
MORB	mid ocean ridge basalt
MN	mantle-normalised
MREE	middle rare earth element
MSWD	mean square of weighted deviates
RBG	Rhythmic Banded Gabbro
REE	rare earth element
UR	uniform reservoir
WR	whole rock

CHAPTER 1

INTRODUCTION

The origin of carbonatites and closely associated alkaline rocks has long provided a subject of controversy for petrologists.

Daly (1910) proposed that alkaline rocks are produced by assimilation of limestone by subalkaline silicate magma. This early theory was espoused by some petrologists and hotly contested by others (see Wyllie and Watkinson, 1970; Wyllie, 1974 for historical reviews of this theory). It was not until evidence from experimental petrology began to accumulate (e.g., Schairer and Bowen, 1935; Fudali, 1963; Hamilton and Mackenzie, 1965; Wyllie and Tuttle, 1959) that opinion against limestone syntexis gained strength. However, the synthetic systems studied do not perfectly mimic the more complex natural systems and so the evidence was not unequivocal. Experimental work by Wyllie and Tuttle (1960) showed that carbonate melts could exist under reasonable geological conditions and Dawson (1962) reported the occurrence of a natural carbonate melt. It was isotopic and trace element data from natural systems that substantiated a primitive origin

for carbonatites. Stable isotope studies (Taylor et al., 1967; Deines and Gold, 1973; Pineau, Javoy and Allegré, 1973; Sheppard and Dawson, 1973) showed a primary or mantle origin for the carbon of carbonatites which have $\delta^{13}\text{C} = -2$ to -9 (vs PDB standard) in sharp contrast to a $\delta^{13}\text{C}$ of zero for limestones. Strontium isotope data (Hamilton and Deans, 1963; Bell et al., 1973; Powell and Bell, 1974) showed carbonatites to be enriched in strontium with low $^{87}\text{Sr}/^{86}\text{Sr}$ ratios, similar to those of mantle-derived basalts (0.703-0.706). High concentrations of rare earth elements (Deans and Powell, 1968) provided a third indicator of a magmatic or primary origin for carbonatites. No single field of study itself produced unambiguous evidence in all cases but the combined evidence clearly showed carbonatites to be products of mantle-derived melts and not of limestone syntexis.

The inverse model, that of sial syntexis in which sialic crustal material is assimilated by primary carbonate magma to form alkaline silicates (e.g., Von Eckerman, 1948; Holmes, 1950; Dawson, 1966) is equally unsatisfactory because isotopic and trace element data indicate a mantle origin for alkaline rocks as well as for the associated carbonatites (e.g., Powell and Bell, 1974).

The problem presently posed is that of elucidating the processes by which both carbonatites and the

interdependent (Le Bas, 1977) alkaline rocks are generated from mantle sources.

An additional factor is added by the presence in many alkaline complexes (Sorensen, 1974; Currie, 1974) of silica-saturated as well as undersaturated rocks. The relationship between the two types is not necessarily the same in all instances (complexes may begin or end with saturated units; Tilley, 1958) although in some cases such as Kangerdlugssuaq, East Greenland it appears (Brooks and Gill, 1982; Pankhurst et al, 1976) that undersaturated magma of mantle origin has reacted with sialic crust to produce the saturated series.

The Big Spruce Lake, N.W.T. alkaline intrusion provides a unique opportunity to examine relationships between all three rock types and to characterise a pre-Cambrian mantle source region. The main complex consists of a silica-saturated series, an undersaturated suite and carbonatite, emplaced within a small area apparently in the order listed (Martineau, 1970). A satellite intrusion exposed 5 km to the southeast consists of potassium-rich rocks. The age of the complex was placed at 2170 ± 40 Ma from Rb-Sr whole rock data (Martineau and Lambert, 1974). The complex is isolated from other intrusive bodies and lies in the western portion of the Slave craton. The Slave province has been relatively stable for

about 2.5 Ga (McGlynn and Henderson, 1970) and the complex appears to be unaffected by major metasomatism and plastic deformation since original textures and compositions are present. The complex was mapped and the petrology described by Martineau (1970). The objectives of the present study are:

- (1) To re-examine the field evidence in order to verify features of the geological map, prepared by Martineau in 1970, which are essential to interpretation of additional geochemical and isotopic data.
- (2) To examine petrogenetic relationships within each of the four major rock types outlined above and to determine the relationships (if any) between them by means of trace element abundances and ratios.
- (3) By means of whole rock Rb-Sr, Sm-Nd and Pb-Pb studies as well as U-Pb of zircons to
 - (a) constrain the age of the complex and, if possible, determine the time span over which the sequence of rock types was emplaced, thus relating the intrusion to the regional tectonic history,
 - (b) provide additional information on relationships between rock types and determine the degree of crustal involvement, and
 - (c) characterise the Sr, Nd and Pb isotopic

composition of the (mantle) source region(s)
which is/are the source of the alkalic complex
and lay beneath the Slave craton at about 2.2
Ga.

CHAPTER 2

GEOLOGY

A. Introduction and General Geology

The Big Spruce Lake intrusive complex is located about 150 km northwest of Yellowknife, N.W.T. The main complex, roughly oval in shape and about 3.5 x 9.0 km, is centred at 63° 33'N, 115° 55'W. Intrusive rocks consist of an alkali gabbro-syenite series, a nephelinitic series and associated carbonatites shown in outline on Figure 1. A satellite intrusion consists of a number of small, scattered, high-potassium mafic bodies exposed about 5 km southeast of the main complex. The complex intrudes granitic to granodioritic gneisses at the western edge of the Slave structural province.

The complex was first mapped by Lord (1942), who noted the diversity of silicate rock types and the presence of a carbonate lens (carbonatite) which he interpreted as limestone intruded by the complex. Two prominent magnetic anomalies (Geological Survey of Canada Geophysical Paper 2966G, 1963) and the earlier outline of the character of the intrusion sparked economic and academic interest. The main complex was examined briefly

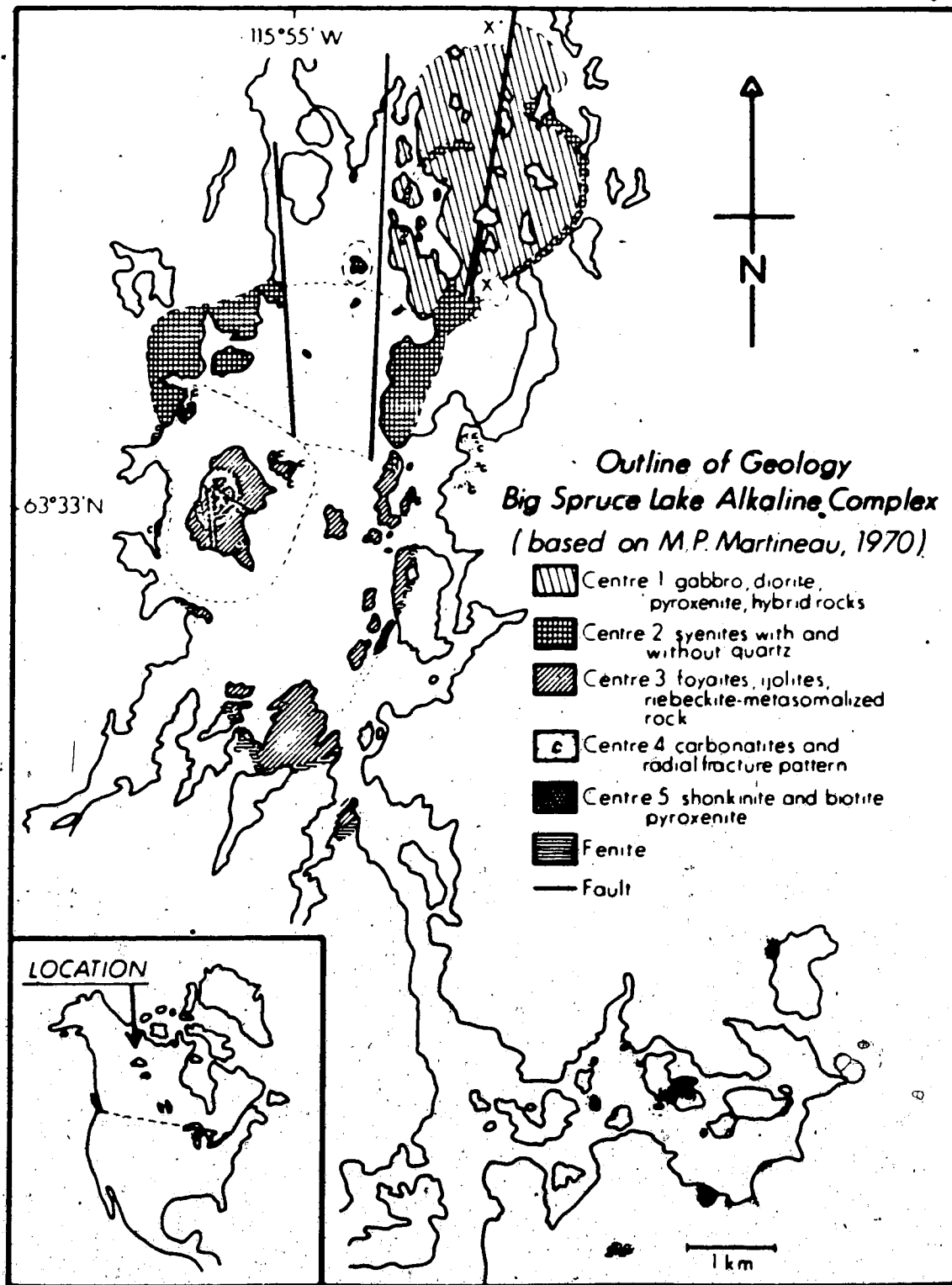


Figure 1. Location map and outline of the geology of the Big Spruce Lake alkaline complex.

by Lambert (1964) and then mapped and described in detail by Martineau (Martineau, 1970; Martineau and Lambert, 1974). Extensive exploration work, including trenching and drilling, was carried out by Giant Yellowknife Mines Ltd. during 1967-1969. No economic deposits of elements commonly associated with alkaline silicate-carbonatite complexes (e.g., rare earth elements, niobium, zirconium, phosphorus, barium) were located but during exploration work several exposures of the satellite intrusion were located and included in Martineau's study.

The complex is presently about 60% covered by the water of Big Spruce Lake which is the reservoir for the Northern Canada Power Commission Snare Rapids hydro-electric plant. The complex is exposed around the lake and the disadvantages of the water-covered area are largely offset by long shorelines of the mainland and numerous islands which afford excellent sections through the complex.

Field work for the present study was carried out during two one-month periods in June 1981 and June-July 1982. The author was accompanied by a field assistant (S. Launspach in 1981, G. Bailey in 1982) and Dr. D.G.W. Smith, Department of Geology, University of Alberta was present for a total of 2 1/2 weeks during field work. Field work followed a prolonged period of very low

precipitation in the area which left the water level in Big Spruce Lake 4 m below normal and produced excellent shoreline exposures. Dense vegetation covers much of the complex and Martineau's detailed mapping of the gabbroic ring complex in the northeast portion of the intrusion was greatly facilitated by a forest fire which had earlier (1964) stripped the vegetation along the east side of the lake. In the present work detailed study and sampling of the recently exposed shoreline is complementary to Martineau's earlier study of exposures now re-covered by vegetation. Martineau's mapping and description of the petrology of the complex provided the background for field work and sampling in the present study. The brief outline of the geology included here to provide a context for the geochemistry follows Martineau's interpretation, revised and/or expanded as needed by the present study. Revised geological maps are included in the map pocket.

The numerous and diverse alkaline silicate rock types of the complex can be separated readily into four major groups, each of which is petrographically and geographically separate from the others. Three of these form the oval shape of the main complex and field relations clearly show a time sequence of emplacement with the centre of intrusive activity progressing from the northeast to the southwest (Figure 1). The earliest group

is composed of silica-saturated diorites, a gabbroic ring complex and massive magnetite pyroxenites (Centre 1) emplaced at the northeast end of the complex. These were followed by massive red-brown weathering syenites with and without modal quartz (Centre 2), emplaced near the centre of the main complex. The syenites in turn were followed by grey to black nepheline-rich rocks emplaced to the south and west of the syenites (Centre 3). The fourth alkaline-silicate group, shonkinites and biotite pyroxenites, is exposed in the satellite intrusion whose relationship to the main complex cannot be determined by field relations. This group is placed last as Centre 5. Intrusive activity listed as Centre 4 in the time sequence is carbonatitic, associated with the main complex. Carbonate rocks are temporally and petrographically, but not geographically, distinct from the silicate rocks of the main complex. Calcitic intrusive rocks lie mainly within the western-southwestern boundary of the complex cutting Centres 2 and 3, while dolomitic rocks intrude the gneisses immediately to the east of the complex.

A prominent aureole of red, feldspathic fenite surrounds the nephelinitic rocks of Centre 3. Porphyry dykes carrying phenocrysts of nepheline and/or feldspar cut gneisses and the silica-saturated rocks of Centres 1 and 2 but not Centre 3. Broad basic dykes, regional and

trending NNW, cut both the main and satellite intrusions. A second set trending ENE also cuts the area of the satellite intrusion. A number of circular and radial fracture systems similar to "gas vents" (Martineau, 1970) are present around the southern portion of the complex but these are largely aerial photo features and no field evidence was found to link them to the complex.

The complex lies on the Snare Fault, a major north-south lineament with sinistral lateral movement. The main fault line enters the study area from the north along the Snare River Channel, changes orientation slightly somewhere within the water-covered area of the complex, and exits to the southeast along the channel leading to the satellite intrusion. The Snare Fault splays to the north and to the south of Big Spruce Lake with smaller fault lines fanning to the northeast and southwest of the main fault line. Some individual splays at the north end are well defined by offset of intrusive rocks: those to the south are not because they cut uniform gneiss. Most of the lateral movement on the Snare Fault occurred prior to emplacement of the intrusive rocks which show little clearly defined offset apart from that of Centre 1.

B. Intrusive Centre 1 - Diorites, Gabbros and Pyroxenites

Intrusive activity began in the northeast corner of the complex,, emplacing a series of silica-saturated rocks. All of the rocks of this centre fall in the hypersthene normative compositional field and some carry modal quartz. Concentric units of an outer diorite and an inner layered gabbro series form an approximately 4.2 km x 2.7 km oval which has been offset by lateral movement on a north northeast-trending splay of the Snare Fault and intruded by magnetite clinopyroxenite (Figure 1).

1. Diorite

The earliest rocks now exposed are the outer diorites which form a ring of variable thickness (150-800 m) around gabbro. (See geological map in map pocket for details.) The diorite exposure is widest to the north where it is in sharp vertical contact with gneiss. To the south and east and much of the western side the ring is narrower and the outer side is in gradational contact with later ring syenite. The remainder of the outer contact on the western side is gradational with intrusive clinopyroxenite. At the inner contact of the ring, gabbro is chilled against coarse leucocratic diorite.

Where diorite is chilled against granodioritic gneiss the gneiss is reddened with recrystallised quartz up to

about 25 m from the contact. In the current study the position of the northwestern diorite-gneiss contact has been revised from that of the earlier work.

Weakly developed laminations and impersistent traces of banding are present in the diorites. The orientation of these features suggests crystal accumulation occurred parallel to near vertical walls of a magma chamber (a relatively mafic diorite) and in layers gently dipping towards the floor (relatively leucocratic diorite) (Martineau, 1970). Troughs within laminated diorite (outlined by mafic bands) indicate that magma currents were active during crystallisation. The evidence suggests a fairly continuous sequence of crystallisation of one or more pulses of similar magma under slightly dynamic conditions; the poor development of laminations and banding, the presence of troughs and a relatively sharp contact between coarse leucocratic diorite and mafic diorite suggest stirring of crystallising magma due to continued fault movement or to the injection of repeated pulses of similar magma, or both.

In outcrop alkali diorite presents an irregular pale pink to white weathered surface, pitted due to differential weathering of mafic and felsic minerals. The mineralogy of the diorites varies across the unit. Chilled diorite is porphyritic with phenocrysts of

plagioclase (An₅₀₋₅₂) and titanite in a matrix of perthitic alkali feldspar, hornblende and quartz. Apatite and Fe-Ti oxides are also present. Away from the contact with gneiss the diorite becomes more equigranular (medium-grained), the range of An content becomes 25 to 35 and the amounts of hornblende and quartz decrease. The more leucocratic inner diorites (weakly laminated parallel to the floor of the chamber) contain plagioclase of An₂₈₋₃₄ in a matrix containing titanite, green hornblende, subhedral to euhedral Fe-Ti oxides; variable amounts of stubby apatite, and quartz appears in the matrix of many samples. Zircon has also been noted (Martineau, 1970).

2. Gabbro Series

An alkali gabbro series comprises the inner portion of Centre 1. A generally massive, coarse-grained dark-weathering gabbro with prominent feldspar (Big Feldspar Gabbro, BFG) is chilled against the outer diorite ring. This outer gabbro consists of phenocrysts of subhedral to euhedral andesine (An₄₀₋₄₅, up to 2 cm in tabular form) in a matrix of titanite, Fe-Ti oxides, brown barkevikitic amphibole and apatite. A vertical lamination, seen in orientation of the plagioclase phenocrysts is evidence that this gabbro crystallised against the wall of the magma chamber. The exposed width of this unit is about

300 m. At the inner edge this gabbro is gradational over about 10 m to a more leucocratic and laminated gabbro (Leucocratic Laminated Gabbro, LLG) which is exposed over about 130 m width. In this unit feldspar (approximately An_{45} , 3-5 mm, tabular), titanite, and Fe-Ti oxides are all cumulate phases while apatite, amphibole, late oxides and feldspar are interstitial. Cumulate feldspar is oriented dipping inwards at about 35° . Aggregation of cumulate clinopyroxene and Fe-Ti oxides into discontinuous lenses low in the unit and then into thin bands higher up in the unit imparts the laminations visible in the field. The low dip of the laminations (and feldspar orientation) towards a central point suggests crystallisation with accumulation of crystals on the floor of a chamber while discontinuities and troughs in the mafic banding suggest continued currents in the chamber during crystallisation.

The upper LLG unit is transitional over about 15 m into a rhythmic banded gabbro (Rhythmic Banded Gabbro, RBG). In the rhythmic banded gabbro an irregular sequence of complementary mafic (clinopyroxene and Fe-Ti oxides) and feldspathic bands is hosted by a fairly uniform and weakly laminated gabbro. The interval between bands is variable, in general 30 to 80 cm. The bands are commonly 5 to 10 cm wide; most often a lower mafic layer of

magnetite-clinopyroxenite is followed by a feldspathic layer which is about 85% andesine. The host gabbro is similar in mineralogy to the earlier marginal feldspar, BFG, with somewhat less apatite and a greater proportion of barkevikitic amphibole. The exposed RBG is about 55 to 60 m thick but the unit, which forms the centre of the ring complex, is disjointed by subsequent faulting. Any differentiates which may have followed the RBG in this magma chamber have been removed by erosion.

Martineau (1970) proposed that the RBG is the result of greatly increased convection currents (convective overturns) which caused crystal sorting into mafic/feldspathic bands during the crystallisation of the homogeneous host gabbro. Such activity could have been triggered by increased faulting with or without the influx of new magma. A detailed electron microprobe study of the mineral chemistry across this unit might reveal cryptic layering indicative of the number of magma pulses involved.

Solidification of the gabbroic series was followed by a period of faulting (lateral offset on fault X-X', Figure 1) and emplacement of magnetite clinopyroxenites within the diorites and gabbros.

3. Magnetite Clinopyroxenite

Magnetite clinopyroxenites were emplaced in two forms, as a large arcuate mass (approximately 1 km across) in the northwest portion of Centre 1 and as numerous small dykes and lenses cutting the central portion of the diorites and layered gabbros. Pyroxenite intrusive activity is inferred to be confined to the conduit system previously used for emplacement of diorite and gabbro because the main pyroxenite body and most smaller ones lie within a volume interpreted (Martineau, 1970) as having been previously occupied by diorite and layered gabbros. Emplacement of pyroxenite was apparently controlled by ring fractures formed during emplacement of gabbro and diorite.

The small dykes and lenses which cut the central layered sequence (vertically) vary from a few cm to 30 m in width, with the larger dykes exposed over lengths of 50 to 1000 m. The longer dykes are approximately concentric with the layered intrusion. Emplacement of these smaller bodies apparently occurred throughout a period of repeated fault movement. The most prominent fault cutting the layered gabbro (labelled X-X', Figure 1) is a splay of the main Snare Fault system and is itself separated into two splays within Centre 1. Repeated movement on this fault during pyroxenite emplacement is revealed by field

relationships of individual small pyroxenite bodies. A small pyroxenite lens which intrudes the northwestern lobe of diorite is offset by the fault (X-X'), yet a pyroxenite body, unfractured, fills the space between the two splays of this fault at the south end of the layered complex.

Smaller pyroxenite bodies are chilled (olivine and pyroxene phenocrysts) against gabbro or diorite but larger bodies often show hybridised contacts.

At the northwest contact with gneiss, intrusion of pyroxenite has remobilised gneiss for distances up to 25-30 m. Assimilation of remobilised material has produced various hybrid rocks, often with mappable lenses or stringers of felsic material.

Most of the larger pyroxenite units are medium to coarse-grained, equigranular rocks, black on fresh surfaces but weathering to a rusty stain. Clinopyroxene (titanaugite), olivine and Fe-Ti oxides are the main minerals, with average proportions of 60-70%:10-20%:20-25% respectively. Proportions, particularly of olivine and clinopyroxene, vary between bodies and within bodies.

Titanaugite, subhedral to euhedral, commonly shows only minor alteration to brown barkevitic amphibole. Fresh olivine is present but rare. Olivine occurs in rounded and fractured grains which are usually but not always replaced by serpentine and veinlets of magnetite.

Where shearing and alteration has occurred, blue-green amphibole, chlorite, carbonate and hematite/goethite are formed from olivine. Fe-Ti oxides are present almost exclusively as an anhedral mosaic interstitial to titanite and olivine. Small amounts of iron sulphides are present in the oxide matrix as pyrite, chalcopyrite and pyrrhotite. Accessory minerals, particularly apatite, are virtually absent.

Metasomatism of gabbro and diorite accompanied faulting and pyroxenite activity. Shearing, associated with repeated faulting or the intrusion of pyroxenitic magma, and introduction of hydrous volatiles into gabbro and diorite caused localised alteration of feldspar to saussurite accompanied by growth of hydrous mafics (amphibole and chlorite). Hydrous alteration of gabbro and diorite is most evident in shear zones and around the pyroxenites.

C. Intrusive Centre 2 - Syenites

Following the period of pyroxenite intrusive activity, fault movement, and metasomatism of the gabbros and diorites, the geographical focus of activity shifted towards the southwest to emplace a series of silica-saturated to oversaturated syenites. They appear to be

the equivalents of late differentiates of Centre 1, which if they existed, have been removed by erosion. No mafic or intermediate rocks are exposed in association with the syenites and differentiation to produce syenitic liquids must have proceeded in a chamber subjacent to that presently exposed as Centre 1.

The syenites occur in a localised area. The main body is an arcuate mass, about 3.5 km in diameter, around the north end of Big Spruce Lake and adjacent to the southwest edge of Centre 1. A separate small stock or plug is exposed on a small island (Figure 1) which lies partway between the geographical centres of gabbroic (Centre 1) and syenitic (Centre 2) activity. Syenite also forms a ring dyke around Centre 1, largely between diorite and gabbro/pyroxenite.

The syenites clearly postdate Centre 1. The eastern portion of the ring dyke intrudes diorite, forming a transitional contact and "pinching out" in massive diorite to the northeast. The western portion of the ring dyke is chilled against pyroxenite and "pinches out" within the main pyroxenite body. The contact of syenite and diorite at the south end of Centre 1 is not exposed but syenite, itself not offset by the sinistral fault movement, was emplaced across the fault X-X'. Lateral offset of the northern diorite exposure is about 350 m along this fault.

Four syenites are distinguishable on the basis of geochemistry and field relations. The sequence of emplacement of these cannot be determined from field relations but a "line of descent" or differentiation trend is apparent in analytical results and the syenites have been numbered 1 to 4 along that trend. Only the salient points of geochemical differences between syenites are mentioned here; a fuller discussion is included with the geochemical data (Chapter 3).

Two of the syenites are free of modal quartz and both of these occur in proximity to Centre 1. Mafic syenite (Mafic Syenite, S1) underlies essentially all of the Island G and is not exposed elsewhere. A second quartz-free syenite (Quartz-free Ring Syenite, S2) comprises the 50-100 m wide ring dyke around Centre 1. The compositions of both of these syenites plot on a single differentiation trend with the gabbros and diorites of Centre 1 (on major element Harker diagrams). Both have positive europium anomalies on chondrite-normalised rare earth element distribution plots (see Chapter 3). Mafic syenite (S1) precedes Ring syenite (S2) on all major and trace element plots.

Quartz-free ring syenite does not constitute the body of syenite emplaced at the south edge of the diorite across the fault X-X' as previously mapped. This body is

a quartz syenite whose composition is indistinguishable from those of the quartz syenites that make up the main arcuate mass.

The main arcuate syenite body is composed of quartz syenites, the exact number of which is not known with certainty. In the field they are not readily separated into individual units because visible criteria such as colour, texture and mineralogy appear to vary as much within possible units as between. Geochemically they are also very similar and form a single compositional field in which element abundances and ratios differ as much within possible units as between. At least two intrusive episodes are indicated by field evidence. At a contact partly exposed on the west side of the lake an early coarse-grained outer syenite was intruded by a more mafic (at least in the chill) syenitic magma. This later syenite forms a clean contact against coarse syenite on the west and encloses large blocks of coarse syenite in a zone up to 25 m from the contact. No such contact is exposed either on the lakeshore or on the eastern side of the lake. A contact between (the same) two syenites is inferred on the east side of the lake from a linear array of pyroxenite and gneiss screens apparently caught between magma pulses (Martineau, 1970). Because a differentiation sequence within the quartz syenites cannot be established

unambiguously from geochemical or petrographic evidence, they are distinguished on the basis of the foregoing field evidence into an Outer Quartz Syenite (S3) and an Inner Quartz Syenite (S4). Outer quartz syenite forms an arcuate mass of about 3.5 km diameter whose centre lies within the north end of Big Spruce Lake. It forms a discontinuous ring, up to 250 m wide, around the inner quartz syenite and includes the syenite body (previously mapped as ring syenite, S2) extending northeast to abut Centre 1 (see Chapter 3). Exposed inner quartz syenite forms an arcuate mass, 2.5 km diameter, within the outer quartz syenite. Martineau (1970) presented evidence to suggest that this unit is a ring dyke, not continuous within the water-covered area. Inner quartz syenite extends southwest to contacts with the foyaites of Centre 3 visible on both shores of the lake.

Petrographically the mafic syenite (S1) is the most distinctive of the four. It weathers to a very pale pink surface spotted with dark clots (2.5-7.5 mm in size) of mafic minerals. Clear sodic feldspar (anorthoclase) is largely subhedral (0.5 to 1.0 cm) with embayed edges, shows no albite twinning or perthite formation and forms about 50% of the rock. Late anhedral feldspar (10%) and mafic aggregates (40%) are interstitial to feldspar. Anhedral to euhedral Fe-Ti oxides, showing exsolution

lamellae replaced with sphene, form up to 50% of the matrix while augitic pyroxene, largely replaced by pseudomorphs of blue-green amphibole and green biotite forms about 50%. Pyroxene is poikilitic to abundant, coarse (up to 0.5 mm), stubby apatite.

Ring syenite (S2) weathers to the red-brown colour more typical of the syenites. Sodid feldspar (anorthoclase) is present in large (1-2 cm) embayed tablets and as late anhedral grains to make up 75% of the rock. Neither form shows albite twinning but both have a string-rod antiperthite exsolution texture. Early feldspar has abundant inclusions of apatite, sparse euhedral Fe-Ti oxides and rims of albite. Mafic aggregates of pyroxene pseudomorphs, Fe-Ti oxides, primary hornblende, brown biotite and abundant apatite, zircon and sphene, similar to those of the mafic syenite, comprise about 25% of the rock. The pyroxene is green hedenbergite, poikilitic to apatite and oxides, and largely replaced by pseudomorphs of green amphibole (hornblende). Primary brown amphibole (ferrohastingsite) is subhedral and poikilitic to apatite and oxides. Red-brown anhedral biotite occurs with amphibole and pyroxene.

The two quartz syenite units distinguished above (Syenites 3 and 4) are very similar hypersolvus syenites. Both are composed of early feldspar rhombs in a

matrix of late feldspar and aggregates containing fine-grained mafic minerals, Fe-Ti oxides, coarse quartz and abundant zircon. The early feldspar (0.5 to 2.5 cm) is sodic anorthoclase with a well developed rosy perthite structure on all scales from crypto- to meso-perthite and it is rimmed with late mesoperthite. Intergrain boundaries are commonly granulated or sutured with a narrow zone of K-feldspar. Late anhedral feldspar grains are also mesoperthite, sometimes continuous with the K-feldspar rims of early feldspar. The fine-grained mafic aggregates, which make up 20-25% of the rock sometimes contain ill-defined pyroxene pseudomorphs along with quartz (40-45% of the aggregate), Fe-Ti oxides (25-30%), subhedral brown amphibole (near ferrohastingsite in composition), brown biotite, carbonate, acicular apatite, abundant zircon and allanite.

Near contacts with foyaite the inner quartz syenite is fenitised with the development of riebeckite and aegirine-augite.

Within both quartz syenite units highly localised alteration has produced patches and veinlets of brown stilpnomelane. This mineral, which is generally regarded as a metamorphic mineral of the greenschist facies (Winkler, 1973; Brown, 1971), appears mainly but not exclusively in the outer quartz syenite and is usually

accompanied by carbonate and fine-grained quartz. Localised alteration of allanite to fine-grained intergrowths of rare earth carbonates and fluorides, thorite, Fe-Ti oxides and chlorite has also occurred. Similar alteration of allanite in granites of the Canadian Shield has been attributed to action by late state magmatic fluids (Littlejohn, 1971; Cerny and Cerna, 1972). That regional metamorphism to greenschist facies has not occurred is shown by the presence of unaltered biotite, amphibole and pyroxene throughout the main complex and in the satellite intrusion.

D. Intrusive Centre 3 - Silica-undersaturated Suite

Succeeding the quartz syenites (immediately adjacent but still further to the southwest) is a series of rocks strongly undersaturated in silica and designated Centre 3 in the intrusive sequence. The grey to black rocks of this group are extremely variable in texture and contain only three main minerals, alkali feldspar, nepheline and aegirine-augite, and hence form foyaite-urtite and urtite-ijolite groups. This centre is 50-60% under water. The exposed intrusive rocks rim the southern half of the lake in an oval roughly 2.5 km x 4.0 km and form numerous islands. The major portion of the area, to the south and

east, is underlain by leucocratic foyaites (Southern Foyaite). These coarse light-grey rocks (which weather to a characteristic angular rubble) are well-exposed on promontories, islands and small reefs.

About 500 m south of the main unit, along the southeastern outlet to Big Spruce Lake, is a newly-mapped exposure of leucocratic foyaite (Southern Foyaite) about 150 m x 200 m in size. It is isolated from the main unit by gneiss and water. This exposure is inferred to be fault-bounded except to the south where a broad transitional contact with gneiss is well exposed.

Mafic foyaite (Northern Foyaite), dark-grey in colour, finer-grained and more resistant than the leucocratic foyaite is confined to the northwestern portion of Centre 3 being exposed on Big Spruce and Little Spruce Islands and on the mainland to the northwest. Much of the rock on Little Spruce Island has been altered by subsequent carbonatite activity but the host rock appears to be the same mafic foyaite as appears on Big Spruce Island. No contact between northern and southern foyaites is presently exposed but a small zone of mafic breccia on the southern tip of Big Spruce Island carries clasts of leucocratic foyaite from which it is inferred that the mafic types post-date the leucocratic foyaite. Contact of mafic foyaite with quartz syenite on the mainland was well

exposed by low water levels during 1981-1982. Mafic foyaites, sharply chilled against syenite, carries a few small subrounded clasts (up to 25 cm across) of fine-grained foyaites and coarse syenite near the contact. However, within 2 m of the contact well-defined layers of mafic minerals have developed.

Laminated mafic foyaites (previously covered) is exposed on all sides of a small syenite promontory at this location revealing the syenite to be a "raft" (Figure 2). Carbonatite has also intruded the zone of weakness between the raft of syenite and the main body.

Ijolite comprises four separate masses which are all intrusive into the mafic foyaites of Big Spruce Island. The resistant, black ijolite bodies tend to form ridges and low cliffs in comparison with the foyaites.

Leucocratic foyaites (Southern) is surrounded by a zone of fenitized gneiss (and syenite) variable in character and width. Foyaites is chilled against coarse quartz syenite on the east side of the lake in a complex contact zone which is well-exposed at low water levels. Syenite is reddened and veined with blue amphibole (riebeckite/arfvedsonite) up to 15-20 m from the contact. The contact itself is not sharp. Highly altered syenite is transitional to fine-grained foyaites over an interval of about 1 m. Much of the foyaites adjacent to

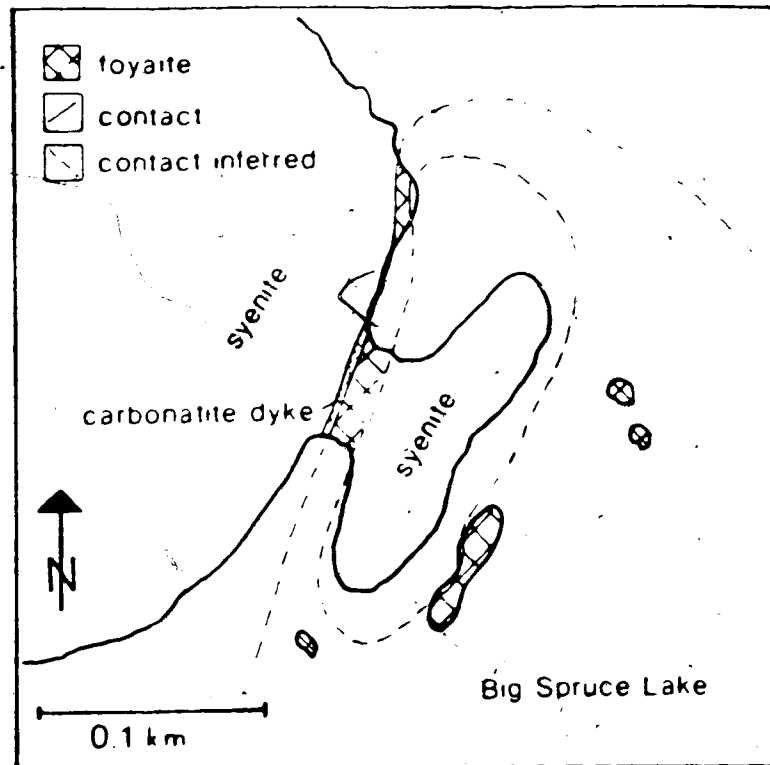


Figure 2. Detailed sketch of the newly-exposed foyaite-syenite contact on the western lakeshore. The peninsula is a syenite "raft" within mafic foyaite. A carbonatite dyke intrudes along the contact.

the syenite carries euhedral nepheline phenocrysts (to 1 cm in size) but there is no foliation or alignment. Beginning with this transitional contact interval and extending up to 5-7 m within the foyaite body is a border zone. The fine- to medium-grained "host foyaite" shows no

layering but the modal mineralogy commonly varies over short intervals (0.5 m) from nepheline-rich to feldspar-rich. A few small lenses of pegmatitic feldspar rock have developed. This variable foyaite carries many clasts up to 1.5 m. These rounded to subrounded clasts are largely foyaitic and some are themselves either extremely variable in modal mineralogy (e.g., zones of ijolite or of sodalite-foyaite) or composites of still earlier phases. The "host" foyaite(s), which cannot be followed as a continuous phase, tends to coarsen away from the syenite, and the border zone passes into coarse leucocratic foyaite. No true layering can be observed above the border zone but about 50 m inside the contact crudely oriented lenses (2-3 m in size) of feldspar pegmatite, urtite and ijolite dip to the southwest.

This complex border zone is present only on the eastern side of the unit. On the western side of the Southern Foyaite coarse foyaite is in abrupt transitional contact with granodiorite. The exact nature of the contact cannot be discerned due to localised fault movement, but fine-grained foyaite is adjacent to reddened and fenitised gneiss along this western margin. The gneiss is remobilised, showing the development of fluidised textures and possibly the injection of new mafic material into the granitic gneiss.

Across most of the southern boundary, including that of the newly-mapped exposure, the contact is very transitional. The rocks pass first from coarse grey feldspathic foyaite to coarse red feldspathic syenite (foyaite/fenite) differing from the foyaite mainly in colour. Continuing away from the foyaite the texture becomes granular gneissic, the colour fades to pink and finally quartz appears. The change from foyaite to granodioritic gneiss can require 20 to 200 m.

The long eastern margin against granodiorite differs yet again in having a chilled and laminated wall zone (Laminated Chilled Foyaite) transitional to a fenite zone in which the innermost rocks are desilicated and recrystallised to the feldspathic foyaite/fenite texture common across the southern contact.

The main part of this leucocratic unit is inhomogeneous in both texture and modal mineralogy. Textures vary from medium-grained to very coarse, sometimes within a single outcrop. Nepheline is usually minor or absent in the coarsest phases. The crude layering immediately above the border zone at the northeastern margin is discontinuous and is not exposed elsewhere in the unit. Other oriented igneous features (apart from the laminated wall zone) are absent from the leucocratic foyaite. The entire body is crosscut by

leucocratic feldspar porphyry dykes and by tinguaitite dykes and veins, and there are internal chilled margins marked by abrupt changes in grain-size and often accompanied by changes in modal mineralogy.

Along the eastern side of the unit post-crystallisation shear and metasomatic activity has created an elongate zone of riebeckite-rich foyaites, associated with both coarse and laminated wall-zone foyaites.

Nepheline and feldspar, in widely varying proportions, are the main phenocryst phases in these undersaturated rocks, in a matrix of fine-grained nepheline, feldspar and aegirine-augite. Cumulus nepheline occurs in blocky hexagonal tablets, up to 1.5-2 cm in size, forming 10-60% of the rock. It exhibits compositional zoning, rings of inclusions (acicular aegirine), resorbed edges, and may be poikilitic to sphene. Nepheline also occurs as late interstitial aggregates. Cumulus feldspar is often Carlsbad twinned antiperthite tablets up to 4 cm long in the coarsest leucocratic foyaites and 1-2 cm in mafic varieties. Microcline and albite can sometimes be distinguished in irregular patch antiperthite exsolution. Feldspar also occurs interstitially as prismatic antiperthite or clear anhedral grains. The major mafic mineral is aegirine-augite which has a significant manganese content. It

occurs as subhedral to euhedral prisms as well as in granular aggregates interstitial to cumulate nepheline and feldspar. Brown biotite occurs in a few foyaites as euhedral-subhedral grains or as interstitial felted masses. Euhedral sphene is a common accessory in leucocratic foyaites; granular sphene appears in mafic varieties. Cancrinite may appear in the interstitial aggregate. Sodalite and fluorite are locally abundant. Granular andradite garnet, associated with and rimming aegirine-augite in mafic foyaites and ijolites on and near Big Spruce and Little Spruce Islands, may be related to high-grade fenitisation processes caused by carbonate activity (Deer et al, 1978, p. 508).

E. Intrusive Centre 4 - Carbonatites

Carbonate intrusive activity has been grouped as the fourth and final phase of the main complex. Carbonate rocks are temporally and petrographically, but not geographically, separate from the silicates and there are two separate foci of carbonatite activity. Calcitic intrusives lie in and around the ijolites and mafic foyaites of Big Spruce and Little Spruce Islands; dolomitic rocks intrude the gneisses immediately east of the complex.

The calcitic carbonatites are extremely varied in intrusive form and in composition. All exposures are small, less than 150 m². They occur as:

- (1) Well-formed sövite dykes up to 3 m in width. The calcite-carbonatite dykes fall into three groups based on mineralogy. Cutting gneiss to the west of Big Spruce Island is a medium- to coarse-grained manganese-rich pink sövite which bears phenocrysts of pyrite (to 1 cm) and magnetite (to 1 mm) as well as fine-grained quartz, barite and bastnaesite. Massive quartz rims portions of this dyke as well. To the northwest of Big Spruce Island a sövite dyke cuts fine- to medium-grained foyaite and syenite and bears riebeckite and abundant fluorite. On Little Spruce Island the sövite dykes are commonly grey and foliated, the colour being derived from mafic aggregates of allanite accompanied by riebeckite and sphene. The foliation appears to be a result of flow, sometimes around feldspathic country rock inclusions. A similar grey sövite dyke is exposed on one of the small islets immediately west of Big Spruce Island. Sharp, chilled contact against gneiss, syenite or foyaite is typical of these dykes.
- (2) Coarse-grained carbonate rocks with silicate in all proportions. Units of these rocks commonly exhibit

no clear field relations. Many of these are found on an islet immediately west of Big Spruce Island and on Little Spruce Island. These rocks may be primary in origin or hybrids due to interaction of host foyaite or ijolite with a later carbonate phase.

- (3) A carbonated minette breccia pipe in the gneiss immediately west of the main complex. The pipe, 10-15 m in diameter, carries subrounded fragments up to 1.25 m across of gneiss, mafic rocks, foyaite and porphyry dyke rock in a matrix of biotite, calcite and Fe-Ti oxides plus sphene and apatite.
- (4) A radial and concentric pattern of recessive rocks outlined in the foliage pattern of Big Spruce Island and visible in air photographs. This was interpreted by Martineau (1970) as due to shear zones floored by calcite carbonatite pegmatite. They were mapped by Martineau from the original air photographs taken in 1946. Much of the pattern discernible on the 1946 photographs has been either altered or obliterated by exploration work (trenching) carried out by Giant Yellowknife Mines Ltd. in 1967-1968 and the distinctive pattern now visible from the air is largely man-made.

In general, exposure on Big Spruce Island is very poor, with muskeg inland and sand and rubble on the shoreline. No pegmatitic carbonatite is presently exposed

on Big Spruce Island. Rubble on the western shore, where the concentric pattern intersects the waterline shows abundant very coarse magnetite and weathered coarse biotite which might be related to the pegmatitic carbonatite reported to underlie the radial and concentric pattern.

Although calcitic activity was centred on and around Big Spruce Island, the entire complex and surrounding area are cut by veins and small dykes inferred to be part of a final carbonate phase. Typically these dykes are coarsely foliated or composite with mafics (commonly biotite) plus quartz and carbonate and often fluorite.

The large limestone lens with abundant fluorite (carbonatite) reported by Lord (1942) to lie in the syenite at the southeastern tip of what is now designated as Island K is covered by water.

All significant dolomitic exposures lie just outside the complex to the east. These carbonatites are dykes and pipes of magnetite-dolomite-carbonatite cutting gneissic country rock. The largest is a pipe about 10-12 m in diameter which extends to a height of about 20 m through and above the surrounding gneiss. It carries many xenoliths of fenitised gneiss and is itself brecciated in places. Around this pipe lie several slightly arcuate and concentric dolomite-carbonatite ring-dykes, together with

other dykes, one of which trends easterly to connect with a second small pipe. In this second pipe phenocrysts of magnetite up to 0.5 cm across are weathered out at the surface. Two additional small (3-5 m) pipes (located in 1982) are exposed on Island P, closer to the main complex. These are the westernmost dolomites yet located. Other small exposures of dolomite may well exist on the linear trend predicted by Martineau, in the covered area to the northeast of the largest pipe or dome.

F. Intrusive Centre 5 - Satellite Intrusion at Moose Island

The satellite intrusion (Moose Island Intrusion), Centre 5, is composed of over twenty individual bodies of potassium-rich mafic rocks (shonkinites, biotite pyroxenite and minettes) lying in an area 3 km x 4 km, centred about 5 km south of the main Big Spruce Lake complex. Each body is separated from the others by granodioritic gneiss, water or both. The relationship of this intrusion to the main complex cannot be established from field relations.

Individual exposures take the form of small pipes with radiating dykes, lenses and irregular bodies which range in scale from 1-2 m across up to 150 x 400 m. On

the large island at the centre of the area (Fish Island; Figure 3) individual outcrops suggest that shonkinite underlies gneiss in a sill-like form. Some inland

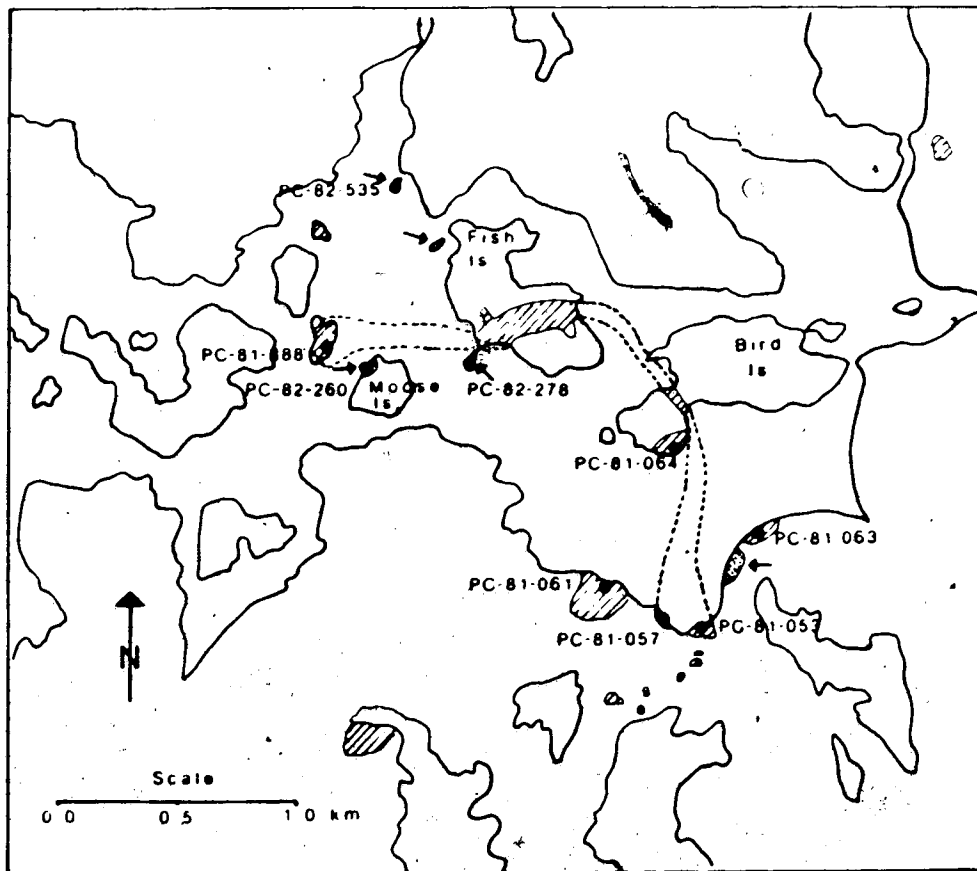


Figure 3. Outline map of the satellite intrusion indicating the arcuate dyke form inferred by Martineau (1970). Originally mapped bodies are cross-hatched, additional bodies mapped in 1981-1982 are stippled.

portions of the area are still incompletely mapped for small exposures but the available evidence suggests that the islands and shorelines of the central area, which have been well examined, are of greater significance. Almost all of the exposures mapped to date are located within the 60,350 gamma contour of the aeromagnetic map (Geological Survey of Canada Geophysical Paper 2966G, 1963); background in the area is about 60,000 gamma. On the basis of then available evidence including an analysis of aeromagnetic data, Martineau (1970) suggested a single main intrusive body, an arcuate dyke, was surrounded by a number of small pipes.

A brief computer-assisted re-evaluation of the aeromagnetic data (J. Samson, Department of Physics, University of Alberta, pers. comm. 1981) confirms that a single body with near-vertical contacts is responsible for the aeromagnetic anomaly. The actual shape and character of this main intrusive body is difficult to determine with any degree of certainty because the area of most interest is largely covered by water. The presence of several previously unmapped bodies (newly or better exposed by lower water levels) suggests that the main body underlies a greater area than that of the narrow dyke originally suggested by Martineau, particularly at the northwestern

and southeastern ends. Present exposure of the linear body suggested by Martineau is not continuous. It is interrupted by gneiss at the northern edge of Bird Island, evidence of the upward discontinuity of the body.

All of the small pipes surrounding the central area carry subangular to rounded gneissic inclusions up to 1 m in size. This suggests wallrock-magma interaction at the boundaries, evidence that the bodies presently exposed represent the upper levels reached by the intrusion.

The many small pipe-like bodies which lie in the outer area and are unconnected on the surface may be individual upward fingers from a single parent body whose major upward extensions lie in and around the water-covered areas to the northwest and southeast ends of the dyke form originally proposed by Martineau.

In the light of the foregoing discussion, water-covered contacts between individual bodies cannot be inferred and are omitted from the accompanying geological map.

All of the intrusive rocks of the Moose Island centre are petrographically similar, differing mainly in grain size and modal abundances of the main minerals. Exposed rocks are composed of clinopyroxene, biotite, olivine, feldspar, Fe-Ti oxides, sphene and apatite. They are classified as shonkinite, olivine shonkinite or biotite

pyroxenite on the basis of modal abundances of the first four of these. Shonkinite contains 10-35% alkali feldspar plus pyroxene, biotite and accessories; olivine shonkinite contains more than 1% olivine; biotite pyroxenite contains pyroxene (>50%), biotite and less than 10% feldspar.

In outcrop all of the intrusive rocks are medium- to coarse-grained, black, and weathering to a characteristic dark brown. Igneous features such as laminations or foliation are weak to absent. Sometimes pyroxene is crudely aligned parallel to the margins of the body. The larger bodies are usually sharply chilled against granodiorite but smaller bodies sometimes have a narrow zone (less than 1 m) of inhomogeneous hybridisation and may carry xenoliths of gneiss or shonkinite chill. Around two biotite pyroxenite bodies the gneiss is reddened and fenitised up to 25 m from the contact.

Clinopyroxene forms subhedral to euhedral prismatic grains up to 5 mm in length and is commonly zoned. Cores are usually augite, rims are either titanaugite or sometimes diopside-hedenbergite. Compositional change is usually abrupt and is accompanied by a band of included olivine, biotite or oxide grains. The size distribution of pyroxene in any one rock may be seriate, bimodal or essentially invariant.

Biotite is anhedral to euhedral, extremely variable in grain size from micro to about 10 mm and strongly pleochroic from straw yellow to deep red-brown. Phenocrysts often have Fe-Ti oxide grains emphasising cleavages. Interstitial biotite may be poikilitic to late pyroxene, Fe-Ti oxides, olivine and apatite but rarely to sphene. Biotite is rarely altered.

Olivine occurs as fractured and rounded grains in some of the coarser shonkinites. Rimming and veining by biotite or green hedenbergitic pyroxene is common. Complete alteration to magnetite veined masses of tremolite/talc/iddingsite occurs in some areas.

Feldspar in the biotite pyroxenites (less than 10%) is clear, anhedral, untwinned alkali feldspar. In the shonkinites feldspar is sometimes anhedral, sometimes subhedral (laths) microcline/cryptoperthite, clear and unaltered.

Iron-titanium oxides, anhedral to euhedral, vary from 5-15% of the rock, being most abundant in shonkinites, least in biotite pyroxenites. Apatite, stubby to prismatic, is most abundant in biotite pyroxenite (up to 10%). Sphene, strongly pleochroic, subhedral to euhedral, is interstitial to pyroxene and biotite and is most abundant in the biotite pyroxenites. Irregular grains occur in some shonkinites.

Little post-intrusive shearing and alteration has occurred and apart from some of the vapour-rich minettes the intrusive rocks are fresh.

CHAPTER 3

ELEMENT GEOCHEMISTRY

A. Introduction

A generalisation can be made that the isotopic composition of an igneous rock reflects the time-integrated history of its precursor(s) while the element composition reflects the processes (partial melting, mixing, fractional crystallisation, metasomatism, etc.) which last acted on the precursor(s) to produce the rock. The two aspects are equally important to a full understanding of the petrogenesis of any intrusion and both have been studied in the present work.

Within the numerous and diverse major units of the Big Spruce Lake intrusion intra-unit differences are sometimes as great or greater than inter-unit differences. Cumulate layering, brecciation near contacts, veining and multiple pulses, modal inhomogeneity on scales from hand-specimen to outcrop and localised late deuteric or metasomatic activity, all visible to some extent in the field, contribute to variable element concentrations. Fully representative sampling is difficult and any comprehensive study of element

geochemistry would involve a large number of samples beyond the scope of presently available facilities.

In the present study emphasis has therefore been placed on determination of isotopic compositions, which are largely independent of the sampling difficulties outlined above, and on determination of concentrations of trace elements for which relative abundances and ratios are discriminant factors for source materials and geologic processes.

Detailed analyses (37 elements) were carried out on 44 whole rock (WR) samples listed in Table 1. XRF analyses (18 elements) were carried out on five others also listed in the table. Individual descriptions are given in Appendix 1 and locations are shown on the Sample Locations Map (map pocket). Initial selections were made to obtain at least one "average" sample from each major unit (as unaltered as possible); additional samples were selected as required to fulfil the following objectives:

- (1) To distinguish and characterise individual units geochemically using major, minor and trace element abundances.
- (2) To determine, in conjunction with isotope analyses, the degree and possible sources of any contamination.
- (3) To examine the geochemical relationships between rock types.

Table 1. List of analysed samples.

Fully Analysed Sample	Rock Unit or Type
<u>Centre 1</u>	
PC-81-001	Magnetite Pyroxenite
PC-81-004	Magnetite Pyroxenite
PC-82-163	Magnetite Pyroxenite
PC-81-363	Diorite, Outer Mafic
PC-82-173	Diorite, Inner Leucocratic
PC-81-235	Big Feldspar Gabbro
PC-81-275	Leucocratic Laminated Gabbro
<u>Centre 2</u>	
PC-81-012	Mafic Syenite (S1)
PC-81-332	Mafic Syenite (S1)
PC-82-124	Ring Syenite (S2)
PC-82-129	Ring Syenite (S2)
PC-82-096	Outer Quartz Syenite (S3)
PC-82-099	Outer Quartz Syenite (S3)
PC-82-151	Outer Quartz Syenite (S3)
PC-81-364	Outer Quartz Syenite (S3)
PC-82-358	Outer Quartz Syenite (S3)
PC-81-285	Inner Quartz Syenite (S4)
<u>Centre 3</u>	
PC-81-482	Leucocratic Southern Foyaite
PC-82-039	Leucocratic Southern Foyaite
PC-81-165	Mafic Northern Foyaite
PC-81-194	Mafic Northern Foyaite
PC-81-287	Mafic Northern Foyaite
PC-82-525	Ijolite
PC-82-526	Ijolite
PC-81-168	Melteigite (reef)
PC-82-041	Melteigite (dyke)

(continued)

Table 1. (Continued)

Centre 4

PC-81-176	Calcitic Carbonatite lens
PC-81-383	Calcitic Carbonatite lens
PC-81-185	Calcitic Carbonatite dyke cuts gneiss
PC-82-088	Calcitic Carbonatite dyke cuts syenite/foyaite
PC-81-178	Calcitic Carbonatite grey, foliated dyke
PC-81-376	Calcitic Carbonatite grey, foliated dyke
PC-82-506	Calcitic Carbonatite grey, foliated dyke
PC-82-408	Magnetite Dolomite Carbonatite
PC-82-412	Magnetite Dolomite Carbonatite

Centre 5

PC-81-057	Shonkinite
PC-81-388	Shonkinite
PC-82-260	Shonkinite
PC-81-061	Biotite Pyroxenite
PC-82-278	Biotite Pyroxenite

Gneisses

PC-81-025	Granodiorite - near damsite
PC-81-483	Granodiorite - southeast
PC-82-074	Granodiorite - southwest
PC-82-281	Granodiorite - northwest

XRF Analysis Only

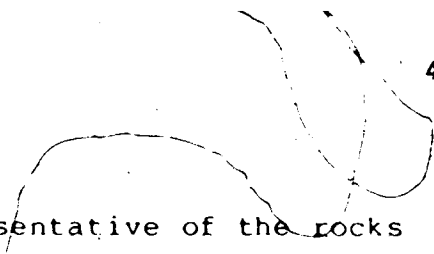
PC-81-392	Centre 5 - Shonkinite
PC-81-053	Centre 5 - Shonkinite
PC-81-063	Centre 5 - Biotite Pyroxenite (sheared)
PC-82-535	Centre 5 - Shonkinite
PC-81-064	Centre 5 - Biotite Pyroxenite

- (4) To confirm sample selection for isotope analysis and provide an aid to interpretation of isotope data.
- (5) To characterise, as far as possible, the magma(s) involved and possibly the source region(s).

Seven samples were selected from Centre 1 for complete analysis. The single sample of leucocratic laminated gabbro selected, a slab 2 cm x 10 cm x 15 cm, was oriented with the long dimension perpendicular to laminations. No sample of the banded gabbro was included because the scale of inhomogeneity precluded selection of a representative whole rock sample. Detailed examination of felsic and mafic portions of this unit for rhythmic and/or cryptic layering has been left for a later study. Two samples of the diorite were included, an outer mafic and an inner leucocratic sample. Three magnetite pyroxenites were chosen to characterise this unit.

A total of ten syenites were included, each from a well-defined location in the field. Two are mafic syenites, two are clearly ring syenites, four are quartz syenites from the main body and two are from the body previously mapped as ring syenite and reclassified in this work as quartz syenite. The syenites were selected for analysis following a thin section and hand specimen survey of over 90 samples from Centre 2.

Nine samples of silica-undersaturated rocks were



selected from Centre 3 to be representative of the rocks now exposed and to cover the range from leucocratic to mafic types. The original selection of samples for whole rock trace element and isotopic analysis was made in the field and unusual localised rock types such as sodalite- or fluorite-rich lenses or the highly metasomatised foyaites adjacent to carbonate activity on Little Spruce Island were not included.

Carbonatites were selected to cover the range of different types of intrusive forms. Two are dykes cutting gneiss or syenite/foyaite cleanly, two are lenses or bodies with indeterminate field relations within the mafic foyaites and three are from similar, foliated sövite dykes which were selected to ascertain the degree of geochemical similarity. The two magnetite dolomite carbonatite samples are from separate pipes.

The five samples selected from the satellite intrusion, each from a different exposure, are insufficient to fully characterize the geochemistry of this unit but they do represent the possible range of compositions. Five additional samples from the satellite intrusion were analysed by XRF only.

A survey of the element geochemistry of the Big Spruce Lake complex was carried out by Martineau (1970) in conjunction with his petrologic study. One hundred and

twenty-nine samples were analysed for 11 major/minor elements and 102 of these were analysed for one or more of Rb, Ba, Sr, La, Ce, Y, Zr and Nb by XRF. Of the 129 analyses 14 are of granodiorite or fenite, 19 of various dykes, 16 from the satellite intrusion and 80 from the 16 major units outlined by Martineau as comprising the main complex. The number of samples selected from each of the 16 units varies from 1 to 12. These data have been correlated with the results of the present study, wherever possible, to enlarge the data base for interpretation.

B. Analytical Methods

Concentrations of 10 major/minor elements and 27 trace elements were determined by four different methods. The method used for each element is indicated in the tables of analytical results which are presented in Appendix 3. Some elements were determined by two different methods and in these cases only the preferred values are reported.

All samples were ground in an agate swing mill to prevent contamination. Ten major/minor elements and eight trace elements (Ba, Mo, Nb, Pb, Rb, Sr, Y and Zr) were determined by fused glass and pressed pellet XRF analysis at Midland Earth Science Associates, Nottingham,

England. Eighteen trace elements were determined by instrumental neutron activation analysis (INAA) at the University of Alberta SLOWPOKE Facility. Uranium was determined by delayed neutron counting (DNC) at the Slowpoke Facility in most samples and by INAA in the remainder. The elements Sm, Nd, Rb, Sr, Pb, and U and Th were determined in some samples by standard isotope dilution techniques. Details of sample preparation and analytical methods are given in Appendix 2.

C. General Geochemical Results

The geochemical data separate readily into four divergent groups, one carbonate and three silicate, that reflect the petrologic divisions and sequence observable in the field. Basic differences between the three silicate groups, each of which will be more fully characterised in later discussion, are readily demonstrated on two commonly used classification diagrams.

The gabbros, diorites and syenites of Centres 1 and 2 can be combined to form a single differentiation series in which $\text{Na} \gg \text{K}$. The compositions of magnetite pyroxenites do not plot on the main trend of this series, so they will be discussed separately. On an alkali-silica diagram (Figure 4) gabbros to syenites form a single trend line in

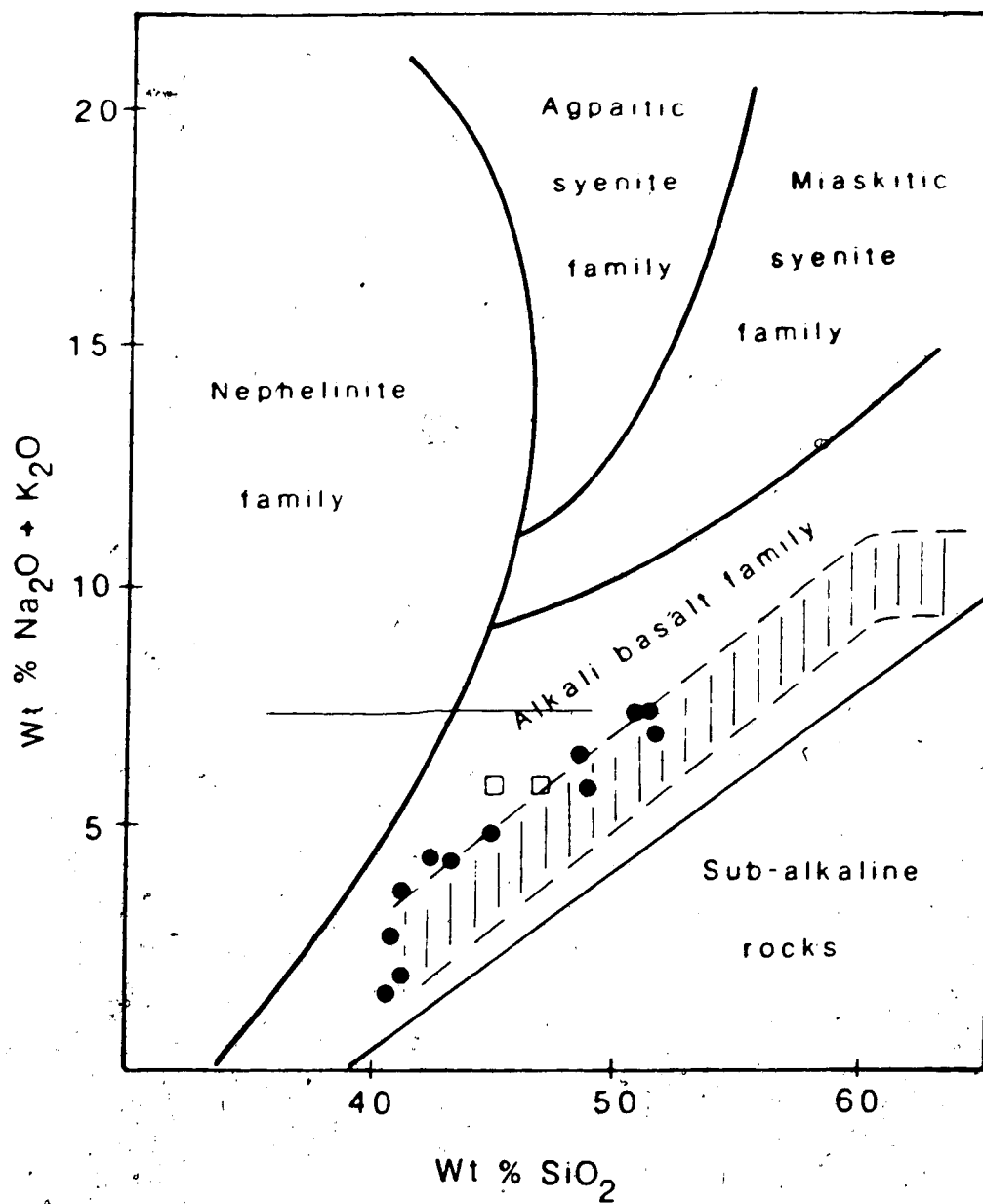


Figure 4. Alkali vs silica classification diagram (modified from Currie, 1974) showing the compositions of analysed samples from intrusive Centres 1 and 2 (gabbro-syenite series, ruled area) and from the satellite intrusion (shonkinites and biotite pyroxenites, solid circles). The composition of two shonkinites from Shonkin Saq, Montana (Hurlburt, 1939) are shown for comparison (open squares).

the field of alkali basalt/gabbro. The series is mildly alkaline, plotting slightly above the Macdonald-Katsura line commonly used to separate alkaline from subalkaline basalts. Similarly on a plot of peralkaline indices (PI) vs silica (Figure 5) this series falls well within the typical alkali basalt field. The $\text{Na}_2\text{O}/\text{K}_2\text{O}$ ratio ranges from 1.0 to 4.8 in this group.

Shonkinites and biotite pyroxenites from the satellite intrusion, another major silicate group, have a more limited compositional range than that of the gabbro-syenite series and form a shorter trend at slightly higher alkali values on the alkali-silica diagram, but still within the alkali basalt field. Lower and variable aluminum abundance (relative to total alkali) produces higher and more variable peralkaline indices. Higher peralkaline indices and the dominance of potassium over sodium in these rocks ($\text{Na}_2\text{O}/\text{K}_2\text{O} = 0.14$ to 0.75) easily separates them from the gabbroic series.

The third silicate group is strikingly different geochemically as well as petrographically, deficient in alumina as well as silica relative to alkalis. These are the foyaites and ijolites of Centre 3. Neither the alkali-silica diagram nor the PI-silica diagram is particularly advantageous in classifying these rocks. Wide compositional variation with no cohesive trend of

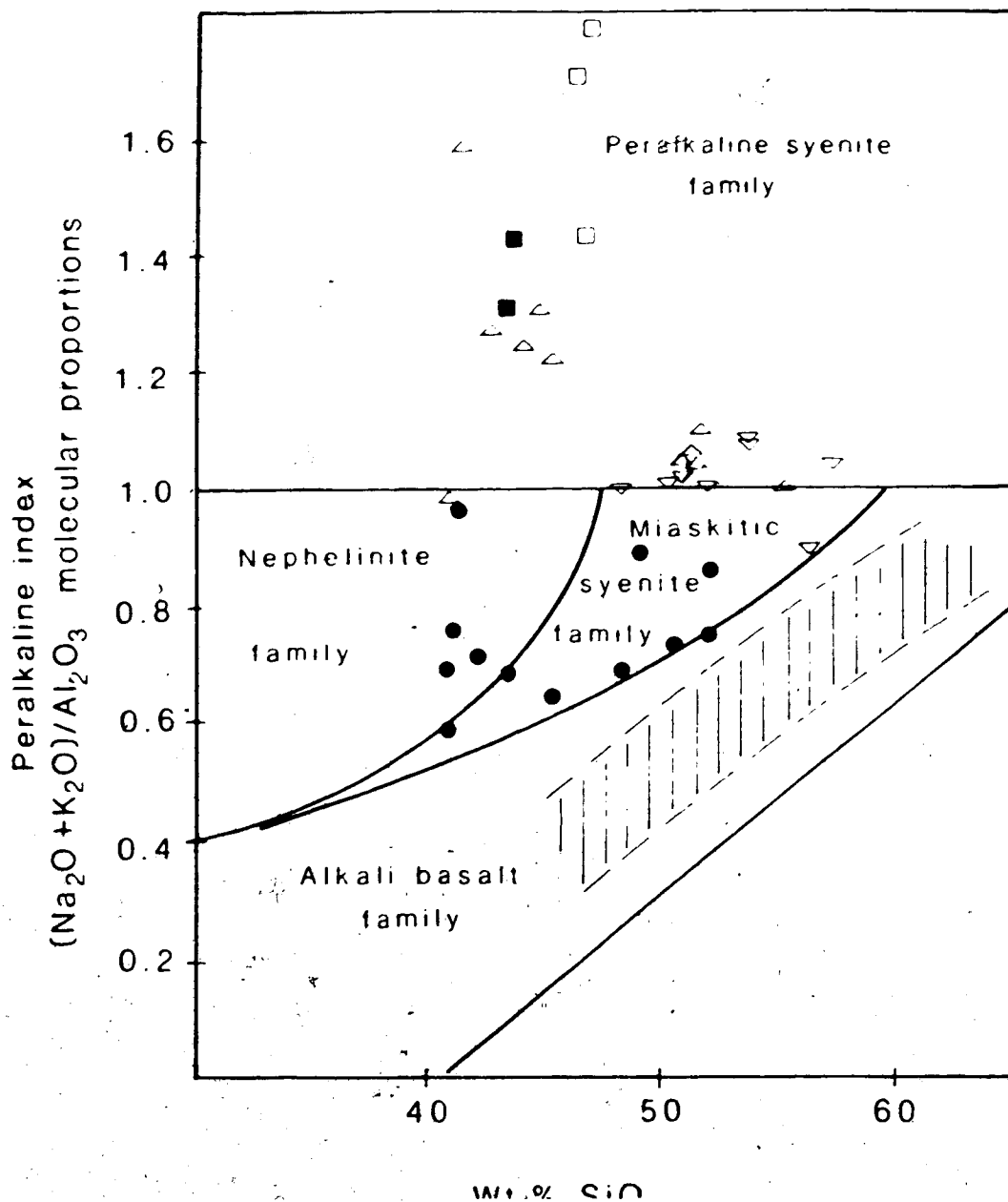


Figure 5. Peralkaline index vs silica diagram (modified from Currie, 1974) for silicate rocks from the Big Spruce Lake intrusion. Ruled area indicates gabbro-syenite series and solid circles indicate shonkinites and biotite pyroxenites of the satellite intrusion. Rocks from Centre 3 are indicated by inverted triangles (southern foyaites), upright triangles (northern foyaites), solid squares (ijolites) and open squares (melteigites).

alkali vs silica is apparent in Figure 6. The classification boundaries shown in Figure 4 have been removed from this diagram because these boundaries are arbitrary (Currie, 1974) and the fields enclosed by them indicate only generalised nomenclature. The boundaries have been replaced by fields for typical analyses of various alkaline rock types taken from Le Bas (1977). The data for any single rock type are scattered and the fields shown here do not include all analyses from Le Bas; they outline the most common compositions. The possible extent of the various fields is shown by outliers to the ijolite group, one from Budeda (King, 1965) and one from Homa Mountain (Le Bas, 1977). Other groups have similar outliers.

Ijolites from the Big Spruce Lake intrusion fall within the feldspathic ijolite classification of Le Bas (1977). Most of the mafic (Northern) and leucocratic (Southern) foyaites cluster in a single group at the alkali-rich end of the nepheline syenite field. The two groups differ from each other in that leucocratic foyaites tend to scatter towards higher silica contents (due to modal alkali feldspar) while the mafic foyaites scatter towards and beyond ijolite compositions.

A similar scattered pattern of peralkaline indices is evident in Figure 5. The lower limit of indices for these

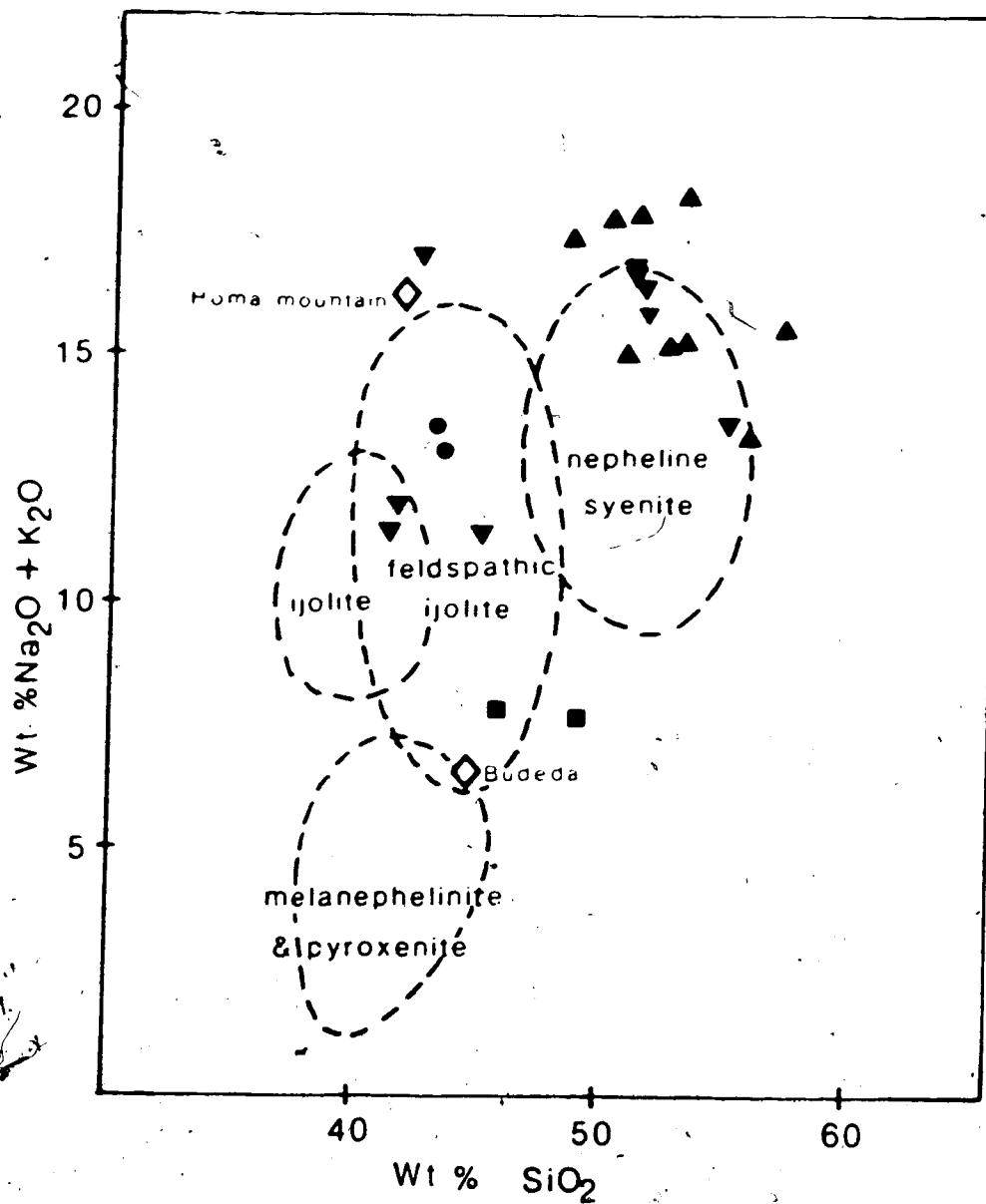


Figure 6. Alkali vs silica diagram for undersaturated rocks of Centre 3. Data and nomenclature for the various fields shown are taken from Le Bas (1977). Upright triangles indicate southern foyaite, inverted triangles indicate northern foyaite, circles indicate ijolites, square indicates melteigites. Open diamonds show outlier compositions of feldspathic ijolites from African localities (see text).

rocks is about 1.0 (few fall below that level but many fall essentially on the line) and the index shows a general increase with decreasing silica content.

D. Intrusive Centres 1 and 2 - Gabbros, Diorites, Syenites and Pyroxenites

The analytical results for gabbros, diorites and syenites analysed in this study are presented in Appendix 3, pages 397 to 399. These data, combined where possible with data from Martineau (1970) have been used to characterise and define individual units not separable in the field (syenites) to define geochemical patterns or trends of the differentiation series and to evaluate possible contamination by granodioritic host rock. The results for pyroxenites are presented in a separate section and discussed in relation to those of the gabbroic series. Evaluation of the geochemical behaviour of several trace elements during crystallisation allows inferences to be made about parent liquid composition.

1. Characterisation of Individual Units

Each of the individual units of gabbro and diorite grouped together as Centre 1 is readily defined by petrographic and field evidence. The syenites of Centre 2, however, separate readily into only three units, each

geochemically distinct; the quartz-free mafic syenite (S1), the quartz-free ring syenite (S2) and the main arcuate body of quartz syenite. The quartz syenites form a compositional group which cannot be further subdivided geochemically. On the basis of field evidence this group is divided into outer and inner units (S3 and S4 respectively).

The alkali-silica variation diagram of Figure 7 demonstrates the positions of individual units within a single, poorly-constrained main trend. The gabbro field is broad and overlaps with that of diorite for most elements (Appendix 3, page 397). Diorite forms a single petrographically-distinct unit with a wide range of major and trace element abundances, overlapping with gabbro at the low-silica end and with mafic syenite at the high silica end.

Mafic quartz-free syenite (S1) compositions overlap with those of the leucocratic diorites in K_2O , TiO_2 , and Fe_2O_3 , but have higher Na_2O and lower CaO and MgO . There is a small compositional gap between mafic syenite (S1) and the ring syenite (S2). The ring syenite composition plots immediately adjacent to the quartz syenites in Figure 7. The quartz syenites themselves form a tight compositional field which is discontinuous with the main or early trend. The cohesiveness of the quartz syenite

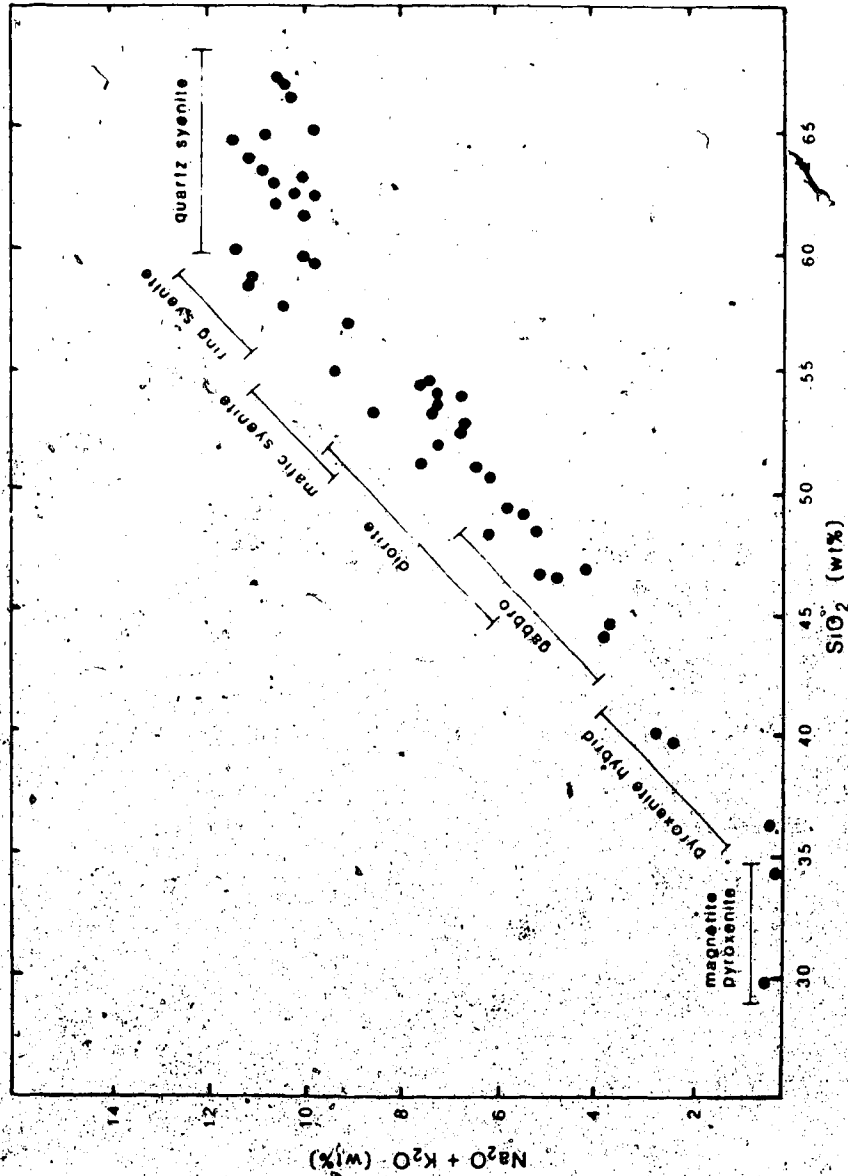


Figure 7. Plot of total alkali vs silica showing individual compositions of analysed samples. Data from Martineau (1970) have been included to augment the data base. Approximate fields for each petrographic unit are indicated.

group is exemplified in the chondrite-normalised rare earth element distribution plots and mantle-normalised lithophile element plots (discussed later) where the individual lines overlap to form narrow bands.

The extent of the outer quartz syenite unit (S4) has been extended, as a result of the present work, to include syenite emplaced immediately adjacent to diorite and across the Snare fault, X-X'. This syenite was previously considered to be a part of the ring syenite (S2). The basis of the change is analytical data for two samples from the body in question. Results for sample PC-82-358 from the centre of the body and PC-81-364 from near the western margin were compared with those for two samples from the main eastern lobe of the ring syenite, PC-82-124 and 129 (Figure 8). While major element compositions of ring syenite (S2) are similar to and overlapping those of the quartz syenites (S3 and S4), making classification of the body in question ambiguous, no such difficulty is presented by trace element compositions. In Figure 9 four examples of plots of incompatible and semi-compatible elements clearly show that the compositions of syenites from the body in question coincide with those of other quartz syenites while those of the quartz-free ring syenite form a field separate from both quartz-free mafic syenite and quartz syenites. Other plots, utilising the

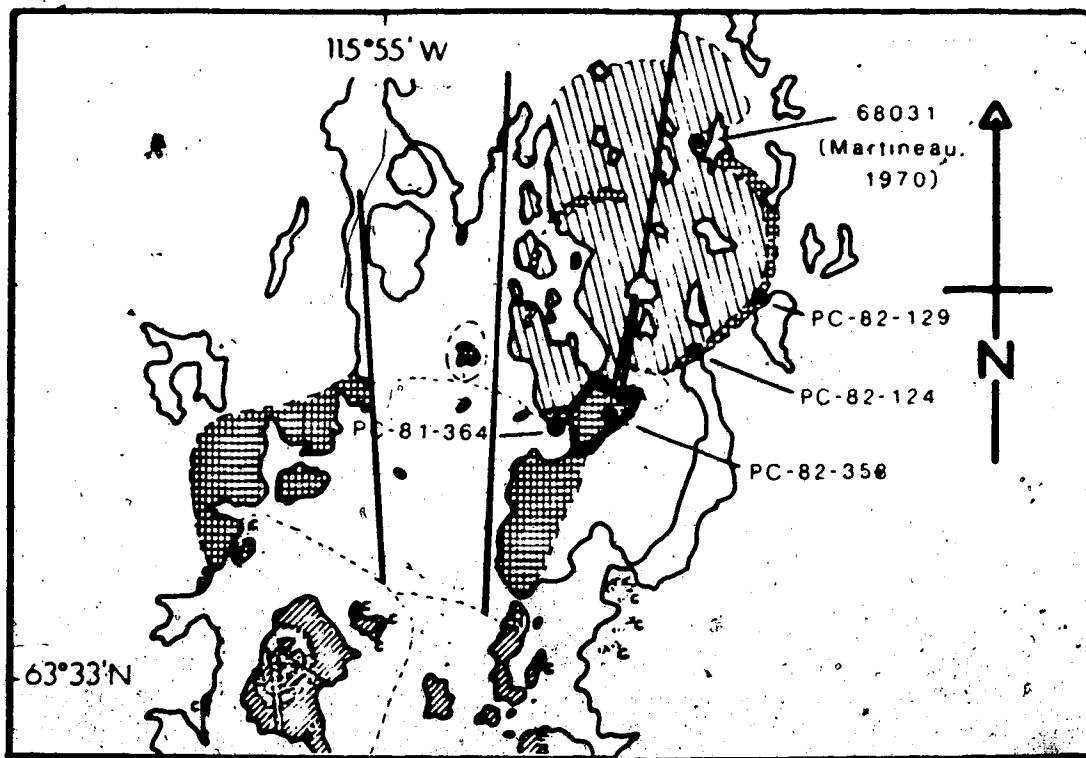


Figure 8. Map of the northeast portion of the main complex showing the location of the reclassified syenite body and locations of analysed samples mentioned in the text.

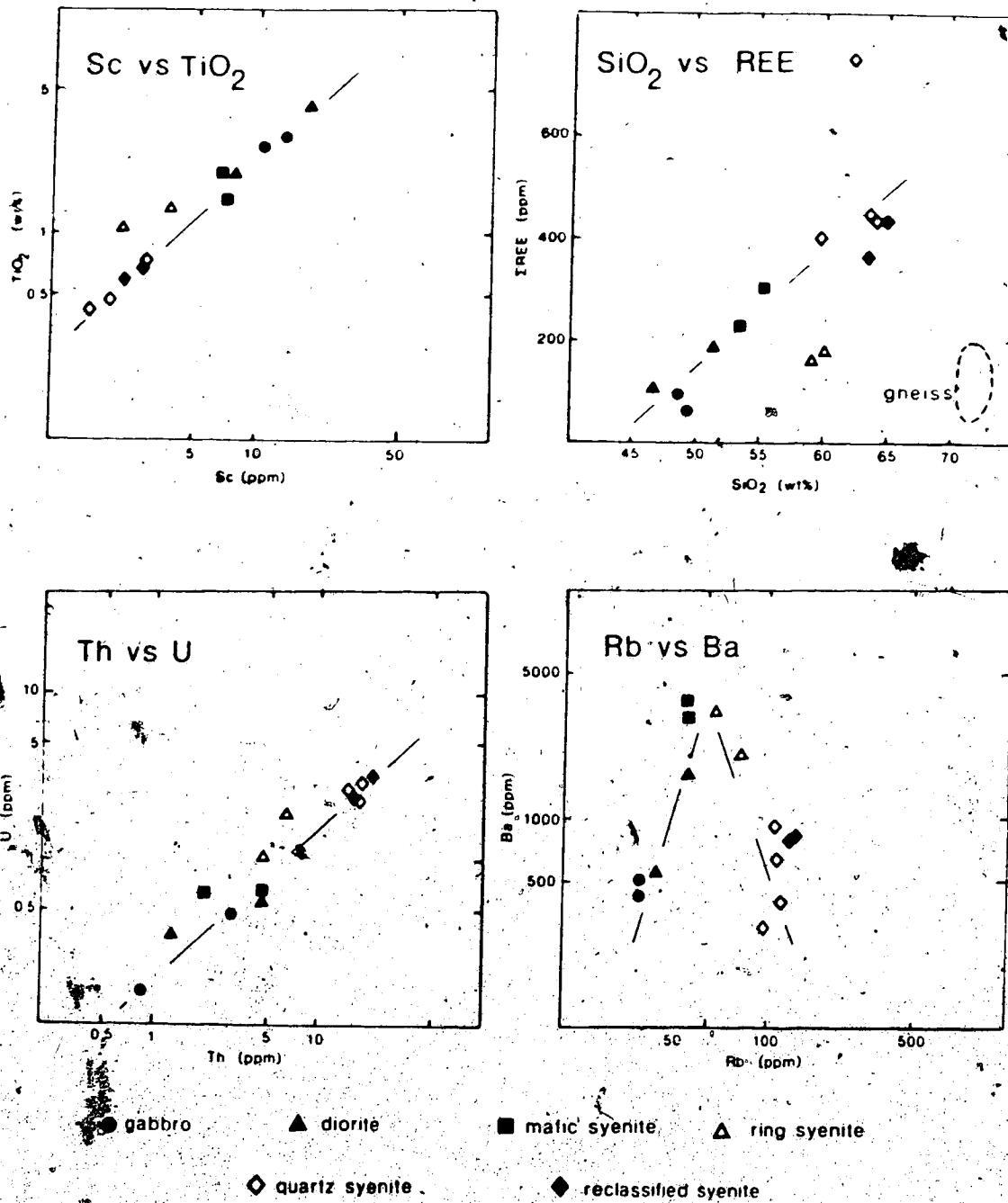


Figure 9. Incompatible and semi-compatible element plots which correlate the composition of the reclassified syenite body with those of the main quartz syenite body.

data of Appendix 3, pages 398 and 399 (but not shown here) indicate a similar separation. A third sample of ring syenite, taken from the northern tip of the eastern lobe and analysed by Martineau (1970) for Rb, Ba, Sr, Y, Zr and Nb (sample 68031 in Figure 8) yielded data which plot adjacent to the ring syenites analysed here. Another striking difference between the ring syenites and quartz syenites, including those of the reclassified body, is the relative concentration of europium on chondrite-normalised rare earth distribution plots (Figure 10). Ring syenites have strong positive Eu anomalies while the quartz syenites have small negative Eu anomalies.

Only this syenite body has been reclassified following analytical work.

2. Differentiation Trend

The overall continuity of the major element compositions (e.g., Figure 7) suggests that the gabbros, diorites and syenites form a single, albeit poorly constrained, differentiation trend. Multiple pulses of similar magma crystallising within the crust by similar processes would explain both field observations and analytical results.

The entire series could not have been generated by fractional crystallisation of a single batch of magma, nor

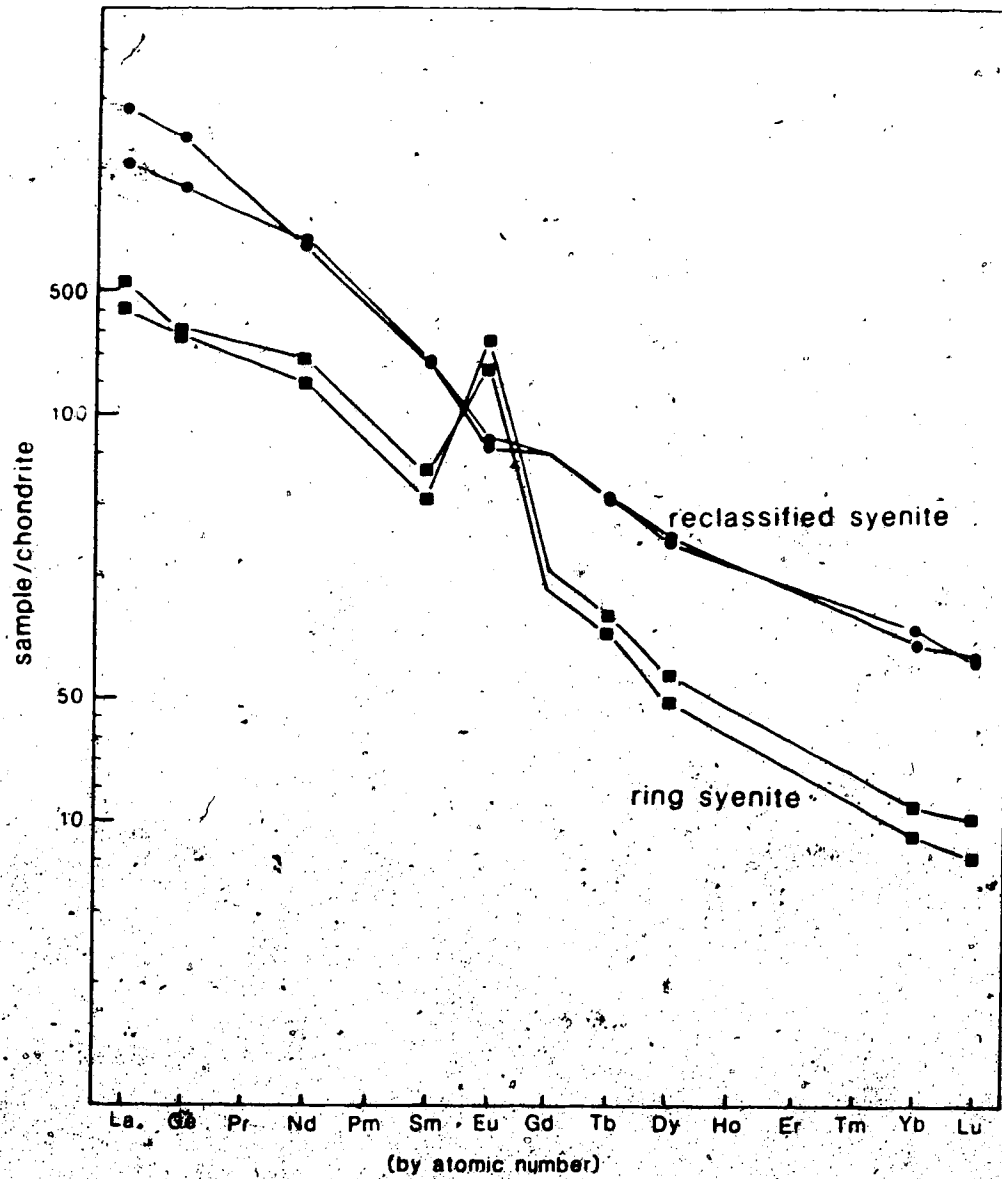


Figure 10. Chondrite-normalised (Nakamura, 1974) rare earth element distribution plots comparing reclassified syenites with ring syenites.

even in a single chamber. The present erosion surface exposes the cumulate gabbros of a magma chamber from which any later syenites have been removed. This chamber was itself emplaced within an earlier one in which the presently exposed outer diorite had already crystallised. Differentiation of gabbros and diorites in yet another chamber, at greater depth than those presently exposed as Centre 1, was required to produce the syenites of Centre 2.

Extraction calculations of changes in major element abundances (using average mineral compositions from the literature; Deer et al, 1966) indicate that the fractionation trend from gabbro to mafic syenite (S1) is controlled by a mixture of clinopyroxene, intermediate feldspar, amphibole and Fe-Ti oxides, a pattern confirmed by petrography. Olivine is not a major fractionating phase within the exposed rocks. Fractionation of silica-poor amphibole produces the final saturated syenites from the alkali basalt parent melt.

There is a marked discontinuity in fractionation trend, apparent on the alkali-silica plot of Figure 7, at about $\text{SiO}_2 = 60\%$ and $\text{Na}_2\text{O} + \text{K}_2\text{O} = 10\%$ reflecting saturation of residual melt with respect to alkali and silica and the onset of crystallisation of alkali feldspar and quartz with minor mafics (biotite and amphibole) and

Fe-Ti oxides. The early mafic trend, the discontinuity and the late leucocratic trend correspond well with the trend for silica-saturated rocks of the Gardar alkaline province, SW Greenland (Upton, 1974) and with the idealised behaviour of a silica-saturated melt outlined in Cox et al (1979). In the Big Spruce Lake series best-fit calculations show that the late-crystallising alkali feldspar must be sodium-rich. The antiperthitic nature of late feldspar has been confirmed by staining and by electron microprobe reconnaissance which showed K-feldspar as the minor phase exsolved from sodic feldspar, host on scales from crypto to mesoperthite. Potassium feldspar forms a final rim on feldspar grains.

Early and late fractionation trends are also apparent on a CaO vs Y plot (Figure 11). The data form a constant and well-defined trend of increasing Y with decreasing CaO from gabbro to mafic syenite while the quartz syenites form a field scattered across approximately the same trend. The slope of the line is essentially parallel to those of other alkaline series reported by Lambert and Holland (1974) to lie on a "pyroxenitic" trend, resulting from crystallisation of pyroxene + plagioclase or Y-poor amphibole such as kaersutite. Yttrium is significantly less abundant in the Big Spruce Lake rocks (0.3 to 0.5 times less) than in the other alkaline series reported by

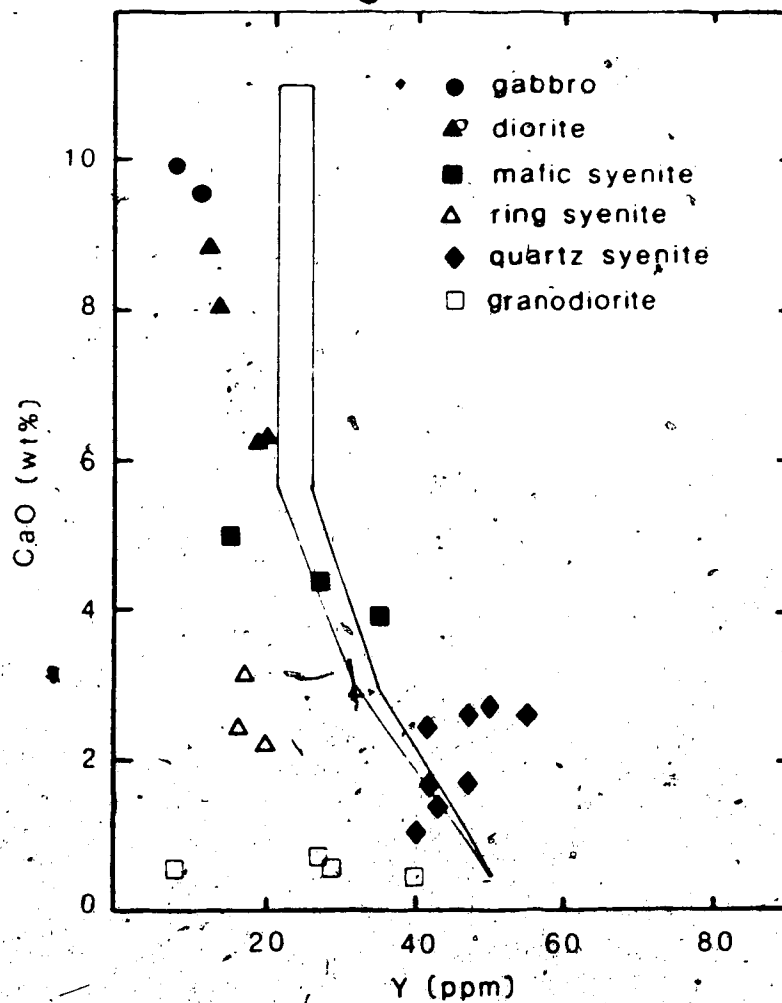


Figure 11. Y vs CaO in analysed samples of the gabbro-syenite series. The "pyroxenitic" trend of Lambert and Holland (1974) is shown for comparison with the Big Spruce Lake suite. CaO/Y varies from 10,000 in early gabbro to 1300 in mafic syenites and 220 in quartz syenites.

Lambert and Holland. Increased scatter within the quartz-syenite group may be due to variable amounts of modal zircon and/or allanite. The ring syenite compositions plot well away from the main trend towards country rock compositions, poor in CaO and Y.

3. Trace Element Variations

Chondrite-normalised rare earth element distribution patterns are shown in Figures 12 to 15. Relevant data derived from these plots, (Σ REE, Eu/Eu^* , and Ce/Yb) are presented in Table 2. Enrichment of total REE (Σ REE) over the series and the lack of increasing fractionation of light rare earth elements (LREE) from heavy rare earth elements (HREE), constant Ce/Yb , are evident in the distribution patterns. Only Eu is anomalous, strongly positive ($\text{Eu}/\text{Eu}^* = 2$ to 3) in all samples along the early mafic trend and weakly negative ($\text{Eu}/\text{Eu}^* = 0.5$ to 0.9) in quartz syenites. Undifferentiated alkali basalts commonly do not show Eu anomalies (Sun and Hanson, 1975a,b; Frey et al, 1978) and the presence of anomalies in all units of Centre 1 indicates the strong contribution that plagioclase crystallisation makes to the whole-rock REE compositions. The Eu anomaly is discussed in detail in a later section with regard to Sr abundances. REE fractionation in these rocks (Ce/Yb ranges from 13 to 18)

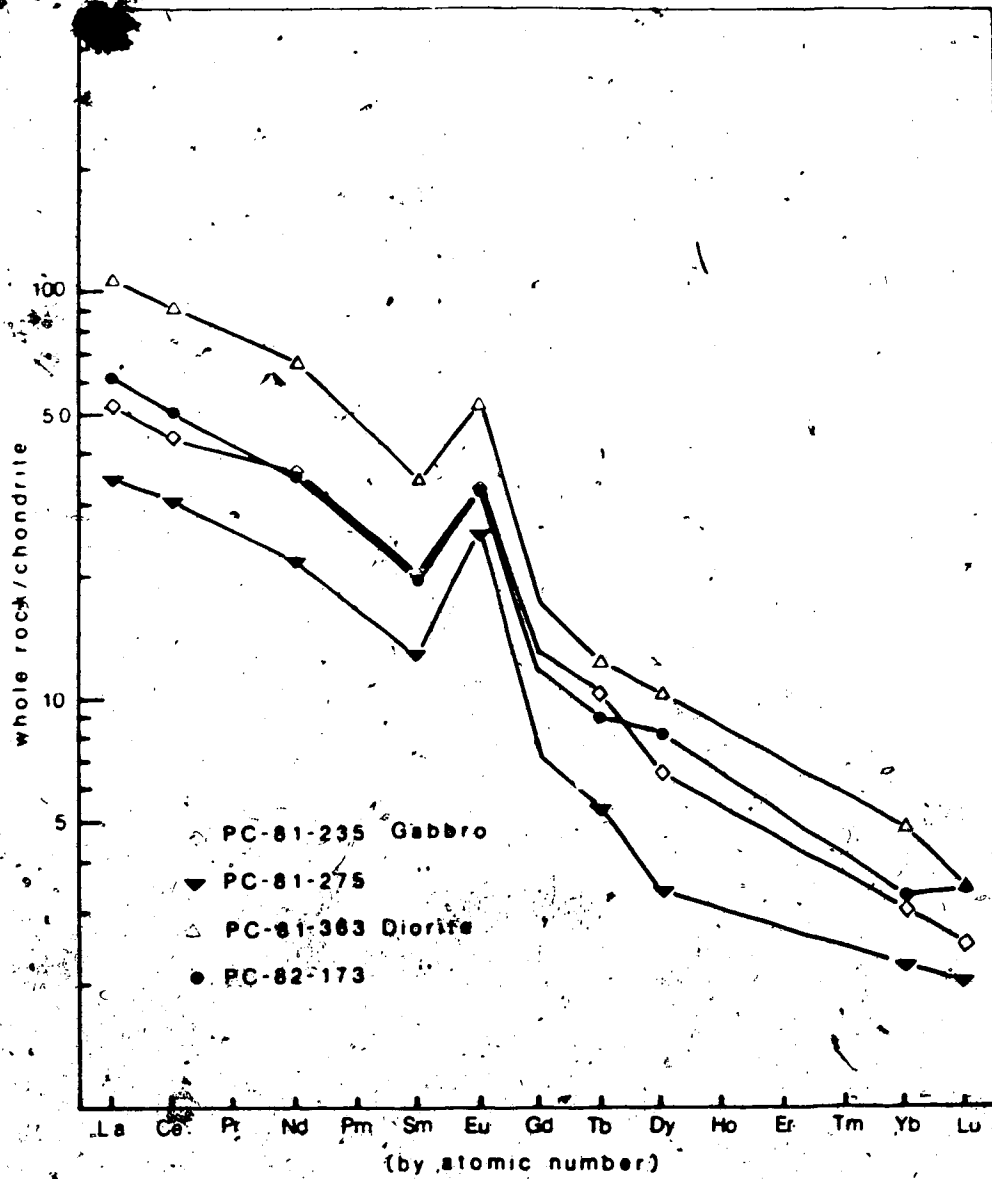


Figure 12. Chondrite-normalised (Nakamura, 1974) rare earth element distribution plots for gabbros and diorites of intrusive Centre 1.

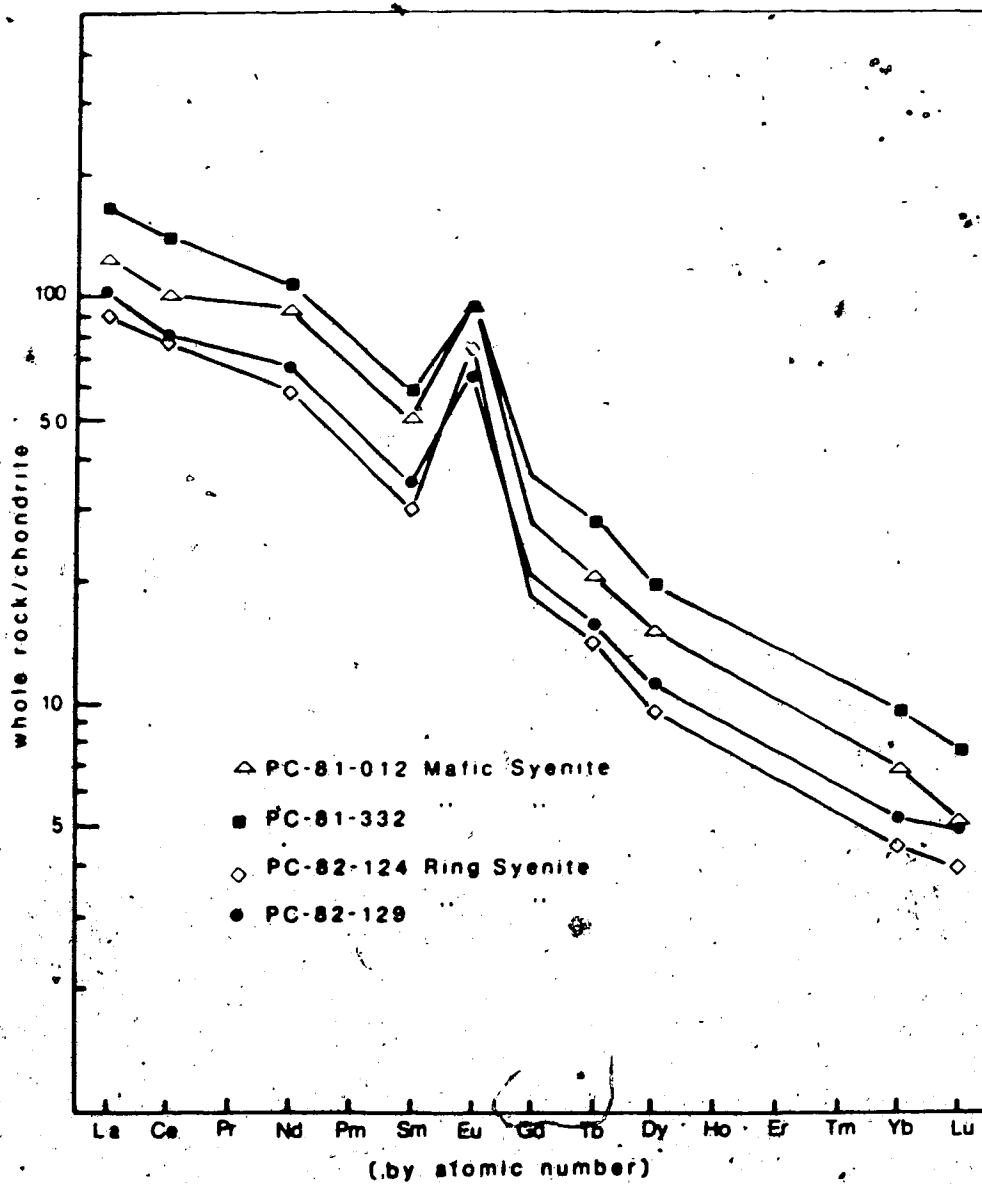


Figure 13. Chondrite-normalised (Nakamura, 1974) rare earth element distribution plots for mafic syenites (S1) and ring syenites (S2) of intrusive Centre 2.

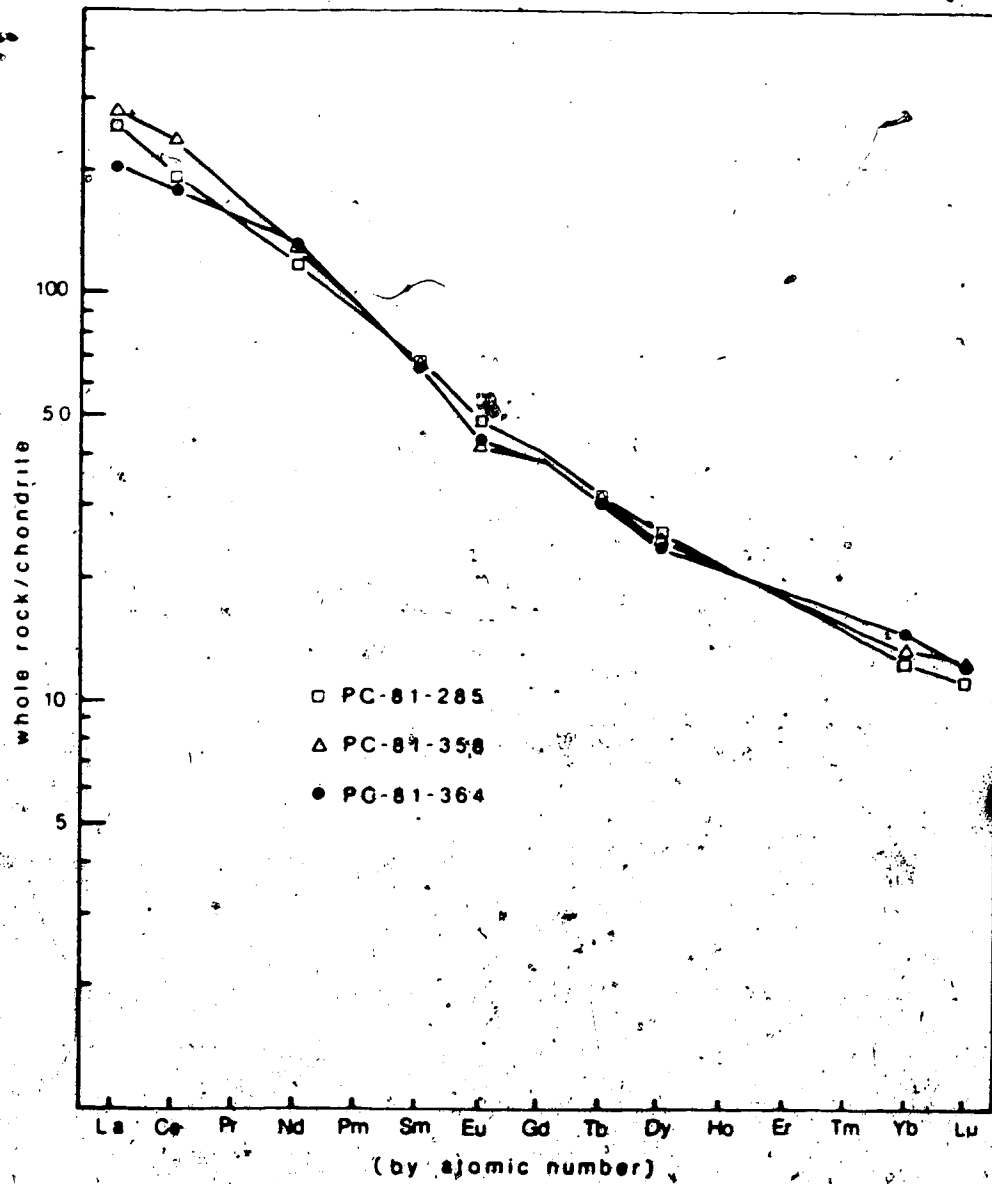


Figure 14. Chondrite-normalised (Nakamura, 1974) rare earth element distribution plots for inner quartz syenite (S4) and reclassified syenites of intrusive Centre 2.

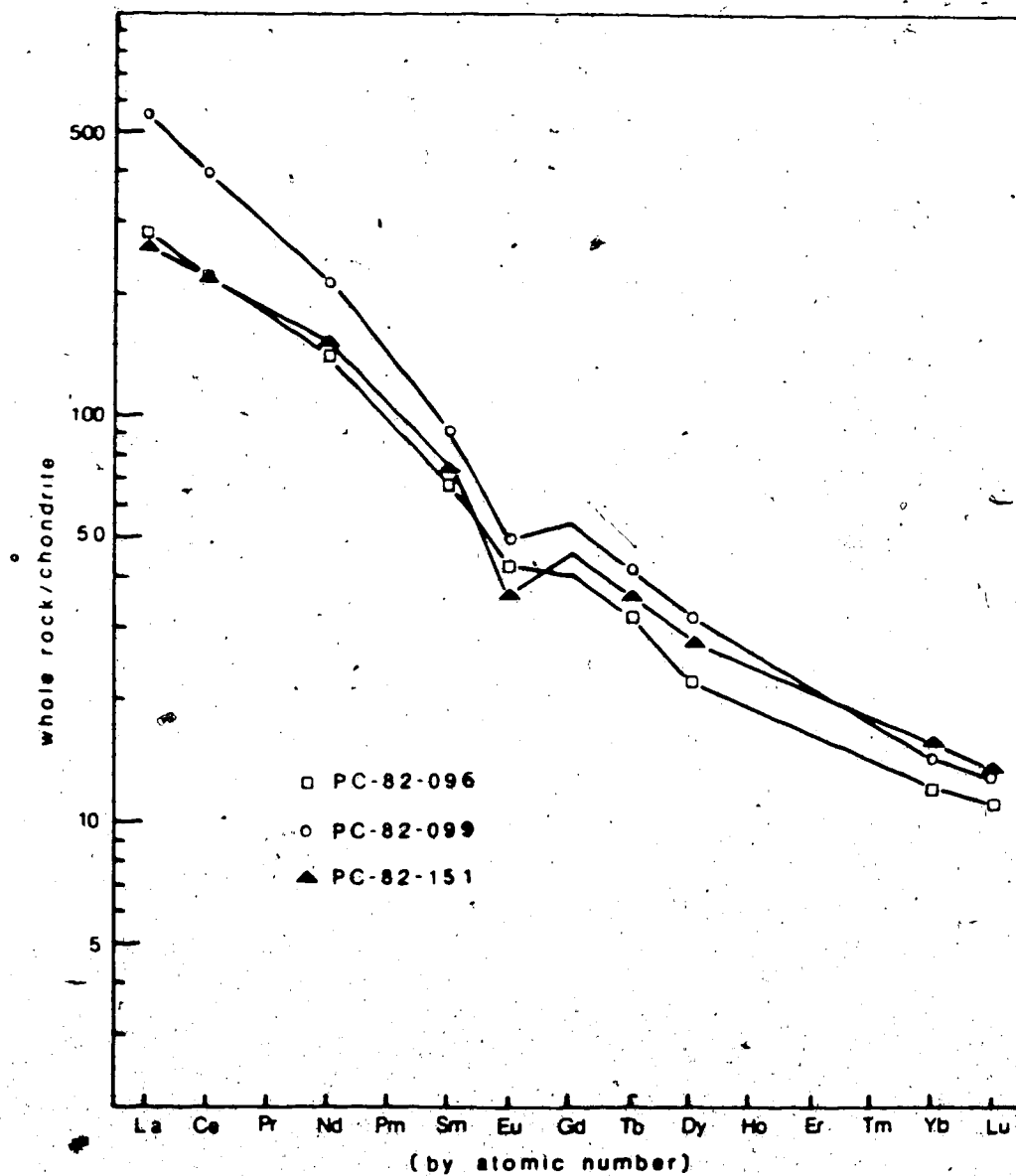


Figure 15. Chondrite-normalised (Nakamura, 1974) rare earth element distribution plots for outer quartz syenites (S3) of intrusive Centre 2.

Table 2. Rare earth element data for intrusive Centres 1 and 2.

Sample Number and Type	Σ REE ¹	Eu/Eu* ²	(Ce/Yb) _{CN} ³
PC-81-235 gabbro	99	2.03	14.2
PC-81-275 gabbro	65	2.75	13.7
PC-81-363 diorite	190	2.15	18.3
PC-82-173 diorite	108	2.19	15.0
PC-81-012 mafic sy.	237	2.63	14.3
PC-81-332 mafic sy.	307	2.11	14.4
PC-82-124 ring sy.	167	3.15	16.9
PC-82-129 ring sy.	182	2.37	14.9
PC-82-096 Quartz sy. (outer)	442	0.80	17.9
PC-82-099 Quartz sy. (outer)	760	0.70	27.6
PC-82-151 Quartz sy. (outer)	455	0.62	13.4
PC-82-358 Quartz sy. (outer)	440	0.83	17.2
PC-81-364 Quartz sy. (outer)	370	0.87	12.0
PC-81-285 Quartz sy. (inner)	406	0.94	15.7

¹ Includes values interpolated from Figures 12 to 15 for elements not analysed.

² Eu* interpolated between Sm and Tb on chondrite normalised plots. Eu is analysed value.

³ CN = chondrite-normalised values.

is high relative to average undifferentiated alkali basalts ($Ce/Yb \approx 8$ to 10 ; Sun and Hanson, 1975b; Frey et al, 1978) but the total REE enrichment is low. Low abundances, particularly in the gabbroic units, are best explained by abundance of cumulate plagioclase which has distribution coefficients (D values) of about 0.1 (Figure 16). Of the samples analysed, the leucocratic laminated gabbro (PC-81-275) has the lowest REE abundances, $La/chondrite (La_{CN})$ is only 35 compared to La_{CN} of 60 to 100 for typical alkali basalts (Sun and Hanson, 1975b).

The Ce/Yb ratio remains essentially constant with increasing Ce content throughout the series. The trend of chondrite-normalised $Ce/Yb ((Ce/Yb)_{CN})$ vs Ce, shown in Figure 17 is consistent with the trend calculated by Tarney et al (1930) for "low pressure" crystallisation of basalts involving olivine, plagioclase, clinopyroxene and Fe-Ti oxides. Low pressure, in that work, apparently means: in the upper crust, above garnet stability. Neither open-system (as in Big Spruce Lake gabbros-syenites) nor closed-system crystallisation of the common minerals mentioned above can significantly fractionate Ce with respect to Yb at low pressures because of the similarity of crystal-liquid distribution coefficients for these elements (Henderson, 1982). Figure 16 illustrates the similarity of distribution coefficients for Ce and Yb

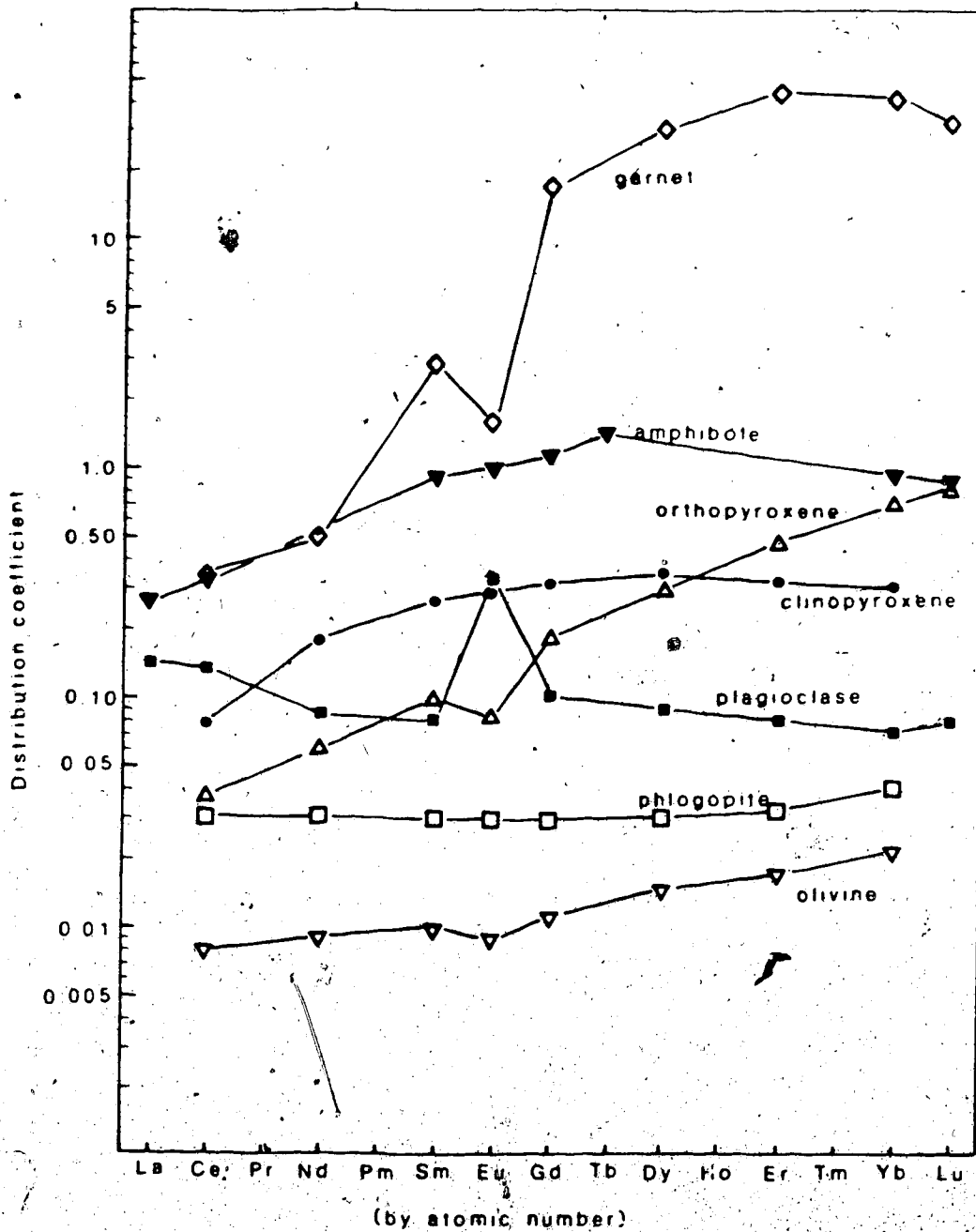


Figure 16. Distribution coefficients for rare earth elements in rock-forming minerals in equilibrium with basaltic liquid. Data are from a compilation in Henderson (1984).

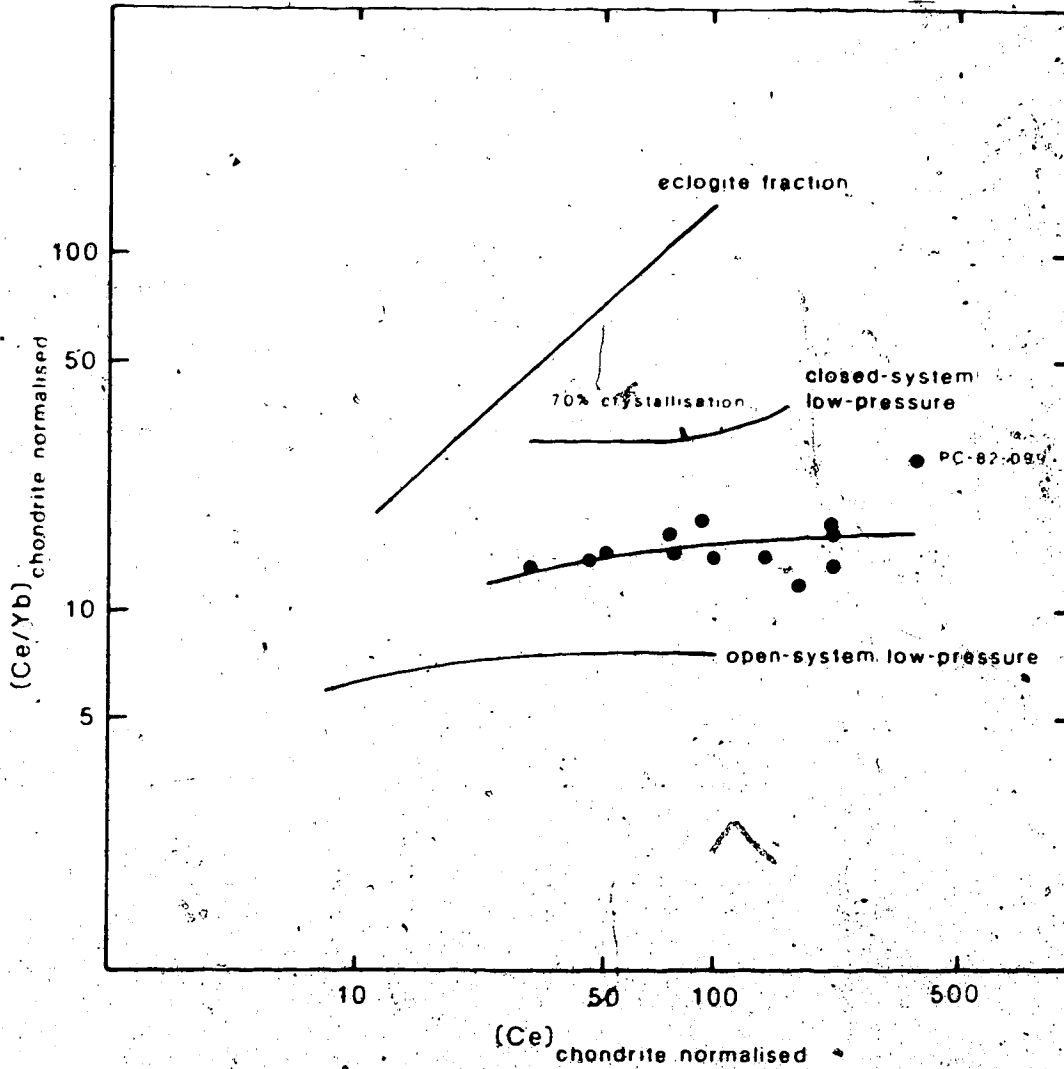


Figure 17. Chondrite-normalised (Nakamura, 1974) Ce vs Ce/Yb for the Big Spruce Lake gabbro-syenite series (solid circles) compared with open- and closed-system low-pressure crystallisation trends modelling fractionation of ol + plag + cpx + Fe-Ti oxides at crustal levels (after Tarney et al, 1980). Also shown is the variation of Ce/Yb during eclogite (high-pressure) fractionation (Tarney et al, 1980).

in the major crystallising phases. Only three processes can significantly alter the Ce/Yb ratio. One is, in fact, low pressure open system crystallisation but with the repeated removal of less than 0.01 of the evolved liquid from the magma chamber (Pankhurst, 1977; Tarney et al, 1980). This model is inapplicable to the Big Spruce Lake intrusion where the open system involved multiple chambers crystallising in succession. Another process is high pressure crystallisation involving garnet (O'Hara, 1975), also inapplicable to the presently exposed sequence. The third process which can alter the Ce/Yb ratio is (low-moderate pressure) crystallisation of significant amounts of any phase with widely different distribution coefficients for Ce and Yb. Application of the calculated trends to the data for Big Spruce Lake requires the addition of amphibole and biotite as major crystallising phases not present in the early basalt crystallisation modelled by Tarney et al (1980) and Pankhurst (1977). Distribution coefficients for Ce and Yb in amphibole and biotite are similar to those of clinopyroxene and olivine (Figure 16), and fractionation of these phases will have little effect on the slope of the calculated trends. Crystallisation of orthopyroxene in significant amounts could fractionate Ce and Yb, but to a lesser extent than the separation of garnet; however, orthopyroxene is not

observed in rocks of this series. Fractionation of apatite and sphene, both common hosts for REE, is unlikely to alter the Ce/Yb ratio to any great extent because of the similarity of D values for heavy and light REE in these minerals. Partition coefficient (D) values for REE in common accessory minerals are shown in Figure 18 and clearly crystallisation of apatite, sphene and magnetite will have little effect on the Ce/Yb of residual liquid. Fractionation of zircon, which is abundant in the later syenites, and allanite, which is sparse but present, will have significant and opposite effects. The presence of variable amounts of zircon and/or allanite in analysed samples may account for the scatter of Ce/Yb at higher Ce levels.

There is a small difference between the calculated open and closed system trends shown in Figure 17. In the closed system Ce/Yb is constant with increasing crystallisation (and increasing Ce content) to about 70% crystallisation at which point it begins to increase slightly. On the other hand the trend calculated for an open system shows a constant small positive slope. The data for Big Spruce Lake are slightly scattered but are more consistent with the open system behaviour than with a closed system model. Geochemical interpretation of REE variations are, hence, in accord with field evidence of

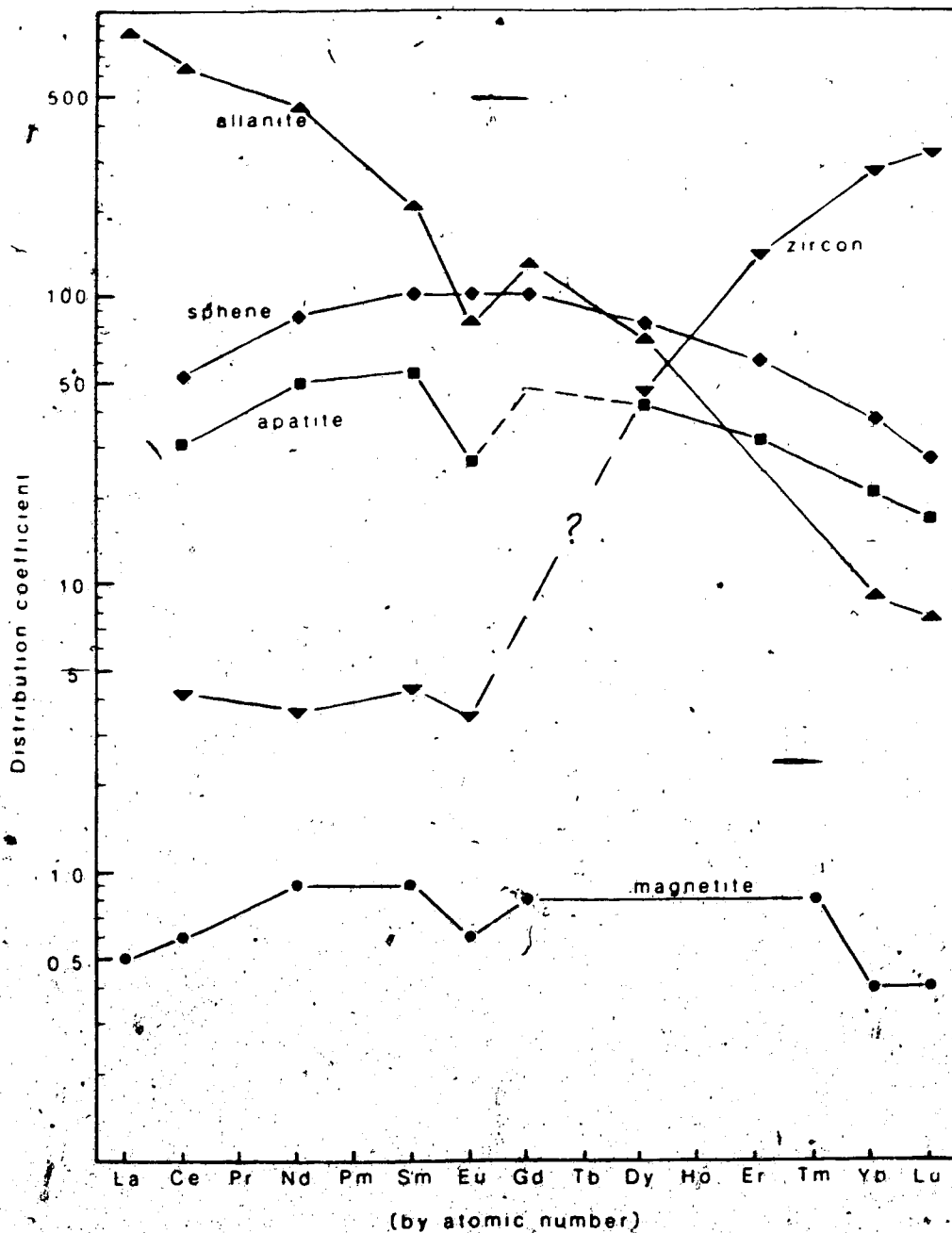


Figure 18. Distribution coefficients for rare earth elements in accessory minerals in dacitic and rhyolitic melts. Data are from a compilation in Henderson (1984). The HREE-enriched pattern for zircon is confirmed by Watson (1980).

system crystallisation within the upper crust.

Of the experimental data points plotted on the Ce/Yb vs Ce diagram (Figure 17) only that for sample PC-82-099 (quartz syenite) lies significantly off a low pressure, open system trend. The absolute abundances of all rare earth elements (REE) are much higher in this quartz syenite than in any of the others analysed (Appendix 3, page 399), and the slope and position of the chondrite-normalised distribution plot for this sample (Figure 15) is clearly anomalous. All other quartz syenites form a tight band on the REE plots. The presence of locally abundant allanite (visible in thin section) is possibly a more reasonable explanation of the REE composition than is localised late deuteric or metasomatic enrichment associated with carbonatitic activity.

A plot of P_2O_5 vs EREE (Figure 19) shows that in the more mafic members of the series both REE and P are incompatible elements and both are enriched in residual liquid. At about 50% SiO_2 apatite becomes a stable phase and P is removed from the liquid leaving the residual melt P-depleted. However, at this point the concentration of REE is decoupled from that of P and enrichment of REE in the liquid continues while P is depleted. For the latter part of the differentiation series, the major host for the REE is not apatite.

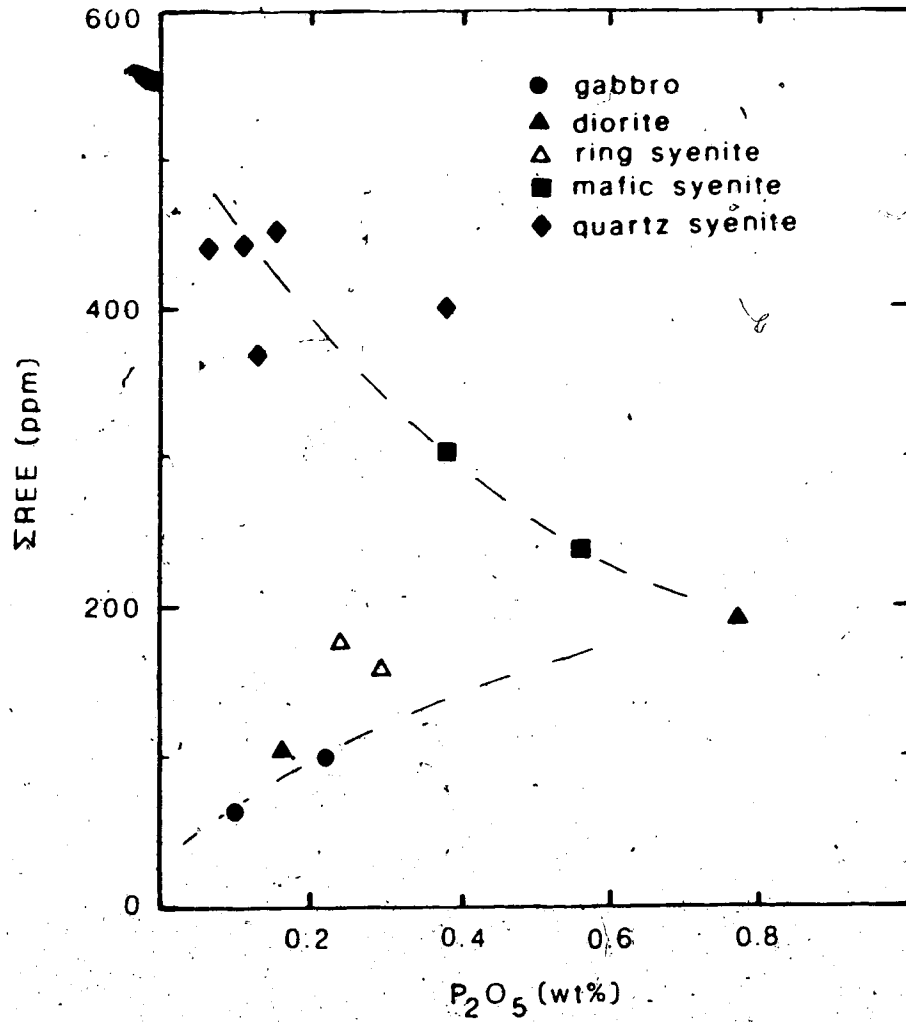


Figure 19. P₂O₅ vs ΣREE for the gabbro-syenite series.

Other possible hosts for REE in the later Big Spruce Lake syenites are accessories such as zircon and allanite. However, allanite has been found in only one quartz syenite thin section. REE might also be contained in late interstitial material or in REE-rich rims on major minerals (Suzuki, 1981). Fourcade and Allegre (1981) attempted, with moderate success, to define the hosts for REE in a quartz diorite and a monzogranite from France. They showed that while most of the REE in the diorite were held in major minerals such as hornblende and biotite they were unable to identify the host for all REE. Up to 40-50% of the light REE (La-Sm) which were present in the whole rock analysis were unaccounted for by the mineral separates (which included accessories) that were analysed. In the monzogranite, biotite and accessory allanite were the main hosts, but (again) 40-70% of all REE present in whole rock analyses were not accounted for in mineral separate analyses. In both cases a major portion of the whole rock REE were apparently lost during mechanical separation procedures. Sparse, REE-rich accessories with highly fractionated REE (major portions of both heavy and light REE were missing from the mass balances reported), or even interstitial REE-rich material may account for the discrepancies reported. From the data presented here it is clear that apatite is neither a main

REE fractionating (light REE/heavy REE) phase nor is it the major host in late differentiates. Zircon and allanite are more likely to fulfil both of these functions in late differentiates.

The examination of relative abundances of a number of elements in each individual sample greatly facilitates the interpretation of variations in absolute abundances of a large number of samples, particularly when these variations result from enrichment in residual liquid or incorporation in stable crystallising phases such as feldspar, apatite or oxide. The large number of trace elements determined in this study is an advantage in this regard.

In the same manner that REE abundances are commonly normalised to chondritic abundances to compare fractionation, total enrichment and anomalous behaviour (Ce and Eu) among samples, other trace elements can be normalised to a set of reference abundances for comparative purposes. A similar procedure has been used by other authors but either fewer elements were included or the system studied showed significantly less differentiation than that of the Big Spruce Lake series.

Azzouzi et al (1982) added Th, Ta, Nb, Zr, Hf, Ti, Y and V to chondrite-normalised REE distribution plots for a series of seven alkaline rocks from the French Central

Massif and noted anomalous behaviour of Ti and V as differentiation proceeded. Normalisation of 19 lithophile elements to primordial mantle abundances was employed by Tarney et al (1980) in an attempt to characterise sources for largely undifferentiated oceanic basalts. The 19 elements used by Tarney et al cover a broader range than those employed by Azzouzi et al. In addition to the lithophile elements previously mentioned (V is excluded as semi-compatible) the group includes Cs, Rb, Ba, U, Th, K, Sr and P, and omits all but 5 REE, retaining Ce, La, Nd, Sm and Tb. The same group of elements is used here in preference to that of Azzouzi et al because of its wider range.

Retention of the five REE, for which data has already been presented in this work in the form of chondrite-normalised plots, is necessary for lithophile element normalisation in order to fix the position of the residual liquid enrichment trend (for incompatible elements) between prominent positive and negative anomalies of semi-incompatible elements (e.g., P, Sr, Ti). The REE group is geochemically coherent and these elements are enriched or depleted as a group. The patterns of the 14 REE can be evaluated for consistency separately from other large ion lithophile elements (LILE) and the validity of analytical results for the five REE included in the 19 LILE can be

established because the relative abundances of the REE are well known (e.g., Evensen et al 1978; Henderson, 1984).

The "primordial mantle abundances" of these elements derived by Tarney et al from earlier work (Ringwood, 1966; Gast, 1968; Ganapathy et al, 1976; Sun and Nesbitt, 1977; Wood et al, 1979) are shown in Table 3 in order of increasing D, where D is the bulk distribution coefficient of the element in basaltic liquid, from Cs to Y. This is the normalising data employed in this work.

The order of the 19 LILE to be used on the abscissa of the normalised plot is that derived by Tarney et al (1980), for increasing D (in basaltic liquid). The absolute abundances used for normalising are not critical to interpretation (within any single study) provided that they are specified for comparison with the data of other workers. The use of "mantle" values is preferred to that of an average alkali basalt or tholeiite because the normalised LILE distribution plots so obtained are thus comparable to the commonly used chondrite-normalised REE distribution plots.

For the five REE included in the group the "primordial mantle" abundances are about twice the commonly accepted chondritic abundances (Nakamura, 1974; Hagkin et al, 1968) and they show a slight light/heavy REE

Table 3. LILE "primordial mantle" abundances (from Tarney et al, 1980).

	<u>ppm</u>		<u>ppm</u>
Cs	0.019	Sr	23
Rb	0.86	Nd	1.29
Ba	7.56	P	90.4
Th	0.096	Hf	0.36
U	0.027	Zr	11
K	252	Sm	0.460 ¹
Ta	0.043	Ti	1526
Nb	0.62	Tb	0.099
La	0.71	Y	4.87
Ce	1.90		

¹Modified from 0.385 in Tarney et al (1980), see text for explanation.

fractionation relative to chondritic values. Lanthanum and Ce primordial mantle abundances are 2.16 and 2.20 times chondritic (Nakamura, 1974), Nd is 2.05 times chondritic and Tb is 1.96 times chondritic. The value used by Tarney et al for Sm (0.385 ppm) is only 1.67 times chondritic and hence the value used here has been revised to 2.00 times chondritic (0.460 ppm; Nakamura, 1974) to make it consistent with the other REE abundances for normalisation. Interpretation and quantification of anomalies expressed using the normalisation abundances given in Table 3 are internally self-consistent for the Big Spruce Lake analytical data.

The mantle-normalised (MN) LILE distribution plots of Figures 20-24 provide trace element profiles or signatures of individual samples. They differ from the more common chondrite-normalised distribution plots of the geochemically coherent REE group in having numerous anomalies. The plots show both fractionation (more incompatible LILE/less incompatible LILE) and progressive enrichment similar to the REE plots. The value of Y_{MN} is 2.0 to 2.5 in gabbros while Cs_{MN} and Rb_{MN} are about 30. The Y_{MN} value rises to about 10 in quartz syenites while Cs_{MN} and Rb_{MN} rise to about 100. All of the plots show a concave-down pattern with the slope of the alkali portion (Cs to Nb) being less than that of the REE portion (La to

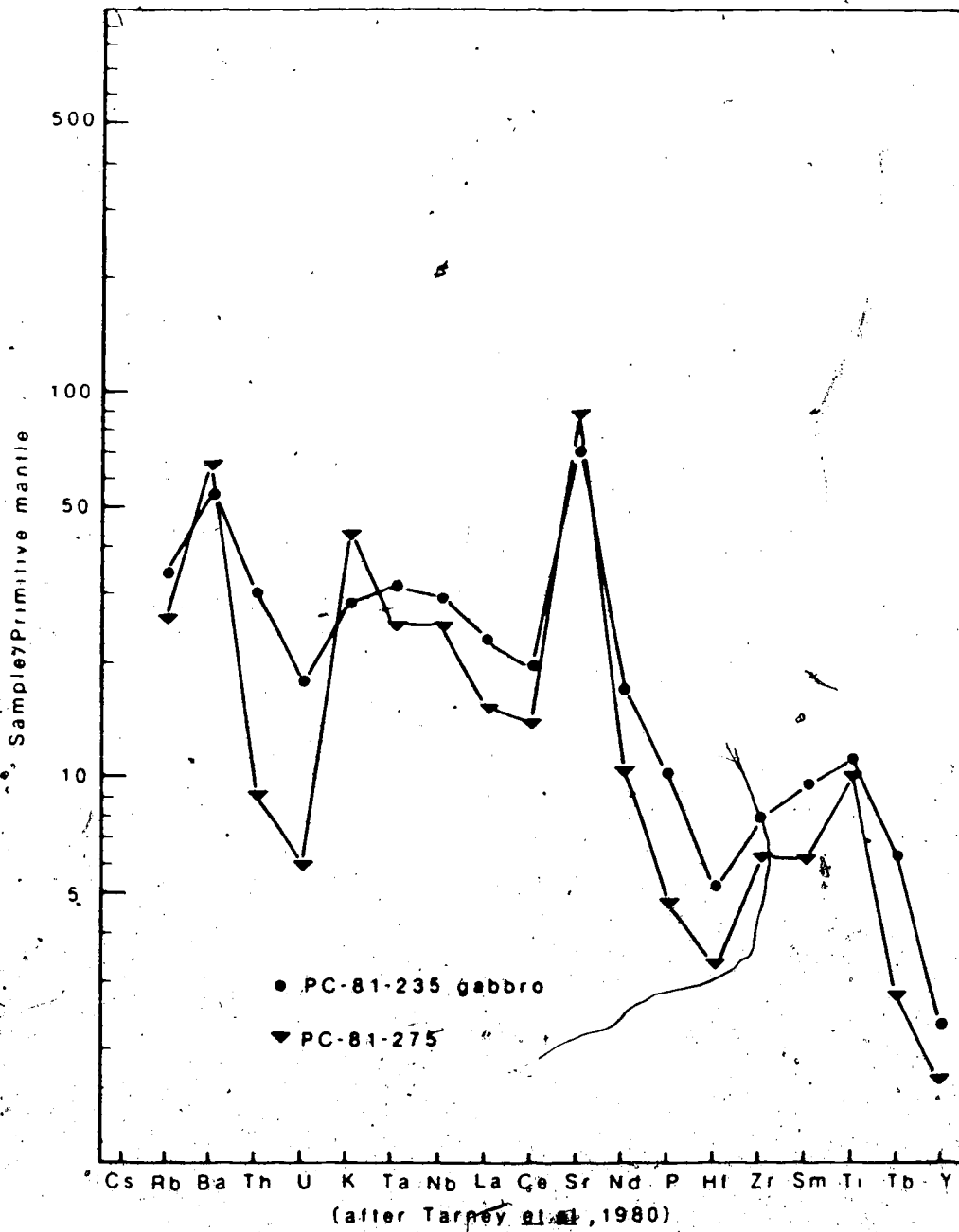


Figure 20. Mantle-normalised LILE distribution plots for gabbros.

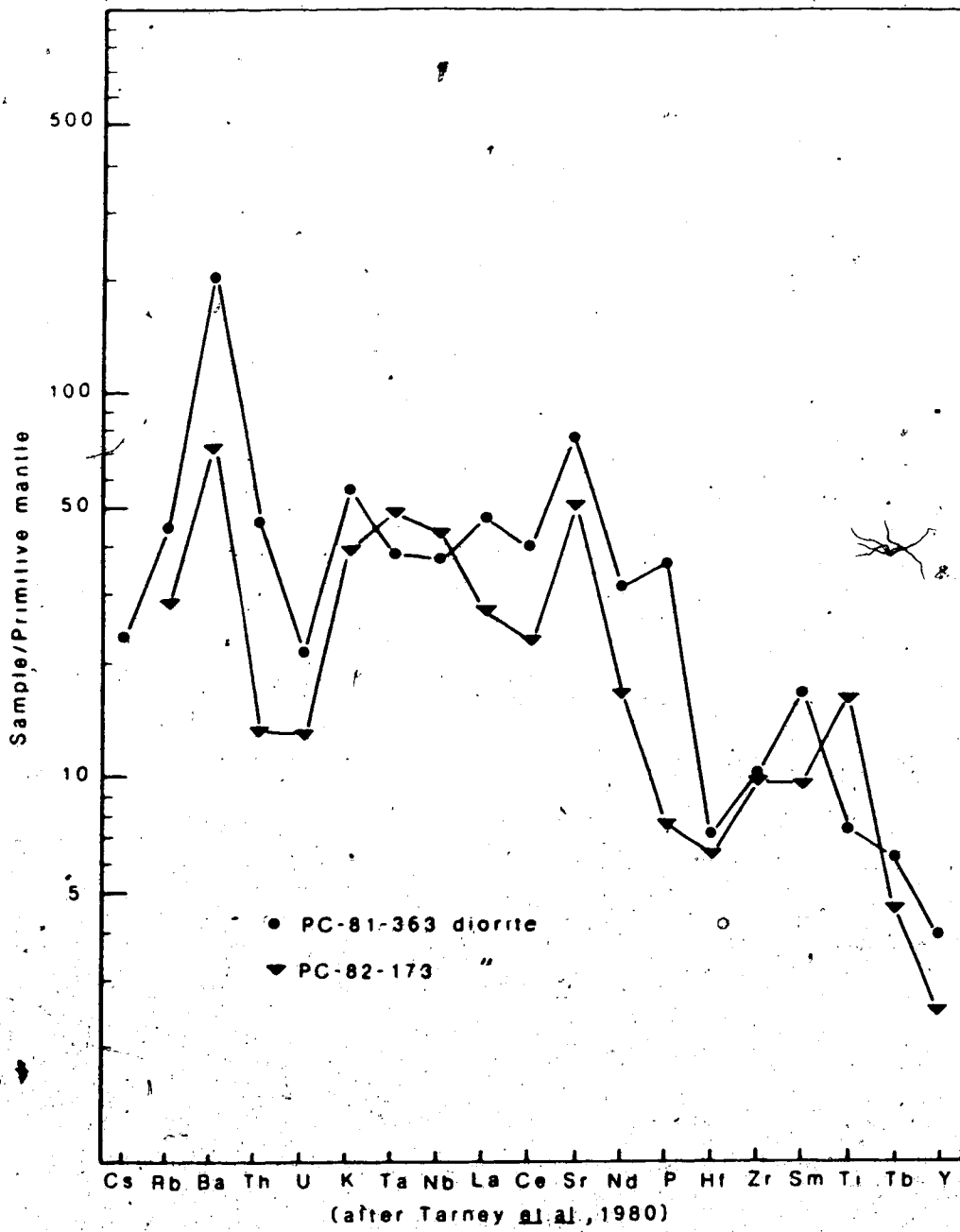


Figure 21. Mantle-normalised LILE distribution plots for diorites.

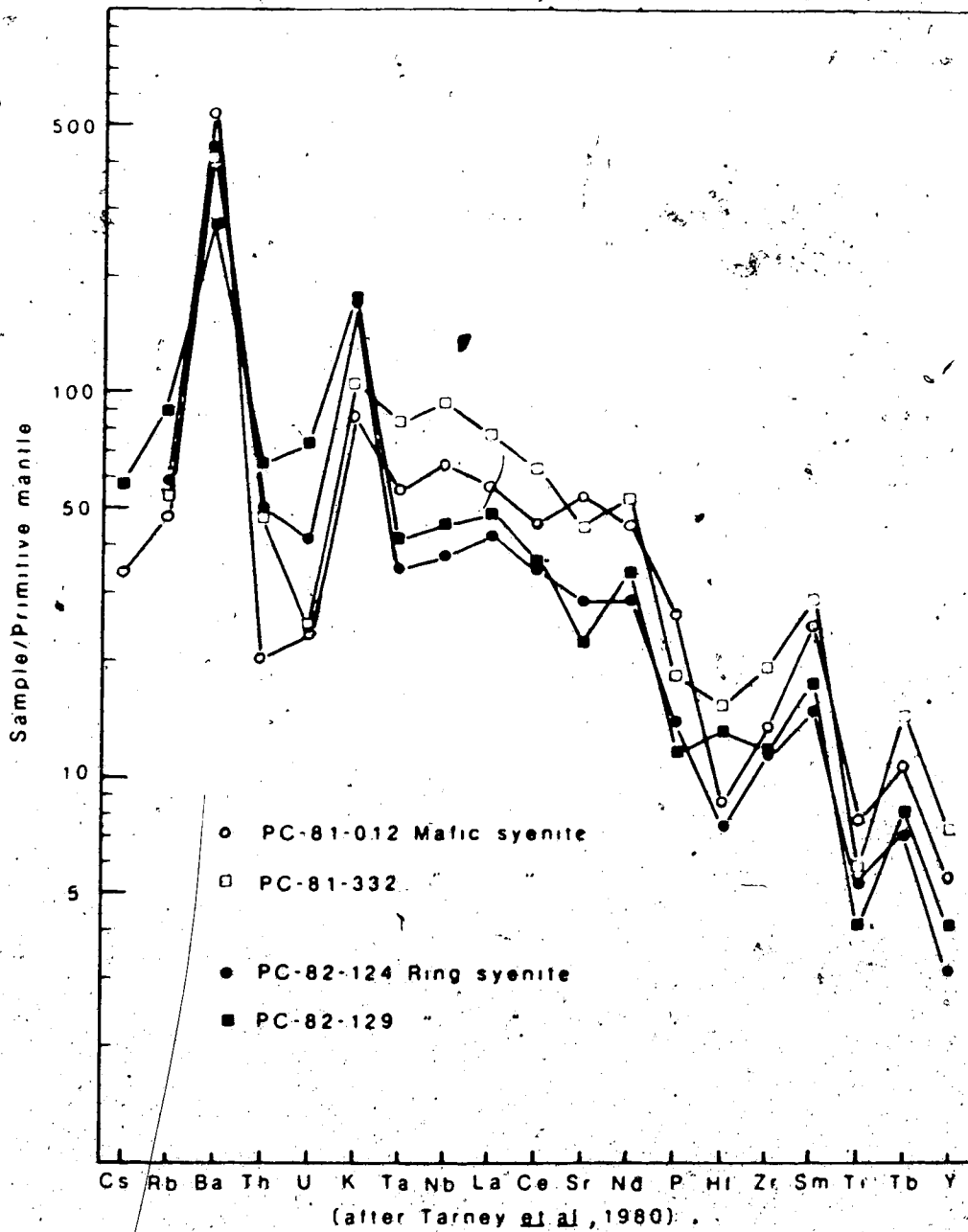


Figure 22. Mantle-normalised LILE distribution plots for mafic and ring syenites.

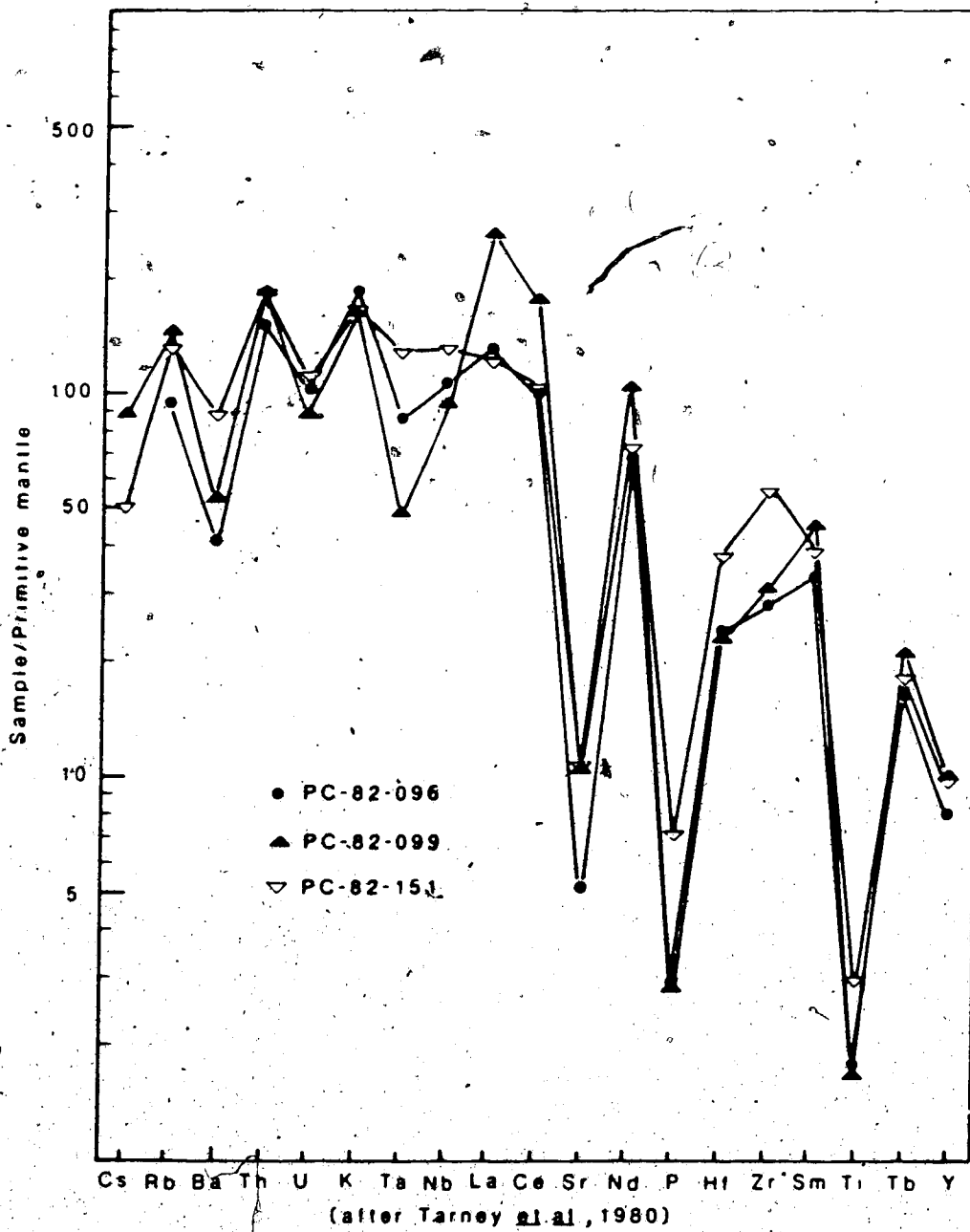


Figure 23. Mantle-normalised LILE distribution plots for outer quartz syenites.

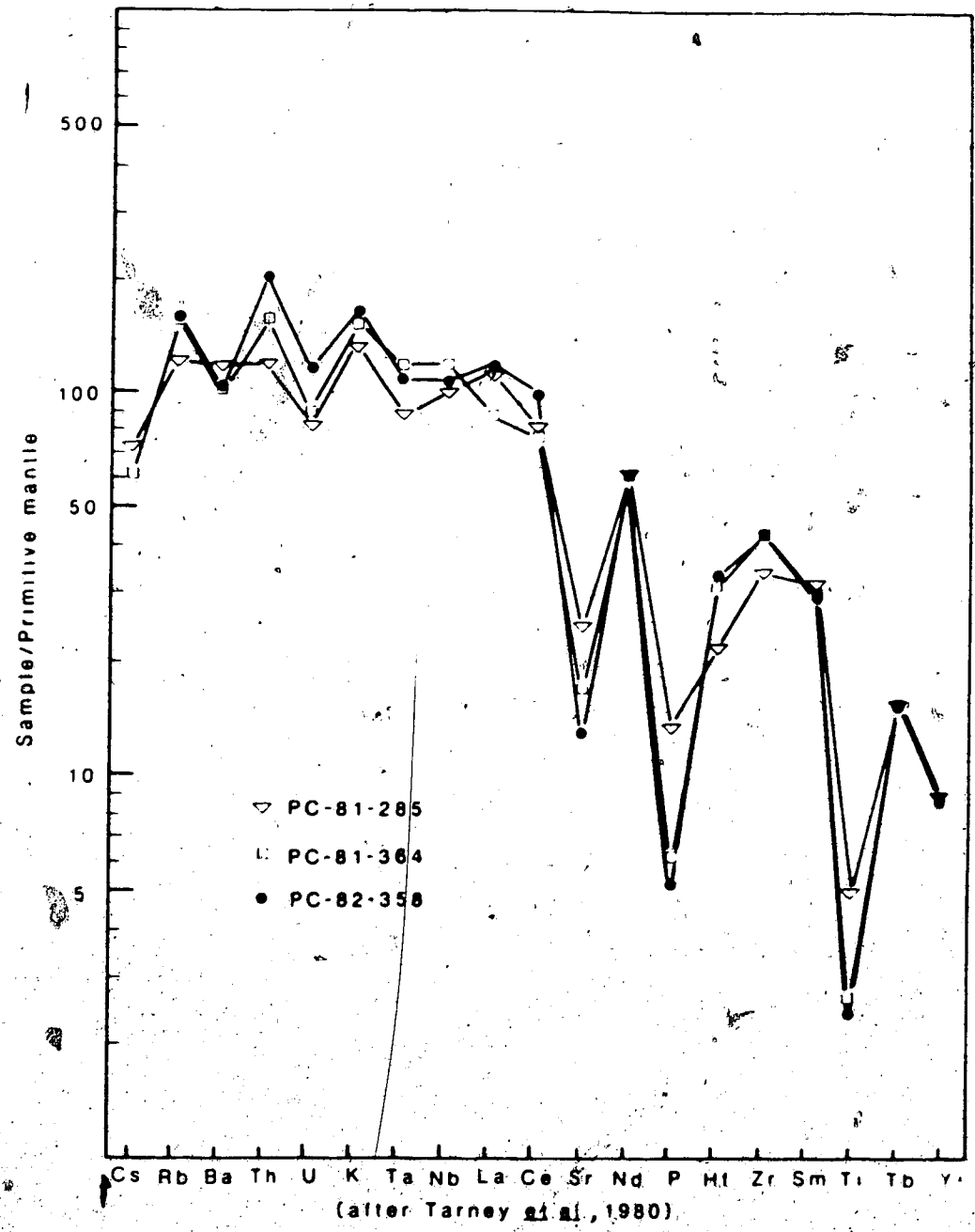


Figure 24: Mantle-normalised LILE distribution plots for inner and reclassified quartz syenites.

Y). Relative mantle abundances of LILE are not well established and the concave-down pattern may be a result of slightly high normalising values for the more incompatible elements. The patterns for undifferentiated basalts reported by Tarney et al (1980) show a similar systematic or smooth concave-down pattern. In the present study the effect is most striking in the late differentiates, the quartz syenites of Figures 23 and 24. The LILE distribution patterns contrast with those for rocks from other intrusive centres of the complex to be discussed later.

This group of 19 elements is not geochemically coherent (as is the REE series) but anomalous behaviour can be inferred for individual elements by assuming that the five REE define a residual liquid enrichment trend or baseline for each sample. Taking the analogy with REE distribution plots a step further, some anomalies can be quantified in a manner similar to that used for Eu on REE plots. A liquid enrichment value (symbolised, for example, Eu^*) can be interpolated for anomalous elements between adjacent (or closest) REE where available, e.g., Ti^* can be interpolated between Tb and Sm and Sr^* between Nd and Ce.

Titanium is a non-hygromagmatophile[†] element (anomalous) in the earliest samples of the series. Early removal of Ti into Fe-Ti oxides results in a strong positive Ti anomaly (Ti/Ti^* up to 2.5 in gabbro and mafic diorite) which is followed by a negative anomaly beginning in leucocratic diorite and dropping to Ti/Ti^* less than 0.1 in the quartz syenites. Using a similar LILE distribution plot to examine the variation of Ti in the alkaline series of the Chaîne des Puys, France, Azzouzi et al (1982) found only progressively negative (0.94 to 0.40) Ti anomalies which they attributed to early separation of Fe-Ti oxides and hornblende. The complementary early positive anomaly attributed to the presence of early Fe-Ti oxides in the analysed gabbros and diorite in this study was absent in the French study.

The non-hygromagmatophile character of Sr can be reasonably quantified by interpolation of a liquid enrichment value, Sr^* , between the adjacent REE, Ce and

[†]The term "a hygromagmatophile element" has become synonymous with "incompatible element" (Henderson, 1982) since its introduction by Treuil and Varet (1973). The two terms are used interchangeably in this study to describe elements which have distribution coefficients $\ll 1$ for the common crystallising minerals during extended stages of magma fractionation and hence "prefer the magmatic liquid" rather than being incorporated into crystals. The term non-hygromagmatophile is used here in preference to non-incompatible (a double negative) to describe elements which are incorporated into crystallising phases and hence no longer "prefer the magmatic liquid".

Nd. A strong positive Sr anomaly reaches a maximum of $Sr/Sr^* = 7.5$ in the plagioclase-rich cumulate gabbros (An_{40-45}), decreases in diorites and changes to negative at some point between the late diorite (An_{28-40}) and mafic syenite then drops to less than 0.1 in the quartz syenite. The position of the Sr maximum anomaly within the series, at intermediate An contents, agrees with published data. Ewart and Taylor (1969) found a well-defined maximum for Sr in volcanic rocks of New Zealand between An_{40} and An_{55} . Korrington and Noble (1971) found that plagioclase/liquid distribution coefficients for Sr rose from 1.5 at An_{90} to 7.0 at An_{30} then dropped to about 3-4 in sodic alkali feldspar.

Partitioning of Sr^{2+} and Eu^{2+} into plagioclase is controlled by the concentration of each species in the melt and by crystal/liquid equilibrium. Philpotts (1970) suggested that identical charges and very similar ionic radii for Eu^{2+} and Sr^{2+} (1.17 Å and 1.18 Å respectively; Shannon, 1976) would lead to almost identical partitioning behaviour of the two ions in rock systems. A plot of Sr/Sr^* vs Eu/Eu^* (Figure 25) indicates that within the Big Spruce Lake series the two plagioclase-controlled anomalies do not correlate on a 1:1 basis in spite of the fact that both are quantified from liquid enrichment values defined by the same REE results—for any given

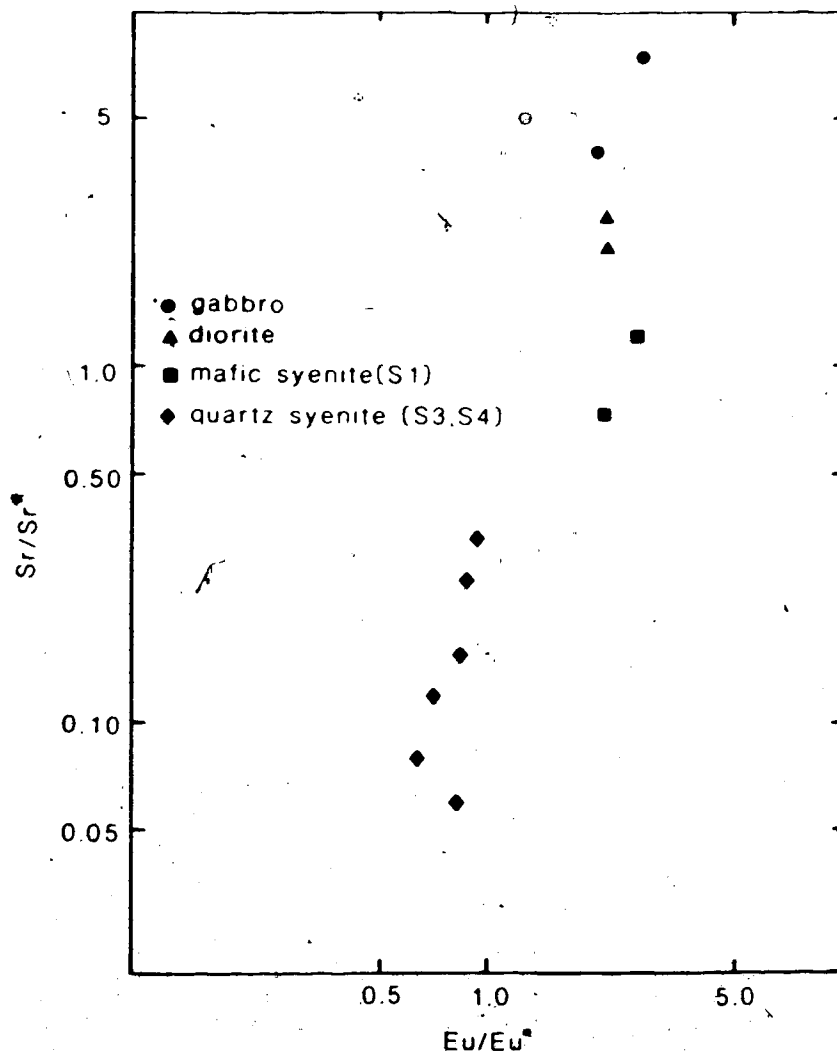


Figure 25. Eu/Eu^* vs Sr/Sr^* in rocks of the gabbro-syenite series. The two plagioclase-controlled anomalies do not correlate on a 1:1 basis. Sr/Sr^* reaches a maximum in the leucocratic-laminated gabbro then decreases as differentiation proceeds. Eu/Eu^* varies over a small range, differing in early and late members of the series.

sample. Any error or discrepancy in normalisation values used would shift all Eu/Eu^* and Sr/Sr^* values by a constant factor but would not alter the geochemical trends observed. The plot of Sr/Sr^* vs Eu/Eu^* clearly shows separate fields for early and late members of the differentiation series, differing slopes for the two fields and Sr/Sr^* and Eu/Eu^* change from negative to positive anomalies (i.e., from <1.0 to >1.0) at different points within the series. Ring syenites are omitted from this plot because trace element data (presented later) indicates possible gneissic contamination of this unit. Sr/Sr^* varies more widely than does Eu/Eu^* . Within the early differentiates Sr/Sr^* varies by a factor of 10, from 0.7 to 7.0, while Eu/Eu^* is almost constant at 2.0-3.0. Within the quartz syenites Sr/Sr^* varies by a factor of 5, from 0.3 to 0.06 while Eu/Eu^* decreases only from 1.0 to 0.6. Sr/Sr^* changes from positive to negative anomaly within the mafic syenites, one of which has $\text{Sr}/\text{Sr}^* >1.0$, the other <1.0 . Within these same mafic syenites Eu/Eu^* remains in the range of 2.0 to 3.0. Eu/Eu^* becomes <1.0 with the first quartz syenite where Sr/Sr^* has already decreased to 0.35.

The observed differences in geochemical behaviour may result from the fact that more than one process is involved in the development of the Eu anomaly. The

concentration of Sr^{2+} in the melt at any time is a function only of the original concentration and the amount removed by crystallisation while that of Eu^{2+} is additionally affected by a dynamic equilibrium between Eu^{2+} and Eu^{3+} . This reaction can be written



(where m and v denote melt and vapour phase, respectively) indicating that the $\text{Eu}^{2+}/\text{Eu}^{3+}$ ratio is strongly dependent upon oxygen fugacity. Several authors have attempted to quantify the behaviour of Eu in order to use this element to determine oxygen fugacity during crystallisation in a similar manner to the commonly-used Fe-Ti oxide equilibrium (Philpotts, 1970; Weill and Drake, 1973; Drake, 1975; Sun et al, 1974). However, in addition to oxygen fugacity, melt composition can markedly affect the amount of Eu^{2+} in the melt (Morris and Haskin, 1974) by preferential stabilisation of Eu^{2+} in alumino-silicate complexes in the melt (Möller and Muecke, 1984). The stabilisation effect should be most pronounced in highly polymerised Al- and Si-rich melts such as the late quartz syenites. Redox control over the concentration of Eu^{2+} available for incorporation into feldspar is thus a function of both oxygen fugacity and melt composition (as

as temperature and pressure). Control of the $\text{Eu}^{2+} \rightleftharpoons \text{Eu}^{3+}$ equilibrium appears to reduce the degree of enrichment of Eu in intermediate feldspar relative to Sr (restrains the size of the positive anomaly) and to cause enrichment (positive anomaly) of Eu^{2+} in feldspar to continue towards more acidic liquid compositions than those which optimise enrichment of Sr^{2+} (single valence state).

Removal of P as apatite is not very clear on the LILE plots. Apatite becomes a stable phase at about 50% silica and forms within a range of silica contents from about 50 to 58% in the Big Spruce Lake series. Thus it appears mainly in late diorite and early syenite. The LILE distribution plots show only one positive P anomaly, for the leucocratic diorite (PC-81-363). The relative depletion of P in all the other samples suggests that either the source liquid from which the gabbros crystallised had a relative P depletion or that the normalising value for P taken from Tarney et al. (1980) is too high. Zirconium and Hf are also low relative to the liquid enrichment trend (as defined by the five REE) until the quartz syenites begin to crystallise significant amounts of zircon. Even in these zircon-rich rocks (zircon is abundant in hand specimen and thin section) Zr shows only a small positive anomaly on the LILE

distribution plots. Either normalising values for Zr and Hf are too high or the source liquid was slightly depleted in these elements. The latter explanation is more probable and is preferred for Zr and P. Tarney *et al* (1980) found no consistently negative P or Zr anomalies using the same normalisation values in their work with relatively unfractionated oceanic basalts. These basalts do commonly show a small negative anomaly for Hf relative to Zr and hence this normalisation value may be in error.

Potassium (incompatible in basaltic melts but compatible in rhyolitic) was retained in the mantle-normalised LILE distribution plots largely as a monitor for stabilisation of K-rich phases (biotite, alkali feldspar) and for evaluation of possible contamination by K-rich gneissic host rock. In the Big Spruce Lake series K shows slightly erratic behaviour. No units show a large enrichment of K over the residual liquid trend (defined by REE) except the ring syenites, which appear to have assimilated significant amounts of gneiss. However, K shows a small positive anomaly even in the earliest samples of the series. Values of K_{MN} are up to 2 times liquid enrichment values (approximated by interpolation between La and Rb), but the enrichment is variable and shows no trend with increasing differentiation. It appears that a K-rich phase is present even in the

gabbros. Both gabbros analysed contain small amounts of amphibole, but the more K-rich one (PC-81-275) also contains late alkali feldspar, the most probable host for K. Enrichment in Ba (positive anomaly) throughout the early series can similarly be attributed to the presence of a K-compatible phase. The relative potassium enrichment of the leucocratic gabbro is not entirely a result of assimilation of gneiss because Ba, Nb and Ta are not depleted in this sample to correspond with the gneissic LILE signature. If K were enriched slightly in parent magma then small differences in crystallisation of K-phases within the different units could result in the constantly positive but erratic anomalies observed.

Of the other LIL elements Rb, Nb, Ta, U and Th show slightly erratic behaviour, not clearly attributable to large amounts of gneissic contamination. Yttrium follows the REE enrichment trend, i.e., the residual liquid trend. Data for Cs are sparse; abundances are at the limit of detection for the INAA procedure employed here.

4. Granodioritic Country Rock

Four samples of the presently exposed granodioritic country rock have been analysed in order to allow assessment of country rock interaction during intrusive activity. The analytical results are presented in Appendix 3, page 400 and as chondrite-normalised REE and mantle-normalised LILE distribution plots in Figures 26 and 27.

Three of the samples from different locations are almost identical in major element composition; the fourth from a position between the main complex and the satellite complex is more felsic. The same three samples have almost coincident chondrite-normalised REE plots and mantle-normalised LILE plots. A strong negative Eu anomaly ($\text{Eu}/\text{Eu}^* = 0.35-0.46$, Table 4) and strong negative anomalies for Ti, P, Sr, Nb, Ta and Ba are characteristic of these samples. The fourth granodiorite, more felsic, is less LILE-enriched with slightly weaker though still negative anomalies for Eu ($\text{Eu}/\text{Eu}^* = 0.27$) and P, similar strong negative anomalies for Ti, Sr, Nb and Ta, and a very strong negative Ba anomaly. None of these mantle-normalised LIL plots show the concave-down pattern that is typical of the gabbroic intrusive series.

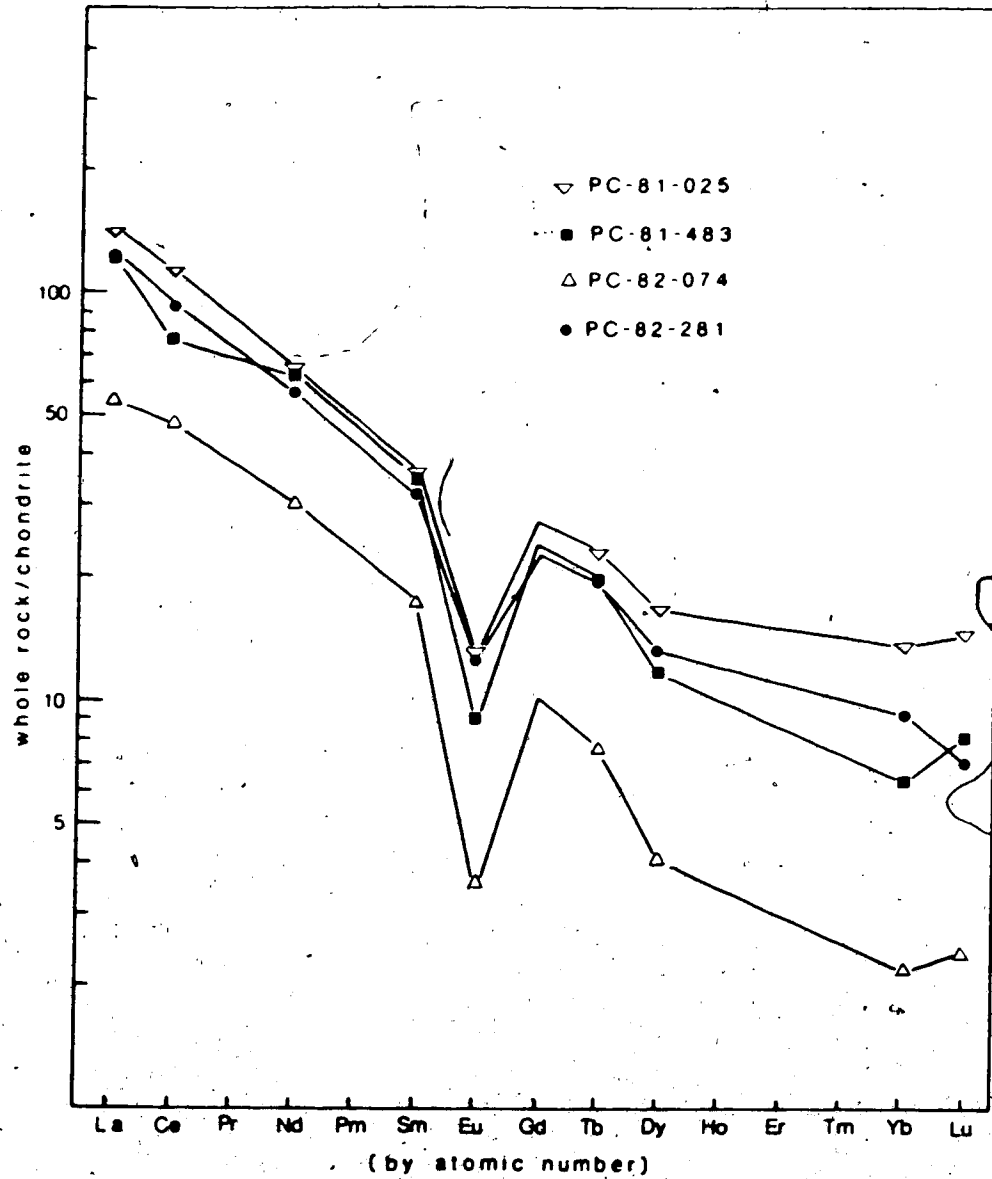


Figure 26. Chondrite-normalised (Nakamura, 1974) rare earth element distribution plots for granodioritic country rock around the Big Spruce Lake alkaline complex.

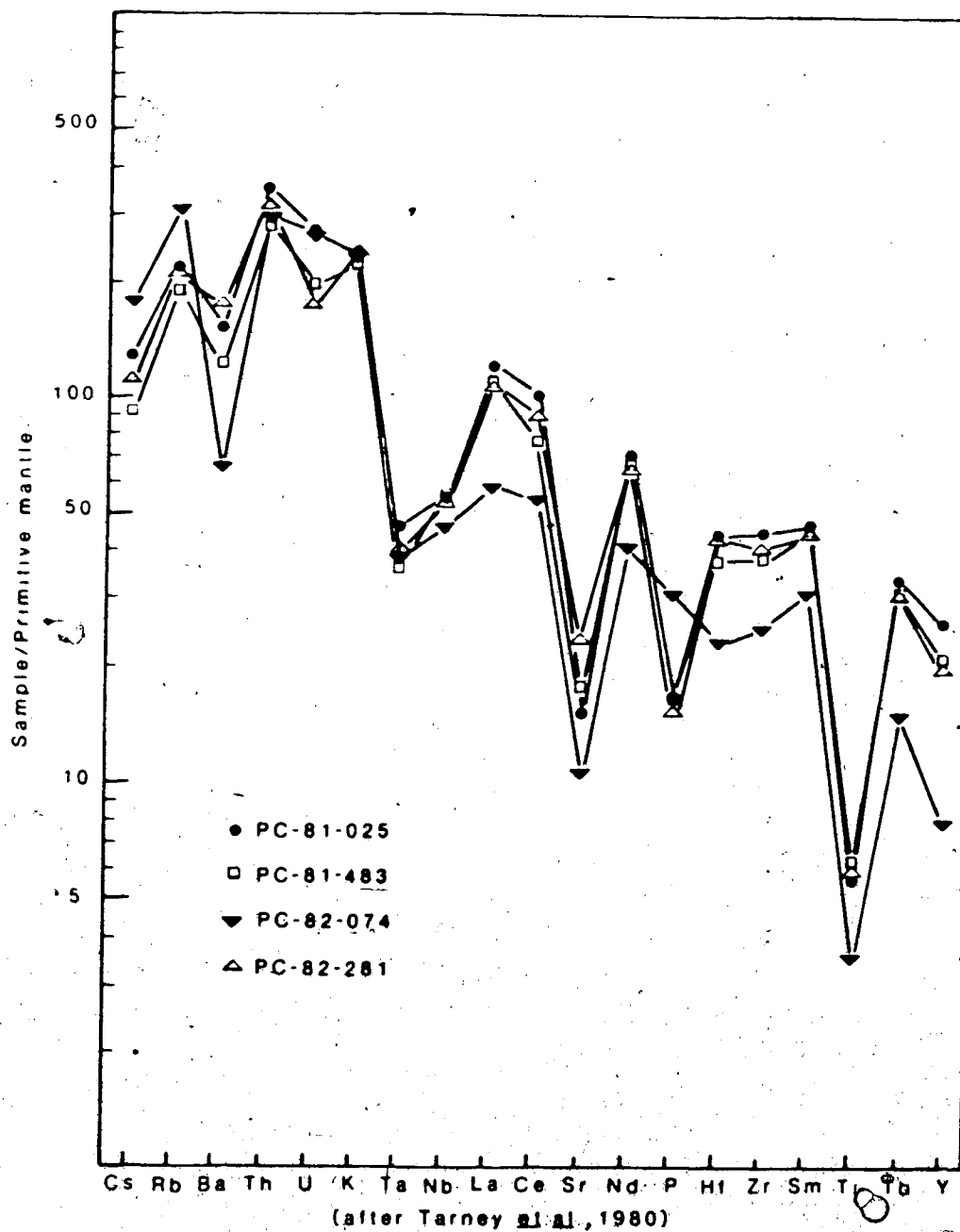


Figure 27. Mantle-normalised LILE distribution plots for granodioritic country rock around the Big Spruce Lake alkaline complex.

Table 4. Rare earth element data for granodioritic gneisses.

Sample Number	Σ REE ¹	Eu/Eu*	(Ce/Yb) _{CN} ³
PC-81-025	227	0.42	8
PC-81-483	179	0.35	12
PC-82-074	94	0.27	22
PC-82-281	191	0.46	10

¹Includes values interpolated from Figure 26 for elements not analysed.

²Eu* interpolated between Sm and Tb on chondrite normalised plots. Eu is analysed value.

³CN = chondrite-normalised values.

5. Evaluation of Effects of Contamination, Open System Crystallisation and Cumulate Formation on Trace Elements

Three mechanisms can produce the major element variations observed in this study, an example of which is the alkali-silica plot (Figure 7). The three (which are not mutually exclusive) are contamination, open-system fractional crystallisation and cumulate formation. Geochemical and field evidence shows that all three occurred during the Big Spruce Lake intrusion. The effects on trace element distributions must be evaluated before inferences about parent magma composition can be made.

If open system crystallisation was the dominant process then variations in element abundances are due mainly to crystal-liquid partitioning during fractional crystallisation and for hygromagmatophile or incompatible elements (very low D values) relative abundances remain constant as absolute abundances increase in residual liquids (incompatible element ratios do not alter). The slope of a logarithmic two-element plot for such elements is one (Allegre et al, 1977) and the data should be well constrained. For the hygromagmatophile elements cumulate formation should have a similar effect.

If contamination is the dominant process then the two-element logarithmic plots should show scatter beyond analytical error, in some cases destroying the fractional crystallisation trend. The concentration of LILE resulting from contamination is dependent upon the magma composition at the time of mixing, the modal and element composition of the contaminant and the degree of melting which occurs during assimilation of contaminant material. The fractional crystallisation path followed after assimilation will vary according to the changes in major element composition caused by assimilation. An obvious corollary to this conclusion is that logarithmic plots of two incompatible elements which have essentially the same relative abundances in the primitive magma and in the contaminant material will not show scatter beyond analytical error regardless of the degree of contamination.

Of the 19 elements plotted on the mantle-normalised distribution plots of the intrusive series Ti, Sr, P, Ba, and K show evolving anomalies typical of inclusion in a fractionating phase. For this reason they are not diagnostic for contamination. Insufficient data for Cs and inconsistent trends for U and Th exclude these elements. Of the remaining elements, Rb, Y, Nb, Ta, Zr Hf and REE, the mantle-normalised plots of gneisses (Figure

27) suggest that Rb and Nb (Ta) are of most value in detecting assimilation of this host rock during intrusive activity. Excellent correlations of Zr with Hf and Nb with Ta (Figure 28) indicate that it is necessary to plot only one element from each of the pairs to evaluate effects on both.

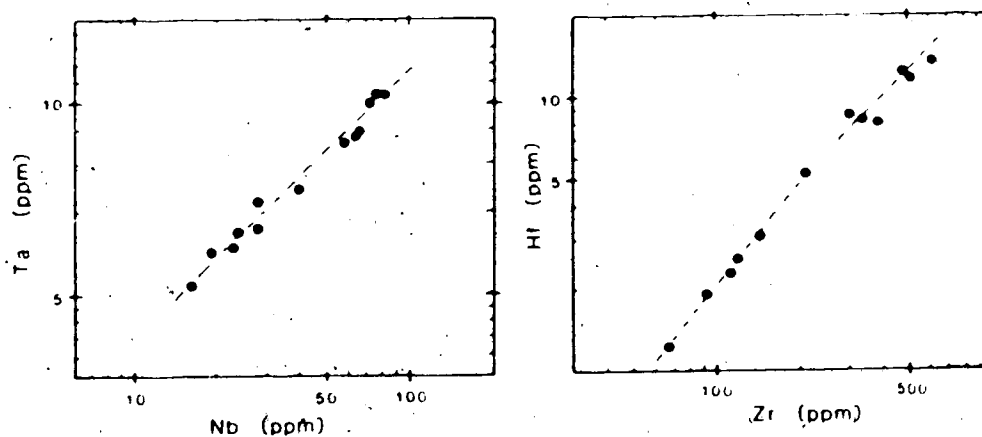
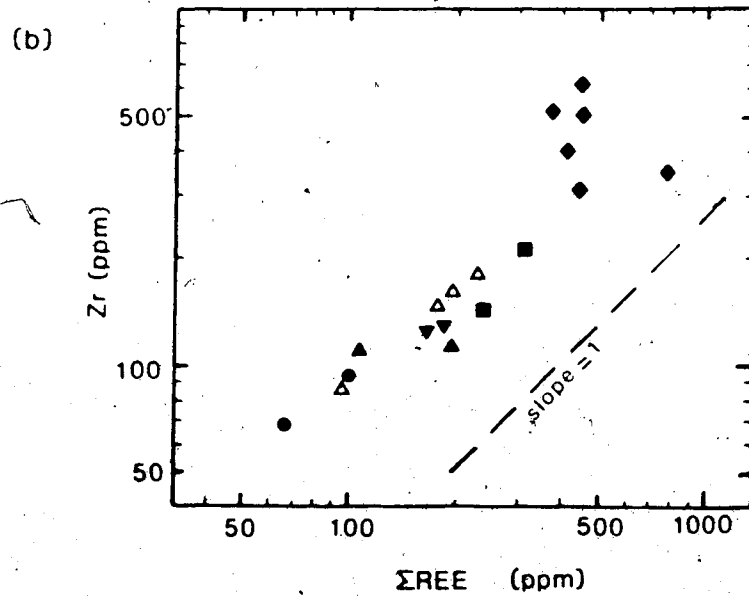
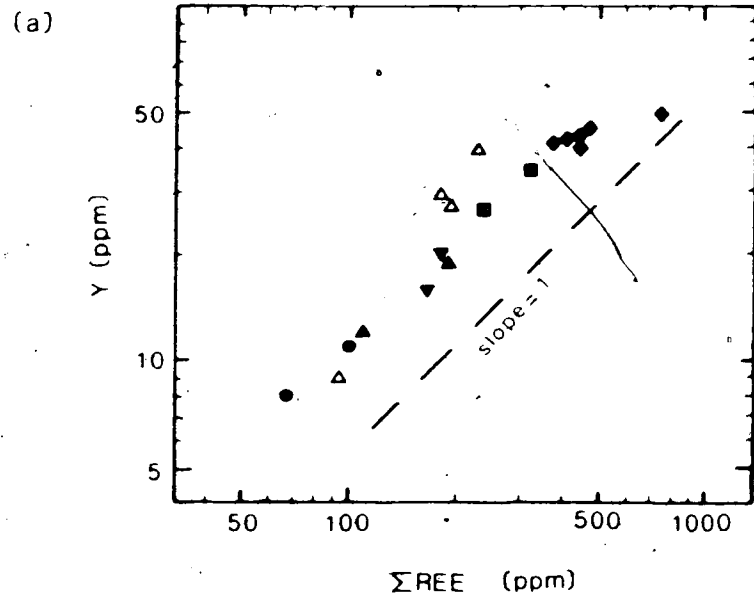


Figure 28. Nb vs Ta and Zr vs Hf in the alkali gabbro to syenite series of the Big Spruce Lake intrusion.

Yttrium, Zr, Nb and Rb are plotted against Σ REE in the logarithmic, two-element plots of Figures 29 and 30. As predicted from examination of the mantle-normalised plots of intrusive and country rocks, Σ REE vs Y and Σ REE vs Zr plots produce a single enrichment trend for both intrusive and country rocks whereas separate fields are formed on Σ REE vs Nb and Σ REE vs Rb.



● gabbro ▲ diorite ■ mafic syenite ▼ ring syenite
 ▲ granodiorite ◆ quartz syenite

Figure 29. a) Σ REE vs Y and b) Σ REE vs Zr for the gabbro-syenite series. Both show data scatter. The compositions of gneisses plot near the trend for intrusive rocks.

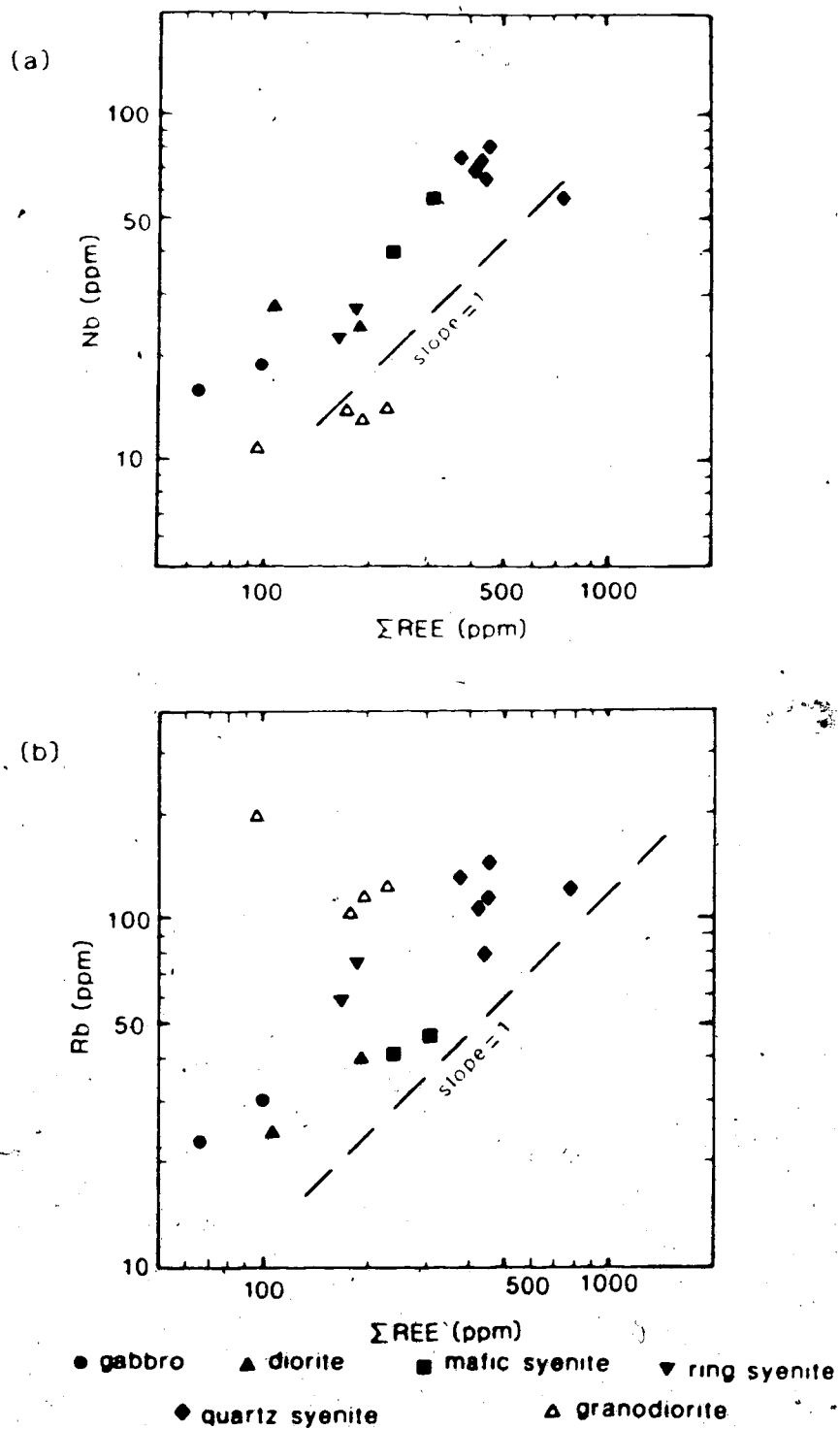


Figure 30. a) Σ REE vs Nb and b) Σ REE vs Rb for the gabbro-syenite series. The compositions of gneisses plot away from the trend for intrusive rocks.

Evaluating each of these two-element plots in terms of possible contamination and open system effects and considering the data for all intrusive rocks as a single unit, it is clear that data scatter exceeds experimental error (e.g., compare Zr vs Hf and Nb vs Ta of Figure 28 with these plots) and that the apparent slopes are not equal to one. Both of these are simple criteria for contamination as outlined above. However, the data do form linear trends and most data points are not scattered towards a common focus (contaminant composition). Combination of incompatible and major element data in Figure 31, which shows $\text{Na}_2\text{O} + \text{K}_2\text{O}$ plotted vs Nb, Zr, and Rb suggests that combined assimilation, open-system mixing and crystallisation effects may be responsible for the scattered trend of trace element relative abundances noted in Figures 29 and 30. The three plots of Nb, Zr and Rb vs alkali, which have the data base expanded to include that of Martineau (1970), clearly show that the individual lithological units lie in separate compositional fields. Each unit is a separate entity within a single major trend. Each petrographic unit appears to be coherent in itself (e.g., gabbro, mafic syenite or quartz syenite), but there are discontinuities between them which can be attributed to small differences in the composition of separate magma pulses, to differences in fractional

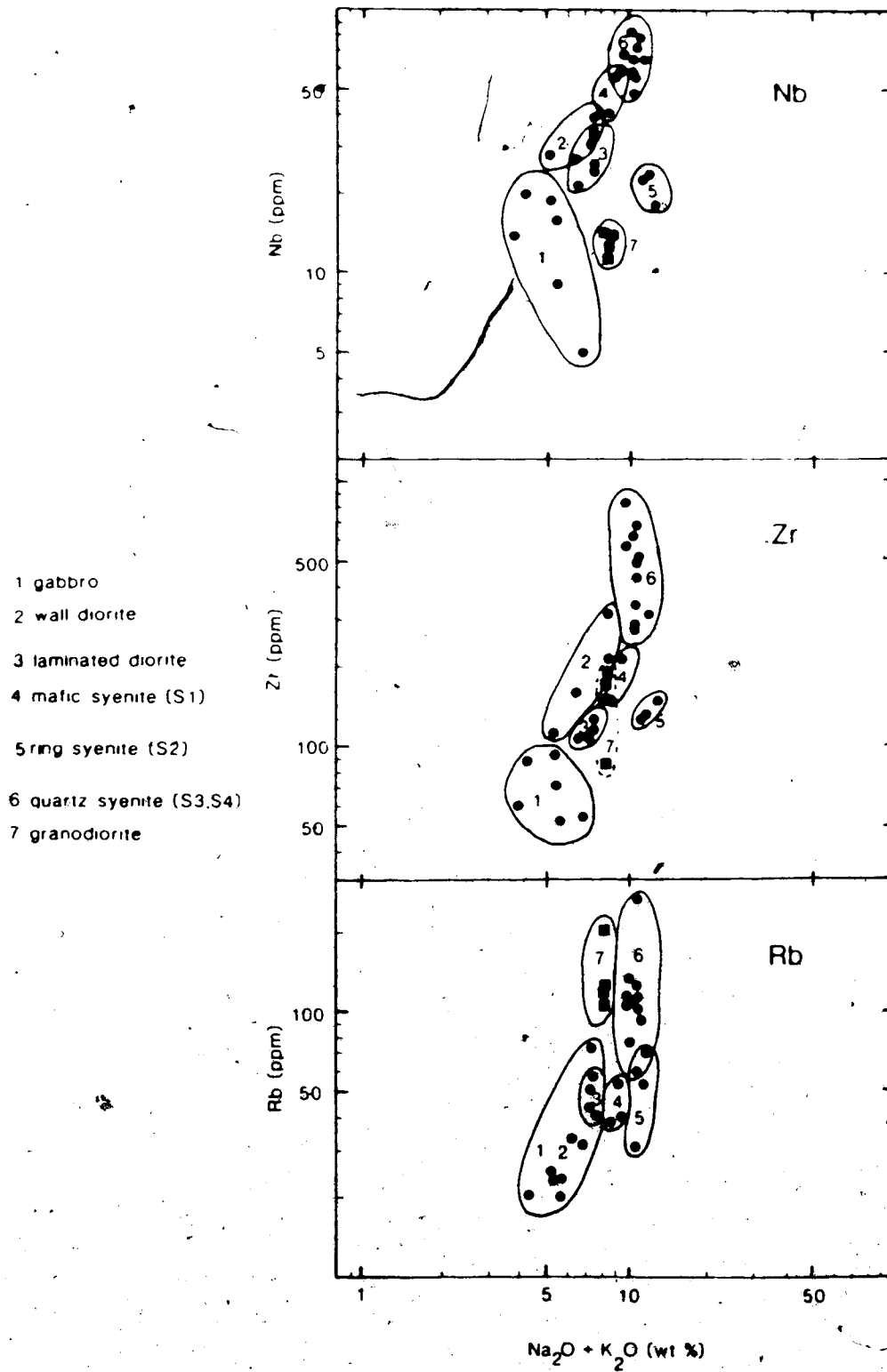


Figure 31. Alkali vs Nb, Zr and Rb for the gabbro-syenite series. The compositions of individual petrological units lie in separate fields.

crystallisation paths (causing variable bulk D values) or to addition of small amounts of contaminant at any stage. When this open system behaviour is taken into consideration the assumption that the slope of the two-element logarithmic plots for these elements is one appears to be valid; the apparent slopes result from differing relative abundances within different units.

For most of the samples analysed it can be inferred from the results that contamination effects are small (isotopic results presented in Chapter 4 suggest less than about 15-20% for most samples) and are not readily separable from those caused by crystallisation of multiple magma pulses in multiple chambers. However, one unit does show possible contamination effects. The EREE vs Nb and vs Rb plots both indicate that the ring syenite could result from mixing of a mafic syenite magma with up to 40% of a granodiorite similar to the felsic sample, PC-82-074, presently exposed on the east side of the Snare Fault between the main and satellite intrusions. Ring syenite lies on an apparent mixing line on the CaO vs Y plot (Figure 11) and on the trace element-silica variation diagrams of Figure 32. If gneissic assimilation occurred shortly before final emplacement and the granodiorite was completely assimilated, then most major and trace element concentrations are consistent with this degree of

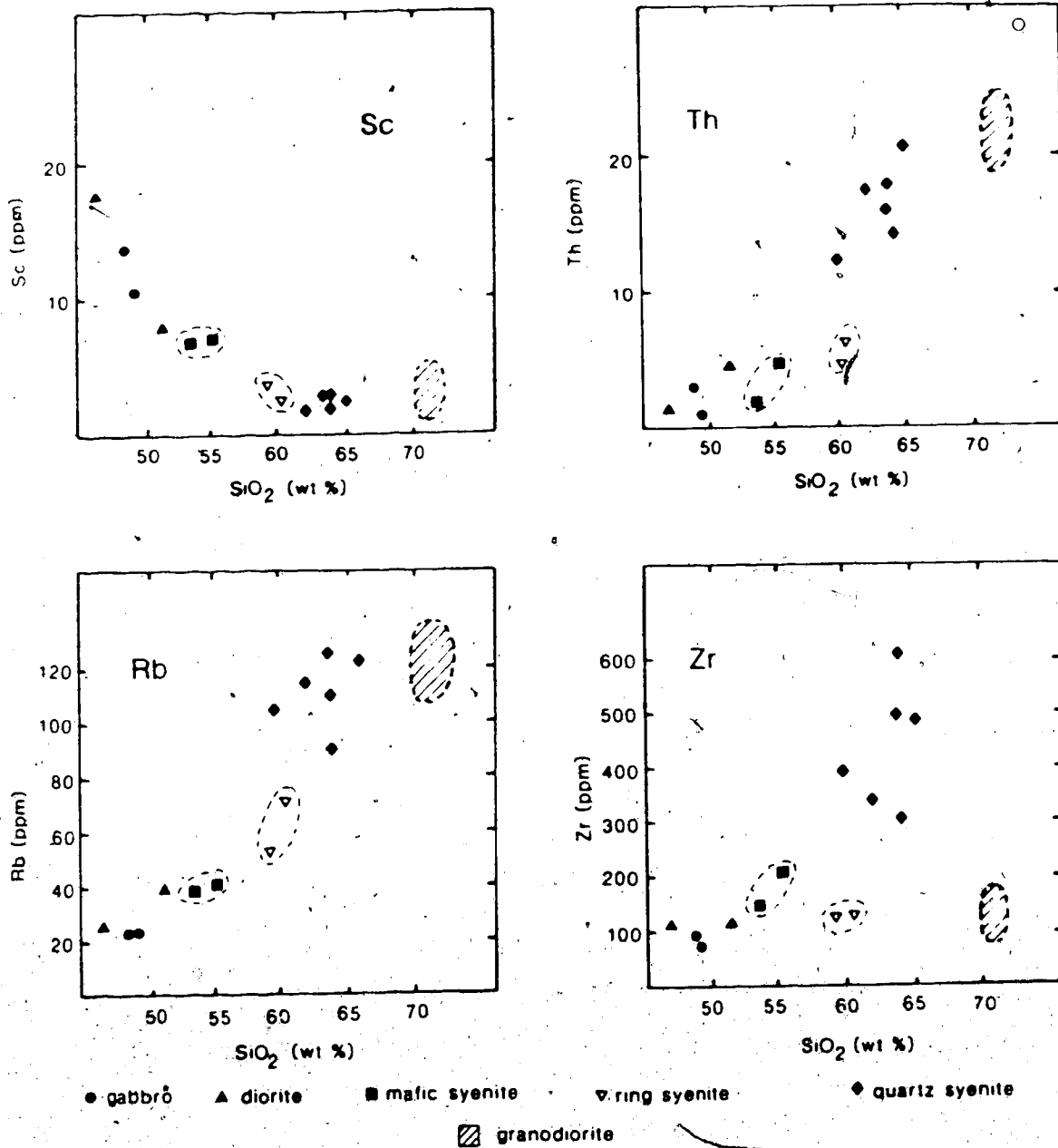


Figure 32. Harker diagrams of Sc, Th, Rb and Zr for the gabbro-syenite series indicating possible contamination of the ring syenite by granodioritic gneiss.

mixing. However, simple two-component mixing is not consistent with all of the data; and the alkalis and relative REE abundances are not in agreement. They introduce a requirement of alkali enrichment to levels above that of gneiss or mafic syenite (Figure 31) and fractionation of the light rare earths. Differentiation following mixing does not account for the alkali enrichment and REE fractionation because other major and trace elements are not similarly affected. Addition of REE-rich (and light REE fractionated) alkali-rich fluids during emplacement of contaminated magma could account for the total ring syenite composition. Later fluid movement should affect adjacent units as well, and no such effects are observed.

No other units show element abundance patterns consistent with systematic mixing of parent magma with significant amounts of granodiorite, nor with any single contaminant composition. The element data for Centres 1 and 2 thus indicate a single differentiation trend, but the data are poorly constrained due to open system crystallisation of several batches of similar magma contaminated with small amounts of crustal rock. The post-intrusive disturbance evident in K-Ar data (Leech et al, 1963; Martineau and Lambert, 1974) and in the Rb-Sr and Sm-Nd isotopic data of this study (Chapter 4) has not

overridden the tight petrologic control of compositions imposed during intrusive activity.

6. Magnetite Pyroxenites

The magnetite pyroxenites, ultramafic rocks which cut the gabbroic ring complex at the northeast corner of the main complex, must be considered in relationship to the gabbro-syenite series because of their close association in space and time (Martineau, 1970). The main body of pyroxenite lies immediately to the northwest of the ring complex in an area interpreted as previously occupied by diorite or gabbro while smaller bodies (dykes and lenses) cut the central gabbros. Pyroxenite may originally have extended further to the southwest into a space now occupied by later syenite. The pyroxenites were emplaced following crystallisation of diorite and gabbros and prior to emplacement of the quartz syenites. The magnetite pyroxenites differ from members of the main gabbro-syenite series in their restricted, ultramafic mineralogy and (apparently) more active mechanism of emplacement.

Complete WR analyses of two samples from the main pyroxenite body (PC-81-001 and PC-81-004) are reported in Appendix 3, page 401. The third WR sample analysed (PC-82-163, Appendix 3, page 401) was taken from a small body which intrudes the large northeastern diorite lobe.

This pyroxene itself is displaced by later movement on the main NE-SW fault splay X-X'.

Because of the high Fe-Ti oxide content of the pyroxenites the WR major element compositions have very low SiO₂ concentrations (SiO₂ = 30 - 36%). On simple Harker diagrams these rocks plot off the main gabbro-syenite trend, somewhat scattered to low SiO₂ values. The alkali elements are largely absent (Rb) or present in very small amounts (K, Na, Sr) as are U and Th. P is present in only PC-82-163' (from the small isolated pyroxenite body). The paucity of incompatible elements in these rocks and the fact that they do not plot on the main gabbro-syenite trend indicates that either

- (1) the present WR compositions are not fully representative of the melt from which these rocks crystallised, or
- (2) the analytical data are fully representative of the parent melt of these ultramafic rocks and this melt differed significantly from that of the gabbroic series and perhaps had a different source.

Relative abundances of REE can be used to distinguish between these two possibilities. Chondrite-normalised REE distribution patterns for the three WR samples are shown in Figure 33. The pyroxenites are strongly depleted in light rare earth elements (LREE), La to Nd, and lack Eu

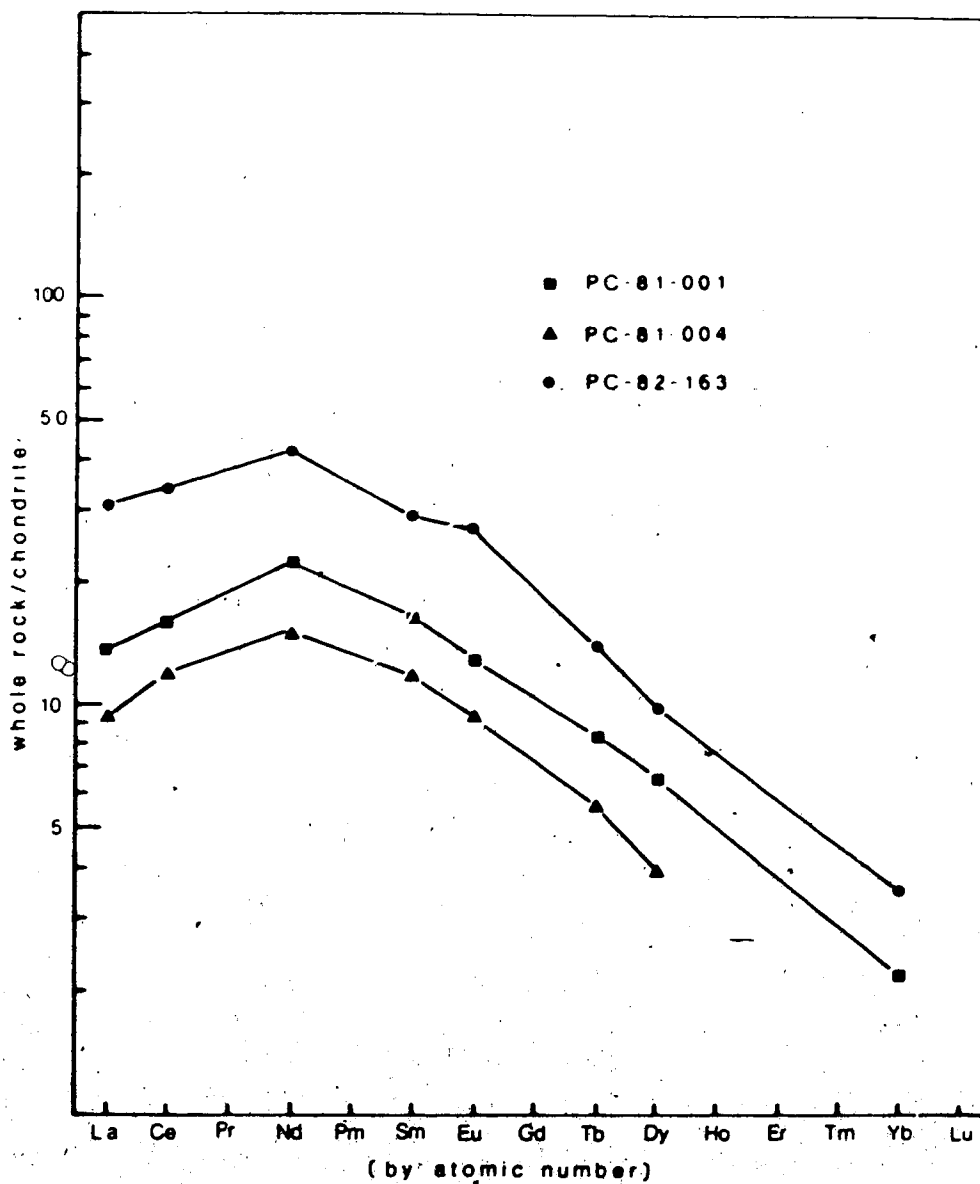


Figure 33. Chondrite-normalised (Nakamura, 1974) rare earth element distribution plots for magnetite pyroxenites of Centre 1. La-Ce depletion and MREE/HREE fractionation are characteristic. Only one sample shows a small Eu anomaly.

anomalies. Sample PC-82-163, which also has 0.14% P_2O_5 , has a small positive Eu anomaly, perhaps a result of this small pyroxenite body having assimilated earlier diorite or gabbro. The middle (MREE) to heavy REE (HREE) (Sm to Lu) abundances show a degree of fractionation similar to that of the gabbroic series. $(Sm/Yb)_{CN}$ is about 7.7 for pyroxenites and 5.6 to 7.0 for gabbros and diorites.

To determine if the strong LREE depletion in these rocks is due to their unusual modal mineralogy (mineralogical control, model 1 above) or to a LREE depletion in the liquid from which they crystallised (melt composition or source control, model 2 above) a pyroxene separate from one of them (PC-81-001) was prepared. The pyroxene was separated from the -80/+100 mesh fraction by standard methods. Magnetite and mixed grains were removed by a hand magnet, then the portion which floated in methylene iodide but sank in acetylene tetrabromide was passed through a Frantz electrodynamic separator. The final sample was hand-picked to obtain a separate estimated to be ~99% pure.

INAA results for this pyroxene separate are presented in Appendix 3, page 401 and in a chondrite-normalised REE distribution plot in Figure 34. The REE distribution plot of the pyroxene separate parallels that of the WR from which it is derived, but at higher concentrations. REE

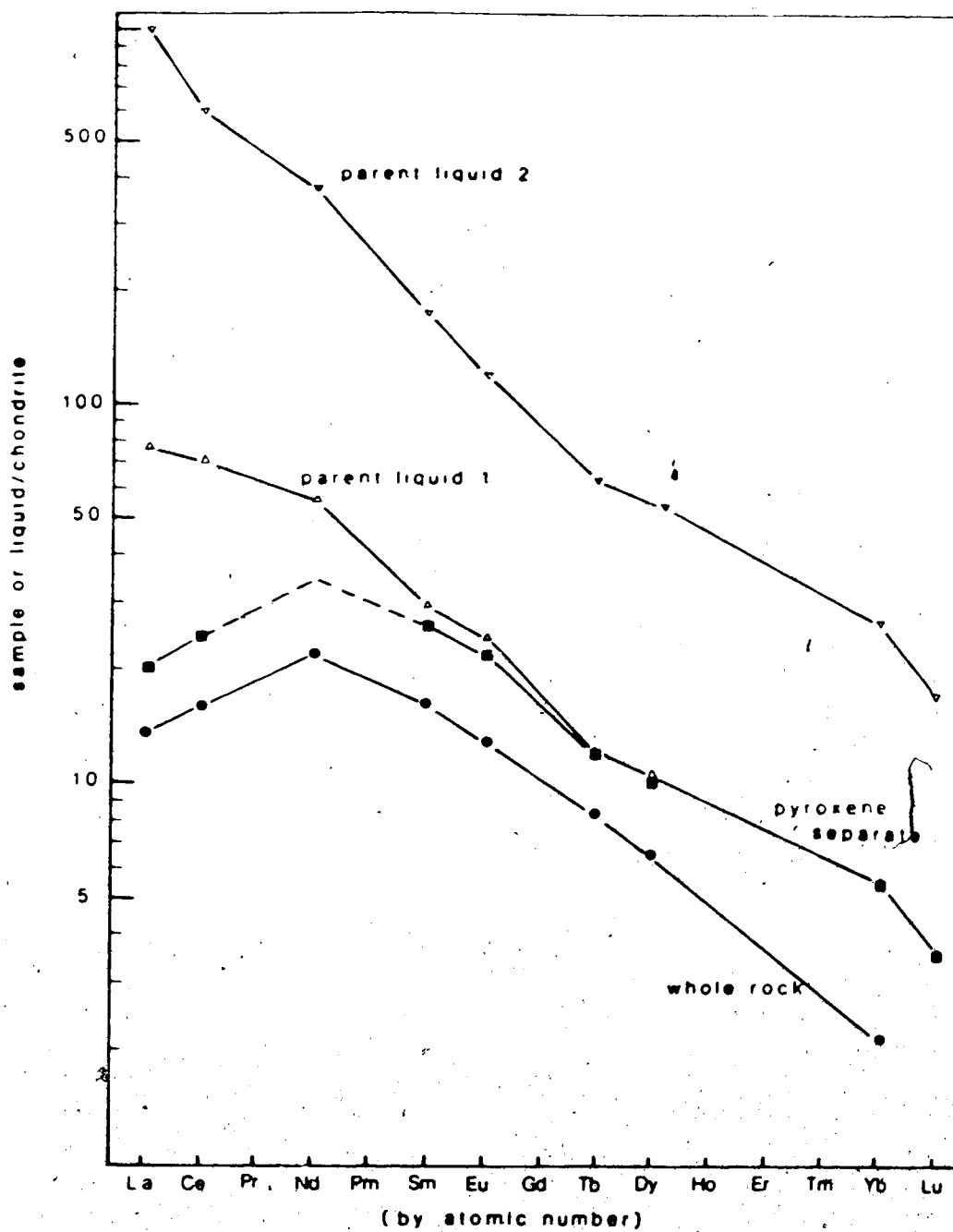


Figure 34. Chondrite-normalised (Nakamura, 1974) rare earth element distribution plots for magnetite pyroxenite PC-81-001, for the pyroxene separated from this sample and for two possible parent liquid compositions calculated from the separate composition and using high and low D values.

from the separate have the same middle to heavy REE fractionation trend and the same strong La-Ce depletion as do the WR REE. The pyroxene, about 40% modal abundance in the whole rock sample, contains 60-65% of the total REE in the WR sample and about 90% of the HREE. Crystal/liquid partition coefficients (D values) for REE in olivine (e.g., Henderson, 1982; Frey et al., 1978) indicate that its contribution to the whole rock abundances would be negligible (Figure 35). D values for REE in olivine are about 1 to 2 orders of magnitude smaller than those for REE in clinopyroxene, and concentrations of REE in olivine coexisting with pyroxene of the separate would be correspondingly low. Data for partitioning of REE between melt and magnetite, the third major phase in these ultramafic rocks, are somewhat sparse, especially for mafic to ultramafic melts. Data which are available from Villemant et al (1981) and Henderson (1982) indicate that magnetite crystallising along with clinopyroxene should contain concentrations of REE of the same order of magnitude as clinopyroxene and that the middle REE should be relatively enriched in the magnetite over both LREE and HREE (Figure 35). The LREE depletion exhibited by the WR samples corresponds to a LREE depletion in pyroxene, and probably also in magnetite, and thus the LREE depleted whole rock distribution pattern can be attributed directly

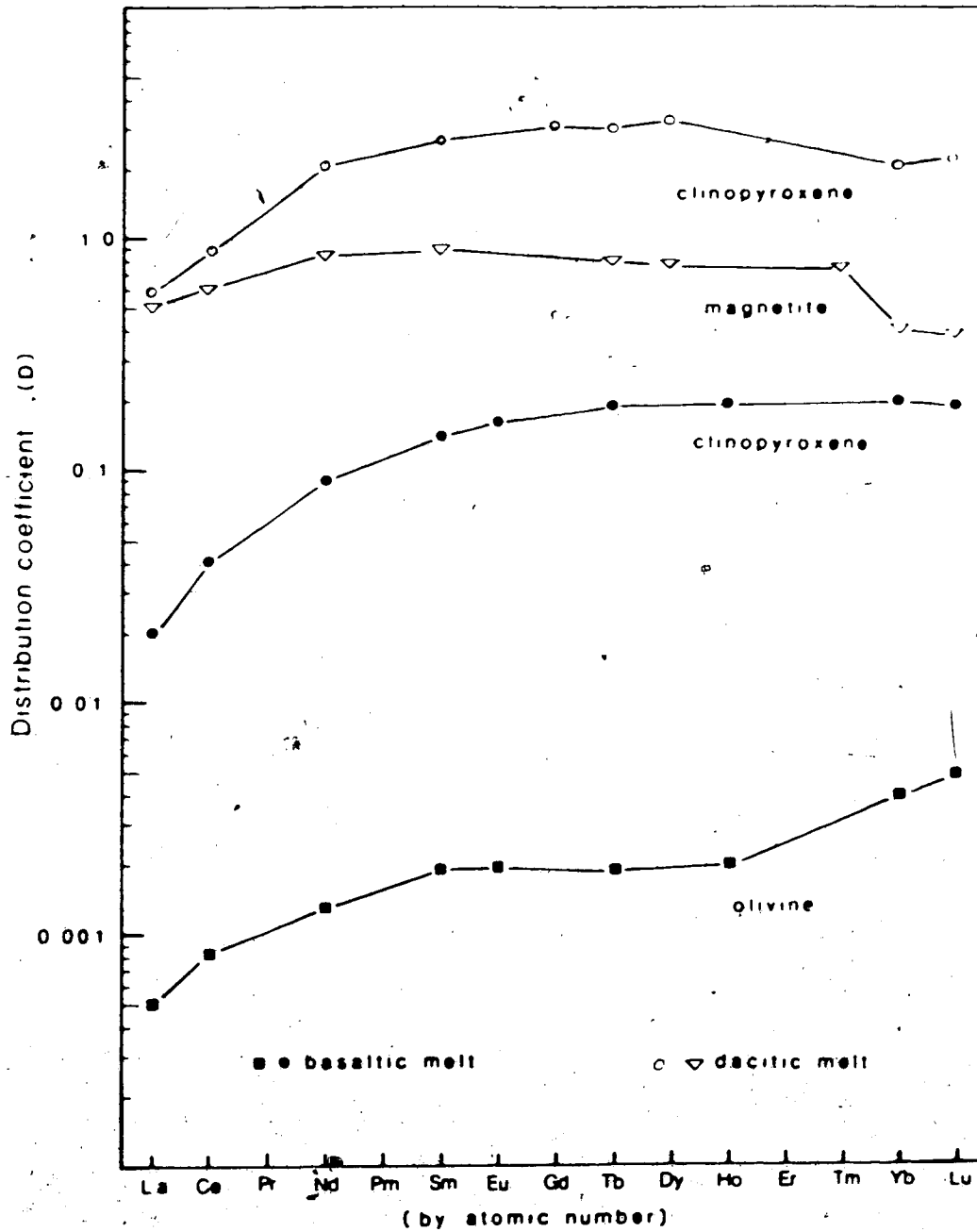


Figure 35. Mineral/melt distribution coefficients for olivine and clinopyroxene in basaltic melt and for magnetite and clinopyroxene in dacitic melt. Data are from Frey et al (1978), Villemant et al (1981) and Henderson (1982).

to the high modal abundance of LREE-depleted pyroxene and magnetite.

The REE composition of the pyroxene separate is a function of the composition of the melt from which it crystallised as well as mineral/melt equilibrium during crystallisation (i.e., the D values for REE in pyroxene). If D values for REE in clinopyroxene are known, then the REE composition of the parent melt can be calculated. There are many reports of D_{REE} values for clinopyroxene/melt equilibrium in the literature (e.g., Irving, 1978; Henderson, 1982; Möeller and Muecke, 1984). These published values vary by at least an order of magnitude, but all show a decrease of D for LREE relative to HREE, similar to the example shown in Figure 39. Approximate limits can be set on the REE composition of the liquid from which the pyroxene of sample PC-81-001 crystallised by using low (Frey *et al.*, 1978) and high (Henderson, 1982) D values from the literature. The calculation uses the simple relationship

$$\frac{C_{\text{pyx}}^i}{C_{\text{melt}}^i} = D_{\text{pyx/melt}}^i$$

where $D_{\text{pyx/melt}}^i$ is the bulk partition coefficient of element *i* in equilibrium with pyroxene, C_{pyx}^i is the concentration of *i* in pyroxene, and C_{melt}^i is the concentration of *i* in the melt.

The D values used and the resulting REE compositions of the parent liquid(s) are listed in Table 5. The chondrite-normalised REE distribution patterns of each of the two liquids is presented in Figure 34 for direct comparison with the REE compositions of the pyroxene and WR samples. Use of the high D values produces REE abundances in the liquid similar to those for an undifferentiated alkali basalt (Sun and Hanson, 1975b; Frey et al, 1978) while use of the low D values produces an enriched REE composition similar to that of a carbonatite. Chondrite-normalised values for La vary from 78 to 1000, while $(Ce/Yb)_{CN}$ varies from 13 to 22 over the range of D values used. Neither calculated liquid pattern shows the La and Ce depletion characteristic of the pyroxene and WR pyroxenites. The melt from which the pyroxene crystallised was not depleted in LREE, but was actually enriched in LREE, La to Nd, which are now absent from the WR magnetite pyroxenites. The presently exposed pyroxenites do not have WR REE distribution patterns fully representative of the melt from which they crystallised. It can be inferred that alkali elements, P, U and Th were also present in the melt and are now absent. The actual composition of the original melt cannot be further quantified because of the uncertainties in D values.

Table 5. Calculated rare earth element abundances in melts parent to magnetite pyroxenite PC-81-001. ✓

Element	High $D_{\text{cpx/melt}}$ from Henderson, 1982		Low $D_{\text{cpx/melt}}$ from Frey et al, 1978	
	D	Parent liquid 1 (ppm)	D	Parent liquid 2 (ppm)
La	0.26 est	25.7	0.02	334
Ce	0.34	63.2	0.04	537
Nd	0.6	36.7	0.09	244
Sm	0.9	6.84	0.14	41.1
Eu	0.9	1.90	0.16	9.50
Tb	1.0	0.62	0.19	3.26
Dy	1.1	3.51	0.20	19.30
Yb	1.0	1.22	0.20	6.10
Lu	1.0	0.12	0.19	0.61
(Ce/Yb) _{CN}		13.5		23

Concentrations in possible parent liquids are calculated from the composition of the pyroxene separate listed in Appendix 3, page 401.

The origin of these ultramafic rocks is not clearly defined. Martineau (1970) interpreted them as products of fractional crystallisation of an olivine magnetite pyroxenite melt, that is on the basis that the present WR compositions closely resemble that of the original melt. Martineau compared relationships between the three main phases of these rocks (their modal abundances) with data for the experimental systems $\text{CaO-MgO-FeO-Fe}_2\text{O}_3\text{-SiO}_2$ and $\text{MgO-FeO-Fe}_2\text{O}_3\text{-SiO}_2$ (diopside-forsterite-iron oxide) (Presnall, 1966). He found good agreement between relationships predicted by experimental data and those observed in the Big Spruce Lake pyroxenites (Figure 36). Field, petrographic and experimental evidence indicated that the pyroxenites could have formed by forceful intrusion of partly-crystalline olivine magnetite pyroxenite magma followed by in situ fractional crystallisation of olivine, magnetite and pyroxene. This model requires that an ultramafic melt of composition similar to the present WR pyroxenite compositions be in close spatial and temporal association with multiple pulses of the alkali basalt melt that formed the remainder of Centres 1 and 2. Not only is such an association of dissimilar magmas unlikely, evidence has been presented above indicating that the parent magma of the pyroxenites was not of an olivine-magnetite pyroxenite composition.

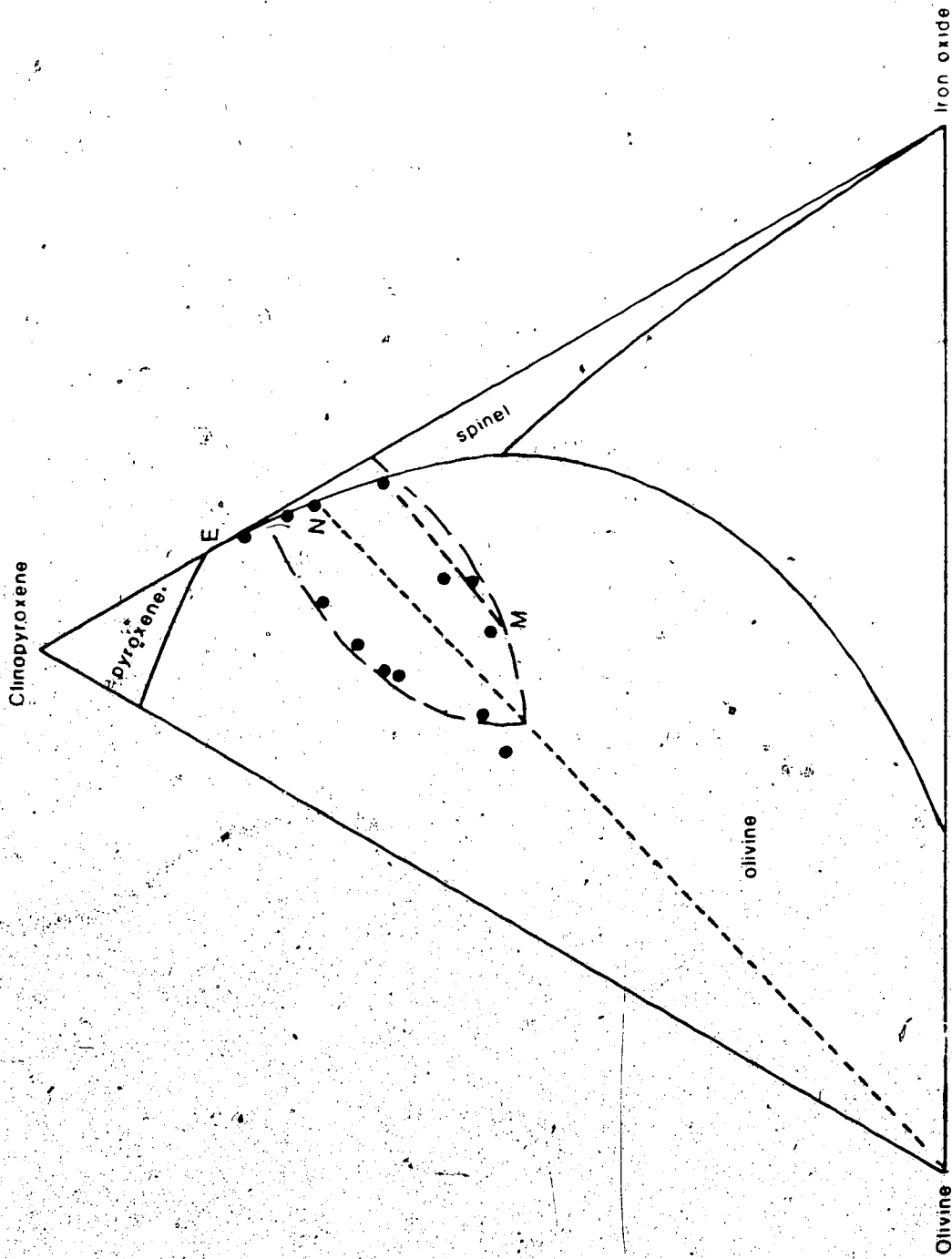


Figure 36. Martineau's (1970) comparison of the modal compositions of Big Spruce Lake magnetite pyroxenites with results from the experimental system diopside-forsterite-iron oxide of Presnall, 1966. M is the inferred melt composition. E is the low-temperature piercing point.

An origin for these rocks incorporating the absence of LREE and incompatible elements could be proposed by postulating the existence of an iron oxide liquid during emplacement. Pyroxene and olivine could have crystallised either in place (i.e., at the present level) or at depth from iron-rich basaltic liquid but outside the plagioclase field. If an immiscible iron oxide liquid then separated from the melt it could displace the remaining silicate liquid which would carry the LREE and incompatible elements to upper levels to be lost through erosion. The oxide melt would then crystallise to form a matrix for olivine and pyroxene phenocrysts. Weidner (1982) recently demonstrated experimentally that iron oxide liquids can exist at reasonable magmatic temperatures ($\sim 950^{\circ}\text{C}$) and over a range of pressures and oxygen fugacities. He also reviewed the literature and pointed out that the mechanism of formation of these unusual melts is still very controversial. Iron ore deposits postulated to have formed from an oxide magma (e.g., Kiruna, Sweden) commonly are associated with abundant apatite, a mineral largely absent from the Big Spruce Lake pyroxenites. A model involving an iron oxide liquid is highly speculative and is not the preferred interpretation of the Big Spruce Lake pyroxenites.

The preferred model for origin of these rocks, integrating data from Martineau (1970) with that of the present study, postulates that pyroxenites were produced by early fractional crystallisation of a basaltic melt similar to that which produced the gabbro-syenite series. The relationships deduced by Martineau for crystallisation of an ultramafic melt to produce olivine, magnetite and pyroxene can also be applied to the early stages of crystallisation of a basaltic melt. Presnall (1966) stated that experimental data for the join forsterite-diopside-iron oxide do not refute the possibility that such ultramafic rocks are part of a larger differentiated gabbroic intrusion and that the early stages of crystallisation of a basaltic melt could be very similar to the crystallisation path of an ultramafic mixture. The crystallisation path of the Big Spruce Lake pyroxenites in the ternary system olivine-spinel-clinopyroxene (Martineau, 1970) shown in Figure 36 cannot be that of a liquid composition lying within the plane, i.e., an olivine magnetite clinopyroxene melt. Trace element data indicate that another component, inferred to be the liquid which was present during crystallisation of pyroxene (and olivine and spinel), is not represented by present WR compositions. The crystallisation path of Figure 36 is thus projected onto

the ternary plane from a more complex (basaltic) system. Evidence has already been presented that multiple magma chambers, with similar batches of alkali basalt magma differentiating at varying depths, are required to explain the sequence of exposed gabbroic-syenitic rocks. The magnetite pyroxenites can be explained, most simply, as early differentiates of the alkali basalt sequence. If the magnetite pyroxenites represent only a small (e.g., 5%) accumulate portion of a basaltic melt then the LREE enrichment of residual liquid created by formation of pyroxene and magnetite would not be detectable in the overall incompatible element enrichment of later gabbros and syenites. Such a model does not require that an unusual parent melt for these rocks be contemporary with and use the same conduit as multiple pulses of alkali basalt melt. The presently exposed pyroxenites are thus interpreted as forming by early olivine, oxide and pyroxene crystallisation and accumulation at the bottom of an upper (above the present erosion surface) magma chamber. This magma was differentiating during a period of fault movement which offset the earlier, already solid and brittle units of diorite and layered gabbro now visible. Minor movement of magma during formation of the cumulates and due to fault movement could produce intrusive features of the pyroxenites such as

hybridisation at contacts and cross-cutting relationships of pyroxenite dykes through earlier layering.

Hybridisation at contacts would be enhanced if the earlier diorites and gabbros were still warm, as would be expected by intrusion of multiple pulses within the same volume.

From the foregoing it is inferred that the magnetite pyroxenites of Centre 1 are very early representatives of differentiation of an alkali basalt melt, multiple pulses of which are responsible for all of Centres 1 and 2. Further evidence of the "primitive" character of these particular rocks has three separate facets.

- (1) The absence of Eu anomalies indicates that plagioclase was probably not a significant phase during partial melting to form the parent basaltic melt, or during crystallisation of the pyroxenite. The original melt probably formed below the plagioclase stability field (~20 km; Green and Ringwood, 1967) in the spinel lherzolite or garnet peridotite field. Crystallisation occurred outside the plagioclase field in terms of temperature, pressure and/or composition of the melt. If crystallisation occurred in a chamber above the present erosion surface, as proposed, then pressure was not a determining factor in non-crystallisation of plagioclase with pyroxene, and either the

temperature was too high or the melt composition had not yet reached the plagioclase field. The small positive anomaly in one sample is best explained by assimilation of host diorite during formation of the isolated, small body.

- (2) The pyroxenite cannot be later in a differentiation series than the gabbro because pyroxene in the gabbro is richer in iron and has higher Fe/Fe+Mg and Mn/Mg ratios than does pyroxene from pyroxenite (Martineau, 1970):
- (3) Nd and Sr isotopic compositions of the main pyroxenite body (see Chapter 4) are apparently least contaminated by either host gneisses or earlier intrusive units. The pyroxenite WR sample which contains 0.14% P₂O₅ and has a small positive Eu anomaly, best explained by contamination during emplacement, also has a lower Sm/Nd ratio than do samples of the main pyroxenite body and a lower ϵ_{Nd} , both consistent with assimilation of acidic, older crustal material.

7. Parent Magma

Relative element abundances which have not been altered by significant crystallisation or by contamination can be used to partially define a parent liquid

composition. Plots of Zr, Hf, Nb, Ta, Rb, Y and REE abundances in samples from gabbros to mafic syenites (omitting the ring syenite) can reasonably be extrapolated to estimate relative abundances of these elements in the parent liquid. Only the early trend can be used for extrapolation because of a sharp discontinuity in trace element behaviour of the quartz syenites which crystallise significant zircon. There is insufficient data for Cs to be of value because Cs contents of the early members is below the INAA detection limit. The effects of fractional crystallisation on Sr, P, Ba and K have been described.

Zr has been selected as the reference element and the abundances of the other elements have been plotted against Zr in Figures 37 and 38. The plots have been extrapolated to a common value of 11 ppm Zr, which is the reference value used earlier for mantle-normalisation. The abundance of Zr in any liquid derived by partial melting of "primordial mantle" containing 11 ppm Zr would be much greater than this value but because the degree of partial melting is not known 11 ppm is used as the reference value for relative abundances of the other LIL elements.

Fractionation during partial melting should be indicated by abundances relative to Zr varying systematically with the bulk distribution coefficient in basaltic liquids, i.e., the order of the elements on the mantle-normalised (Tarney et al, 1980) plots.

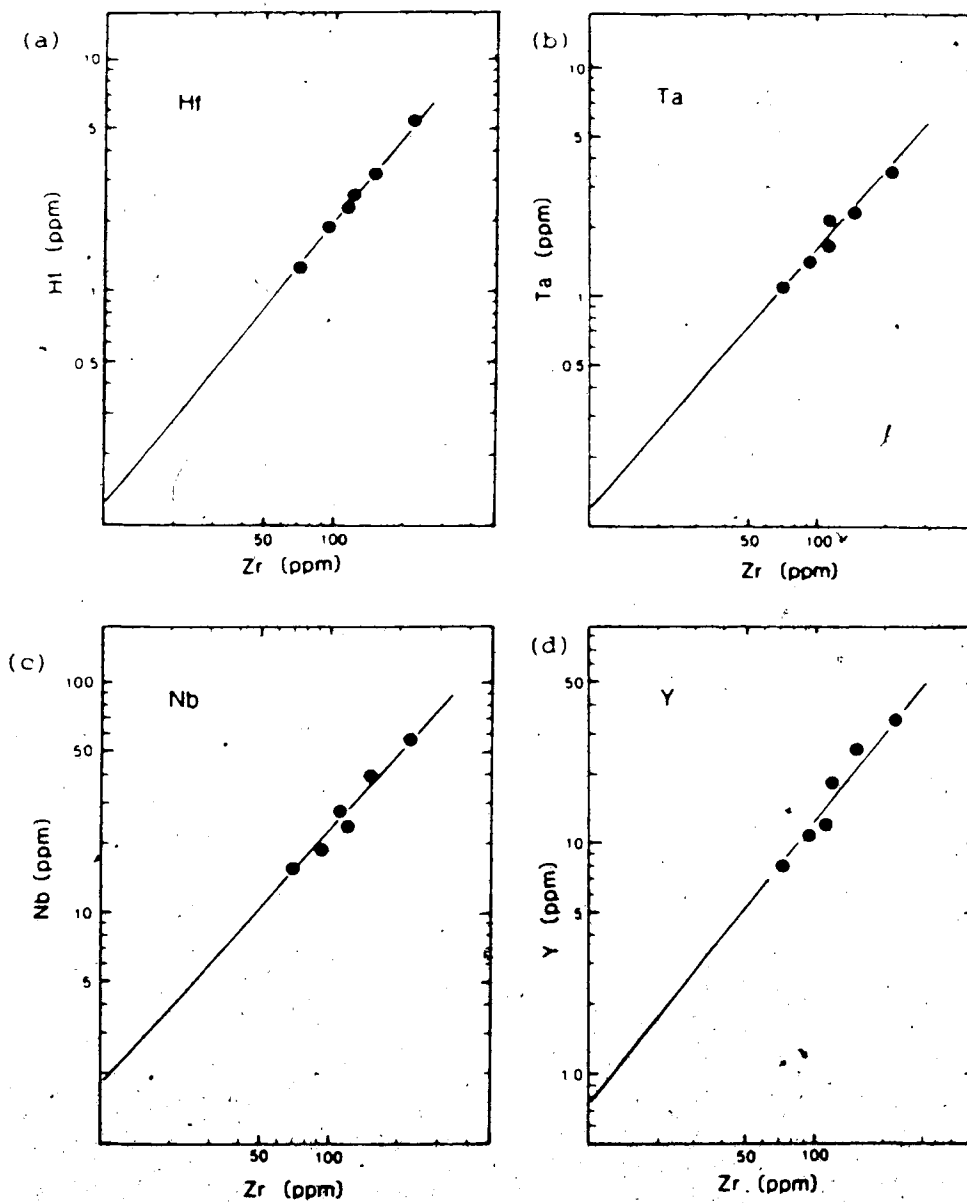


Figure 37. Plots of Zr vs (a) Hf, (b) Ta, (c) Nb and (d) Y for the early gabbro-mafic syenite differentiation trend. At Zr = 11 ppm, Hf is 0.14 ppm, Ta is 0.14 ppm, Nb is 1.95 ppm and Y is 0.83 ppm.

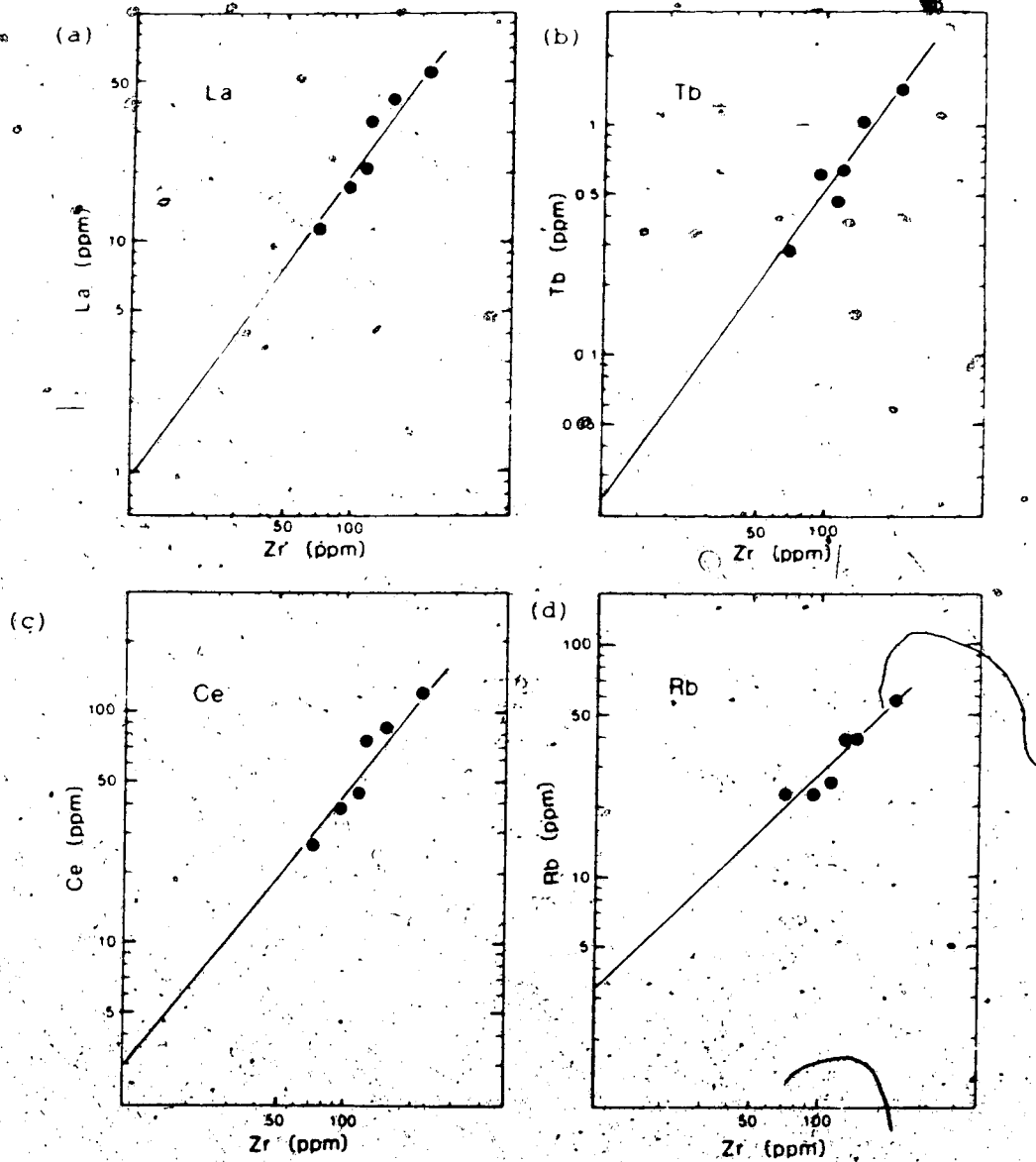


Figure 38. Plots of Zr vs (a) La, (b) Tb, (c) Ce and (d) Rb for the early gabbro-mafic syenite differentiation trend. At $Zr = 11$ ppm, La is 1.1 ppm, Tb is 0.026 ppm, Ce is 3.2 ppm and Rb is 3.7 ppm.

The Hf, Ta, Nb and Y plots are well constrained and extrapolation produces reasonable estimates of relative element abundances. The Rb, Ce, Tb, La plots are somewhat scattered but can be extrapolated to approximate relative abundances. Uranium and Th data are erratic and have not been included. Table 6 shows the abundances of eight elements relative to Zr = 11 ppm, along with the "primordial mantle values" of Tarney et al (1980) discussed earlier.

Considering the approximations involved in the extrapolations to derive the relative abundances, the ratios of melt (relative) abundances to primordial mantle show excellent internal consistency. Incompatible elements in the parent liquid from which the series was derived were strongly fractionated. Rubidium, Nb, Ta and Zr show fractionation similar to the LREE enrichment indicated by the La and Tb values. The Hf relative abundance is anomalously low. The correlation of Hf and Zr is excellent and extrapolation should yield a reasonable value, but it is obviously low relative to the mantle values of Tarney et al. A systematic error in INAA analysis can be ruled out as the cause since the same analytical procedure yields accepted values (Gladney et al, 1983) for USGS rock standards. Because the Hf analytical values are considered to be accurate the

Table 6. Relative abundances (at Zr = 11 ppm) of incompatible elements in a possible parent melt for Centres 1 and 2.

Element	Abundance in Melt at Zr=11 ppm	Primordial Mantle Abundance ¹ ppm	Melt Abundance/ Primordial Mantle ppm
Rb	3.7	0.86	4.3
Ta	0.14	0.043	3.26
Nb	1.95	0.62	3.15
La	1.1	0.71	1.55
Ce	3.2	1.90	1.68
Hf	0.14	0.36	0.4
Zr	11	11	1.0
Tb	0.026	0.099	0.26
Y	0.83	4.87	0.17

¹From Tarney et al (1980).

apparently anomalous behaviour of Hf must arise from a fractionation of Hf and Zr or from an error in the primordial mantle value for Hf. The latter explanation is preferred. Mantle-normalised LILE distribution plots for basalts reported by Tarney et al (1980) commonly show anomalously low Hf.

Because only relative abundances can be derived in the above manner, the degree of incompatible element fractionation (but not that of enrichment) can be estimated. From the REE abundances derived here for the parent melt the mantle-normalised La/Tb is 5.90. If the La and Tb abundances of Table 6 are normalised to chondritic abundances (Nakamura, 1974) then La/Tb is 6.51, the difference being a direct reflection of the LREE enrichment of the "primordial mantle" composition over that of the chondrite composition (Nakamura, 1974). Assuming a linear REE distribution on the common semi-log plot for the parent melt, then a La/Tb ratio of 6.5 is equivalent to a Ce/Yb ratio (the more commonly reported parameter) of about 16. This agrees closely with the range of 13 to 18 found for the gabbro-syenite series.

The calculated REE compositions of the melt from which cumulate pyroxene of the magnetite pyroxenites crystallised have $(\text{Ce/Yb})_{\text{CN}}$ ranging from 13 (using high D values) to 22 (using low D values). The lower ratio is in

agreement with those obtained for the remainder of the series. The pyroxenite is inferred to be an early cumulate from a now eroded gabbro-syenite sequence similar to the rocks analysed. The early crystallisation of olivine and clinopyroxene would increase the $(\text{Ce}/\text{Yb})_{\text{CN}}$ of residual liquids slightly so that the melt from which the clinopyroxene separate crystallised would have had the minimum Ce/Yb of melts which were emplaced in the crust. A value of 13 for $(\text{Ce}/\text{Yb})_{\text{CN}}$ is thus a reasonable estimate of the degree of fractionation of REE elements which occurred in the parent melt prior to intrusion. The parent melt had a slightly more fractionated incompatible element composition than an average alkali basalt, which has $(\text{Ce}/\text{Yb})_{\text{CN}} \sim 8$ to 10 (Sun and Hanson, 1975b; Frey et al, 1978). The total abundances appear to be slightly lower than average. Zr/Nb derived for the melt (Table 6) is 5.6, close to the 6.6 suggested by Hanson (1977) for alkali basalts. The slightly lower value for this ratio in the Big Spruce Lake series is again in agreement with an increase in the Nb abundance relative to Zr, or slightly greater fractionation of the more incompatible elements compared to that of typical alkali basalts.

Absolute abundances in the parent melt are less readily estimated. The total REE content of the leucocratic laminated gabbro (PC-81-275) is low relative

to that of an average undifferentiated alkali basalt (Sun and Hanson, 1975b, Frey et al, 1978) probably due to high modal plagioclase. However, the total REE content of gabbro (PC-81-235) and diorite (PC-82-173) (inferred from field evidence to be crystallised against chamber walls and hence close to chilled margin compositions) are 99 and 108 ppm, near the range of alkali basalt. Similarly the composition of melt calculated from that of the pyroxene separate using high D values ($D = 1$ for heavy REE) falls in the same range. Only still higher D values would produce a significantly lower total REE content in the melt. Most experimentally determined D values for clinopyroxene (Henderson, 1982; Möller and Muecke, 1984) are actually <1 which would make the melt composition even higher in REE. Thus a value of Σ REE about 100 ppm (75 to 150 ppm) is a reasonable estimate of the Big Spruce Lake alkali basalt melt composition.

8. Summary and Discussion

The gabbros, diorites, syenites and pyroxenites of Centres 1 and 2 form a single differentiation series. An alkali basalt parent which had a significant H_2O content and was both LILE-enriched and LILE-fractionated underwent open-system crystallisation within the crust to produce the observed series. Crystallisation of olivine,

pyroxene, plagioclase and amphibole was followed by that of alkali feldspar, biotite, quartz and zircon. Small differences in relative abundances of LILE between petrographically distinct units can be attributed to crystallisation (under variable conditions of heat flow, pressure and volatile content) of several batches of similar alkali basalt magma contaminated during ascent and crystallisation by small amounts of host granodiorite. Post-intrusive disturbance was localised and has not overridden original petrologic control of whole rock compositions. Only one unit, the quartz-free ring syenite (S2), shows discernible gneissic contamination of element compositions.

The magnetite pyroxenites are inferred to be early cumulates of the alkali basalt series formed in a late, now eroded, chamber which was only one of a number using the same conduit system over a period of time.

Only the composition of the alkali basalt melt which actually reached the upper crust can be derived directly from the whole rock data obtained from the presently exposed units. Extrapolation of the early differentiation trend is, of necessity, linear and takes no account of discontinuities in crystallisation that may have occurred prior to formation of the earliest observable units (gabbros). For example, eclogite fractionation at depth,

cannot be discerned from the present data. Similarly, information about melt composition derived from the magnetite pyroxenite composition reflects the sum of all processes which produced or altered the melt prior to pyroxenite crystallisation. A common problem in dealing with plutonic sequences is that even the earliest rocks obtainable may have been subjected to considerable fractionation, making it difficult to determine the original melt composition. Two factors suggest that the enriched and fractionated LILE compositions derived here for the Big Spruce Lake alkali gabbro series approach that of the primary magma:

- (1) The incompatible element composition derived for the Big Spruce Lake parent melt by extrapolation of the early differentiation trend is close to that for typical undifferentiated alkali basalts which have been reported (Sun and Hanson, 1975; Frey *et al.*, 1978). The primitive nature of those basalts was determined by presence of included mantle xenoliths, high Ni contents (300-400 ppm) and high Mg/Mg + Fe²⁺ ratios (0.68 to 0.72).
- (2) The pyroxenite parent liquid is inferred to be very early in the crystallisation sequence from its lack of Eu anomaly and the necessary early coexistence of olivine, clinopyroxene and spinel as crystallising

phases in basaltic melt (Presnall, 1966). Depleted mantle Sr and Nd isotopic signatures for this unit indicate little crustal interaction during emplacement within the crust. Relative REE compositions inferred for this unit are thus close to those of the mantle-derived melt.

Schwarzer and Rogers (1974) showed from a study of major element compositions that alkali basalts in oceanic islands, in back of island arcs, in continental provinces and in rift zones are a primary magma type with similar petrogenetic history regardless of the tectonic setting in which they occur. The trace element similarity of mantle source regions for alkali basalts from the various tectonic settings has also been noted (Frey et al, 1978). The parent melt composition inferred in this study for the intrusive, highly differentiated series of the Big Spruce Lake intrusion is similar to that of undifferentiated alkali basalts which represent unmodified (undifferentiated) partial melts of mantle material (Sun and Hanson, 1975a; Frey et al, 1978), hence generalised results or conclusions from the studies of other workers (e.g., Gast, 1968; Green and Ringwood, 1967; Kay and Gast, 1973; Sun and Hanson, 1975a; Frey et al, 1978) are applicable to the present study. Zone refining, in which a partial mantle melt equilibrates with upper mantle

during ascent, increases trace element abundances but does not produce the observed fractionation (Hanson, 1977).

Fractional crystallisation models do not satisfy the enrichment and fractionation patterns observed (Gast, 1968; Kay and Gast, 1973; Sun and Hanson, 1975a; Frey et al, 1978) so emphasis has been placed on partial melting models. There is general agreement on several aspects of alkali basalt genesis by this process.

The behaviour of REE during mantle partial melting was modelled for direct comparison with the composition derived here for the Big Spruce Lake alkali basalt parent melt. D values were taken from Cullers et al (1982), chondritic abundances of REE were taken from Nakamura (1974) and varying degrees of equilibrium melting and varying mantle compositions (modal as well as REE abundances) were used. The calculations yielded results in agreement with the following summary which generalises the results of the reports mentioned above.

Partial melting produces both enrichment and fractionation of incompatible elements in the resulting melt and the concentrations of incompatible elements in the melt are dependent upon the degree of melting which occurs, the modal composition of the residue and the original (chemical and modal) composition of the source. As the degree of melting increases the abundances of

incompatible elements in the liquid decrease as does the ratio of LREE/HREE or more incompatible/less incompatible. Even very small degrees of partial melting ($\ll 1\%$) of spinel lherzolite with near chondritic REE abundances cannot produce the highly fractionated relative REE abundances of the alkali basalt magma. In order to produce the necessary REE fractionation by a reasonable degree of melting a phase with a high D value for HREE, such as garnet, must be present in the residue and garnet peridotite is thus a more probable mantle source for alkali basalt generation than is spinel lherzolite. While the relative REE abundances of alkali basalts can be generated by direct partial melting of garnet peridotite, the absolute abundances cannot be so generated if the source has near chondritic abundances. The source must be enriched in REE and other incompatible elements at the time of magma formation in order to produce the alkali basalt LILE abundances by direct partial melting. A 2 to 5 times enrichment of all REE over chondritic (La/Lu up to 2.5) has been suggested by Kay and Gast (1973) as sufficient. Sun and Hanson (1975b) proposed that alkali basalts are produced from a source in which HREE are already enriched to 3 times chondritic abundances, similar to the enrichment proposed by Kay and Gast, but Sun and Hanson proposed, in addition, that La/Lu of the source

should be about 4.5. Frey et al (1978) similarly found that partial melting of a source which had the more incompatible elements (Ba, Sr, Th, U, LREE) enriched to 6-9 times chondritic and the less incompatible (HREE, Y, etc.) to 2.5 to 3 times chondritic (La/Lu ~3.6) best satisfied constraints imposed on alkali basalt magma formation by minor and trace element data as well as by experimental results and major element compositions. If the LILE content of the mantle source is both enriched and fractionated at the time of magma formation (i.e., either prior or concurrent enrichment) then the degree of partial melting required to produce alkali basalts is 7 to 15% (Sun and Hanson, 1975b; Frey et al, 1978).

The analytical results obtained for the Big Spruce Lake gabbro-syenite suite of intrusive Centres 1 and 2 are in agreement with formation by such a model of 7 to 15% partial melting of an LILE-enriched and LILE-fractionated mantle source region.

E. Intrusive Centre 3 - Silica-Undersaturated Suite

The second major silicate group of the main complex comprises the foyaite-ijolite suite, the third centre of intrusive activity, whose compositions form a scattered field rather than a cohesive trend of silica vs total alkali or vs peralkaline index (Figures 5 and 6).

Representative samples of the wide range of compositions presently exposed in Centre 3 were selected for detailed element analysis. Analytical results are presented in Appendix 3, pages 402 and 403.

1. Major and Minor Element Results

The analysed samples display wide variations in major element abundances. Silica varies from 41 to 53%, and Al_2O_3 from 6.6 to 23.5%. Total iron as Fe_2O_3 ranges from a low of 2% in the most leucocratic foyaite sample to over 22% in melteigite. Aegirine-augite is the major iron-bearing mineral; oxides are not abundant. Throughout the suite MgO is low, ranging from almost zero in leucocratic members to about 2.5% in mesocratic ones. There are no Mg minerals such as olivine, and Mg crystallises largely in aegirine-augite and minor biotite. The abundance of CaO varies from less than 1% in leucocratic members to over 10% in the melanocratic ones. The abundance of CaO is generally less than that of Na_2O , but in the melteigites CaO becomes greater than Na_2O . Apatite, sphene and aegirine-augite are the principal Ca minerals found in these rocks. In this suite MnO is somewhat enriched ranging from 0.1 to 0.7%. There is no systematic increase or decrease of TiO_2 from leucocratic to melanocratic members. It ranges from 0.2 to 2.5% (<0.3% in most

samples). Spinel is the major host for Ti. The dominant alkali is Na in this suite with $\text{Na}_2\text{O}/\text{K}_2\text{O}$ ranging from 1 to 30. No consistent trend is shown by Na_2O , its value remaining almost constant in a broad range from 5-14%. The abundance of K_2O varies from about 7% in leucocratic rocks to less than 1% in darker ones.

CIPW normative compositions are presented in Table 7. Normative compositions were calculated following the method of Iddings (1909). Total iron was reported as Fe_2O_3 (XRF analysis) in the present study. Martineau (1970) reported $\text{Fe}_2\text{O}_3/\text{FeO} + \text{Fe}_2\text{O}_3$ ratios of 0.52 to 0.74 for 7 samples from Centre 3, clustering around 0.65 to 0.74. Normative compositions were calculated using values of 0.6 and 0.75 for this ratio but little significant difference was noted and those at the higher ratio are reported in Table 7. Normative leucite was recalculated to Or + Ks (to be combined with Ab and Ne, respectively, for plotting) and reported as such. All of these rocks contain a relatively large volatile component; loss on ignition ranges 2-6% (Appendix 3, pages 402 and 403). Because of its low molecular weight a small amount of CO_2 can have a significant effect on normative compositions by uniting with Ca which would otherwise be free to form normative diopside in samples with abundant Fe^{2+} and Mg. The proportion of CO_2 present in the volatiles reported as

Table 7. CIPW normative compositions of foyaites, ijolites and melteigites analysed in this study.

	PC-81-462	PC-82-039	PC-81-165	PC-81-194	PC-81-287	PC-82-525	PC-82-526	PC-81-168	PC-82-041
O									
Or	39.1	44.5	2.3	12.0	7.5	2.2	6.2	10.1	14.0
Ab	13.4	15.8		15.7	0.7			16.1	22.4
An		0.2							
Lc ¹									
Ne	38.2	25.4	31.6	49.4	28.5	39.8	41.2	4.7	2.1
Ks			0.9	3.0			1.2		
Ac	4.7		30.4	18.7	15.0	27.9	23.2	24.0	15.5
Wo		0.2	9.0	1.5	7.7	9.6	8.9	10.4	3.4
Di		0.1	3.8	0.5	4.8	4.0	3.9	7.2	2.9
Fs			5.3	1.0	2.5	5.7	5.0	2.3	
En									
Hy									
Fs									
Fo		0.3				0.3			
Fa	0.5		1.3	2.4		0.5			
Mt		0.6			7.2		1.5	11.4	9.1
He		5.3							1.8
Il	0.5	4.2	0.4	0.3	0.6	0.4	0.4	2.8	4.8
Ap	0.1	0	0.5	0.2	0.2	0.2	0.2	0.1	0.2
Cc	2.3	2.3	9.3	6.1	5.0	5.7	5.2	2.5	0.9
NMet ²	0.1		0.4	0.8		0.2			
Wo					2.9			6.9	22.1

¹Lc recalculated as Or + Ks.

²NMet = Na₂O·SiO₂.

loss on ignition (LOI) was determined by vacuum fusion of selected whole rock powders at 400°C and 1100°C to determine H_2O^- , H_2O^+ and CO_2 . Fluorine and chlorine, common volatiles in apaitic rocks (e.g., Gerasimovsky et al., 1966; Piotrowski and Edgar, 1970), are not determined by this technique because of their solubility in the melt and their great reactivity. In the samples analysed the amount of F and Cl volatilized from the melt was negligible. Full details of the vacuum fusion method of determining volatiles are given in Metcalfe (in preparation). The volatiles determined are listed in Table 8. For calculation of the normative compositions.

Table 8. Weight percent volatiles determined by vacuum fusion of whole rock powders of foyaite and melteigite.

Sample	400°C		1100°C		Total Volatiles (Loss on Ignition)
	H ₂ O	CO ₂	H ₂ O	CO ₂	
PC-81-165 North foyaite	0.769	-	0.465	2.904	4.138
PC-81-287 North foyaite	0.388	-	1.317	1.967	3.672
PC-81-168 Melteigite	0.552	-	0.189	0.390	1.131

the CO₂ contribution was set at 50% of the total LOI. This approximation appears to be valid as only small amounts (0.3 to 3.5%) of potential olivine, which is not present in the mode, appear in the normative compositions, commonly when potential pyroxene is already abundant. In these cases any error in normative diopside due to a small error in the CO₂ estimate is not significant to interpretation of the results.

Normative compositions were also calculated for 13 analyses of foyaites reported by Martineau (1970). No LOI was reported for these samples so no amount of CO₂ could be estimated. The Fe₂O₃/FeO + Fe₂O₃ ratio was either that reported directly or, where only total iron as Fe₂O₃ was reported, 0.75 as described above. The normative compositions obtained are reported in Table 9.

Twelve normative compositions (Tables 7 and 9) have total salic components (Q, Or, Ab, Ne, Lc in CIPW normative compositions) comprising greater than 80% of the total composition, and these have been plotted on a Ne-Ks-Q diagram shown in Figure 39. This diagram represents Petrogeny's Residua System (referred to simply as residua system in later discussion) and phase fields at P = 1 atm, P_{H₂O} = 1 kbar and 2 kbar are shown along with the Morozewicz-Buerger normal nepheline composition and the ternary minima at P = 1 atm (a) and P_{H₂O} = 1 kbar (a').

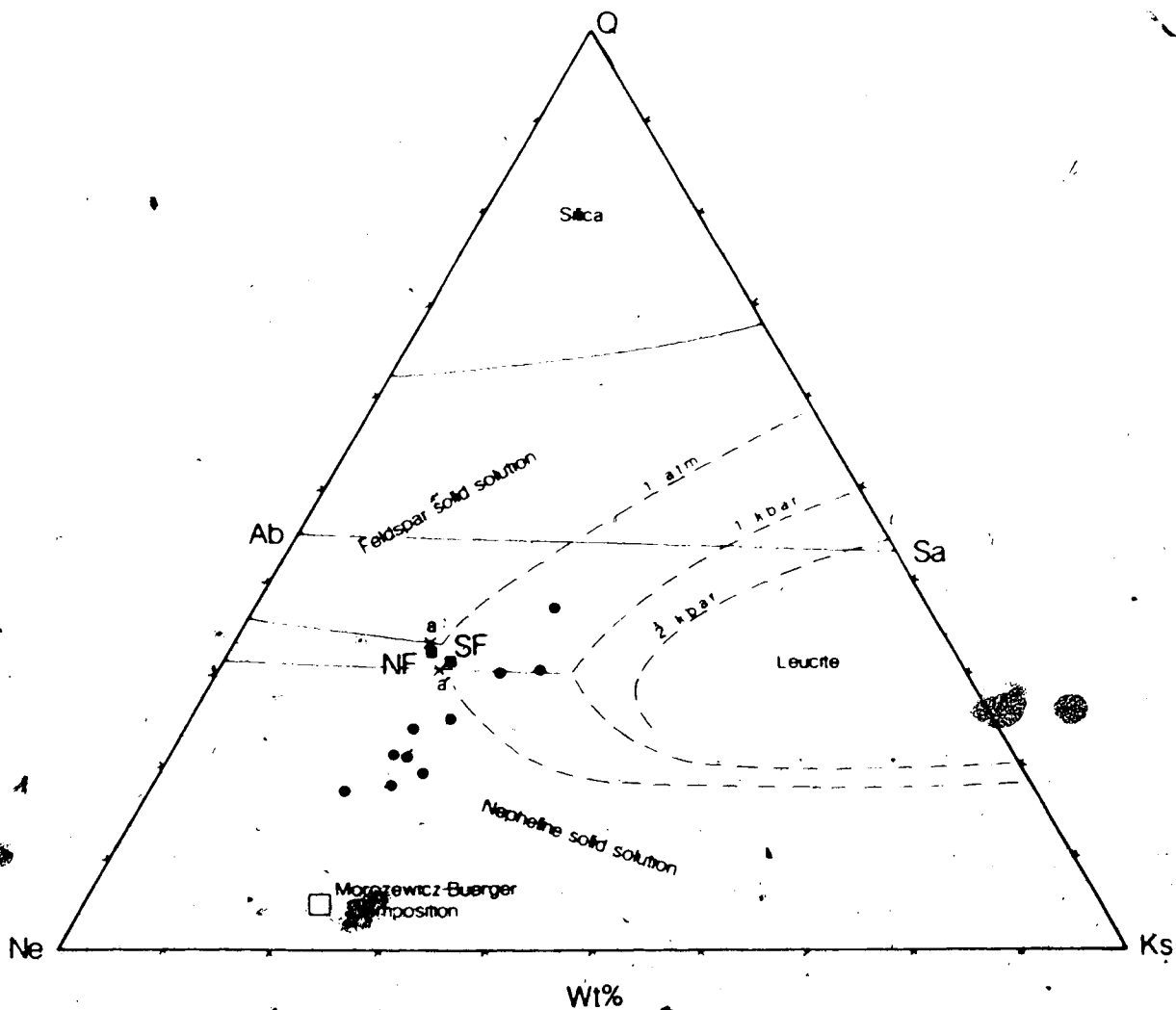


Figure 39. The compositions of analysed foyaites and ijolites in the residua system, Ne-Ks-Q. SF and NF are the compositions of chilled margin samples of southern and northern foyaite, respectively (data from Martineau, 1970). Also outlined are phase relationships in the undersaturated portion of the system at $P = 1 \text{ atm}$, $P_{\text{H}_2\text{O}} = 1 \text{ Kbar}$ and $P_{\text{H}_2\text{O}} = 2 \text{ Kbar}$. a and a' indicate the ternary minima at $P = 1 \text{ atm}$ and $P_{\text{H}_2\text{O}} = 1 \text{ kbar}$ (adapted from Gittins, 1979).

Table 9. CIPW normative compositions for samples from Martineau (1970).

	Southern Foyaites				Northern Foyaites							
	67374	2814	67003	2821	68339	67130	68091	68352	68351	68295	67116	68357
Or	33.6	40.1	39.3	37.3	27.9	34.5	29.9	27.1	30.7	31.1	24.3	31.6
Ab	30.0	20.1	28.7	1.1	5.7	14.3	34.2	5.2	7.8	9.9	1.0	11.3
An	0.1	8.0					0.1				1.6	
Lc ¹												
Ne	26.5	26.8	12.8	48.4	53.9	33.3	23.1	39.8	43.2	44.3	36.3	41.5
Ks ¹												
Ac	4.4			5.9	2.0	3.0	8.0	9.5	5.6	3.0		3.6
Wo	0.1	0.5	1.5	1.0	0.5	4.7	1.4	3.2	2.4	1.3	8.2	0.8
Di	0.1	0.4	0.4	0.3	0.3	0.4	1.2	1.6	0.8	0.4	7.1	0.7
Fs		1.1	0.7	0.1		4.6		1.5	1.7	1.0		
En												
Hy												
Fs												
En												
Fo						0.4						
Ol						1.2						
Mt	1.0	5.8	5.1	0.7	3.4	2.0	0.9	5.5	2.0	2.9	3.4	14.0
He		1.3				0.3		1.8			4.7	0.2
Il	1.0	2.7	1.3	0.7	1.1	0.8	1.1	1.0	0.7	0.1	0.7	2.2
Ap					0.3					0.1	0.2	1.3
Cc												
NMet ²												
Wo	3.4	2.1		3.8	4.5	5.1	2.4	6.6	5.5	3.7	4.3	2.7
												5.3

¹Lc recalculated as Or + Ks. ²NMet = Na₂O·SiO₂

Two points represent the compositions of chilled margins of the mafic Northern Foyaite unit (NF) and the leucocratic Southern Foyaite (SF), samples 68051 and 67374 respectively in Table 2. The chilled margin from which NF was collected is very sharp; fine-grained mafic foyaite grades to coarse quartz syenite, not significantly fenitised, over about 25 cm and the actual syenite/foyaite contact can be placed within about 3 cm at this point. The contact represented by SF at the southern boundary of Centre 3 is slightly more transitional (broader) but is not part of the wide fenite zone described earlier (Chapter 2). These samples contain total salic components (normative) of 84.5% (NF) and 90.1% (SF) and plot near the ternary minima at a and a' ($P = 1 \text{ atm}$, $P_{\text{H}_2\text{O}} = 1 \text{ kbar}$ respectively) thus, both chilled margin compositions lie within the silica-undersaturated low temperature "sink" of the residual system. The compositions of these chilled margin samples cannot be assumed to be wholly representative of initial magma(s) (Cox et al, 1979), largely because of the high volatile content. Escape of volatiles from the quickly cooled margin itself or the passage of volatiles through the margin from the more slowly cooled interior are unknown factors. However, these two samples can be inferred to be more representative of initial or parent magma than any others

analysed. The composition of magma(s) emplaced at the level of the present erosion surface was close to that of the ternary minima of the residua system at $P_{H_2O} < 1$ kbar, suggesting that crystal-liquid equilibrium processes were involved in derivation of the melt as well as in its rapid crystallisation into the chilled margins.

The other rocks plotted in the diagram have total normative salic components ranging from 81 to 91%, and all plot away from the ternary minima. Most of the plotted compositions lie away from the initial liquid (chill) composition within the low temperature "sink" and towards that of the Morozewicz-Buerger normal nepheline. Two compositions lie on the potassic side of the cotectic and one lies in either the feldspar or leucite field depending upon P_{H_2O} . If the chill does indeed closely represent the initial liquid, then the other compositions plotted cannot be late derivatives of fractional crystallisation and thus representative of successive liquid compositions. Crystallisation of such a sequence would require that successive compositions move from that of SF and NF at less than 1100°C "up-temperature" to about 1300°C. Such a fractional crystallisation temperature path is not possible. There are two explanations for the observed distribution of compositions.

- (1) The two chilled margin compositions are far removed from that of the parent magma, which must then lie well within the nepheline field near the other plotted compositions, at an unlikely liquidus temperature of about 1300°C.
- (2) The compositions lying in the nepheline field, as well as the more potassic ones lying on the cotectic or within the feldspar field, are those of cumulates rich in nepheline (and/or feldspar) but derived from liquids such as SF and NF.

The latter is the more probable explanation and is in agreement with field observations of mineral segregations and crude layering. From a study of the melting relations of agpaitic rocks Piotrowski and Edgar (1970) suggested that such rocks probably had a long liquidus-solidus interval which would facilitate or enhance cumulate formation. The results described above indicate that the high temperature compositions (nepheline-rich) obtained in this study are the result of cumulate formation and not the cause of it.

Why the majority of these rocks plot in the nepheline field is not so straightforward. If the parent melt compositions actually lay within the ternary residual system as plotted, with no feric component, to form mafic minerals, then neither feldspar nor nepheline alone could

crystallise from NF or SF in sufficient amounts to drive the remaining melt composition to the observed positions in the feldspar and nepheline fields unless the two minerals were physically separated after crystallising. Cooling of magma of composition NF or SF in the synthetic system would begin close to the nepheline-feldspar cotectic and the liquid composition would quickly move to the cotectic to crystallise both phases. The liquid would remain on the cotectic and move to the minimum as crystallisation proceeded. Differential accumulation of nepheline and feldspar during such crystallisation would form apparent whole rock compositions lying in both the nepheline and feldspar fields although such compositions would not be representative of the melt from which the cumulate minerals were derived. Cumulate compositions should lie on a line from Na-rich nepheline (normal nepheline) to K-rich feldspar reported by Gerasimovsky et al (1966) to be the major K-bearing phase in such systems. The room-temperature densities of nepheline and alkali feldspar cover almost identical ranges (Deer et al, 1966) and, assuming this relationship persists to liquidus temperatures, no large-scale differential accumulation of these phases should occur. The compositions of cumulates from SF or NF crystallising in the residua system thus should lie near the cotectic or be scattered on either

side of it. The compositions determined in this study are predominantly nepheline-rich and probably not the result of crystallisation of NF or SF in the residua system.

Although the chilled margin compositions NF and SF project onto the ternary minimum of the synthetic Ne-Ks-Q system (from a femic component of 10 to 15% in the more complex natural system), they probably lie within the nepheline field of the natural system because crystallisation apparently began there. Only prolonged crystallisation and accumulation of nepheline could produce the predominance of nepheline-rich compositions observed in this suite.

The compositions of leucocratic samples thus show cumulative characteristics and not an evolutionary sequence in the residua system, apparently because the crystallisation path is largely perpendicular to the plane of this system. It is of interest to examine the more mesocratic samples in this regard and to determine if an evolutionary trend is discernible when femic components are included. In practice there is no single ternary system with a femic component which has the usefulness and general applicability of the residua system for leucocratic systems. The synthetic ternary systems of most interest in this case are Ne-Ab-Ac and Ne-Ab-Di (nepheline-albite-acmite/diopside respectively). Bailey and Schairer (1966) examined the system $\text{Na}_2\text{O}-\text{Al}_2\text{O}_3-\text{Fe}_2\text{O}_3-$

SiO₂ and found phase relationships to be complex and dominated by the incongruent melting of acmite to hematite. In the dry system the final low temperature melt is leucocratic, containing only 10% Ac (acmite), but it also contains normative sodium disilicate. Bailey and Schairer provided a detailed schematic or flow diagram showing the univariant and invariant equilibria involved, from which crystallisation paths can be deduced, but not a simple plot on which natural compositions can be plotted and interpreted. Interpretation of the analytical results in this study is more straightforward using the diagrams prepared by Nolan (1966) who studied melt relations in the system Ab-Ne-Ac-Di-H₂O at P_{H₂O} = 1000 kg/cm². Results of his study are summarised in Figure 40. Nolan found that in the Ab-Ne-Ac join (Figure 40a), when P_{H₂O} = 1000 kg/cm² a composition of Ab₁₅Ne₃₀Ac₅₅ (point P) represents the piercing point (low temperature) at 715°C. This is a much more mafic or ijolitic composition than that found by Bailey and Schairer in the dry system. Incremental addition of diopside to the system, in closer approximation to natural systems, moved the phase boundary between plagioclase and pyroxene (Figure 40b) to successively lower pyroxene contents. If diopside is the only pyroxene (i.e., the Ab-Ne-Di plane) then a low temperature point at Ab₇₇Ne₂₉Di₁₅ and 885°C results (point

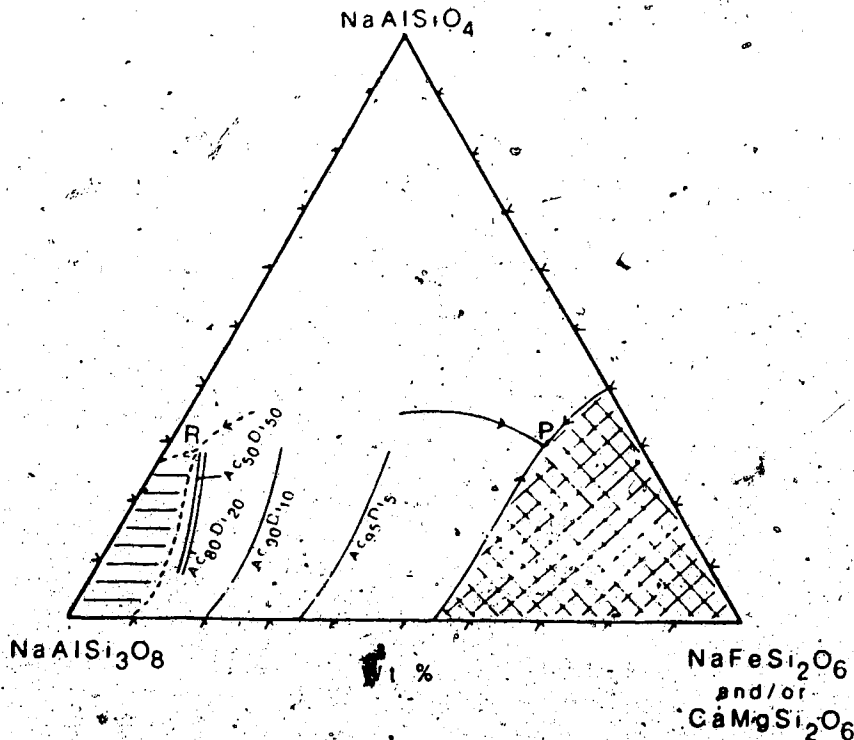
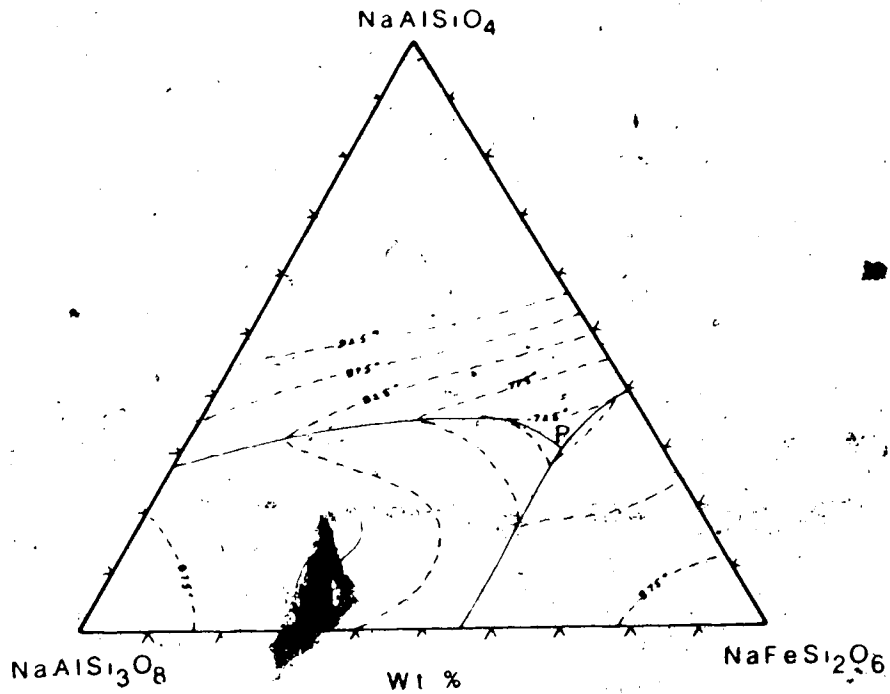


Figure 40. Phase relationships in the system $\text{Ne-Ab-(Ac}\pm\text{Di)}$ at $P_{\text{H}_2\text{O}} = 1000 \text{ kg/cm}^2$. (After Nolan, 1966.)

- a) Isotherms in the system Ne-Ab-Ac . P represents the piercing point at 715°C .
- b) Variation of clinopyroxene (crosshatched) and plagioclase (horizontal striped) fields with pyroxene composition. P is the low-temperature composition in the acmitic system, R in the diopsidic system.

P). Clearly both the presence of volatiles such as H_2O and the relative and absolute abundance of mafic components affect the crystallisation sequence of the alkaline silica-undersaturated rocks.

To compare the natural assemblages of the Big Spruce Lake suite with each other and with the synthetic systems, a triangular plot of $(Ab+Or)-(Ne+Ks)-(Ac+Di)$ has been used. This plot approximates the synthetic system $Ab-Ne-(Ac \text{ or } Di)$ (Nolan, 1966). Figure 41 shows the positions of 18 samples (Tables 7 and 9), each of which contains over 80% of these six components (normative). The positions of the Ac and Di piercing points (P and R respectively) have been added from Figure 40 for comparison. The most striking feature of this plot is that the compositions of the Big Spruce Lake suite are not associated in any single field, nor is there any trend along or near a cotectic. They are clustered near the $(Ne+Ks)-(Ab+Or)$ and $(Ab+Or)-(Ac+Di)$ joins. The two chilled margin samples, NF and SF, plot near the $(Ne+Ks)-(Ab+Or)$ join at about $(Ab+Or)_{70}(Ne+Ks)_{25}$ a point which reflects the position of the cotectic and minimum in the leucocratic residua system. These inferred parent magma compositions have about 5% $Ac+Di$ and plot very close to the piercing point for the synthetic $Ne-Ab-Di$ (diopsidic) system (R) although SF contains mainly normative Ac .

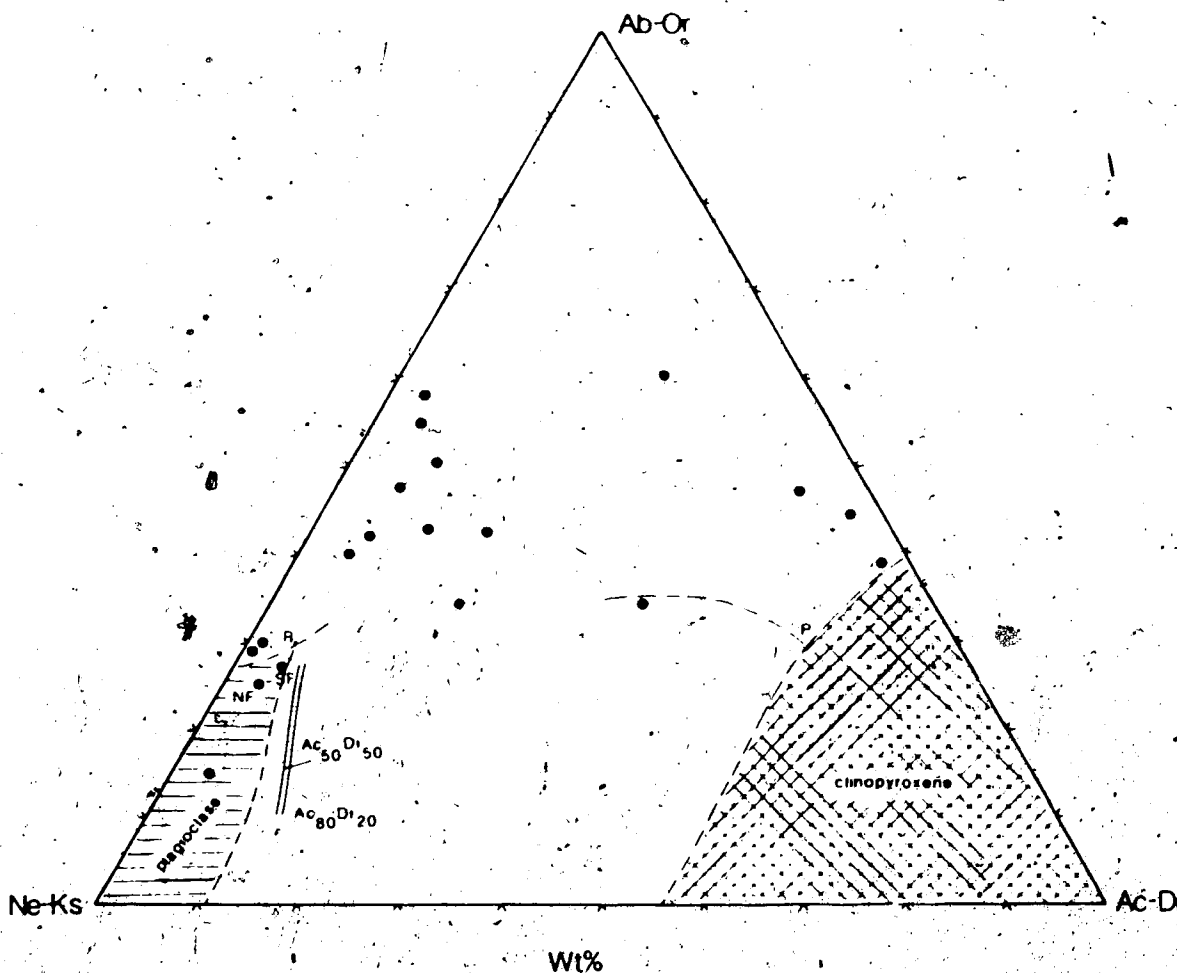


Figure 41. Compositions of analysed foyaites and ijolites in the system (Ne+Ks)-(Ab+Or)-(Ac+Di). Compositions of the chilled margins of southern foyaites (SF) and northern foyaites (NF) are also shown. Pertinent information from the diagrams of Figure 40 (after Nolan, 1966) has been included for comparison.

These two compositions also plot well within the field for 102 plutonic alkaline rocks outlined by Nolan (1966) in the (Ab+Or)-(Ne+Ks)-(Ac+Di) system and by Hamilton and Mackenzie (1965) in the residua system. The majority of the other samples (those which plot in the nepheline field of the residua system) are not only scattered towards nepheline in Figure 41, they also show a variable feldspar component and are scattered towards Ac+Di along a band with similar Ne:Fd ratios. Three normative compositions could not be plotted in either ternary diagram because they have high normative wollastonite and magnetite.

In summary, the chilled margin compositions, NF and SF, lie near the piercing and reaction point of the Ab-Ne-Di synthetic system and near the nepheline-feldspar cotectic of the Ab-Ne-Ac system. Most other samples from the Big Spruce Lake suite plot "up-temperature" in the nepheline field with variable amounts of feldspar. Accumulation of variable amounts of nepheline formed during the crystallisation of liquid(s) initially near NF or SF in the Ne field is the most probable explanation for the distribution of compositions observed on this plot. This interpretation is in agreement with that for the residua system.

The normative compositions of the two melteigite samples analysed in this study could not be plotted on

either ternary diagram because of high normative magnetite and wollastonite. One, PC-81-168, is a "reef" with indeterminate field relations within mafic foyaite. The other, PC-82-041, is a dyke 1 m in width cutting leucocratic foyaite. The major element compositions of these two are somewhat removed from those of the foyaite-ijolite suite.

2. Trace Element Results

Apart from the alkali and alkaline-earth elements, most trace element abundances increase with the mafic content ($MgO + CaO + \Sigma Fe_2O_3$) in these silica undersaturated rocks. Rubidium and Cs range from approximately 20 to 230 and 0.6 to 4.5 ppm, respectively, highest in leucocratic rocks. Barium ranges from 2450 ppm in a leucocratic sample to 340 ppm in an ijolite. Strontium ranges from 900 to 1900 ppm, independent of major element composition.

Cobalt and Sc abundances are low in all of these rocks but increase with mafic content to about 16 and 2.5 ppm respectively (Figure 42). These Co values are comparable to those reported for the ijolite series at Fen, Norway (Mitchell and Brunfelt, 1974), which ranged about 5 to 25 ppm. Scandium abundances are somewhat lower than those reported for the ijolite series from Fen,

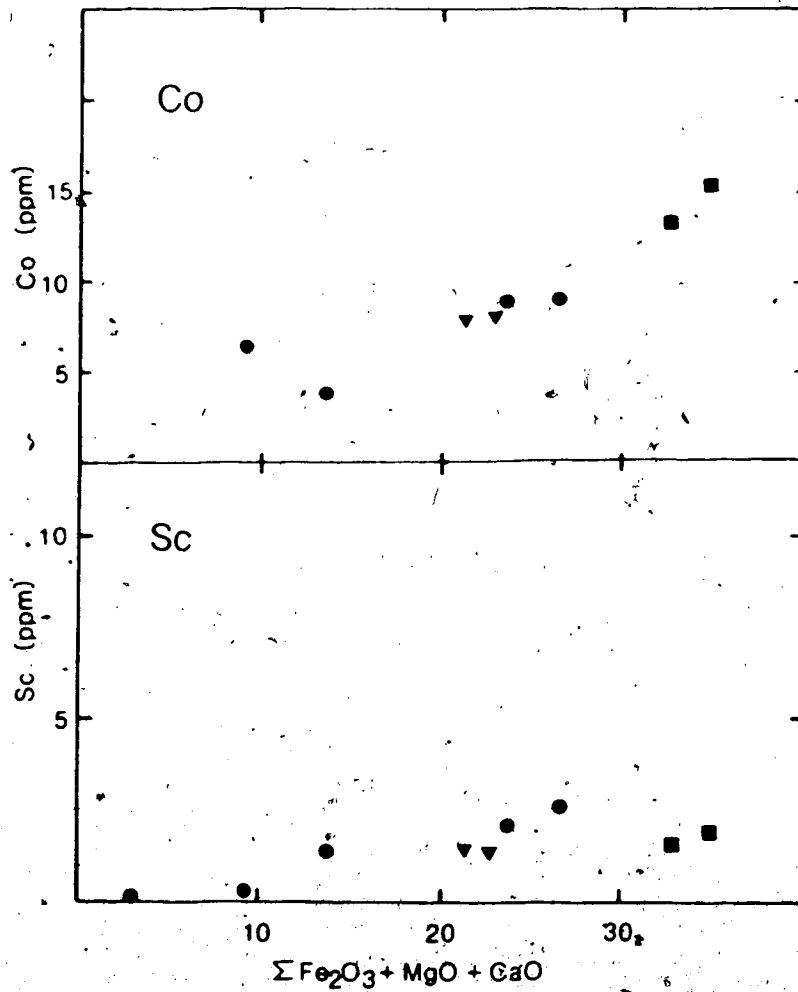


Figure 42. Variation of Co and Sc with the total mafic content ($\Sigma \text{Fe}_2\text{O}_3 + \text{MgO} + \text{CaO}$) in rocks of the foyaite-ijolite suite. Solid circles indicate foyaite, inverted triangles indicate ijolite and squares indicate meltegitte.

Norway (Mitchell and Brunfelt, 1975) and Oka, Quebec (Eby, 1975). In both of those studies Sc ranged about 5 to 7 ppm although urtites from Fen had as little as 1 ppm. Increasing Sc with mafic content (pyroxene) is in agreement with data from both Oka, Quebec and Fen, Norway. Vanadium is below the detection limit of about 20-25 ppm (dependent upon whole rock composition) in 5 of the 9 samples analysed and ranges from 22-32 in the other four, being slightly higher in mafic foyaites than in ijolites and melteigites. Chromium is very low in ijolites and melteigites, at or below the detection limits of 1-4 ppm. In the foyaites Cr increases from 2.5 to 28 ppm with increasing mafic content.

Within the foyaite-ijolite group abundances of REE, Zr, Hf, Th and Y increase consistently with mafic content (Figure 43) while those of U and Nb are erratic (Figure 44). The two melteigites are discontinuous with the trend of the foyaite-ijolite group.

Trace element profiles are presented as mantle-normalised LIL element distribution plots in Figures 45 to 48. The parameters used for normalising are those discussed earlier (Tarney et al, 1981) despite the fact that these whole rock compositions are far removed from those of "primordial mantle" or typical MOR basalts. Use of the same parameters throughout this study allows for

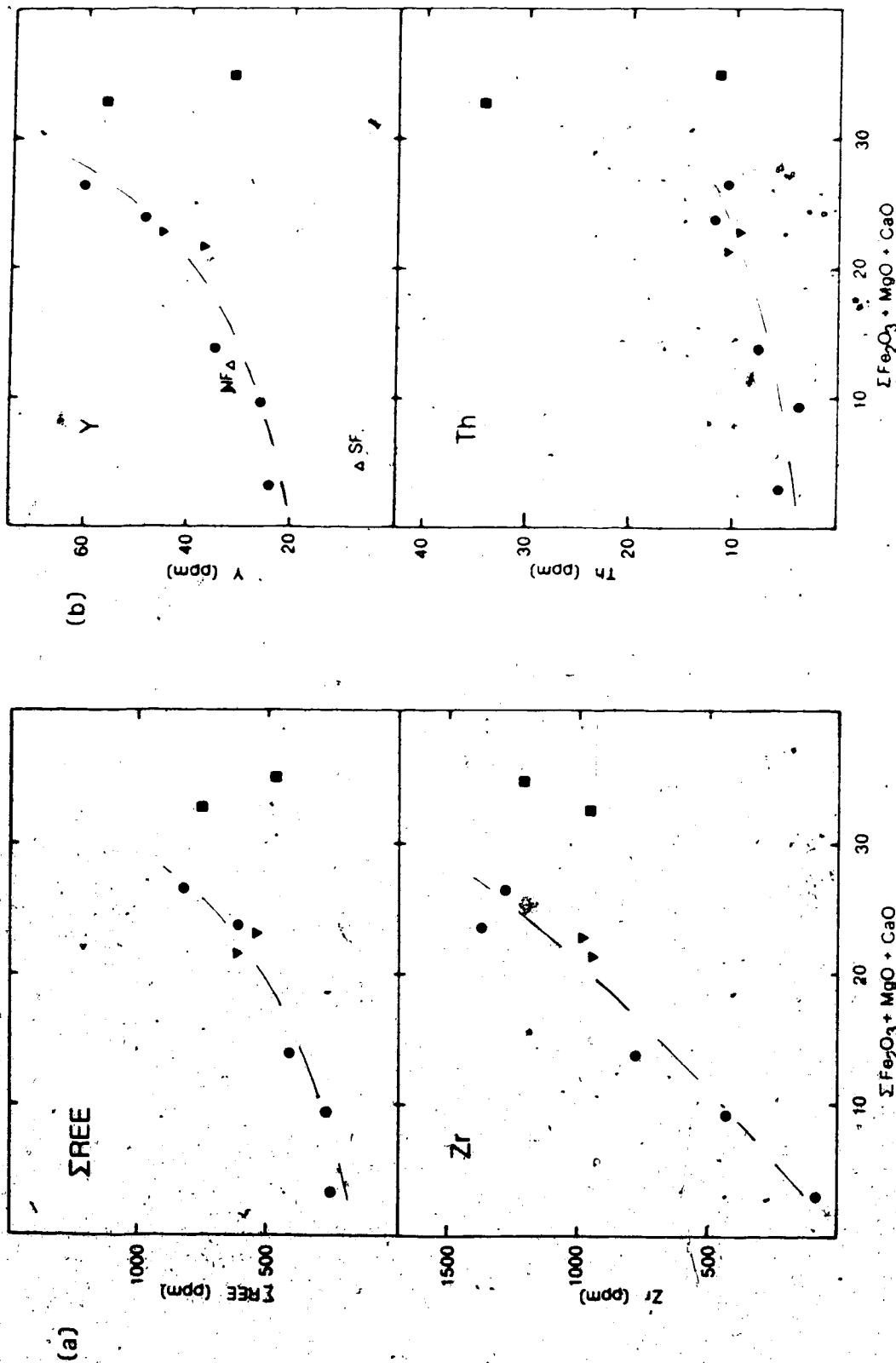


Figure 43. Variation of (a) ΣREE and Zr and (b) Y and Th with the total mafic content (ΣFe₂O₃+MgO+CaO) in rocks of the foyaitite-ijolite suite. Solid circles indicate foyaites, inverted triangles indicate ijolites and squares indicate melteigites. The compositions of foyaitite chilled margins SF and NF (from Martigneau, 1970) are included.

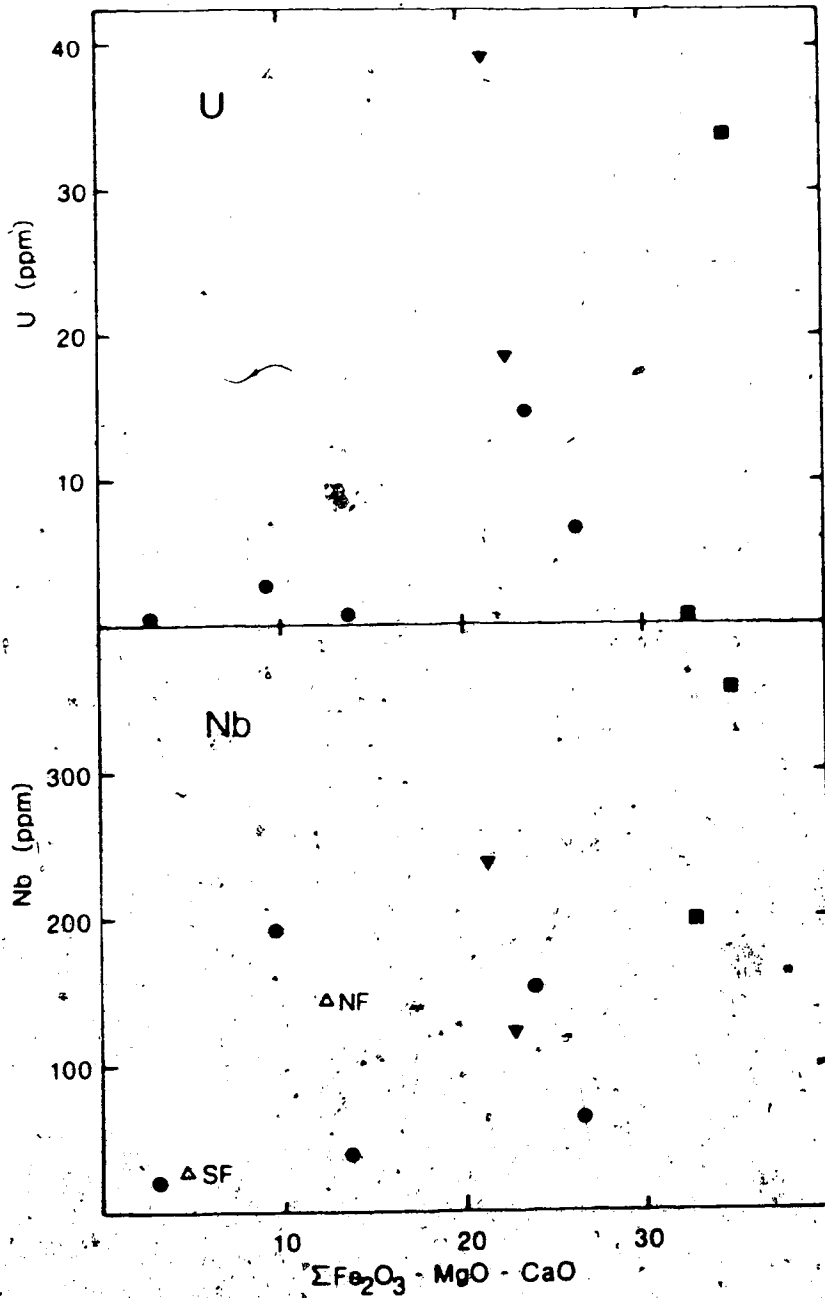


Figure 44. Variation of U and Nb with the total mafic content ($\Sigma\text{Fe}_2\text{O}_3 + \text{MgO} + \text{CaO}$) in rocks of the foyaitite-ijolite suite. Solid circles indicate foyaites, inverted triangles indicate ijolites and squares indicate melteiqites. The compositions of foyaitite chilled margin samples (SF and NF, Martineau, 1970) are included.

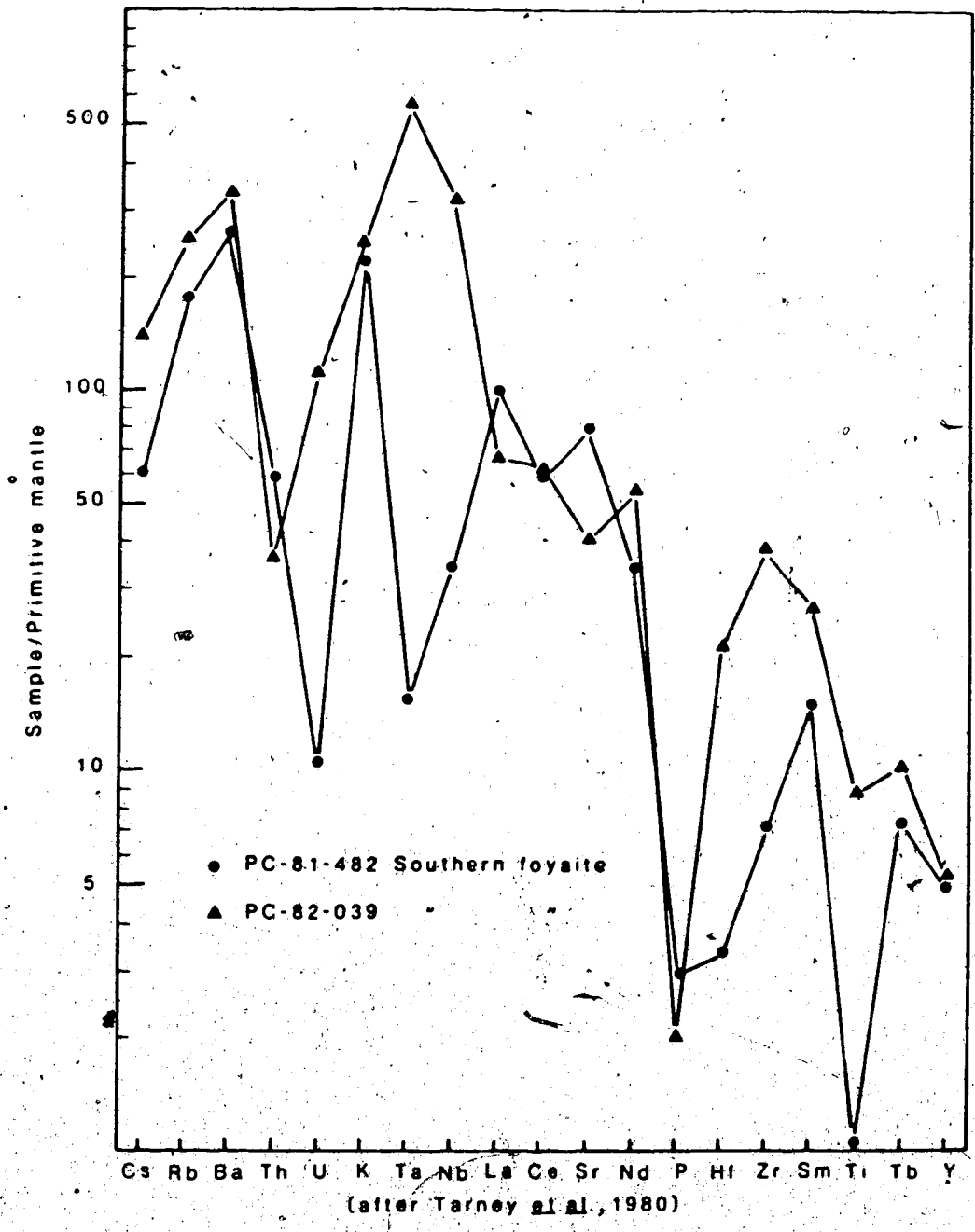


Figure 45. Mantle-normalised LILE distribution plots for southern foyaites from the Big Spruce Lake intrusion.

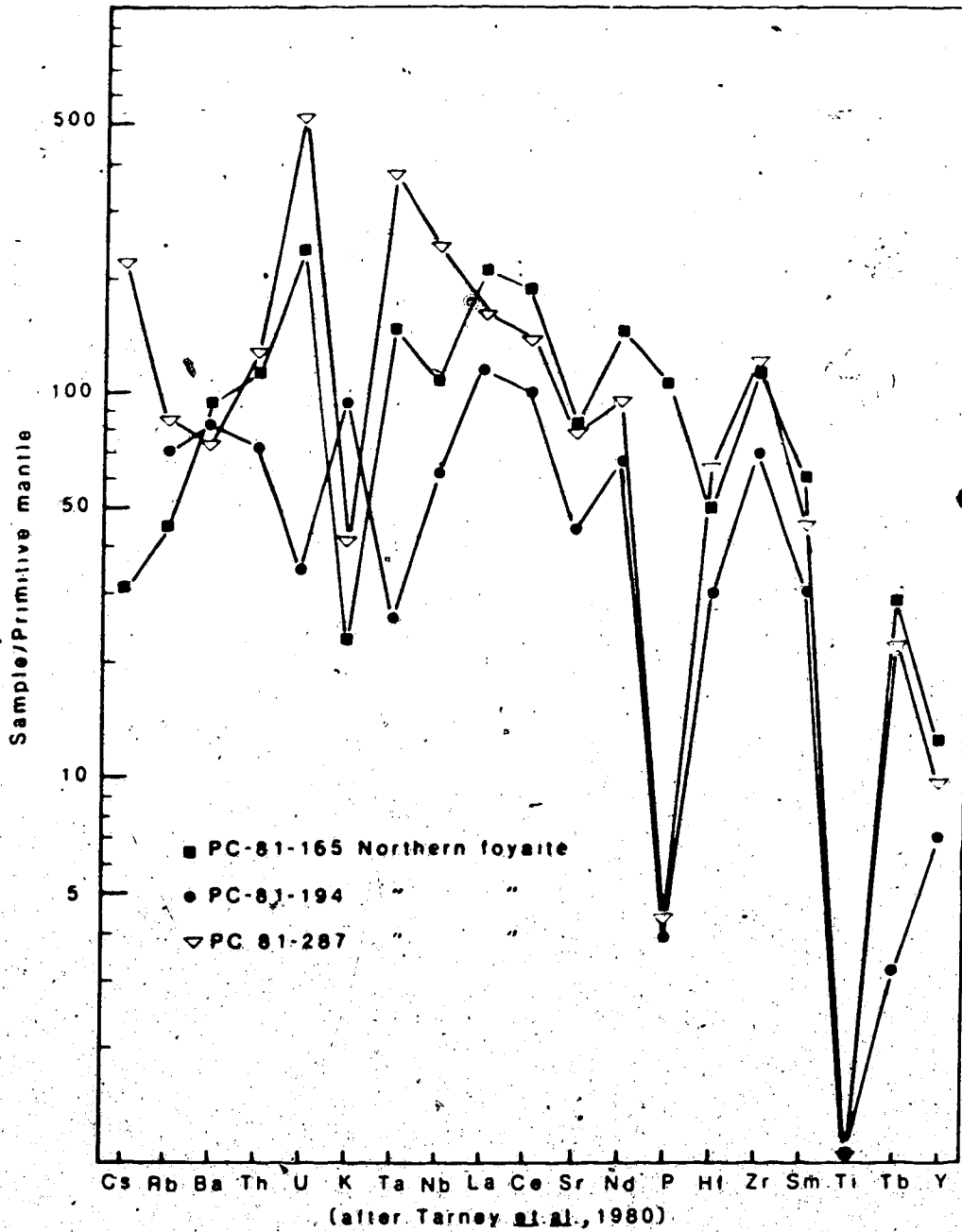


Figure 46. Mantle-normalised LILE distribution plots for northern foyaites from the Big Spruce Lake intrusion.

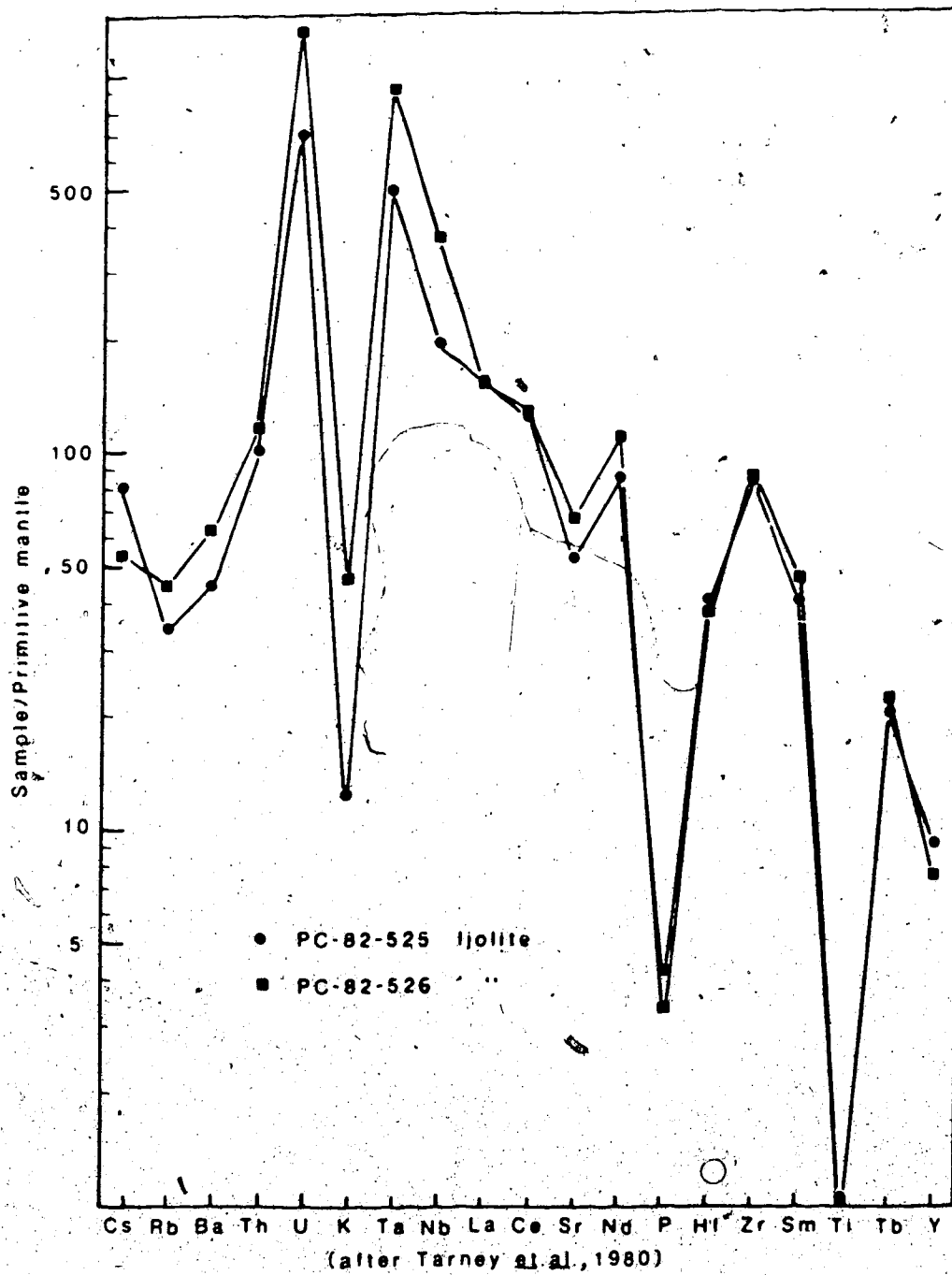


Figure 47. Mantle-normalised LILE distribution plots for ijolites from the Big Spruce Lake intrusion

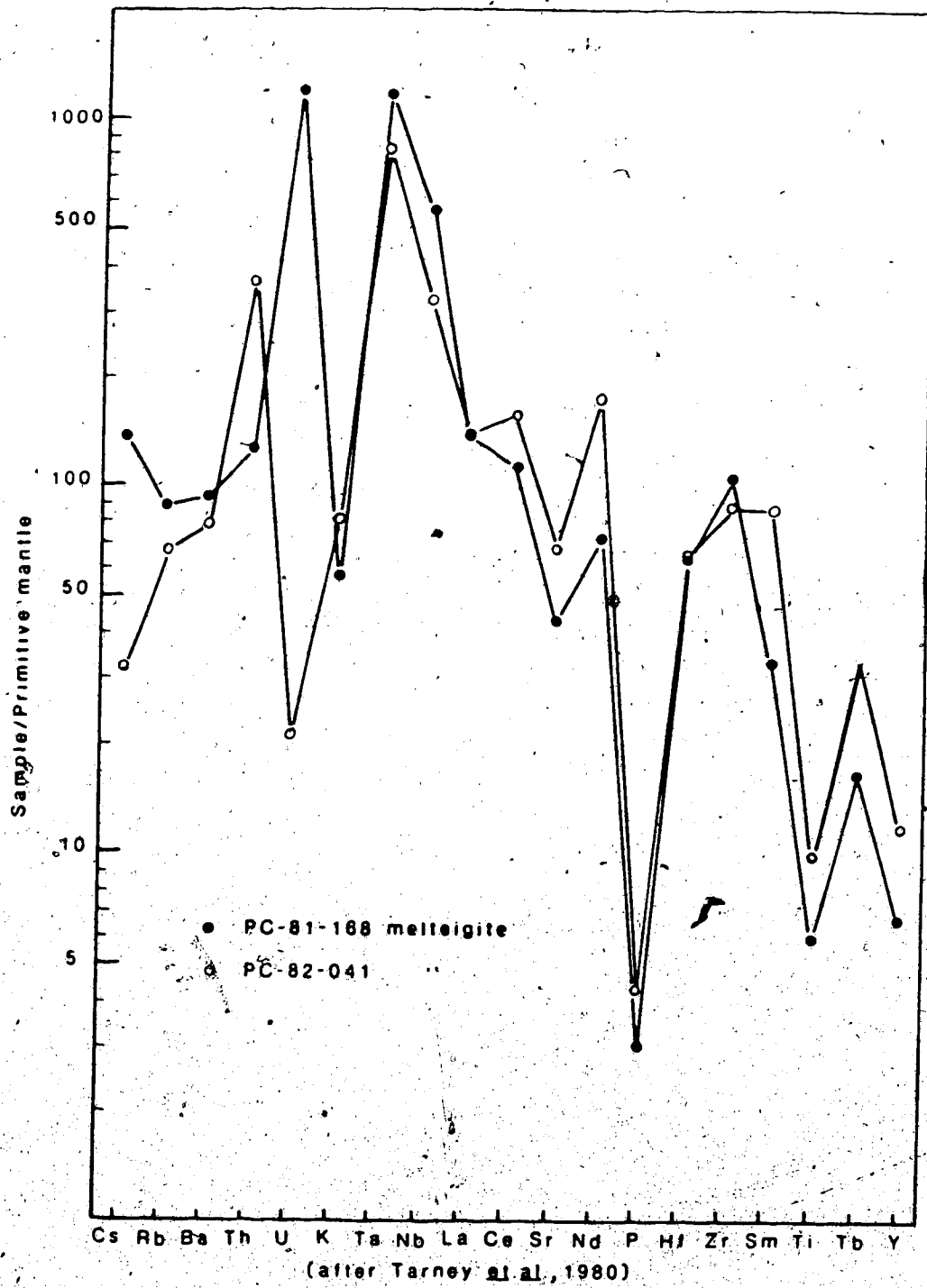


Figure 48. Mantle-normalised LILE distribution plots for melteigites from the Big Spruce Lake intrusion.

direct comparison of the profiles and demonstrates similarities and differences in behaviour of the 19 trace elements among the different igneous systems. For Centre 3 the various mantle-normalised patterns are arranged in approximate increasing total REE content.

The main features of interest in these plots are the systematic depletion in Ti and P relative to the REE enrichment trend and the sample-to-sample variability of the patterns (or "trace element signatures") which is in contrast to the evolving patterns of the gabbro-syenite series.

Titanium and P are semi-compatible or minor elements in more common igneous systems but are striking in their absence throughout the entire suite (including the chilled margins) relative to all other LIL elements on these plots. The Ti that is present appears largely in sphene and (possibly) as complex Na silicate accessories rather than as Fe-Ti oxides. Phosphorus is extremely low ($P_2O_5 = 0.1\%$) in all but one sample; TiO_2 is 0.1 to 0.2% in most samples, jumping to 1.5 and 2.5% in the melteigites. In both chilled margin samples P_2O_5 is low (Martineau, 1970), 0.01 and 0.02% for southern foyaite (SF) and mafic northern foyaite (NF) respectively. The abundance of TiO_2 is similarly very low in SF and NF. These P and Ti contents are very similar to those of the quartz syenites of Centre 2, where both elements have been depleted in

residual liquids by prior crystallisation as Fe-Ti oxides and apatite. Comparison with other alkaline intrusions shows Ti and P abundances are both low in the peralkaline rocks of the Illimaussaq intrusion (Ferguson, 1970), near those of the Big Spruce Lake suite. Both are higher in the Lovozero and Khibina intrusions where $P_2O_5 = 0.15$ to 0.3% and $TiO_2 = 0.9$ to 2.5% (Gerasimovsky et al, 1974).

In spite of the fact that several elements show consistent increases in abundance with mafic content (Figure 43), it is evident from the mantle-normalised plots there are sample-to-sample irregularities for these elements. Two pairs of elements which are geochemically closely related in most igneous systems, Nb/Ta and Zr/Hf, are variable in these rocks (Figure 49). The data scatter is greater for these apaitic rocks than for the gabbroic suite (Figure 28) indicating that the variation lies in the rocks and not in the analytical accuracy.

Nb/Ta varies from about 32 at low concentrations to about 5-6 in the most enriched samples. A variable Nb/Ta ratio contrasts with that of the apaitic rocks of the Lovozero massif, reported by Gerasimovsky et al (1966) to be constant at about 10 to 12, a range close to the mean of the Big Spruce Lake suite. The Zr/Hf ratio ranges from about 35 to 70 in these rocks independent of total enrichment. This range is comparable to that reported by

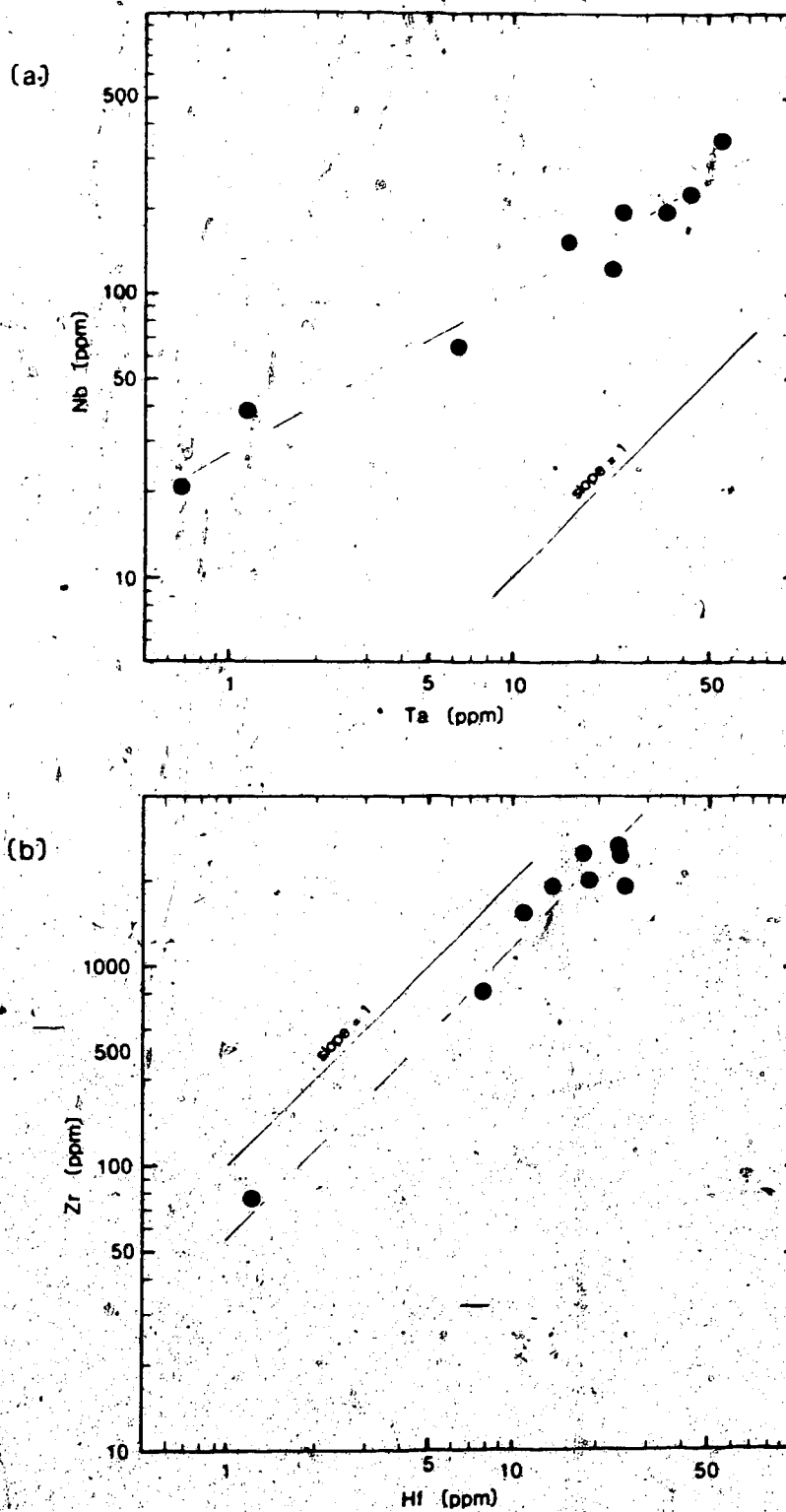


Figure 49. Plots of (a) Ta vs Nb and (b) Hf vs Zr in rocks of the foyaitite-ijolite suite from the Big Spruce Lake intrusion. Data scatter is greater than for rocks of the gabbro-syenite series and the slope of Ta vs Nb is not one.

Gerasimovsky et al (1974) for nepheline-syenites and similar variability within a single complex, the Lovozero massif, Russia, was reported by Gerasimovsky et al¹ (1966).

The rare earth elements behave as a cohesive group within but not between individual samples of the suite. Individual chondrite-normalised REE distribution plots are smooth (Figures 50 and 51), and total rare earth contents (ΣREE) vary from 260 to 820 ppm with the more leucocratic samples having the lower values (Table 10). A concave-down light REE pattern is typical of these rocks except for one (PC-81-482, southern foyaite) sample. The most strongly concave-down pattern, that of melteigite PC-82-041, is similar to the pyroxene-controlled patterns of the magnetite pyroxenites of Centre 1. The general concave-down distribution patterns of these rocks may be the result of cumulate formation.

There are no Ce anomalies indicative of highly oxidising conditions during crystallisation; all samples but one (PC-82-526, ijolite, $\text{Eu}/\text{Eu}^* = 0.96$) have small positive Eu anomalies ($\text{Eu}/\text{Eu}^* = 1.0$ to 1.35) indicative of the preferential incorporation of Eu^{2+} in feldspar. The ubiquitous presence of Eu^{2+} implies that:

- (1) a distribution of valence states between Eu^{2+} and Eu^{3+} existed due to the oxidation conditions (e.g., Philpotts, 1970; Drake, 1974) or melt composition.

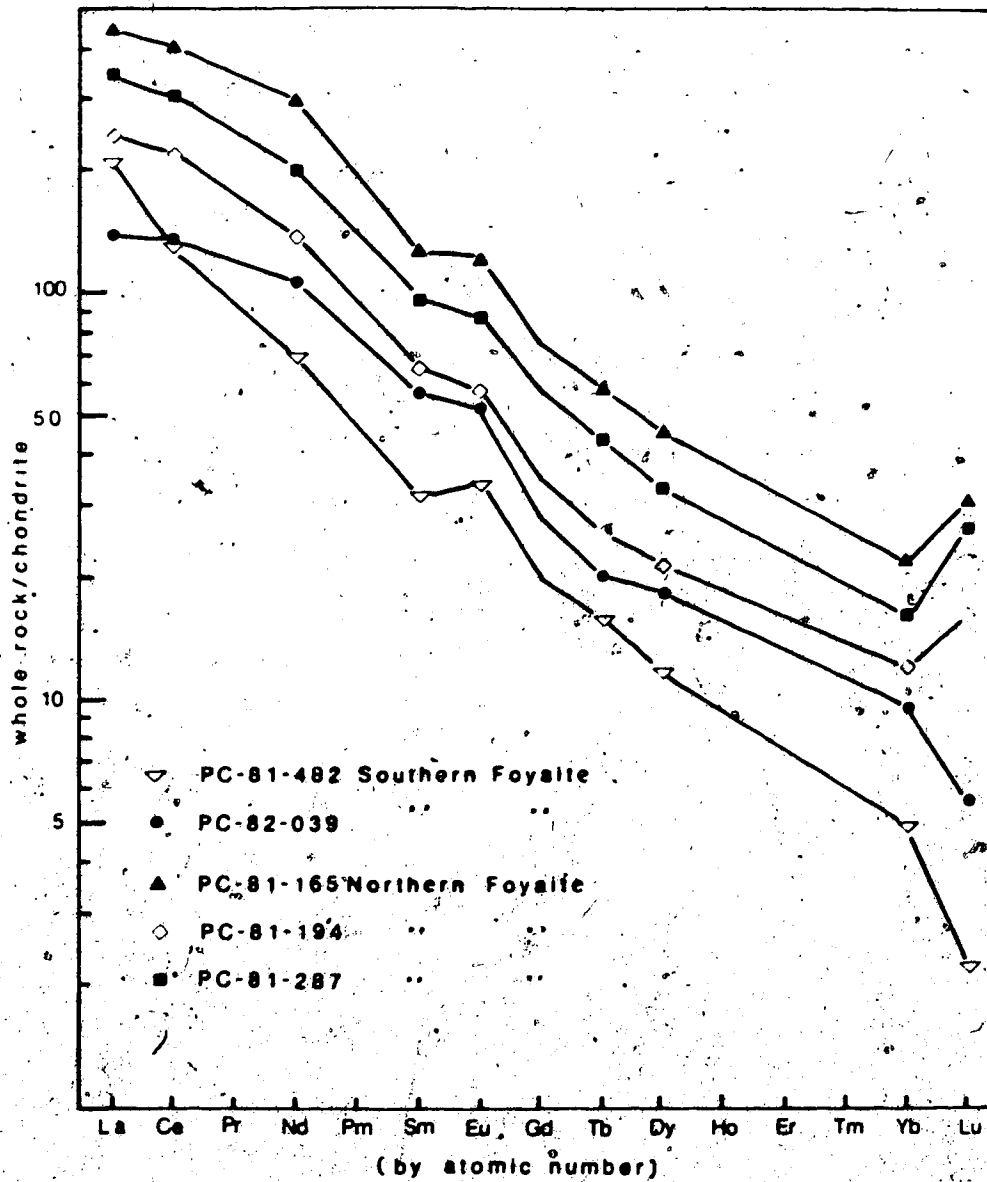


Figure 50. Chondrite-normalised (Nakamura, 1974) rare earth element distribution plots for foyaites of intrusive Centre 3.

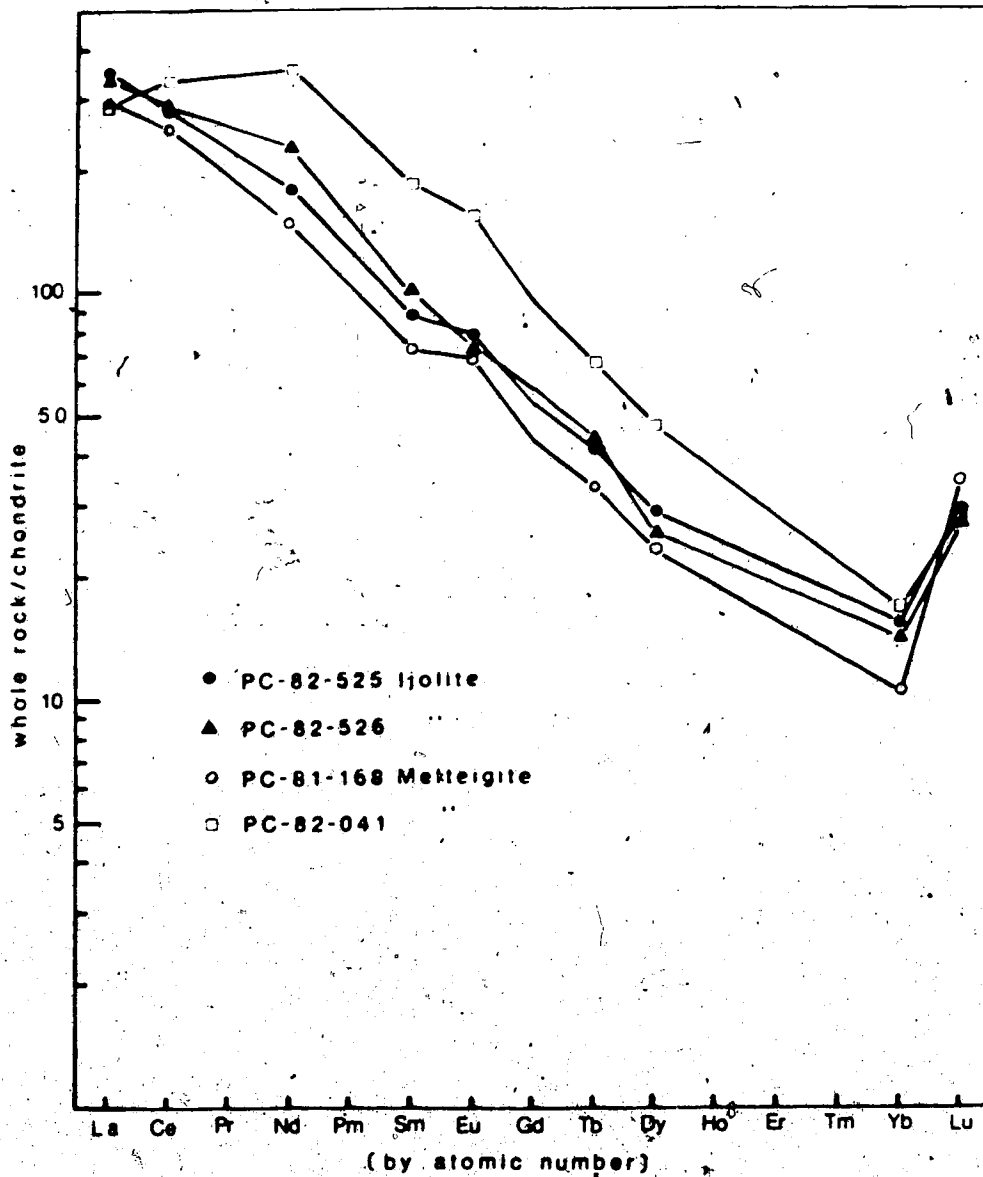


Figure 51. Chondrite-normalized (Nakamura, 1974) rare earth element distribution plots for ijolites and melteigites of intrusive Centre 3.

Table 10. Rare earth element data for intrusive Centre 3.

Sample	Σ RFE ¹ ppm	Eu/Eu* ²	(Ce/Yb) _{CN} ³
PC-81-482 Southern Foyaite	262	1.35	26.3
PC-82-039 Southern Foyaite	285	1.30	14.0
PC-81-165 Northern Foyaite	823	1.26	16.1
PC-81-194 Northern Foyaite	429	1.23	18.4
PC-81-287 Northern Foyaite	608	1.22	19.0
PC-82-525 Ijolite	557	1.14	18.1
PC-82-526 Ijolite	607	0.96	20.3
PC-81-168 Melteigite	489	1.21	23.5
PC-82-041 Melteigite	771	1.17	19.8

¹ Includes values interpolated from Figures 50 and 51 for elements not analysed.

² Eu* interpolated between Sm and Tb on chondrite normalised plots. Eu is analysed value.

³ CN = chondrite-normalised values.

(e.g., Möeller and Muecke, 1984; Morris and Haskin, 1974).

- (2) the parent melt probably had not been significantly depleted in Eu prior to emplacement. If, during evolution of the parent melt and its ascent to the present level, a large portion of original Eu had been removed by fractionation of a phase such as feldspar, then at some point late in crystallisation of this melt a negative anomaly (relative depletion) must occur. No negative anomalies were found and it is unlikely that a major proportion of Eu was removed prior to emplacement of the analysed rocks.
- (3) because all of the samples analysed have small positive Eu anomalies none of them represents the last liquid to crystallise.

A measure of light/heavy REE fractionation ($(\text{Ce}/\text{Yb})_{\text{CN}}$), varies from 14 to 26 in a random manner with total rare earth content or ppm Ce. On a plot of Ce/Yb vs Ce (Figure 52) the data points are scattered and there is no clear trend of fractionation with enrichment.

The concave-down whole rock patterns obtained in this study are similar to those reported by Eby (1975) for the alkaline silicates at Oka, Quebec, but differ somewhat from those of ijolitic rocks at Seabrook Lake, Ontario (Cullers and Medaris, 1977) and at Fen, Norway (Mitchell

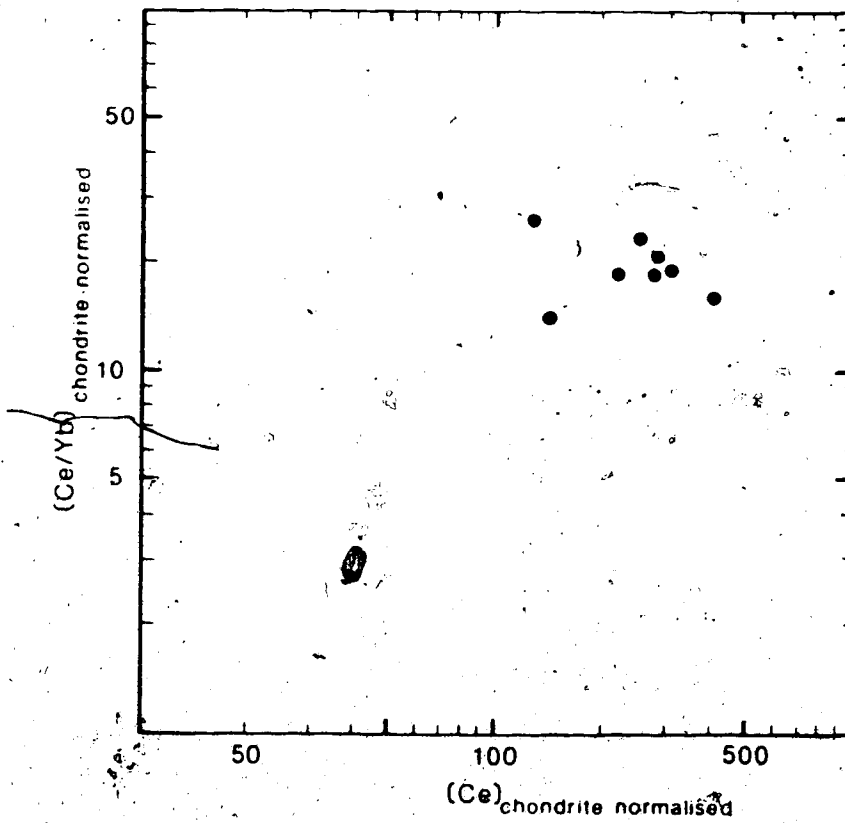


Figure 52. A plot of Ce/Yb vs Ce in rocks of the foyaite-ijolite suite from the Big Spruce Lake intrusion indicating that there is no pattern of increasing LREE/HREE fractionation with total enrichment of REE.

and Brunfelt, 1975). At Oka (Eby, 1975), the three ijolites and one urtite reported as whole rock samples have concave-down distribution patterns similar to those of the Big Spruce Lake suite. However, the urtite from Oka has a very strong positive Eu anomaly ($\text{Eu}/\text{Eu}^* = 7$) while the ijolites show no Eu anomalies in contrast to the typical small positive anomalies from Big Spruce Lake. REE values at Oka are similar to those from Big Spruce Lake but show a greater range with enrichment up to 1400 ppm compared to a maximum of 800 ppm obtained at Big Spruce Lake. Neither Lu nor Yb were determined at Oka so Ce/Yb cannot be compared quantitatively but, by extrapolation of the distribution patterns reported, values for Yb_{CN} and hence $(\text{Ce}/\text{Yb})_{\text{CN}}$ can be approximated. $(\text{Ce}/\text{Yb})_{\text{CN}}$ at Oka is about 14 in urtite and 20-30 in ijolites suggesting that in this case light REE fractionation has occurred. There is insufficient data to determine unequivocally whether the REE data from Oka differ in this respect to those from Big Spruce Lake.

Only one ijolite was included in the study of REE at Seabrook Lake (Cullers and Medaris, 1977). The chondrite-normalised pattern obtained is linear with no Eu anomaly. REE is 3734 ppm and $(\text{Ce}/\text{Yb})_{\text{CN}}$ is about .35, similar to values for the Big Spruce Lake rocks.

At Fen, Mitchell and Brunfelt (1975) noted considerable variability of REE distribution patterns within the urtite-ijolite-melteigite series, which they attributed to cumulate formation. Patterns at Fen were controlled by predominance of nepheline, pyroxene, apatite or melanite garnet in various samples. Most samples showed a slightly concave-down pattern for La and Ce but definitely concave-up heavy REE distribution pattern. No Eu anomalies were found at Fen. $(Ce/Yb)_{CN}$ ranges from 12 to 40 at Fen, and is variable with respect to total enrichment. This is directly comparable to the lack of correlation of fractionation and enrichment of REE at Big Spruce Lake.

The REE evidence for cumulate formation within the undersaturated rocks at Big Spruce Lake is not so strong as that at Fen, but the present data support inferences drawn earlier from major element results. The lack of any systematic variation of REE fractionation (Ce/Yb) with respect to enrichment (ΣREE or ppm Ce) is inferred to be due to mineralogical control over relative and absolute REE abundances. Such control suggests that the whole rock patterns obtained do not reflect the total REE composition of the liquid at the time of crystallisation but are modified by fractional crystallisation and cumulate formation.

3. Melt Composition

Both major and trace element data for the suite of silica-undersaturated rocks from Big Spruce Lake indicate a cumulate character. For this reason only the WR compositions of the two chilled margin samples, southern foyaite (SF) and northern foyaite (NF) can be inferred to approximate melt compositions. In addition to the elements determined in these samples (Table 11, data from Martineau, 1970), the concentrations of several others can be approximated from the data obtained in this study. From Nb vs Ta (Figure 49) Ta abundance is estimated to be 0.8 to 1.0 ppm in SF and about 15 ppm in NF. From Zr vs Hf, the Hf abundances are about 3 ppm and 14 ppm, respectively. From the plots vs total mafic content of Figures 42, 43 and 44, abundances for U, Th, Co, Sc and Σ REE can be approximated. The abundance estimates so obtained (Table 12) are not well-constrained. A cross check on Y by plotting Σ REE vs Y (Figure 53) yielded a reasonable Σ REE = 400 ppm for NF. The abundance of Y in SF is anomalously low at 7 ppm (Figure 43b). If the Y abundance is actually about 22 ppm as suggested by Figure 43b, then Σ REE can be estimated at about 260 ppm from Y vs Σ REE, and is in agreement with the value from correlation with the total mafic content (Figure 43). Also shown in Table 12 are the compositional ranges obtained in this

Table 11. Compositions of foyaite chilled margins reported by Martineau (1970).

	Northern Foyaite (NF) 68051	Southern Foyaite (SF) 67374
<u>Major Elements (%)</u>		
SiO ₂	55.65	57.71
Al ₂ O ₃	19.95	21.52
Fe ₂ O ₃	5.54	
FeO	1.97	2.75
MgO	0.48	0.02
CaO	3.92	1.69
Na ₂ O	9.08	9.92
K ₂ O	4.58	5.69
TiO ₂	0.53	0.54
MnO	0.20	0.06
P ₂ O ₅	0.02	0.01
<u>Trace Element (ppm)</u>		
Rb	163	94
Y	32	7 ¹
Zr	858	179
Nb	144	28
K/Rb	230	500

¹Believed to be too low (Martineau, 1970).

Table 12. Minor and trace element compositions of foyaite chilled margins and of saturated syenites.

Element	SF Leucocratic Foyaite	NF Mafic Foyaite	Mafic Syenite ¹	Quartz Syenite ²
TiO ₂ (%)	0.54	0.53	1.5-2.0	0.4-1.3
P ₂ O ₅ (%)	0.01	0.02	0.4-0.6	0.06-0.3
MnO (%)	0.06	0.20	0.2-0.3	0.08-0.2
Sc* (ppm)	~0.1	=1	6-7	1.6-5.3
Co* (ppm)	~1	=4	7.5-10	1.5-11
Zr (ppm)	179	858	150-200	310-600
Hf* (ppm)	~3	~14	3-5.5	8-14
Nb (ppm)	28	144	40-60	60-80
Ta* (ppm)	0.8-1.0	15	2-4	2.0-5.5
Y (ppm)	7	32	25-35	40-50
ΣREE* (ppm)	150-300	275-450	230-300	370-760
U* (ppm)	<1	<5	0.5-1.0	2.3-3.3
Th* (ppm)	3-6	5-8	1.9-4.6	12-20
Rb (ppm)	94	163	38-40	90-130

* Approximated values for chilled margin samples.

¹ Range of values from Appendix 3, page 398.

² Range of values from Appendix 3, page 399.

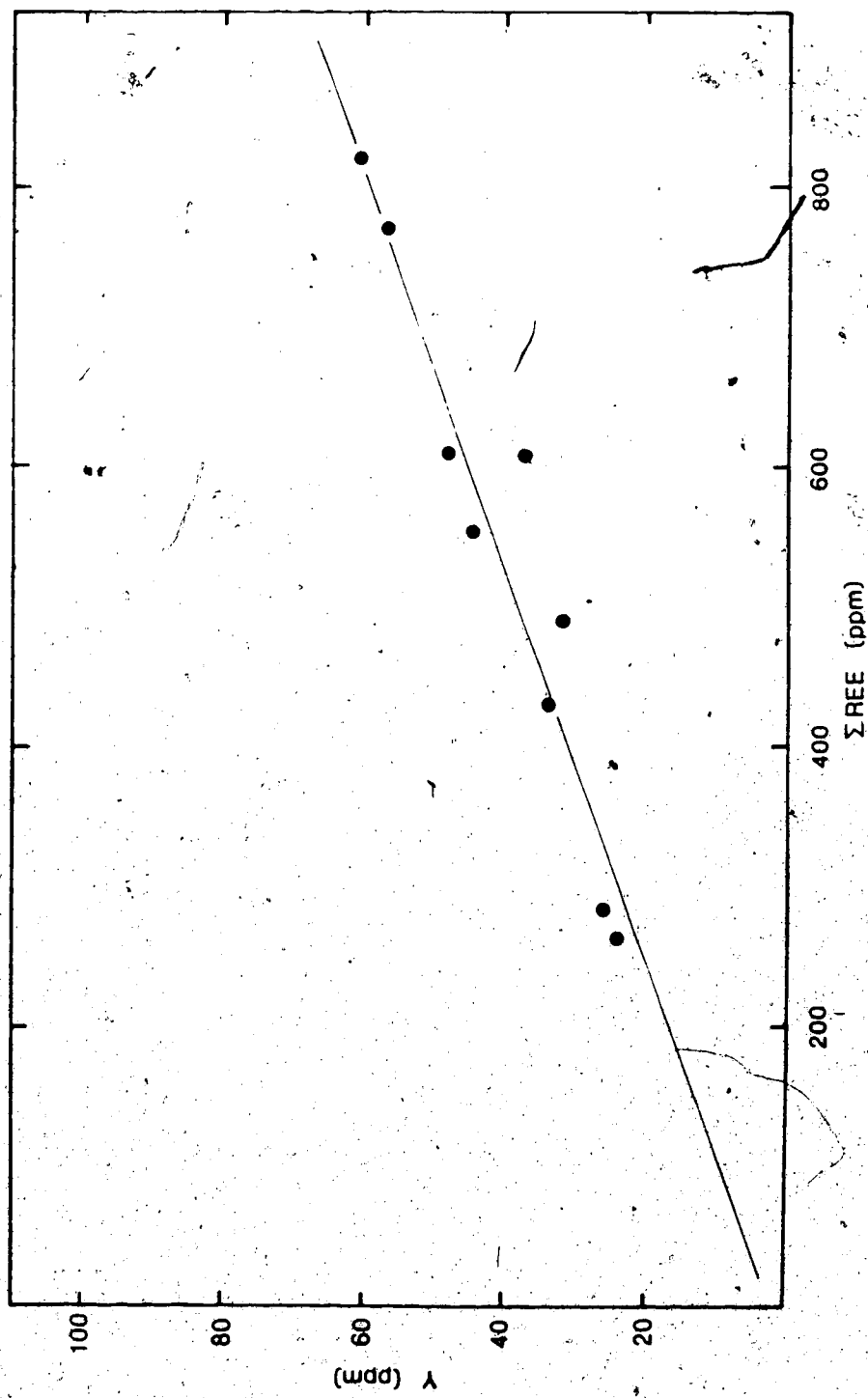


Figure 53. Σ REE vs Y in analysed samples of the foyaitite-ijolite suite.

study for mafic syenites and for quartz syenites of the second intrusive centre.

From the table it is apparent that the behaviour of semi-compatible trace elements such as Co and Sc and the incompatible group (Zr, Hf, Nb, Ta, Y, REE, U, Th, Rb) differ in the silica-saturated and -undersaturated systems. In the silica-saturated system semi-compatible Co and Sc decrease in abundance with increasing differentiation from mafic to quartz syenite, while abundances of the incompatible elements increase. In the peralkaline undersaturated system semi-compatible and incompatible element abundances increase together from leucocratic to melanocratic compositions.

4. Summary and Discussion

The chilled margin compositions of the northern and southern foyaite units (NF and SF) indicate that both melts were leucocratic with normative femic components of about 15 and 10% respectively. Both compositions plot close to the low temperature composition of the residual system and of the Ne-Ab-Di system (Nolan, 1966).

Normative compositions of other foyaite and ijolite samples lie "up-temperature" in both diagrams providing strong evidence of cumulate formation. In the synthetic system, Q-Ne-Ks, crystallisation of NF and SF would have

begun near or at the nepheline/feldspar cotectic, depending upon the pressure and volatiles present. In the more complex natural system represented by the compositions of the foyaite-ijolite suite, the predominance of nepheline-rich normative compositions indicates that crystallisation began in the nepheline field and continued while nepheline accumulated. Later co-crystallisation and accumulation of nepheline plus feldspar accounts for compositions on and near the cotectic. Crystal sorting following co-crystallisation of these two minerals is unlikely to occur if the close similarity of densities at room temperature (Deer et al, 1963) persists to melt temperatures. One normative composition is feldspar-rich. Such a composition might be achieved from an originally silica-undersaturated melt by a mechanism similar to one which has been postulated for abrupt felsic-mafic layer formation in calc-alkaline complexes (Wager et al, 1960; Cox et al, 1979). As nepheline crystallises and accumulates, removing nepheline components from the magma, the intercumulus liquid becomes depleted in nepheline but enriched in feldspathic (and possibly mafic) components. If this intercumulus liquid is removed from the cumulate nepheline, possibly during sporadic fault movement, then on its return to the adjacent magma chamber it will contribute to a hybrid melt.

which is enriched and possibly oversaturated in feldspathic (and mafic) components. This is one possible mechanism by which the abrupt feldspar-rich/nepheline-rich segregations observed in the field might have been produced.

Of the trace elements determined in this study both semi-compatible (Co, Cr, Sc, V) and incompatible elements are enriched in more mafic samples. The variations in semi-compatible elements are best explained by a simple increase in modal abundances of the mafic host minerals such as biotite, aegirine-augite and possibly oxides. The abundances of incompatible elements display two patterns relative to mafic content. The Σ REE, Zr, Th and Y increase directly with mafic content of foyaites and ijolites, and it is postulated that these elements are either incorporated directly into the mafic minerals and/or into accessories which are closely associated with mafic aggregates (e.g., zircon). Uranium, Nb (and Ta) abundances are more erratic and only generally increase with the mafic content. These elements might be incorporated into specific accessory minerals (e.g., perovskite) such that the presence of single crystal in a WR sample affects trace concentrations.

Some of the more mafic and LILE-enriched rocks may have been produced by co-crystallisation of nepheline +

feldspar + mafics (in approximately eutectic proportions) followed by differential accumulation or crystal sorting. Erratic distributions in abundances of some trace elements (e.g., U, Nb) might best be explained by such a process. An alternative process by which mafic and LILE-enriched rocks might have been produced is by crystallisation of a mafic, LILE-enriched liquid residual to the crystallisation of significant amounts of nepheline (and possibly of feldspar). The gabbros are the most mafic and LILE-enriched rocks, apart from the unusual melteigite dykes and "reefs". These units may be the product of late, LILE-enriched liquids produced within another magma chamber. However the possibility that they are cumulates and apparently intrusive in the same manner as the magnetite pyroxenites of Centre 1 cannot be ruled out at present.

The same leucocratic to melanocratic REE enrichment trend has been reported for the alkaline rocks of Fen, Norway (Mitchell and Brunfelt, 1975) and of Oka, Quebec (Eby, 1975) but the processes involved were not discussed.

The two chilled margins, NF and SF, whose compositions are presented in Tables 11 and 12 are inferred to represent liquids which crystallised free of cumulate formation. These two differ in that NF is both more mafic and more enriched in incompatible elements.

The more leucocratic liquid composition (SF) can be derived from the more mafic (NF), by a normal sequence of mafic + felsic differentiation, but only if all of the incompatible elements are removed from the melt along with early mafic minerals.

Le Bas (1977) has suggested that nepheline syenites could be produced by palingenesis of fenites followed by fractional crystallisation. Such a model is not valid for the intrusive suite from Big Spruce Lake, all of which carry mantle isotopic compositions for Nd, Sr and Pb (see Chapter 4). There is no major crustal contribution to these undersaturated rocks and a mainly mantle origin is clearly indicated.

The degree of incompatible element enrichment of the leucocratic and mafic foyaite liquids, SF and NF, is comparable to that of mafic and quartz syenites, respectively, which were derived by extensive fractional crystallisation of an alkali basalt parent melt. Combined with the leucocratic major element character and semi-compatible element (Co, Cr, V, Sc, Ti, P) depletion, such enrichment implies derivation by extensive fractional crystallisation. Additional characteristics of the foyaite-ijolite suite which must be accounted for in any petrogenetic model are low Si/alkali, low Al/alkali and low Fe^{2+}/Fe^{3+} .

On the basis of REE studies, Eby (1975) and Cullers and Medaris (1977) suggested that extensive (50-60%) fractionation of olivine and clinopyroxene (plus <1% garnet; Eby, 1975) from an alkali olivine basalt magma could produce the REE enrichment and fractionation of the ijolites of Oka, Quebec and Seabrook Lake, Ontario.

Extensive fractionation of magnesian olivine and clinopyroxene from a dry, highly-oxidised alkali olivine basalt could produce the required LILE-enriched, Fe^{3+} and alkali-rich and silica-undersaturated melt. With progressive crystallisation the composition of the clinopyroxene should become increasingly enriched in aegirine because of Na and Fe^{3+} enrichment in the liquid. Fractionation of aegirine ($SiO_2 = 53\%$) would further reduce the silica content of the liquid.

The Al content of the foyaites and ijolites is not compatible with the fractionation scheme outlined above. An average alkali olivine basalt has a high Al/alkali ratio. Based on average compositions from Frey et al (1978) and Cox et al (1979) alkali basalts have peralkaline indices ($(Na_2O+K_2O)/Al_2O_3$, molecular proportions) of about 0.5 to 0.6. The foyaite chilled margin compositions of this study, NF and SF, have indices of 1.0, and thus Al must be removed relative to alkali to produce foyaite melt from alkali olivine basalt.

Fractionation of aegirine, which does occur in later stages, produces the opposite effect of depleting Na relative to Al. Fractionation of early anorthite is usually omitted from fractionation schemes to produce foyaites and ijolites because negative Eu anomalies are not observed (Cullers and Medaris, 1977). However, if $\text{Eu}^{3+} \gg \text{Eu}^{2+}$ under highly oxidising conditions, then early removal of anorthite might account for Al removal and not produce a negative Eu anomaly. Crystallisation of garnet at depth is restricted to <1% (Eby, 1975) by the $(\text{Ce}/\text{Yb})_{\text{CN}}$ and hence does not account for the final low Al abundance. Some Al is probably removed in Al-rich clinopyroxene. Augitic clinopyroxene can contain 5-7% Al_2O_3 with Al:Na (atomic) up to about 7 or 8:1 (Deer et al, 1978) but it is improbable that clinopyroxene fractionation alone would change the alkali/aluminum ratio to the extent required by NF and SF compositions.

Nephelinite or olivine nephelinite has been suggested as another possible parent melt for the alkaline rocks associated with carbonatites (Middlemost, 1974; Le Bas, 1977). Such a melt has a higher peralkaline index, about 0.8 to 0.9 based on data from Frey et al (1978) and Cox et al (1979), more in accord with the Big Spruce Lake foyaite chilled margin compositions. However, the average ΣREE is

higher in nephelinites than in alkali basalts (for nephelinite Σ REE = 200 to 600 ppm; Cullers and Graf, 1984). This presents significant difficulties for derivation of NF and SF by fractional crystallisation of nephelinite.

Average alkali olivine basalt and nephelinite both can be produced by direct partial melting of an LILE-enriched pyrolite mantle. The alkali basalt requires 7 to 15% melting (Sun and Hanson, 1975b; Frey et al, 1978) and the nephelinite, 5 to 7% melting (Frey et al, 1978). The major and trace element data of this study are not wholly compatible with derivation of the foyaite-ijolite suite by fractional crystallisation of either "average" mantle-derived magma. Elucidation of the relationships within the foyaite-ijolite suite might be provided by:

- (1) Experimental determination of incompatible element behaviour in peralkaline, silica-undersaturated melts.
- (2) Detailed electron microprobe study of mineral compositions to define a crystallisation sequence.
- (3) Determination of the effects of volatiles, particularly CO₂, on the crystallisation and incompatible element behaviour in peralkaline systems.

F. Carbonatites

1. Major and Trace Element Results

In the nomenclature and classification scheme for carbonatites recently proposed by Woolley (1982), compositions are plotted on a CaO-MgO-(FeO + Fe₂O₃ + MnO) triangle divided as shown in Figure 54. The compositions of the 9 carbonatites analysed in this study (Appendix 3, pages 404 and 405) are plotted in the figure. The 7 calcitic samples plot well in the sövite field with very low Mg and minor Fe and Mn. Only one sample, PC-81-185, which carries phenocrysts of pyrite and magnetite, has a significant Fe content. Use of the name sövite for these 7 rocks is reasonable and is also in agreement with the Streckeisen (1980) nomenclature scheme which is based on modal abundances of carbonate phases.

The two samples from the separate carbonatite focus to the east of the main complex plot within the ferrocarnatite field on the Woolley classification triangle. However, these rocks contain abundant phenocrysts of magnetite in a dolomitic matrix and the name originally assigned, magnetite dolomite carbonatite (Martineau, 1970), is retained in this study in preference to ferrocarnatite because it is indicative of the oxide nature of the iron phase and hence of the possible crystal accumulation during crystallisation.

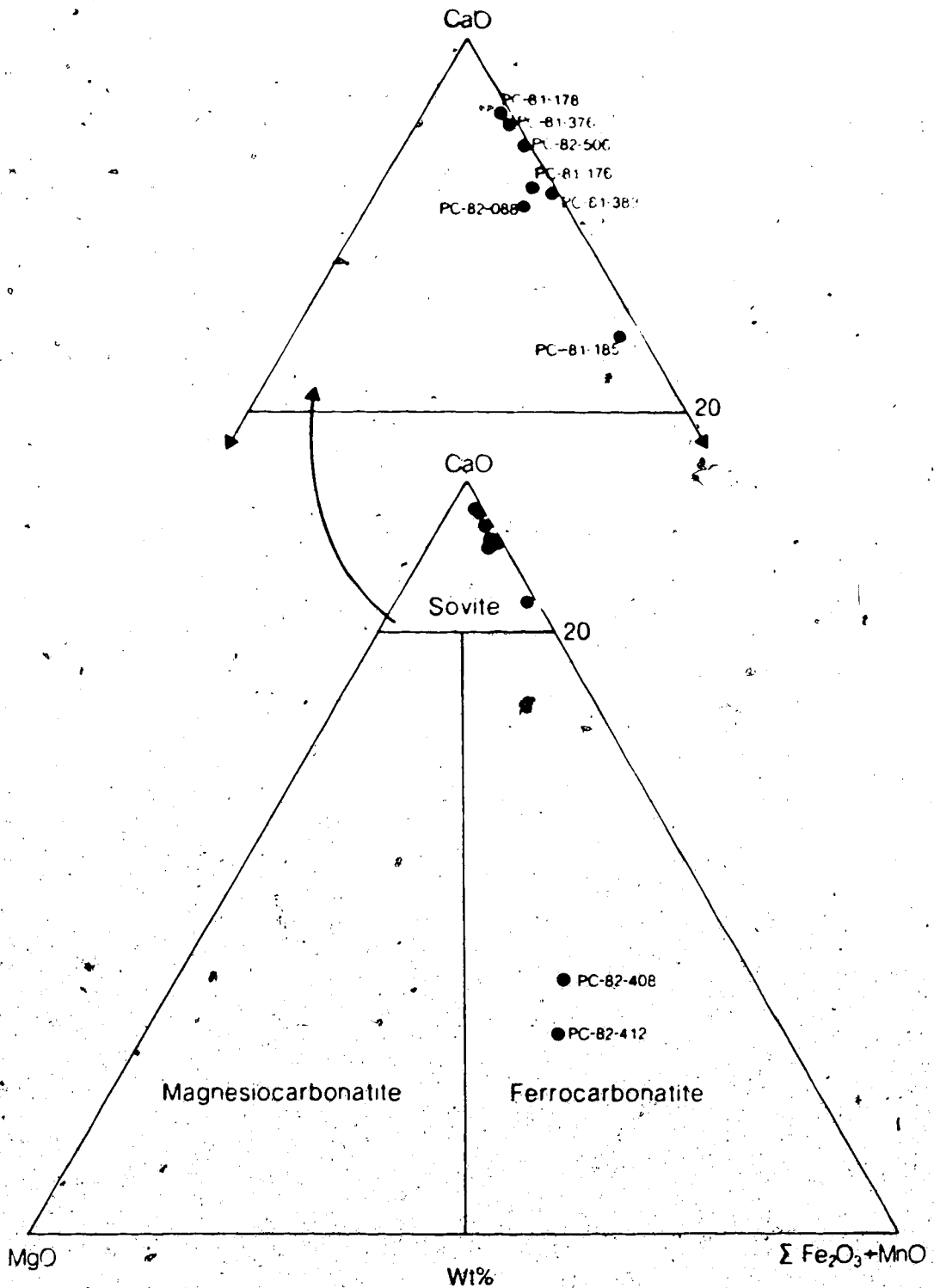


Figure 54. Carbonatite classification diagram (according to Woolley, 1982) showing compositions of analysed samples from the Big Spruce Lake intrusion.

The most striking feature of the analytical results of Appendix 3, pages 404 and 405) is the wide variation in abundances of major and trace elements. Although the 7 sövites plot very close to each other in the classification triangle, elements not considered in the diagram vary widely. Table 13 presents the abundance range for each element in the sövites in comparison with the two magnetite dolomite carbonatites. The variability of carbonatite compositions has been noted in the past (e.g., Gold, 1966) and it has even been stated that an "average" carbonatite analysis is meaningless (Woolley, 1982). Element abundances and the range within the Big Spruce Lake group are of the same magnitude as those reported previously (e.g., Gold, 1966; Le Bas, 1977; Woolley, 1982).

Several generalisations can be made about the sövite compositions. Both Na and K are almost totally absent. Only one sample, which also has $\text{SiO}_2 = 25\%$, has $3\% \text{Na}_2\text{O}$, all others, regardless of SiO_2 and Al_2O_3 contents contain $<0.3\% \text{Na}_2\text{O}$ and $<0.3\% \text{K}_2\text{O}$. This is in agreement with the low to absent alkali content of all known carbonatites (Freestone and Hamilton, 1980; Le Bas, 1981; Woolley, 1982) apart from the Oldoinyo Lengai natrocarbonatite (Dawson, 1966). The abundance of MgO is $<0.9\%$ in the sövites and Fe is not abundant. Although Na, K, Mg and Fe

Table 13. Range of compositions of carbonatite from the Big Spruce Lake intrusion.

Element	Abundance Range for 7 Calcitic Carbonatites*	Abundance in 2 Dolomite Carbonatites*
SiO ₂	0.8-25.5	11.1, 23.6
Al ₂ O ₃	0.3-8.8	4.6, 4.8
TiO ₂	0.03-0.19	3.0, 3.4
ΣFe ₂ O ₃	0.8-6.5	23.3, 22.0
MgO	0.07-0.9	12.2, 12.2
CaO	33.6-53.8	18.2, 12.9
MnO	0.2-2.1	0.6, 0.5
Na ₂ O	nd-3.3	0, 0.2
K ₂ O	nd-0.4	1.4, 1.5
P ₂ O ₅	nd-0.15	1.9, 2.6
Ba	70-1725	399, 467
Co	nd-3	51, 46
Cr	5-62	447, 864
Cs	nd-1	2, 1
Hf	nd-nd	6, 6
Mo	1-7	7, 7
Nb	9-182	105, 100
Pb	23-132	7, 12
Rb	3-36	74, 56
Sb	nd-0.6	nd, 0.5
Sc	nd-1.5	14.6, 18.4
Sr	2410-9030	1580, 1390
Ta	nd-4	5, 5
Th	29-74	9, 32
U	0.2-2.7	4.1, 5.9
Y	68-187	48, 89
Zr	18-36	250, 315
ΣREE	960-9560	1380, 2890
(Ce/Yb) _{CN}	18-307	99, 197

*Major element oxides quoted in percent; trace elements quoted in ppm. nd = not detected.

readily form carbonates CaCO_3 is clearly the dominant phase here. The small amounts of Na, K, Mg and Fe are largely present in identifiable silicate and oxide minerals such as riebeckite, alkali feldspar, biotite, epidote, magnetite and pyrite (sulfide). P_2O_5 (as apatite) is almost absent and several lithophile elements such as Zr, Hf, Nb, and Ta are low in spite of their common association, in economic amounts, with carbonatite complexes (Currie, 1974).

Relative abundances of various LIL elements are as variable as absolute abundances. The Nb/Ta ratios can be calculated for only 4 samples because Ta was not detected in the others. (Detection limit is approximately 0.5 ppm.) In both magnetite dolomite carbonatites and in the most silica-rich sövite the Nb/Ta ratio is 19 to 20, but in one sövite which is Nb-rich and silica-poor the ratio is 47. Hf (detection limit approximately 0.5-0.7 ppm) is present only in the magnetite dolomite carbonatites where Zr/Hf is 40 and 53. The low K and Rb contents produce K/Rb ratios varying from 55 to 223 independent of total abundance.

Both enrichment and fractionation of the rare earth elements (REE) is obvious from comparison of the chondrite-normalised REE distribution plots of Figures 55 to 57 and the data of Table 14. There is some correlation

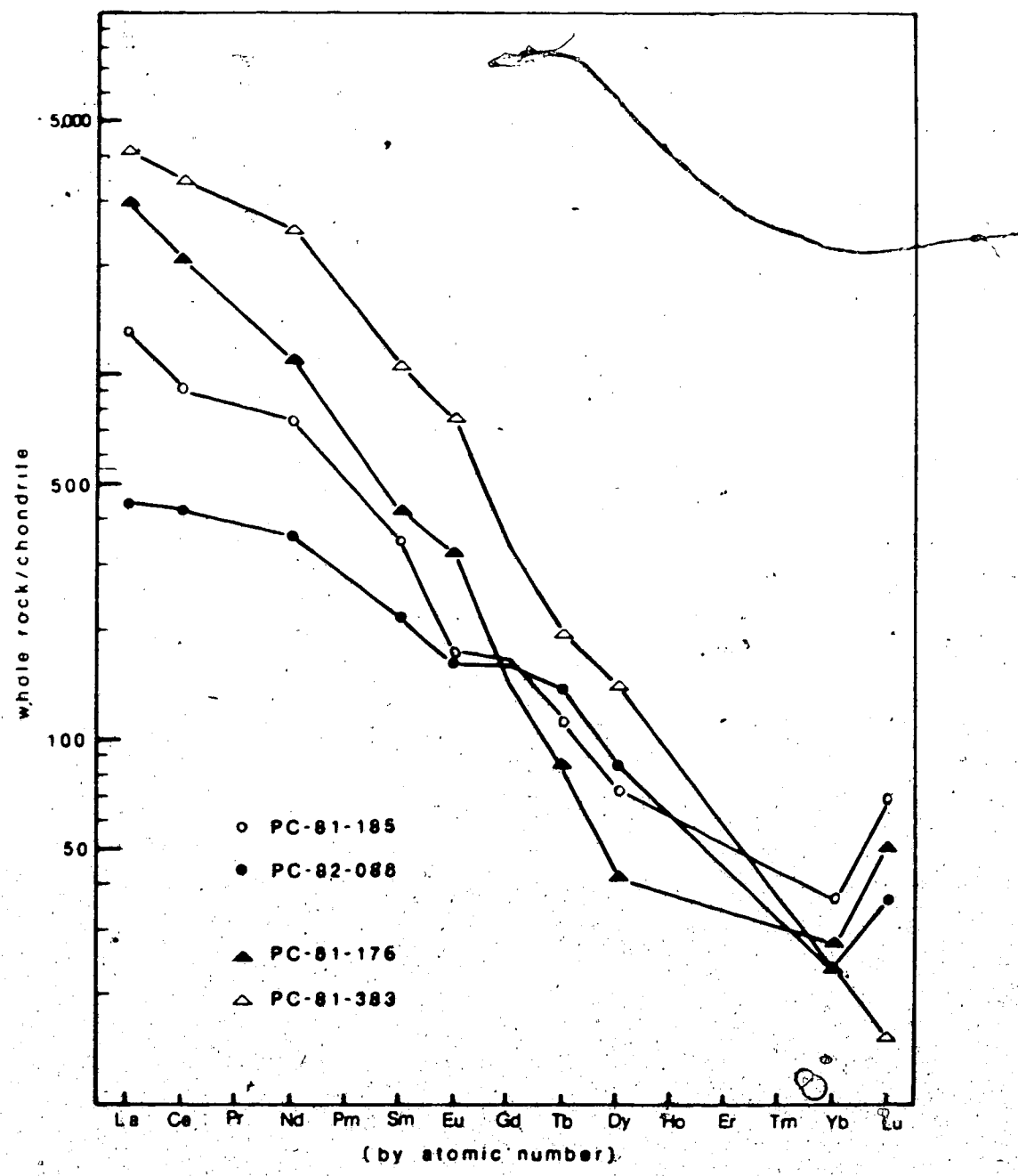


Figure 55. Chondrite-normalised (Nakamura, 1974) rare earth element distribution patterns for sövite dykes. Negative Eu anomalies are associated with the least enriched sövites, both of which are possibly contaminated by gneissic host rock.

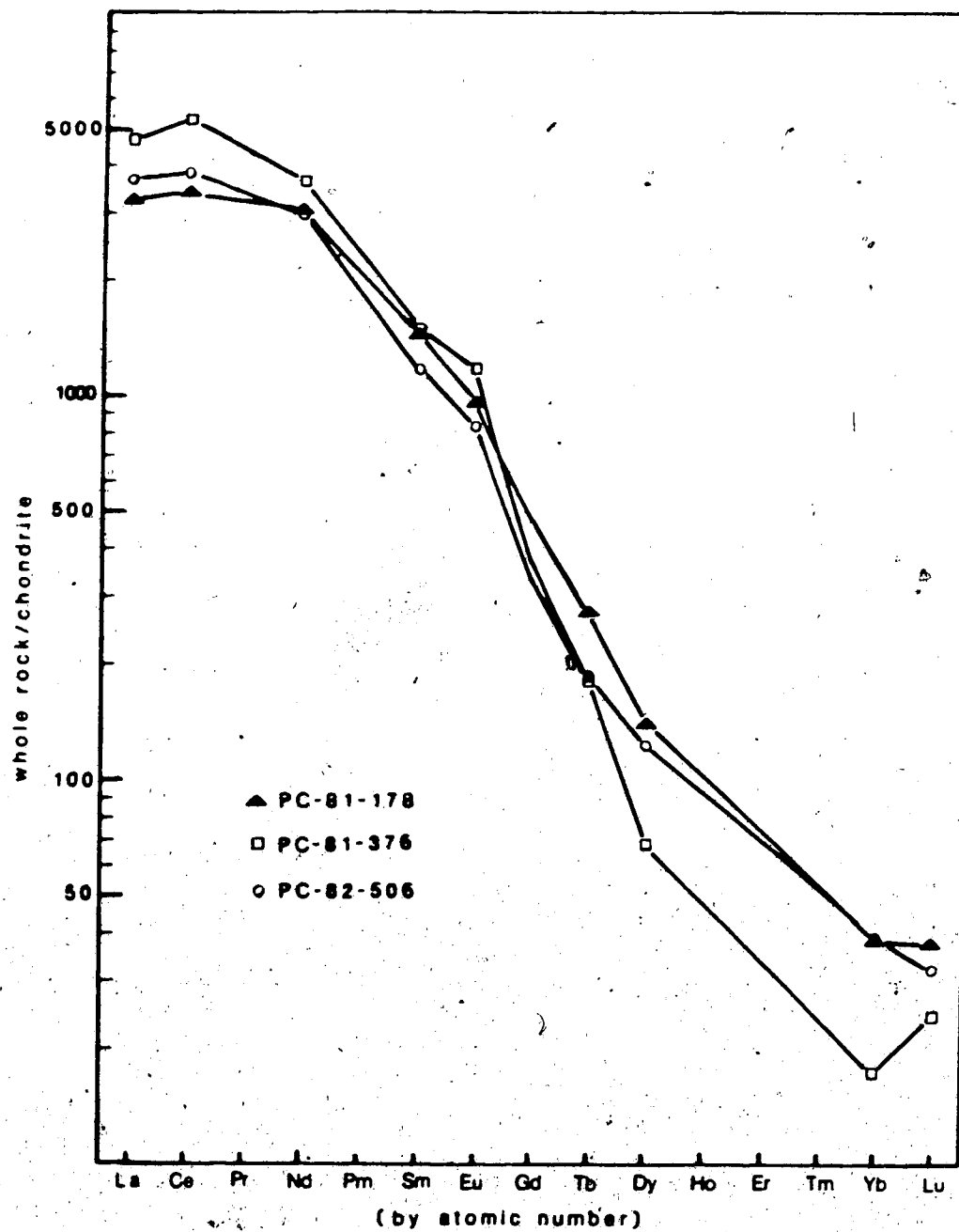


Figure 56. Chondrite-normalised (Nakamura, 1974) rare earth element distribution patterns for three similar grey, laminated sövite dykes.

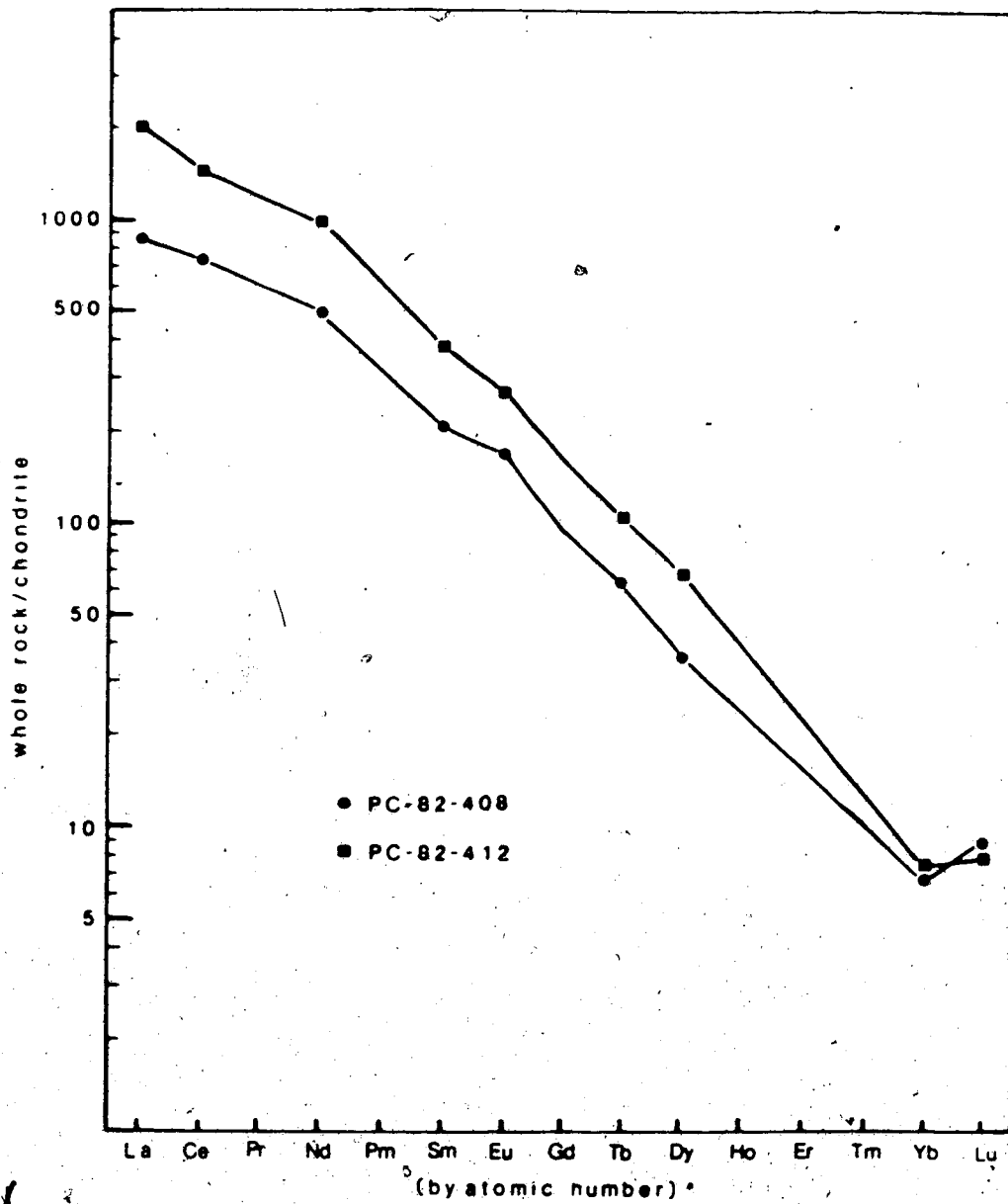


Figure 57. Chondrite-normalised (Nakamura, 1974) rare earth element distribution patterns for magnetite dolomite carbonatites from the separate focus to the east of the main complex.

Table 14. Rare earth element results for carbonatites.

Sample Number	Σ REE ¹	Eu/Eu* ²	(Ce/Yb) _{CN} ³
<u>Sövites</u>			
PC-81-176	3853	1.35	74.3
PC-81-178	6981	1.19	88.8
PC-81-185	2007	0.72	24.8
PC-81-376	9562	1.62	307
PC-81-383	6798	1.28	145
PC-82-088	964	0.85	18.0
PC-82-506	7351	1.28	98
<u>Magnetite Dolomite Carbonatites</u>			
PC-82-408	1378	1.22	98.7
PC-82-412	2887	1.08	197

¹ Includes values interpolated from Figures 55 to 57 for elements not analysed.

² Eu* interpolated between Sm and Tb on chondrite normalised plots. Eu is analysed value.

³ CN = chondrite-normalised values.

of distribution patterns with intrusive form and location. The two sövite samples with lowest Σ REE, PC-81-185 and PC-82-088, also have the only negative Eu anomalies ($\text{Eu}/\text{Eu}^* = 0.72$ and 0.85) observed in the carbonatites. The $(\text{Ce}/\text{Yb})_{\text{CN}}$ ratios in these rocks are 18 and 25, much lower than those of other carbonatites (75 to 300) and comparable to those of the foyaite-ijolite suite. These two carbonatites form well-defined dykes which cut gneiss or cut syenite near gneiss at the western edge of the complex. The low $(\text{Ce}/\text{Yb})_{\text{CN}}$, negative Eu anomalies and outcrop location within or near gneiss suggest that these two dykes may have significant granodiorite contamination. This conclusion is supported by a low $^{143}\text{Nd}/^{144}\text{Nd}$ ratio in these samples relative to other carbonatites (Chapter 4).

Sövites closely associated (spatially) with the foyaite-ijolite suite have high Σ REE, 3850 to 9560 ppm, comparable to abundances in carbonatites from other localities (Loubet et al, 1972). The general range of $(\text{Ce}/\text{Yb})_{\text{CN}}$ of 75-145 is also comparable to ratios in carbonatites from other localities (Loubet et al, 1972). One sample is HREE depleted and this produces an anomalously high $(\text{Ce}/\text{Yb})_{\text{CN}}$ of 300.

Magnetite dolomite carbonatites are moderately REE-enriched with Σ REE 1400 to 2900, slightly lower than in

the main sövite group. The ratio $(Ce/Yb)_{CN}$ in these two samples is slightly higher than in sövites, ranging from 100-200.

2. Discussion

Wyllie (1965) in a study of the system $CaCO_3$ - $MgCO_3$ - $FeCO_3$ determined a crystallisation or differentiation sequence of calcitic + dolomitic + ferroan carbonates, a sequence confirmed by field evidence (Le Bas 1977, 1981). Among the sövites from Big Spruce Lake there is no differentiation trend towards magnesian and ferroan carbonatites. The geographically separate magnetite dolomite carbonatites may represent late products of carbonatite differentiation at depth, but there is no continuity of major element chemistry between the presently exposed calcitic and dolomitic types.

Le Bas (1981) suggests that $Ca + Mg + Fe$ differentiation in major elements is accompanied by changing proportions of various trace elements as well. Sr decreases with carbonate differentiation while Ba, Mn and REE increase, possibly by an order of magnitude. The magnetite dolomite carbonatites should be the most differentiated products according to the major element composition and they do have the lowest Sr contents of all of the carbonatites analysed. However, Ba, Mn and REE are

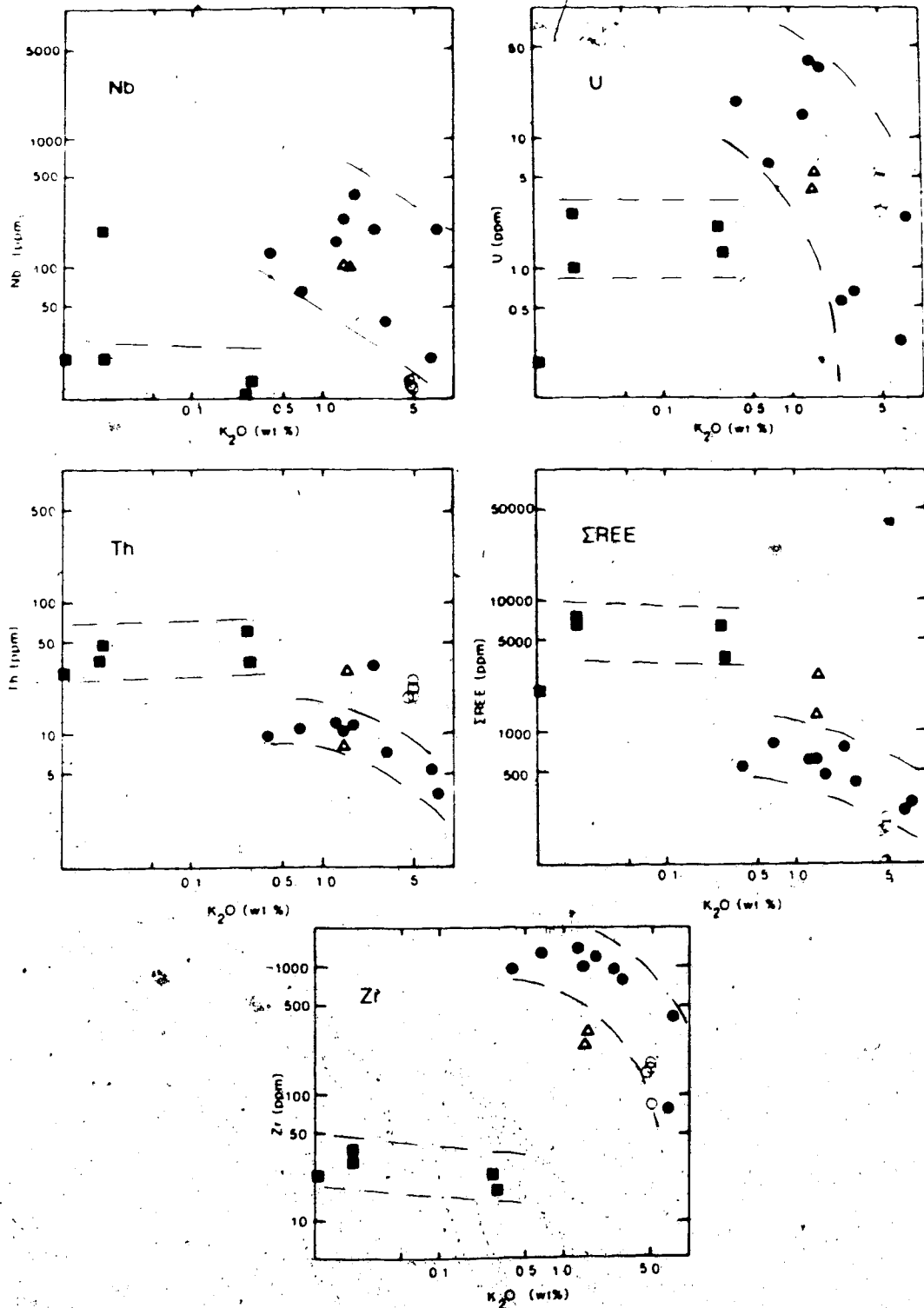
not enriched in these rocks (Table 13). It thus appears that the sövites and dolomite carbonatites from Big Spruce Lake are not related by differentiation of a single parent carbonate melt. Similarly within the sövite group there is no consistent differentiation trend in trace element abundances. The most Fe- and Mg-rich sövites are inferred to have been contaminated by granodiorite. The other sövites plot close together in the classification diagram but the most calcitic sövites which should be earliest in a carbonatite differentiation scheme (Wyllie, 1965; Le Bas, 1981), have the highest REE contents, moderate Sr and MnO, and low Ba. This LILE abundance pattern is in opposition to an origin as early carbonatite differentiates for these sövites.

Carbonatites and the foyaité-ijolite suite are closely associated at Big Spruce Lake in a relationship that has been termed interdependence by some authors (e.g., Le Bas, 1977). Various authors have recently used REE data in attempts to determine the relationship between carbonatites and the associated silicates. In all studies (Eby, 1975; Mitchell and Brunfelt, 1977; Cullers and Medaris, 1977) the REE abundances in carbonatites were much greater than those in the most enriched silicates (ijolites). The enrichment factors of REE carbonatite/REE ijolite varied from 5.6 at Oka, Quebec (Eby, 1975) to 1.5-

2 at Fen, Norway (Mitchell and Brunfelt, 1977) and Seabrook Lake, Ontario (Cullers and Medaris, 1977). No acceptable model of fractional crystallisation could be found to explain the data and carbonate/silicate liquid immiscibility was inferred.

A similar conclusion can be quickly reached for the Big Spruce Lake carbonatite-ijolite association on the basis of REE data. Omitting the two sövites which perhaps are contaminated, the lowest Σ REE for a sövite is 3850 ppm whereas the highest Σ REE in a silicate is 600 ppm (in an ijolite). The ratio of Σ REE carbonatite/ Σ REE ijolite is 6.4; similar to, but even higher than the 5.6 reported by Eby (1975) for the carbonatite/ijolite association at Oka, Quebec. Thus carbonate/silicate liquid immiscibility more reasonably explains the relationship between carbonatites and associated silicates than does fractional crystallisation.

The abundances of other trace elements in carbonatites and foyaite/ijolites from Big Spruce Lake show similar discontinuities which are indicative of carbonate/silicate immiscibility. The concentrations of trace elements in individual carbonatites is extremely variable. In Figure 58 abundances of Rb, Zr, Nb, Σ REE, U and Th in carbonatites and in the foyaite-ijolite samples are plotted against %K₂O. The two sövites inferred to be



■ sovite ● foyaite-ijolite suite ▲ magnetite dolomite carbonatite ○ granodiorite

Figure 58. Abundances of Nb, U, Th, Σ REE and Zr vs K_2O in carbonatites and rocks of the foyaite-ijolite suite. "Discontinuities" suggest carbonate/silicate liquid immiscibility.

contaminated are omitted to simplify the figure.

Percentage of K_2O is an arbitrarily chosen plotting parameter by means of which similarities and differences can be graphically illustrated. There are "discontinuities" for all elements between carbonatites and the most LILE-enriched silicates. Only REE and Th are enriched in carbonatites over silicates. Thorium is enriched in carbonatites relative to silicates by a factor of 3 to 6 times (to 15 times if Th-poor foyaite is compared). In sövites Zr, Nb and U are depleted relative to abundances in the most enriched silicates, Zr by a factor of about 40 to 60, Nb by a factor of about 15 to 30 (apart from the single Nb-enriched sövite) and U by a factor of about 15 to 40. Depletion of Hf and Ta coincides with that of Zr and Nb.

These "discontinuities" emphasise that no continued fractional crystallisation of the foyaite-ijolite group will produce the trace element compositions of the sövites. An immiscibility relationship between silicate melt/carbonate melt is the most reasonable explanation of the trace element data.

The two magnetite dolomite carbonatites are richer in K_2O than the sövites, and they differ in LILE concentrations as well. Some of the difference might be ascribed to assimilation of granodioritic wall rock,

because these carbonatites carry angular clasts of gneiss. The compositions of the granodiorites are included in Figure 58. It is apparent that high Zr content (relative to sövites) and a high Nb content do not result from assimilation of gneissic country rock. Contents of U, Th and Σ REE are ambiguous on that point but isotopic results (Chapter 4) also indicate no significant gneissic contamination. The dolomitic melt appears to have separated from and equilibrated with a different silicate melt than has the sövite melt(s). The dolomitic melt ascended to its present level through a conduit removed (across the Snare fault) from that employed by sövites and their associated silicates. No alkaline silicate intrusive rocks which might be associated with the dolomitic carbonatites are presently exposed, but it must be inferred that processes similar to those which generated the sövites also generated the dolomitic rocks.

The similarity of major element compositions of the sövites combined with the variability of trace element compositions and the lack of clear crystallisation trends is perhaps best explained by emplacement of similar but separate small carbonate magma pulses. The separate pulses could have had slightly variable initial compositions and have equilibrated to varying degrees with a variety of gneissic and intrusive wall rocks. There is

no evidence within the complex of a single large volume of carbonatite magma.

Separate, relatively small volumes of carbonate magma could have been produced from a carbonated nephelinitic melt by fractional crystallisation and liquid immiscibility. In a recent study of carbonate/silicate melt immiscibility Freestone and Hamilton (1980) found that the degree of immiscibility, the miscibility gap, is dependent upon composition, decreasing away from alkali-rich compositions. Carbonate/silicate melt separation is more likely in silic than in mafic melts. Immiscibility increases with increasing P_{CO_2} and with decreasing temperatures. In addition Freestone and Hamilton (1980) found that the composition of the carbonate phase becomes richer in CaO as the miscibility gap increases. That is, the tie-line between equilibrium silicate and carbonate melt compositions rotates towards more calcitic carbonate compositions as the miscibility gap decreases with increased P_{CO_2} or decreased temperature. The Big Spruce Lake sövites are postulated to have been generated by exsolution of carbonate melt from carbonated nephelinitic magma which had undergone extensive fractional crystallisation during ascent from a mantle source region. There is field evidence (Chapter 2) for the presence of multiple magma pulses within the foyaite-

ijolite intrusive centre. If individual parent melt pulses were slightly variable in composition (major and trace elements) and in volatile content, then fractional crystallisation would follow slightly different paths to reach saturation in carbonate content. Exsolution of individual batches of carbonate melt from silicate melts under varying conditions of temperature and pressure could account for variable sövite compositions. Differences upon exsolution could be later enhanced by (partial) equilibration with different wall rocks.

The Fe- and Mg-rich nature of the separate dolomitic carbonatite suggests that it may be the product of fractional crystallisation of a large body of carbonate melt which crystallised at depth.

G. Intrusive Centre 5 - Satellite Intrusion

The shonkinites and biotite pyroxenites of the satellite intrusion show strong geochemical coherence which corresponds to petrographic similarities. The data also show significant differences between individual exposures which are geographically related or even adjacent.

Complete analyses (37 elements) of five samples are presented in Appendix 3, page 406, XRF analyses (17

elements) of four others are presented in Appendix 3, page 407. Normative compositions are presented in Table 15. Samples were analysed in which the degree of visible gneissic assimilation (significant in many outcrops) is considered negligible. Data from Martineau (1970) were not included in plots for this intrusive centre because they could not be assessed for contamination.

1. Compositional Variations

All but one of the samples analysed are nepheline or leucite normative, slightly undersaturated. The one hypersthene normative sample, PC-81-063, is sheared and has low total alkali.

The rocks of the satellite intrusion are similar to the shonkinites of the Highwood Mountains, Montana (Hurlburt, 1939; Nash and Wilkinson, 1970, 1971). They have similarities to the mildly undersaturated, orenditic group of Sahama (1974) in having high K and Mg and enrichment of Ti and P. The characteristic alkali excess over Al of the orenditic group is found together with a high Ba/Sr ratio (1.2 to 4.2) and enrichment of Zr and Cr. The rocks of the satellite intrusion differ from the typical orenditic rocks described by Sahama (from Fitzroy Basin, W. Austr., from S.E. Spain and from Leucite Hills, Wyoming) in having lower total alkali (and silica) and

Table 15. CIPW normative compositions of samples from the satellite intrusion.

	PC-81-057 ¹	PC-81-061 ²	PC-81-388 ¹	PC-82-260 ¹	PC-82-278 ²	PC-81-053 ¹	PC-81-063 ²	PC-81-064 ²	PC-82-535 ¹
Q									
Or	25.3	10.5	8.7	25.6	6.5	19.9	10.0	6.6	26.3
Ab	15.3			24.4	3.6	2.8	3.0		12.3
An	3.4		3.0	4.5	2.8	1.7	4.5	0.4	1.5
Lc		4.7	4.6					5.6	
Ne	3.0	3.1	1.6	1.5	1.6	4.5		4.1	2.6
C									
Ac		0.1							
Wo	15.0	25.1	24.1	12.1	27.8	21.4	21.4	27.0	18.0
Di	10.2	16.9	17.1	8.0	18.2	14.4	14.8	18.3	12.4
Fs	3.6	6.2	4.9	3.2	7.6	5.3	4.8	6.6	4.1
Wo									
En							3.7		
Fs							1.2		
Po	6.7	8.5	11.5	5.5	6.0	6.6	8.3	6.6	5.1
Fa	2.6	3.4	3.6	2.5	2.8	2.7	3.0	2.7	1.9
Mt	6.8	9.6	9.1	6.2	11.0	8.8	10.5	9.7	6.8
He									
Il	4.4	5.5	5.6	4.1	7.3	6.0	7.9	6.3	4.9
Ap	1.5	4.8	3.4	1.4	3.0	3.9	3.8	4.0	2.1
Cc									
MMet ³									

¹Shonkinite.²Biotite pyroxenite.³MMet = Na₂O·SiO₂

higher Ca, Mg and Fe. The silica content varies from 39 to 52% and over that range the major elements show well-constrained trends. The field for gneissic compositions is included on the Harker diagrams of Figures 59 and 60 to illustrate possible mixing (contamination) lines. It is evident that effects of contamination by gneisses cannot be discerned on most of these major element plots because mixing lines would be close to the intrusive trend. Mixing of a low silica intrusive with gneiss might show scatter of Na and K to higher SiO_2 , but none is readily apparent for the samples analysed. Biotite pyroxenites are widely dispersed in the field but form a tight compositional field at low SiO_2 . Compositions of various shonkinites with widely variable modal pyroxene, biotite and olivine plot to higher SiO_2 abundances along well-defined trends. Correlation of whole rock compositions to sample locations (shown in Figure 3) indicates the discrete nature of individual exposures. In the southeast section of the area shonkinite (PC-81-053) lies adjacent to olivine shonkinite (PC-81-057) and the two lie between biotite pyroxenites (PC-81-061 and 063). In the northwest section, the nearest outcrop to biotite shonkinite PC-81-388 (45% pyroxene, 45% biotite) is olivine shonkinite; PC-82-260. Nearby is a very low-K biotite pyroxenite, PC-82-278 (80% pyroxene). The most northerly

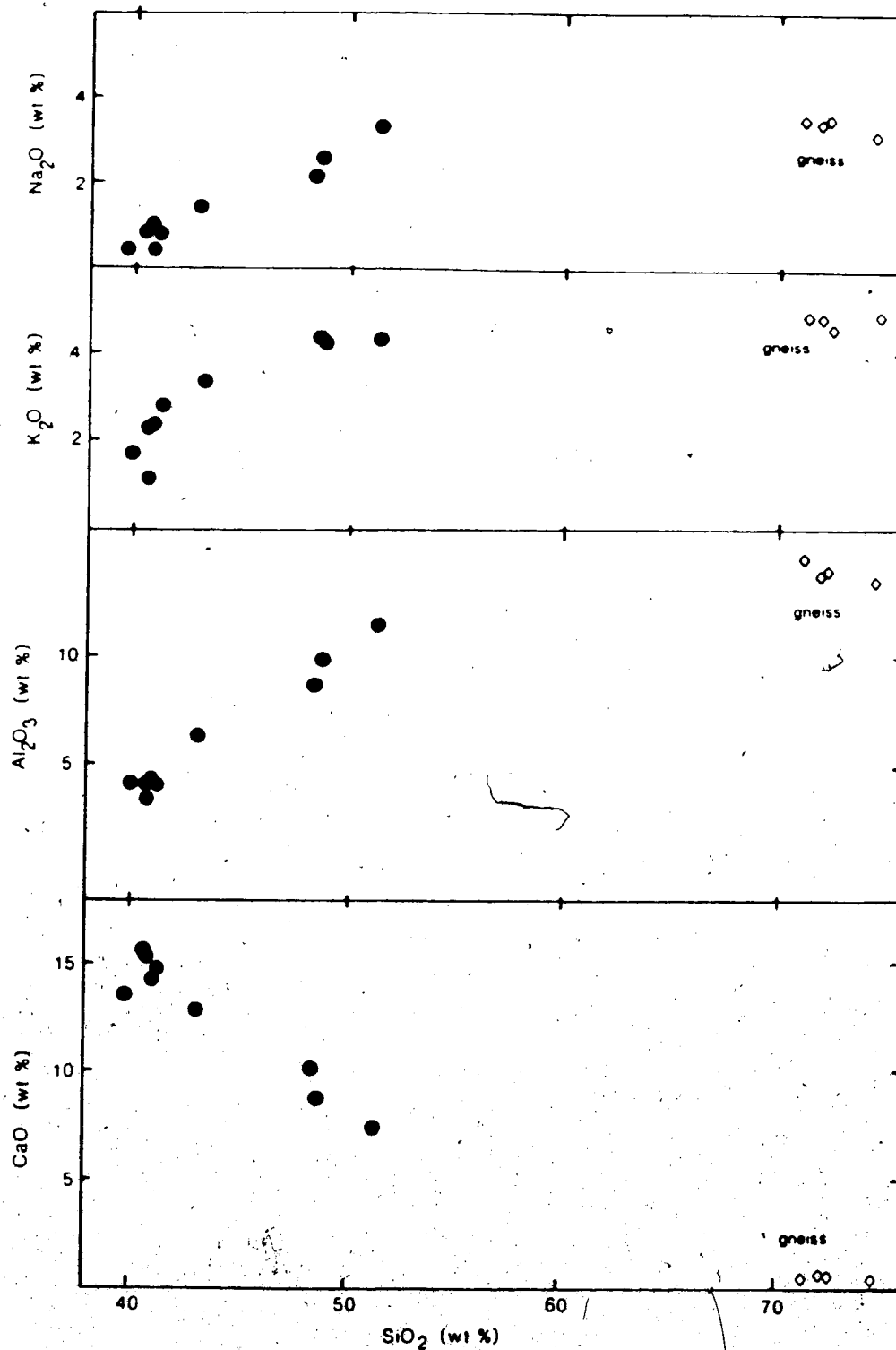


Figure 59. Harker diagrams of CaO, Al₂O₃, K₂O and Na₂O in biotite pyroxenites and shonkinites of the satellite intrusion.

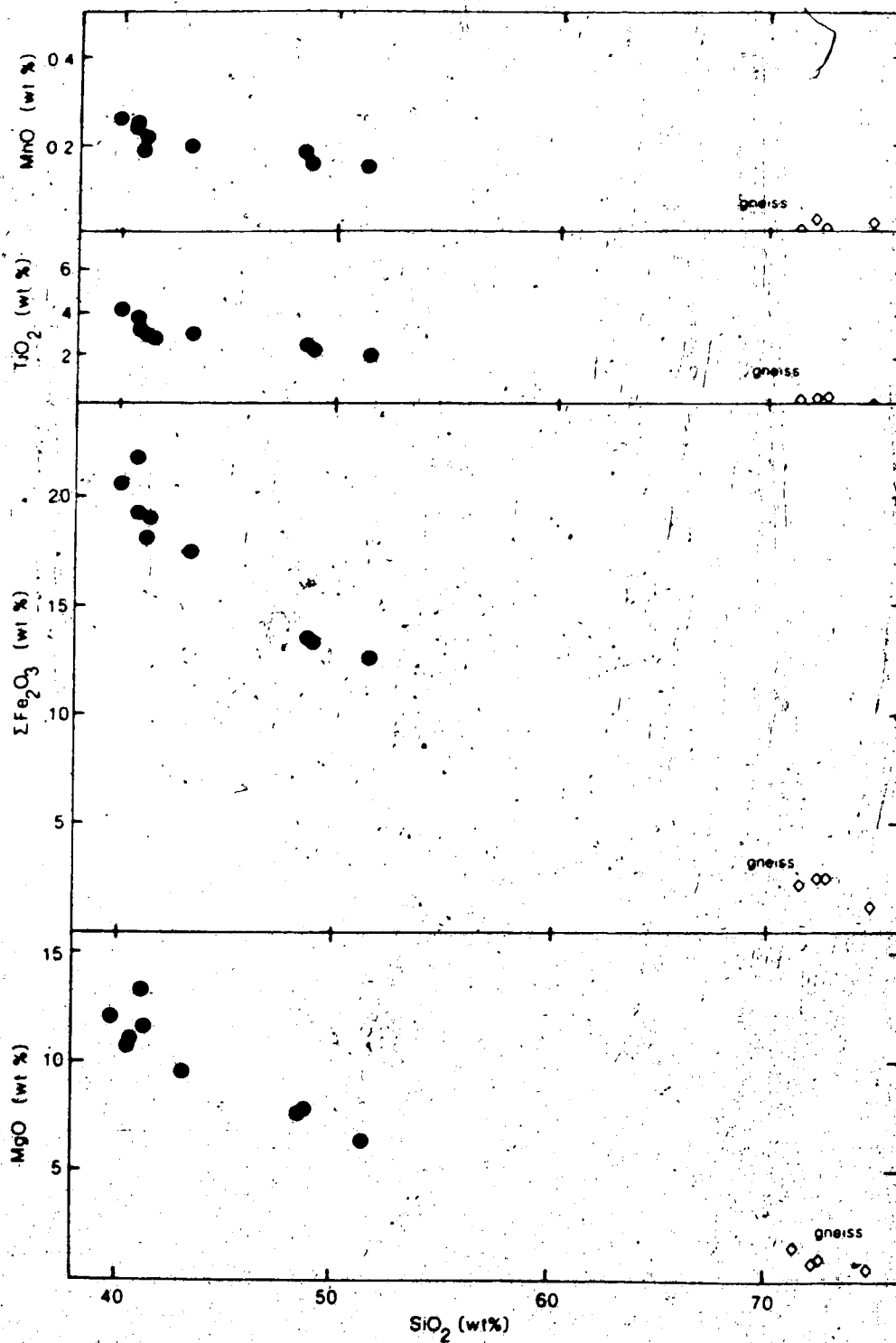


Figure 60. Harker diagrams of MgO , $\Sigma\text{Fe}_2\text{O}_3$, TiO_2 and MnO in shonkinites and biotite pyroxenites of the satellite intrusion.

sample analysed, shonkinite PC-82-535, is closely related geochemically to the southern olivine shonkinite PC-81-057.

The coherence as a group coupled with the discrete nature of individual small exposures is in agreement with the model outlined earlier, of a single parent body at depth producing separate upward extensions so that the present surface reveals both interfingering of different compositions and geographic separation of similar compositions.

The apparent major element trends on silica variation plots reflect the varying modal abundances of the three main phases: pyroxene (titanaugite-augite-hedenbergite), alkali feldspar and biotite. Olivine is a very minor phase in the more silica-rich shonkinites. Variable abundances of Fe-Ti oxides account for scatter in Fe and Ti among the pyroxenites. Magnesium numbers ($Mg/Mg + Fe^{2+}$, atomic ratios) vary from 0.45 to 0.70.

Abundances of K and Na both increase with SiO_2 content in this series, but in very different trends. The Na_2O increases at a constant rate, while K_2O increases rapidly from 1.5 to 3% over a SiO_2 range of 39-42%, then more slowly (Figure 59). Of the incompatible elements Rb, Zr, Hf, Nb and Ta increase in the same manner as K (Figure 61).

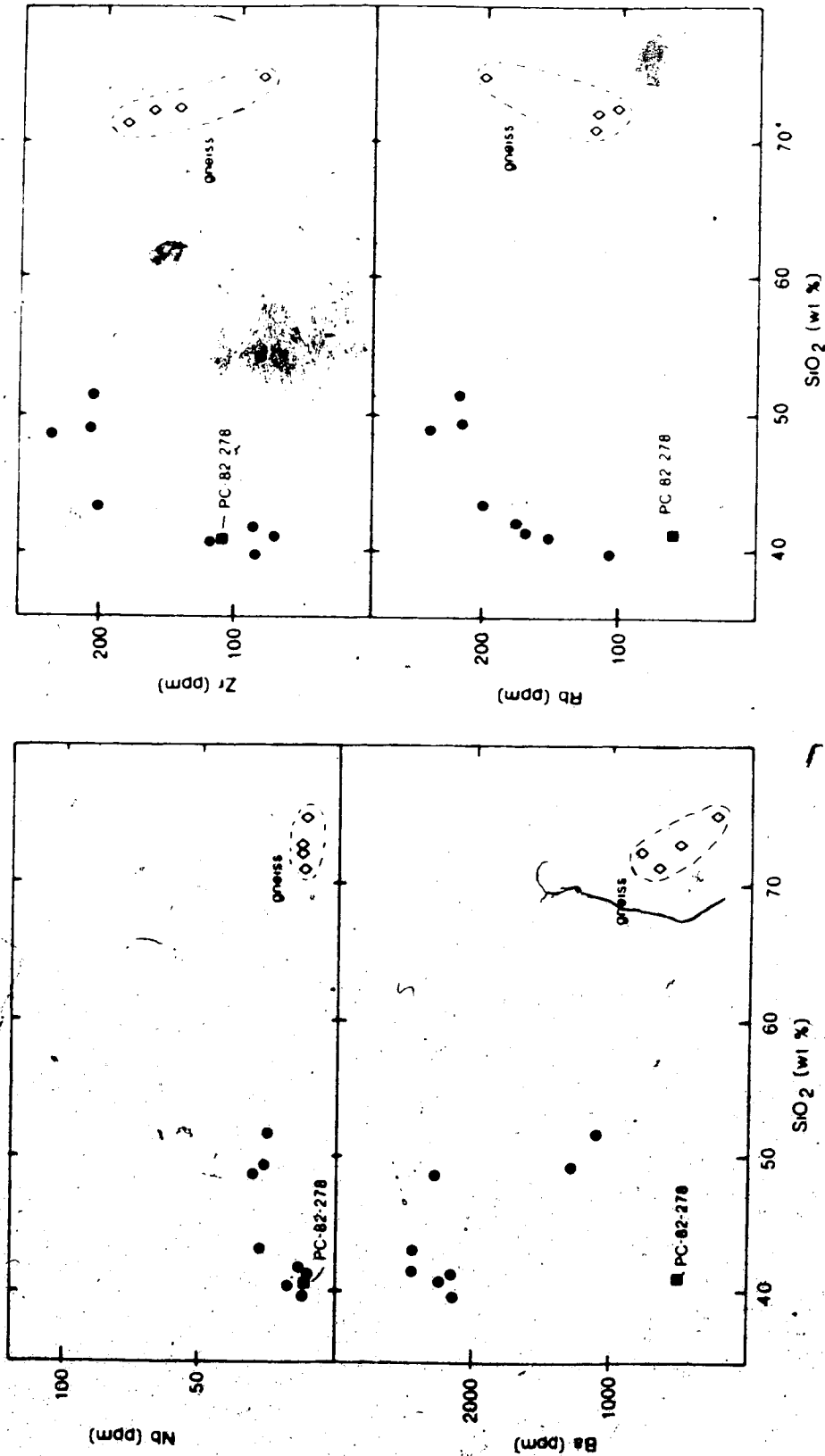


Figure 61. Harker diagrams of Nb, Ba, Zr and Rb in shonkinites and biotite pyroxenites of the satellite intrusion.

A logarithmic plot of Rb vs K_2O shows an excellent correlation between the two elements (Figure 62). The linear trend produces K/Rb varying from 112 at the low silica end to 160 at the high silica end. Increasing modal biotite with decreasing silica content accounts for the K/Rb variation. All of the K/Rb ratios are lower than those of the gabbro or foyaite series (K/Rb range ~175 to 400).

In contrast to the other incompatible elements (Zr, Hf, Nb, Ta), the rare earth elements do not correlate well with silica content although in general ΣREE decreases with increasing silica. Apatite is present in all units in variable amounts (1.5 to 5% normative), most abundant in biotite pyroxenites and the total REE content is partly due to modal apatite. In addition to apatite and biotite the most REE-rich sample (PC-81-061) contains abundant sphene, another common host for REE.

Chondrite-normalised REE distribution plots (Figure 63) display no Eu anomalies ($Eu/Eu^* = 1.00$ to 1.06, Table 16). It is improbable that the variable modal abundancies of REE-bearing minerals would exactly balance in all samples to produce $Eu/Eu^* = 1$ if significant Eu^{2+} were present. The most reasonable explanation for the lack of Eu anomalies is the absence of significant amounts of Eu^{2+} during crystallisation due to high oxidising conditions.

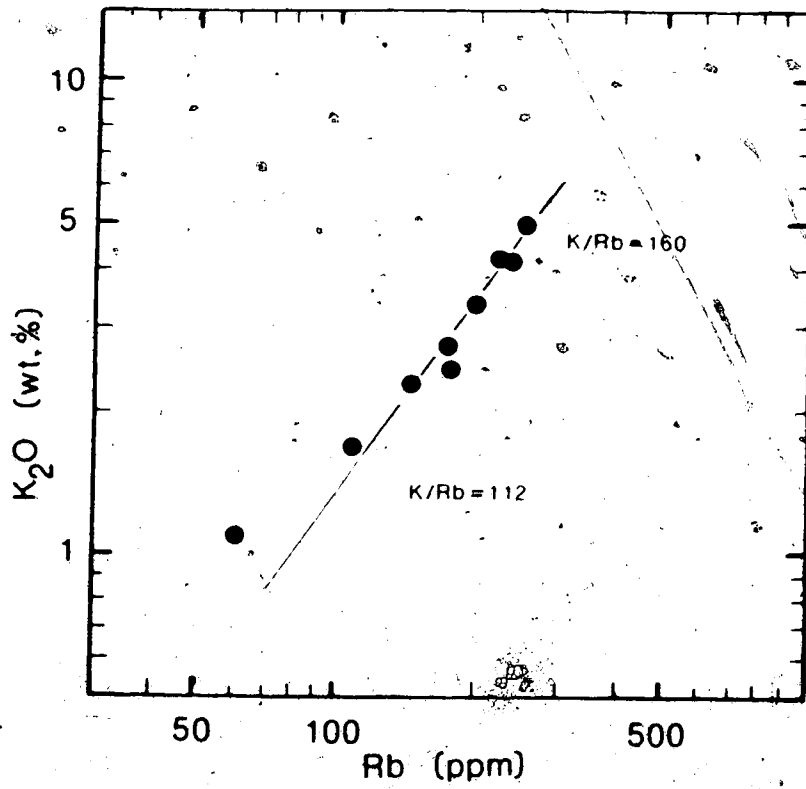


Figure 62. Rb vs K₂O in biotite pyroxenites and shonkinites of the satellite intrusion.

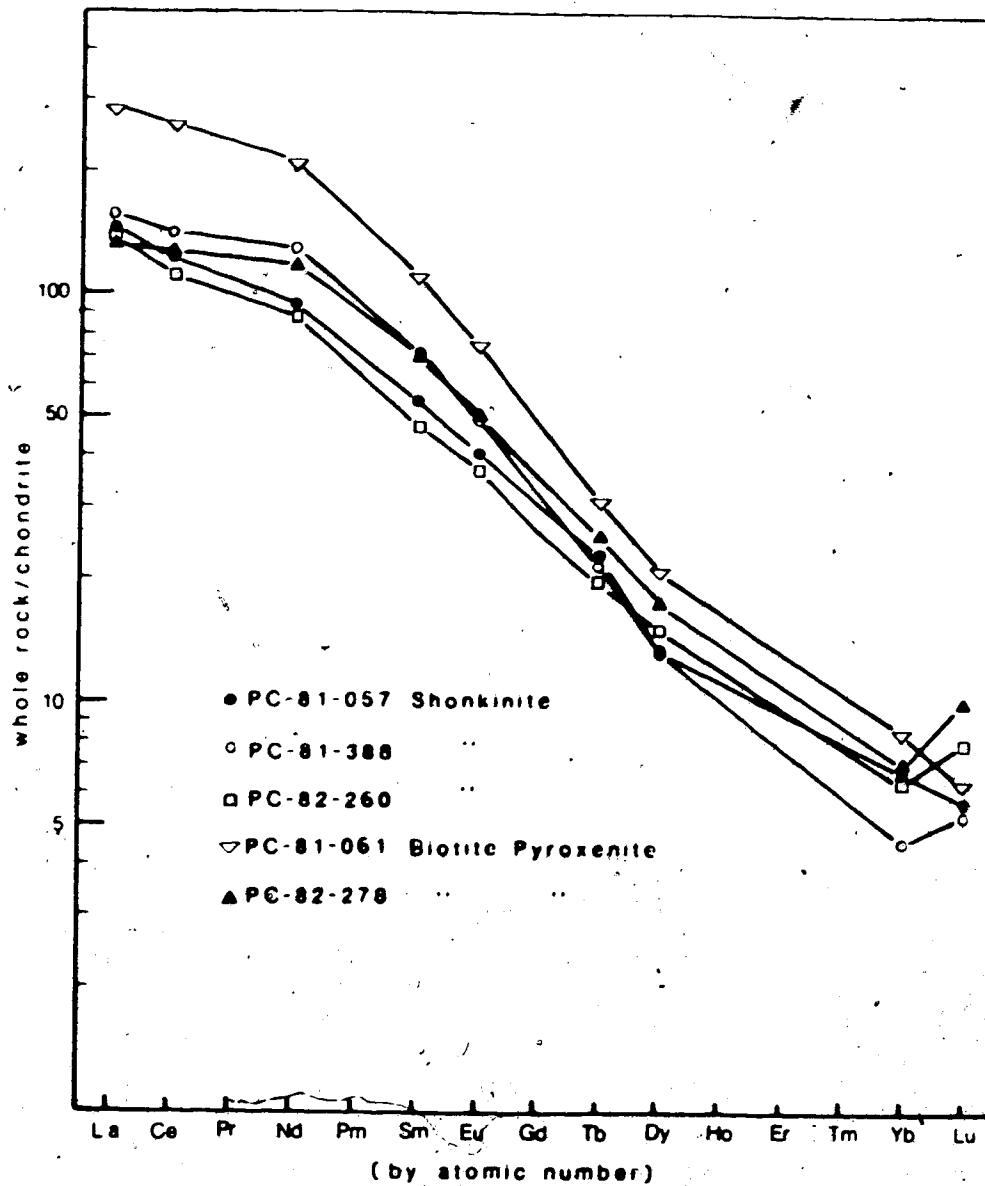


Figure 63. Chondrite-normalised (Nakamura, 1974) rare earth element distribution patterns for shonkinites and biotite pyroxenites of the satellite intrusion, Centre 5 of intrusive activity.

Table 16. Rare earth element data for satellite intrusion.

Sample Number and Type	Σ REE ¹	Eu/Eu* ² (ppm)	(Ce/Yb) _{CN} ³
PC-81-057 shonkinite	260	1.00	17.7
PC-81-061 biotite pyroxenite	539	1.00	30.0
PC-81-388 shonkinite	313	1.02	30.9
PC-82-260 shonkinite	241	1.06	17.6
PC-82-278 biotite pyroxenite	278	1.00	18.1

¹Includes values interpolated from Figure 63 for elements not analysed.

²Eu* interpolated between Sm and Tb on chondrite normalised plots. Eu is analysed value.

³CN = chondrite-normalised values.

The lowest Σ REE (240 ppm in shonkinite) is at the same level as that of mafic syenites of the gabbro series or the chill zone of the foyaite suite. All of the REE distribution patterns are slightly concave-down and yet $(\text{Ce}/\text{Yb})_{\text{CN}}$ is higher in all samples from the satellite intrusion (17.6 to 31) than in the gabbro-syenite series (13 to 18), a difference intrinsic to melt compositions. A similar concave-down REE distribution pattern was reported by Nash and Wilkinson (1971) for the shonkinites of the Highwood Mountains, Montana. Although only LREE were determined in that study, the total REE content is estimated to be similar to those found for Big Spruce Lake shonkinites.

There is no clear trend of LREE/HREE fractionation with total enrichment but the degree of fractionation in the parent melt can be estimated. It can be reasonably inferred that the total REE content of individual samples is dependent upon modal mineralogy which is affected by minor crystal accumulation. The phenocryst nature of pyroxene and biotite supports this inference. Minor accumulation of biotite and apatite rather than pyroxene would result in $(\text{Ce}/\text{Yb})_{\text{CN}}$ closer to that of the original liquid than if pyroxene accumulated (see Figures 16 and 18 for distribution coefficients of these minerals). The two REE-poor samples (PC-81-057 and PC-82-260) have the lower

(Ce/Yb)_{CN} values. These two rocks are both biotite-poor, pyroxene-rich shonkinites while the two REE-rich samples, PC-81-061 and PC-81-388, have higher biotite/pyroxene ratios and slightly more abundant apatite. Accumulation of pyroxene reduces (Ce/Yb)_{CN} hence the higher ratio, 30 to 31, in pyroxene-poor samples, is probably close to that of the original melt. No evidence has been found of accessory minerals such as allanite whose presence could raise the (Ce/Yb)_{CN} ratio.

One sample (PC-82-278) from a newly-exposed biotite pyroxenite outcrop has a slightly anomalous REE distribution pattern. The (Ce/Yb)_{CN} ratio is 18.1 for this sample, very similar to those of the two REE-poor shonkinites but in this case the ratio is meaningless as a parameter to indicate fractionation of REE. La and Ce are much depleted in this sample, while the middle to heavy REE are enriched and strongly fractionated in a pattern reminiscent of those for magnetite pyroxenites of Centre 1. The low La and Ce abundances found for this biotite-rich sample were confirmed by analysis of a second aliquot, employing an alternative INAA scheme (a different detector and a different γ energy were used) as well as the regular scheme.

On mantle-normalised LILE distribution plots (Figures 64 and 65), all samples have a pronounced fractionation trend from low Y (5 to 7 times mantle abundances) to high Cs (200-500 times mantle abundances). All samples thus show increased abundances of the LILE as well as increased fractionation over that of the gabbro series (Figures 20 to 24). Y_{MN} ranges from 2 to 10 in the gabbro-syenite series, similar to values for the potassic suite. The more incompatible elements are much more enriched in the potassic suite than in the gabbros. The difference in incompatible element enrichment trends of the two series is most readily observed by a comparison of the mantle-normalised LILE plots for most enriched quartz syenites (Figures 23 and 24) with those of the potassic rocks.

Similarities and differences in the mantle normalised profiles of samples from the potassic suite are notable. Cs, Rb, Ba and REE are all enriched relative to Nb, Ta, Zr and Hf. The two biotite- and apatite-rich samples with highest Σ REE (Figure 64) have positive Ba anomalies and strongly negative Th and U (not seen in the other three samples, Figure 65). Negative strontium anomalies are present in all plots as are positive P and Ti anomalies.

By comparison of Figures 64 and 65 with the mantle-normalised profiles of gneisses presented earlier (Figure 27), relative abundances of Rb, Cs, Zr and Nb are most

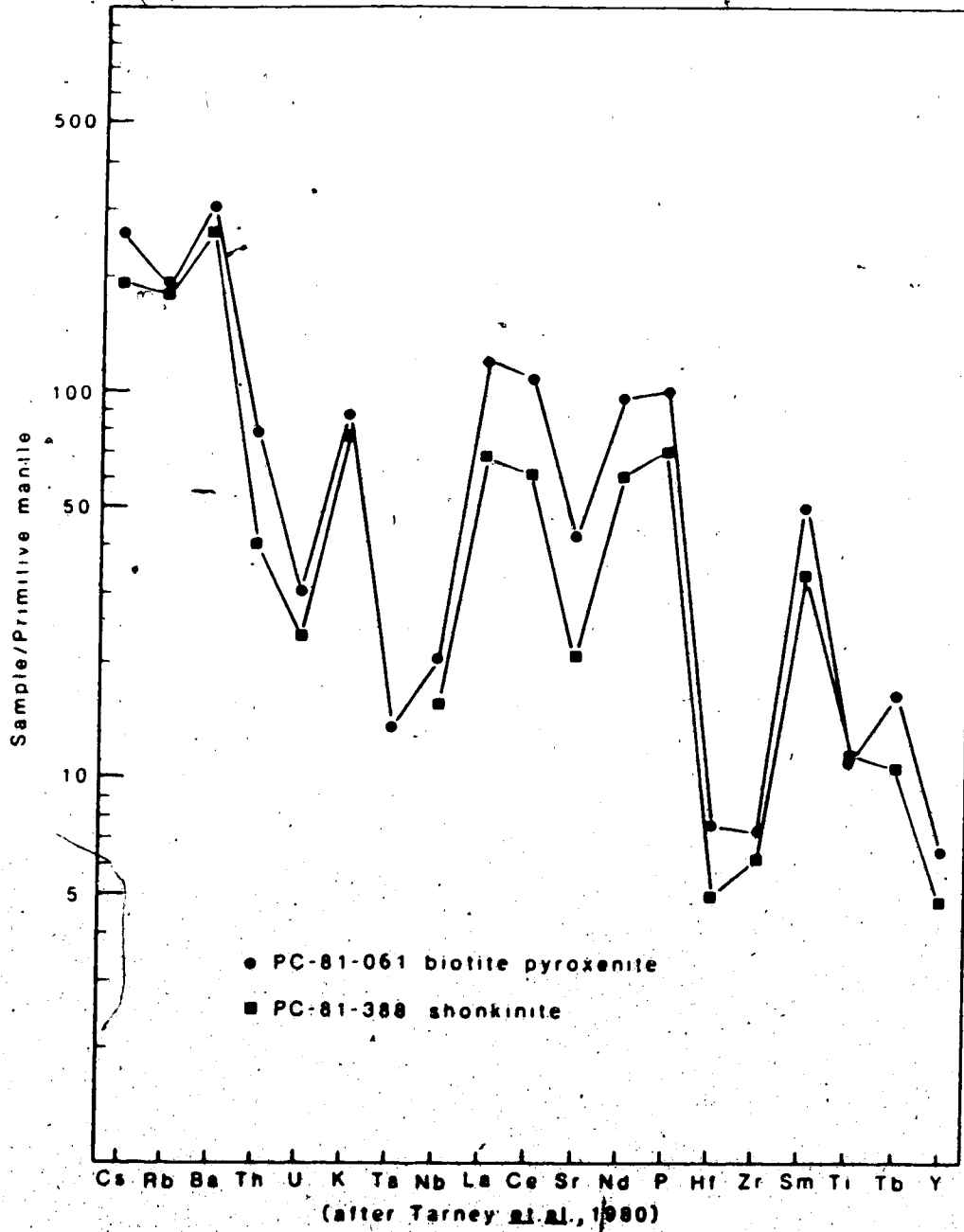


Figure 64: Mantle-normalised LILE distribution plots for Ba-enriched shonkinite and biotite pyroxenite from the satellite intrusion.

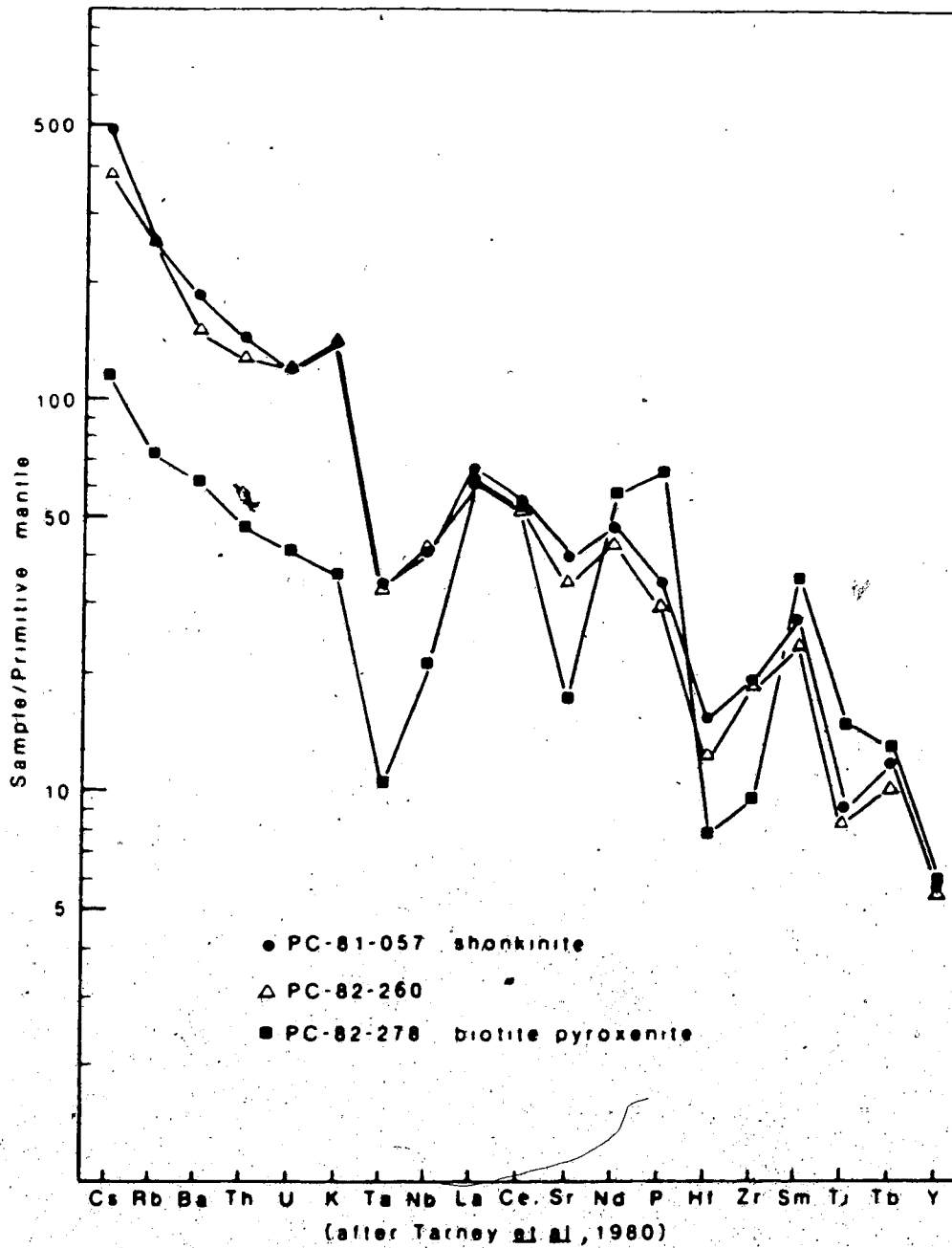


Figure 65. Mantle-normalised LILE distribution plots for alkali-enriched shonkinites and biotite pyroxenites from the satellite intrusion. Note the alkali depletion of sample PC-82-278 relative to the others.

likely to indicate gneissic assimilation. The logarithmic two-element plots of Figure 66 show that no systematic mixing lines exist between the potassic intrusive trend and gneissic compositions. What is emphasised by these plots, however, is the discordant position of biotite pyroxenite PC-82-278. This sample is not significantly contaminated by granodioritic gneiss. Both Rb and Cs are depleted relative to Zr in this sample and Cs is further depleted relative to Rb. Therefore, the alkali composition of this sample moves further away from the gneissic field than the intrusive trend. On the silica variation diagrams of Figure 61, it is apparent that Rb and Ba are strongly depleted in this sample. The Zr and Nb are not, however, and the composition does not tend towards the gneissic field. This sample also shows the LREE depletion/HREE enrichment discussed earlier along with a slight enrichment in $\Sigma\text{Fe}_2\text{O}_3$ and TiO_2 . This body lies almost directly above the inferred location of the parent body, and contamination by a Fe-Ti enriched, alkali- and LREE-depleted source may have been achieved by assimilation of a mantle xenolith (alkali-deficient ultramafic) carried from depth. Data from this sample must be omitted from consideration of any parent liquid composition.

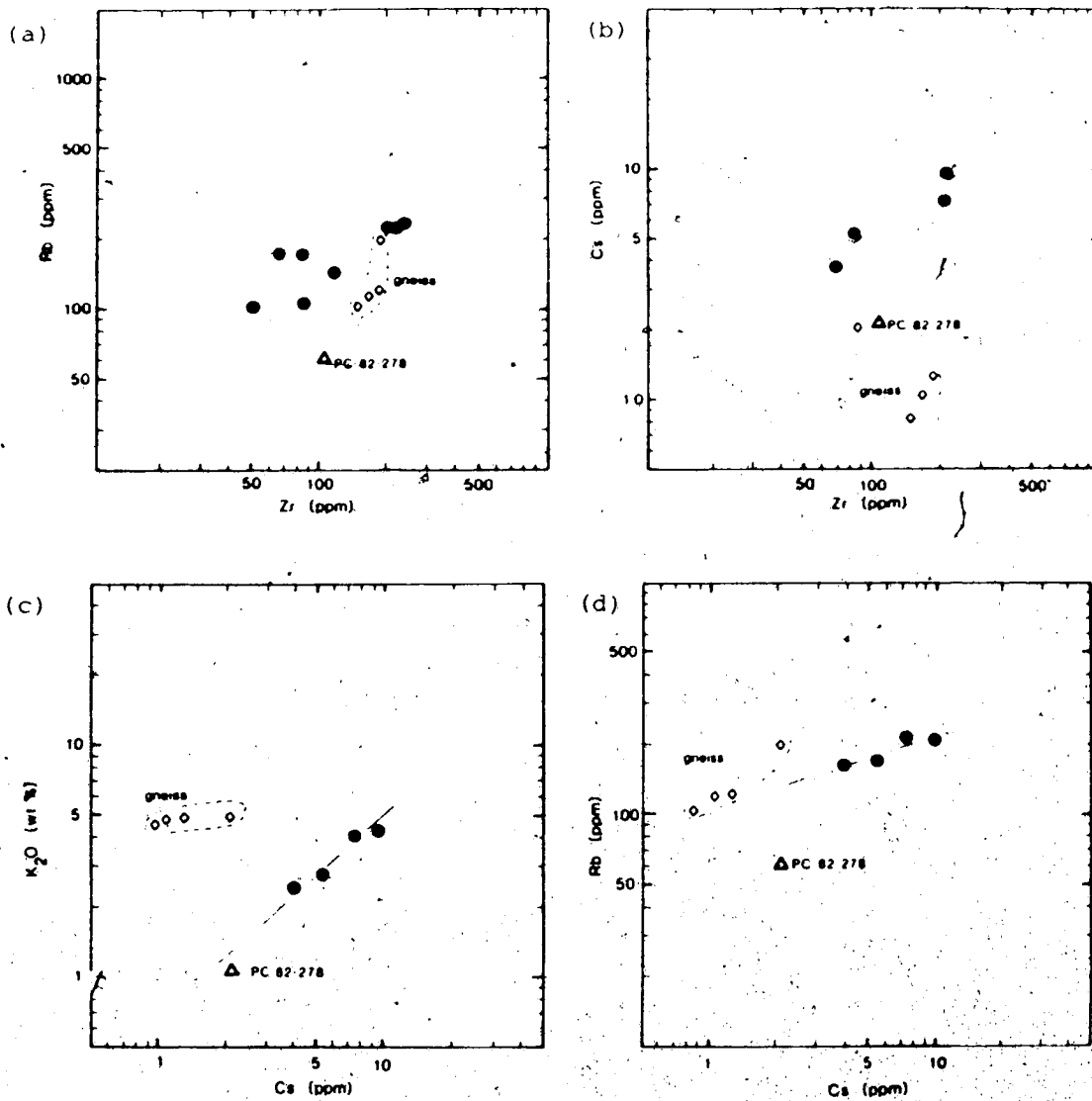


Figure 66. Logarithmic plots of (a) Zr vs Rb, (b) Zr vs Cs, (c) Cs vs K₂O and (d) Cs vs Rb in rocks of the satellite intrusion and in granodiorites. Note that PC-82-278 does not appear to be contaminated by granodiorite.

2. Parent Magma

A parent liquid composition with respect to alkalis (Cs, Rb, Ba, K), the rare earth elements and Y cannot be derived because of variable modal abundances of major and accessory minerals which incorporate these elements (biotite, pyroxene, apatite, sphene). Because Zr (Hf), Nb (Ta), U and Th are largely hygromagmatophile elements throughout the series, their relative abundances, in a possible parent melt can be approximated for comparison with those of the alkali-gabbro parent liquid. Omission of the (possibly) contaminated sample, PC-82-278, from the approximations leaves insufficient data for extrapolation of the Ta vs Zr plot. Extrapolation of logarithmic two-element plots vs Zr, to Zr = 11 ppm (Figure 67) produces the following results (Table 17).

These results suggest a fractionation pattern, Th being much enriched over Zr, but do not show the internal consistency of the extrapolated composition of the alkali gabbro parent melt. The extrapolated Th value is very uncertain and could be as low as 0.38 ppm, leading to a parent liquid/mantle ratio as low as 4.0. Complete trace element analyses of several more samples will be necessary to more closely approximate the parent liquid composition.

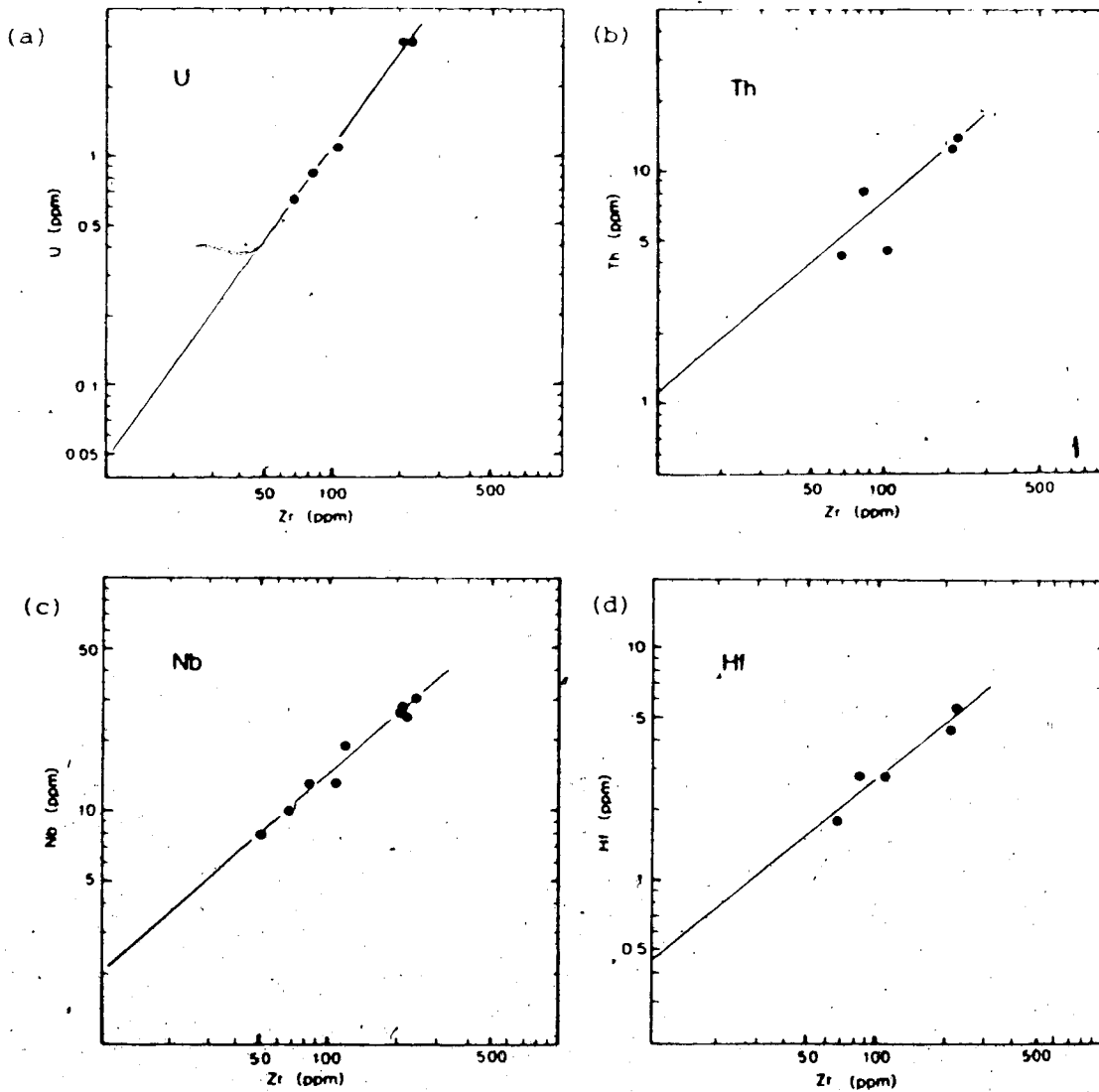


Figure 67. Plots of Zr vs U, Th, Nb and Hf in the biotite pyroxenites and shonkinites of the satellite intrusion from which relative abundances in parent melt can be extrapolated (at Zr = 11 ppm). Extrapolated values are given on page 234.

Table 17. Relative abundances of incompatible elements in parent liquid of the satellite intrusion.

Element	Abundance in Melt at Zr=11 ppm	Primordial Mantle Abundance ¹ ppm	Melt Abundance/ Primordial Mantle ppm
Th	1.2	0.096	12.5
U	0.052	0.027	1.9
Nb	2.25	0.62	3.6
Hf	0.48	0.36	1.3
Zr	11	11	1.0

¹From Tarney et al (1980).

3. Summary and Discussion

Field evidence suggests that the present erosion surface represents the uppermost level reached during emplacement of the satellite intrusion. The low Mg numbers (0.45 to 0.70) suggest that significant fractionation had occurred prior to magma emplacement at the present level. Olivine was probably the main early fractionating phase (Edgar et al, 1976; Edgar and Condliffe, 1978).

The presently observed compositional range of major and trace elements is attributed to variations in modal abundances rather than to a differentiation sequence.

The magma emplaced was silica-undersaturated and LILE-enriched. Although the composition of the parent magma cannot be quantified at present a pattern of $Cs > Rb \gg K$ and $LREE > HREE$, (with REE absolute abundances close to those of mafic syenites of Centre 1) is clearly evident from the LILE and REE distribution plots. If one compares the alkali, Cr and Sc enrichment and the $(Ce/Yb)_{CN}$ of the potassic satellite intrusion with those for the sodic gabbro-syenite series of intrusive Centres 1 and 2, the source magmas are distinctly different. One was not derived from the other through differentiation.

Possible sources of a potassic-magma, distinct from the sodic melts which were responsible for the main complex are:

- (1) Assimilation of a potassium and LILE-enriched crustal component by a mantle derived magma.
- (2) Partial melting of a discrete potassium- and LILE-enriched mantle source region.
- (3) Mixing of a potassium- and LILE-rich mantle component with a melt formed from a primitive mantle.

Minor assimilation of the presently-exposed granodioritic host rock is evident in the partially absorbed gneissic xenoliths present in many outcrops; however, such contamination does not fully account for the parent melt composition derived here. This conclusion is supported by the high concentrations of incompatible and semi-compatible elements in the potassic intrusive suite. Cesium, Ba and Rb are more abundant in the potassic intrusive rocks than in the country rock or in the alkali basalt parent magma, and more abundant than in the most differentiated quartz syenites of Centre 2. Similarly, semi-compatible elements such as Co, Cr and Sc are higher in the potassic suite than in gneisses or in the gabbro-syenite series. Total REE in the potassic rocks ranges from 250 to 500 ppm, equivalent to the abundances in mafic syenites (semi-compatible depleted) and greater than the gneisses (90 to 225 ppm). Fractionation of LREE/HREE is much greater in the potassic suite with $(Ce/Yb)_{CN}$ estimated at ~30 compared to 10 to 20

in both gneisses and in the gabbro-syenite series. Clearly the potassic melt of the satellite complex cannot be the result of simple mixing of an alkali basalt melt or even mafic syenite with host granodiorite. Production of the enriched melt by zone refining, ascent of a basaltic melt through enriched crustal rocks, is precluded by the fact that zone refining would require large volumes of crust to interact with the magma with concomitant increase in element abundances before any significant change in element ratios occurs (Hanson, 1977). The Σ REE, $(\text{Ce}/\text{Yb})_{\text{CN}}$ and Cs or Rb/Y results discussed above provide evidence against zone refining producing the potassic rocks.

A mantle origin for the satellite intrusion (possibilities 2 and 3 above) is thus clearly indicated; however, the processes which may have been involved are dependent upon the temporal as well as spatial relationship of this intrusion to the main complex. For this reason further discussion is deferred, to follow geochronological interpretation of isotopic results.

CHAPTER 4

ISOTOPE GEOCHEMISTRY

A. Introduction

Previous isotope studies of the Big Spruce Lake intrusion have included K-Ar dating of biotite and a WR Rb-Sr study.

K-Ar on biotite from mafic foyaitite/ijolite on Big Spruce Island in the main complex gave a date of 1785 Ma (Leech et al., 1963), which was initially interpreted as the age of the complex. Biotite from sövites (also from the main complex) gave dates of 1810 ± 22 Ma and 1835 ± 32 Ma (R. St. J. Lambert, pers. comm. in Martineau, 1970). These dates were also interpreted as the age of the complex (Martineau, 1970) and intrusive activity was considered to be related to the formation of the Bear structural province.

WR Rb-Sr data reported by Martineau and Lambert (1974) gave an age of 2184 ± 40 Ma for the main complex and 1980 ± 40 Ma for the satellite intrusion (recalculated to $\lambda^{87}\text{Rb} = 1.42 \times 10^{-11} \text{ yr}^{-1}$). The former date was interpreted as the actual age of intrusion of the main complex, the K-Ar system having been reset by mild

metamorphism at about 1800 Ma. No initial ratio was reported and it was noted (R.St.J. Lambert, pers. comm., 1980) that the data were scattered. Martineau (1970) reported measured $^{87}\text{Sr}/^{86}\text{Sr}$ of 0.7021 ± 24 and 0.7024 ± 24 for non-magnetic separates from syenites of the main complex (low Rb) and interpreted these low values as mantle-derived initial ratios. Scatter in the Rb-Sr data was attributed to variable initial ratios, metasomatism, and to analytical error due to high Sr and low Rb contents in these rocks.

• In the present study four radiogenic systems have been examined in whole rock samples from the main and satellite intrusions; Rb-Sr, Pb-Pb, Nd-Sm and U-Th-Pb. In addition, the U-Pb system has been studied in zircons separated from the syenites of Centre 2. A major objective of this isotopic study is determination of the geochronologic relationships between the various units and an attempt has been made to obtain an age for each unit and thus determine the time span of igneous activity. The other basic objectives of the isotopic study deal with the petrogenesis of the complex. From the initial Sr, Nd and Pb ratios obtained here the source (crustal or mantle) of the various magma types has been inferred, an assessment has been made of the degree of crustal contamination and/or metasomatic activity which may have affected any

mantle-derived initial ratios and finally the mantle source which lay beneath the Slave craton at about 2200 Ma has been characterised in terms of Nd, Sr and Pb isotopic compositions.

B. Samples and Analytical Methods

All of the samples analysed for isotopic compositions have been analysed for element composition and are described in this section (see Appendix 1). Zircon samples are described in Cavell and Baadsgaard (1986). The analytical methods for Rb-Sr, whole rock Pb-Pb and U-Pb zircons are described in Chaplin (1981). The Sm-Nd method is described in detail in Cavell and Baadsgaard (1986).

C. Geochronology of the Complex

The geochronology of the complex has been reported and discussed in Cavell and Baadsgaard (1986). This paper is an integral part of the study. The following is an abstract (Figure 68) of that report which is reproduced in its entirety as Appendix 4.

ABSTRACT

A zircon age of $2188 \pm 16/-10$ Ma has been determined for the silica-saturated syenites of the Big Spruce Lake alkaline complex. A whole-rock Pb-Pb age of $2165 \pm 21/-22$ Ma was obtained for the silica-undersaturated rocks of the complex, and 2155 ± 16 for the complex as a whole. The Sm-Nd whole-rock data yield an age of 2183 ± 75 Ma for the complex as a whole. Weighting the ages by the inverse square of the standard deviations, an average age for the complex of 2174 ± 20 Ma is determined. However, it is felt the zircon age is the most reliable for the time of crystallization of the complex. Minor contamination by country rock (Sm-Nd model ages of 2467 to 2595 Ma) and metasomatism contribute to scattered Sm-Nd data points and large errors in the ages obtained for the five individual units. The Pb-Pb data enable a limiting estimate of about 50 Ma for the maximum timespan for the intrusion of centres 1 to 4.

Figure 68. Abstract of "Geochronology of the Big Spruce Lake Alkaline intrusion" by P.A. Cavell and H. Baadsgaard. Canadian Journal of Earth Sciences. In press, 1986. Full text of this paper is reproduced in Appendix 4.

D. Rb-Sr Systematics

Because WR Rb-Sr had been measured previously, only a few samples were analysed to study variations in initial ratios in some of the same samples for which the Nd and Pb isotopic compositions had been determined. The data are discussed first with respect to geochronological applications to exemplify the problems which arise with the Rb-Sr system in this case.

Six syenites were chosen on the basis of XRF analyses to have the broadest range of Rb/Sr ratios for an isochron plot, and a possible initial ratio determination. The sample data are reported in Table 18 and presented on a standard isochron plot in Figure 69a. Least squares regression of the data, using a program based on York (1966), with $\lambda^{87}\text{Rb} = 1.42 \times 10^{-11} \text{yr}^{-1}$, yielded an age of $1857 \pm 132 \text{ Ma}$ (error quoted is $2\sigma/\text{MSWD}$) with an initial ratio of 0.70466 ± 10 (Table 19). The regression line is strongly controlled by the single data point at highest Rb/Sr, PC-82-096. A second aliquot of this sample was analysed and the initial results confirmed. Zircons from four of these six syenites were included in the set which yielded an age of $2188 \pm 16/-10 \text{ Ma}$, the emplacement age of the complex (Cavell and Baadsgaard, 1986).

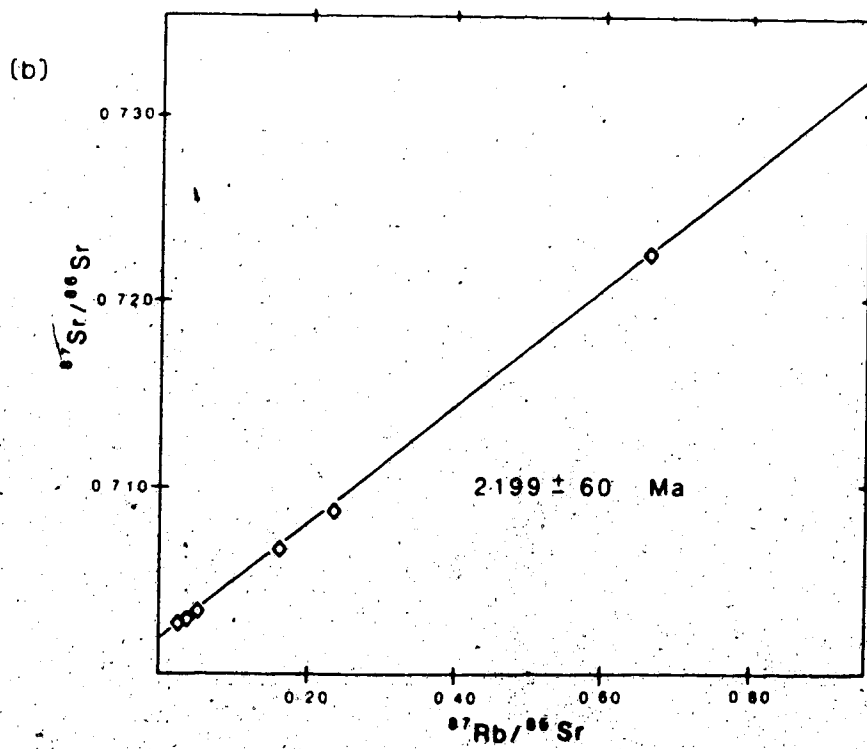
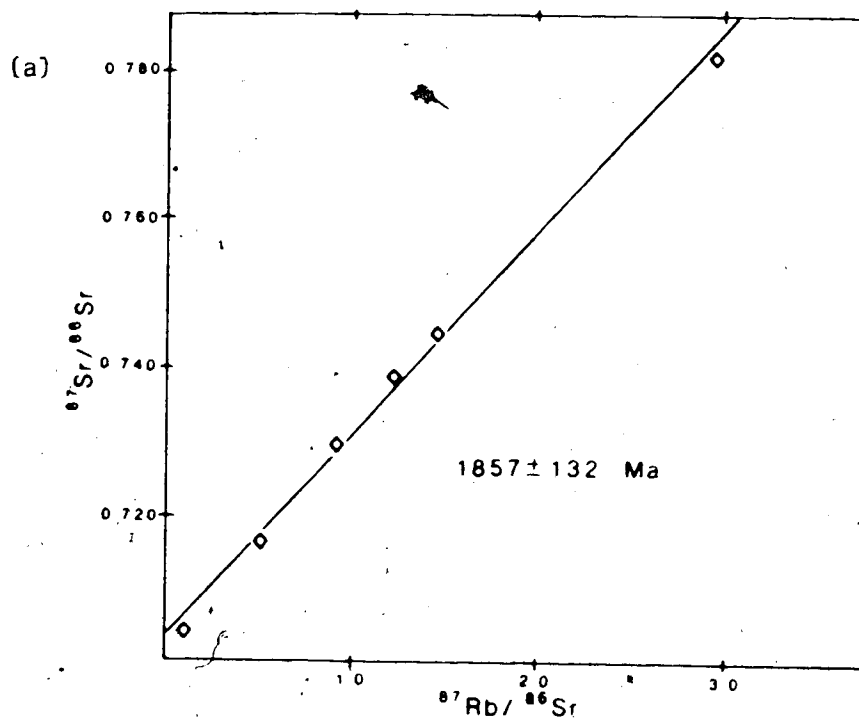


Figure 69. Rb-Sr results for WR samples from the Big Spruce Lake intrusion. (a) Syenites from Centre 2. (b) Gabbro, pyroxenite, foyaite and ijolite from Centres 1 and 3.

Table 18. Rb-Sr analytical results for silicates from the Big Spruce Lake intrusion.

Sample	Rb ¹ ppm	Sr ¹ ppm	⁸⁷ Rb/ ⁸⁶ Sr	⁸⁷ Sr/ ⁸⁶ Sr ¹ measured	⁸⁷ Sr/ ⁸⁶ Sr ² model initial
<u>Centre 1: gabbro, pyroxenite</u>					
PC-81-001	0.789	72.4	0.03036	0.702819	0.70186
PC-81-275	21.97	2357	0.02598	0.702755	0.70194
<u>Centre 2: syenite</u>					
PC-81-012	38.08	1353	0.07847	0.704755	0.70228
PC-81-285	107.4	613.8	0.48780	0.716640	0.70125
PC-81-364	128.6	404.3	0.88622	0.729514	0.70155
PC-82-096	92.6	87.5	2.9515	0.781144	0.68800
PC-82-151	114.2	220.1	1.4458	0.744369	0.69874
PC-82-358	126.3	289.5	1.2153	0.738839	0.70049
<u>Centre 3: foyaite, ijolite</u>					
PC-81-194	117.2	2097	0.15583	0.706337	0.70142
PC-81-482	158.0	1922	0.22909	0.708716	0.70149
PC-82-039	229.1	976.9	0.65371	0.722562	0.70193
PC-82-525	23.21	1309	0.04943	0.703323	0.70176
<u>Centre 5: shonkinite, biotite pyroxenite</u>					
PC-81-053	205.8	996.7	0.57560	0.718448	0.70028
PC-81-057	230.7	963.4	0.66755	0.721017	0.69995
PC-81-064	149.7	904.3	0.46126	0.716012	0.70146
PC-81-388	177.2	518.8	0.95211	0.728911	0.69887
PC-82-260	234.3	842.9	0.77490	0.723700	0.69925
PC-82-278	60.35	388.3	0.43323	0.714802	0.70113

¹ Estimated error on concentrations is $\pm 0.1\%$, on ⁸⁷Sr/⁸⁶Sr measurement error is ± 0.0001 .

² Model initial ratio calculated using $t = 2188$ Ma, $\lambda^{87}\text{Rb} = 1.42 \times 10^{-11} \text{yr}^{-1}$.

Table 19. Rb-Sr geochronological results.

Sample set	Number of Samples	Slope	Age Ma ¹	MSWD	⁸⁷ Sr/ ⁸⁶ Sr initial
Centre 1 & 3: gabbro, pyroxenite, foyaites	6	0.03172	2199±60	2.8	0.70170
Centre 2: syenites	6	0.02672	1857±132	4.74	0.70466
Centre 5: shonkinites, biotite pyroxenite	6	0.02659	1848±90	4.2	0.70335

¹Error quoted is $2\sigma/\text{MSWD}$.

Two samples from Centre 1 (gabbro and pyroxenite) and four from Centre 3 (foyaite and ijolite) were analysed and the data are included in Table 18. Regression of data for these six samples, combined in an isochron plot in Figure 69b, produced a date of 2199 ± 60 Ma, within error of the age of 2188 Ma.

Rb-Sr analytical results for six samples from the satellite intrusion, included in Table 18, are plotted in Figure 70. Regression of these data produced a date of 1848 ± 90 Ma; omission of sample PC-82-278, which might be contaminated (see Chapter 3) produced an even younger date of 1840 ± 122 Ma. The large errors allow these dates to overlap with the Rb-Sr date of 1980 ± 40 Ma reported by Martineau and Lambert (1974).

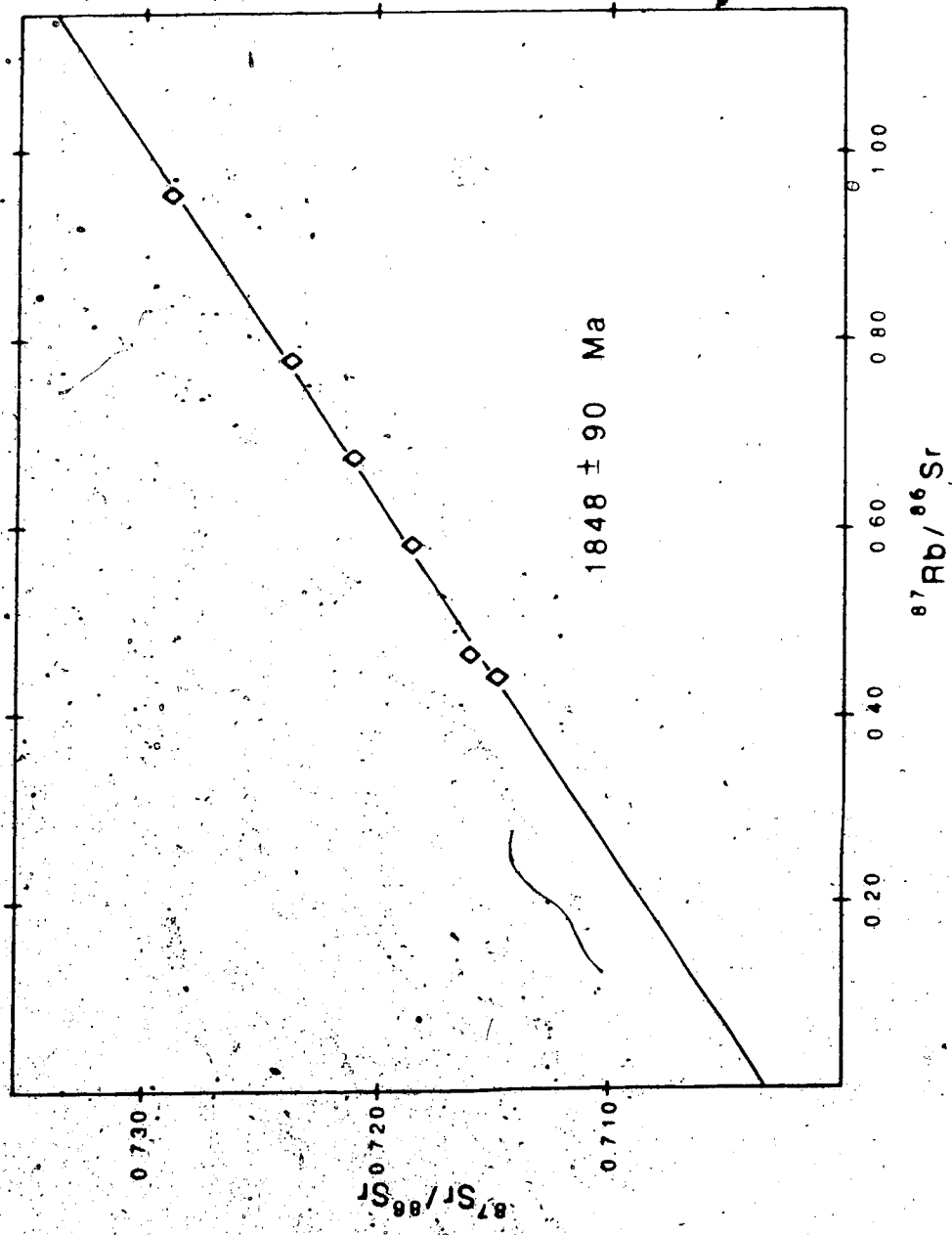


Figure 70. Rb-Sr results for WR samples from the satellite intrusion of the Big Spruce Lake complex.

Clearly the Rb-Sr system does not produce well-constrained ages of intrusion for the Big Spruce Lake complex nor reliable initial $^{87}\text{Sr}/^{86}\text{Sr}$ ratios from the isochrons. Analytical error is not the cause of scattered data points; repeat analyses in this study and previously (R:St.J. Lambert, pers. comm., 1980) indicate that the data scatter is real and the variation lies within the samples themselves. Variable initial ratios and open system behaviour are causes of scattered data.

The most likely candidates to retain an initial (magmatic) isotopic composition are the carbonatites, and especially the sövites. These rocks contain 2400 to 9000 ppm Sr and only 3 to 15 ppm Rb so correction of the measured $^{87}\text{Sr}/^{86}\text{Sr}$ ratio for Rb decay is small. One sövite, PC-82-088, inferred from its REE distribution pattern to be contaminated by gneiss (see Chapter 3), contains a much higher Rb content, 36 ppm and the magnetite dolomite carbonatites contain somewhat lower Sr (1400 to 1500 ppm) and much higher Rb (56 and 74 ppm). Nine carbonatites (7 sövites and 2 magnetite dolomite carbonatites) were analysed for $^{87}\text{Sr}/^{86}\text{Sr}$ and, using XRF data, these ratios were corrected to initial ratios at an age of 2188 Ma. The data for carbonatites are presented in Table 20. The Rb-corrected ratios of sövites, initial ratios, are all low but they vary from 0.70163 to 0.70323,

Table 20. Rb-Sr analytical results for carbonatites.

Sample	Sr ppm	Rb ppm	$^{87}\text{Sr}/^{86}\text{Sr}$ measured	$^{87}\text{Sr}/^{86}\text{Sr}$ ¹ initial
<u>Sövites</u>				
PC-81-176	6980	12	0.70227	0.70212
PC-81-178	2760	3	0.70221	0.70211
PC-81-185	5373	6	0.70331	0.70321
PC-81-376	2414	5	0.70219	0.70201
PC-81-383	9029	14	0.70337	0.70323
PC-82-088	3199	36	0.70336	0.70236
PC-82-506	3717	6	0.70177	0.70163
<u>Magnetite-Dolomite-Carbonatites</u>				
PC-82-408	1508	74	0.70488	0.70072
PC-82-412	1389	56	0.70466	0.70108

¹ Corrected for Rb content using $t = 2188 \text{ Ma}$ and $\lambda^{87}\text{Rb} = 1.42 \times 10^{-11} \text{ yr}^{-1}$.

a range beyond experimental error, which is estimated to be ± 0.00010 . The Rb-corrected ratios for the two dolomitic carbonatites are lower than those of any syenite and they too differ from each other beyond experimental error at 0.70072 and 0.70108. These latter two ratios must be considered less reliable than the others as true initial ratios because of the larger Rb corrections.

For the silicate samples analysed individual model initial $^{87}\text{Sr}/^{86}\text{Sr}$ (Table 18) ratios were calculated because reliable initial ratios could not be obtained from the isochron plots. These individual values were then evaluated to determine if any of them were representative of parent magma isotopic compositions.

The model initial Sr ratios were calculated by assuming an age of 2188 Ma (U-Pb zircon age of syenites) and a closed Rb-Sr system since crystallisation. Easton (1983) has recently shown that Rb-Sr and K-Ar isotopic systems in the Bear province and western Slave province were reset at about 1770 Ma. Resetting is common up to about 50 km east of the Bear-Slave boundary. In the light of resetting of the biotite K-Ar system at Big Spruce Lake, 30 km east of the boundary, at about 1800 Ma the assumption of a closed Rb-Sr system is not valid and the calculated values for silicates are thus model ratios in contrast to the measured (Rb-corrected) values obtained

for the carbonatites. All of the silicate model initial ratios are low, less than 0.7023, and they show an even wider range than do those of the carbonatites. The wide variation in initial ratios obtained for both carbonatites and associated silicates precludes definition of separate initial Sr ratios for the various intrusive centres. Variations of initial Sr ratios in carbonatites and associated alkaline silicate rocks have been reported previously by many authors. Rock (1976) prepared a comprehensive collection of earlier Sr isotopic data for carbonatites and associated alkaline rocks. He noted widespread variability of initial Sr ratios, of both carbonate and silicate rocks, between samples from different complexes. He also noted variability between samples of a single rock type (either carbonate or silicate) within a single complex. The variations within individual complexes are often of a magnitude similar to that obtained here for the Big Spruce Lake complex. The literature reports also indicate that there is no systematic difference between initial ratios of different rock types. Recent studies of carbonatites from Alnö, Sweden (Brueckner and Rex, 1980) and Jacupiranga, Brazil (Roden et al, 1985) revealed variable initial Sr ratios within each of these complexes.

Assimilation of wallrock mantle or crustal material during emplacement of magma as well as subsequent metasomatism can change the apparent initial Sr ratios. The effects of both can be identified in the data obtained from Big Spruce Lake samples.

The model initial Sr ratios of the silicates clearly show effects of localised disturbance. All of the silicates have low initial ratios relative to a calculated whole-earth uniform reservoir (UR) value at 2188 Ma of $^{87}\text{Sr}/^{86}\text{Sr} = 0.70233$. This UR value was calculated using the mean of current literature values (De Pablo and Wasserburg, 1976b; Allegre et al, 1979; Zindler et al, 1982) for present day $^{87}\text{Sr}/^{86}\text{Sr}$ (0.7050) and Rb/Sr (0.030). Some model initial ratios for the intrusive silicates are lower than BABI (0.69897, Faure, 1977) and cannot be accounted for by any contamination of magma during emplacement and crystallisation. There is no known source which could be assimilated to reduce the initial magmatic $^{87}\text{Sr}/^{86}\text{Sr}$ to values below 0.6990. Several silicates listed in Table 18 have model initial ratios in that range, and hence the Rb-Sr systematics of those samples have been disturbed subsequent to crystallisation. The modelling assumption of a closed system since crystallisation is not valid; some $^{87}\text{Rb}/^{86}\text{Sr}$ ratios have been altered (increased) by movement of fluids within the

crust and probably the $^{87}\text{Sr}/^{86}\text{Sr}$ ratios have also been altered.

Movement of Rb could be recent and have the observed effect, but the more probable time is about 1800 Ma, the time at which the biotite K-Ar was reset. There is no strong petrographic evidence for regional metamorphism to the greenschist facies; highly localised alteration with the formation of stilpnomelane, particularly of the quartz syenites, is described in the geology section. Pb isotope data, presented in a later section, supports the conclusion that movement of fluids was highly localised.

All of the model initial ratios calculated for silicates are low, a fact which constrains possible mechanisms of disturbance. Either a less radiogenic Sr component was added to that of the intrusive rocks or the Rb/Sr ratio was increased after crystallisation. Contamination by less radiogenic Sr during emplacement as the dominant mechanism has already been ruled out by the presence of model ratios $< \text{BABI}$. Addition of a less radiogenic Sr component following crystallisation is unlikely because there is no such crustal source; the country rock gneisses contain highly radiogenic Sr. Mixing of Sr through fluid movement within the complex itself, where some intrusives are Rb-poor, is the only reasonable mechanism of decreasing the $^{87}\text{Sr}/^{86}\text{Sr}$ ratios

after crystallisation and could not reduce ratios to less than true initial ratios. Addition of Rb to the magma at the time of crystallisation, i.e., contamination, would not affect the model initial ratios, so the Rb/Sr ratio must have been increased during post-crystallisation fluid movement.

Because metasomatism occurred within the granodioritic crustal host rocks the Rb-Sr composition of the gneisses would strongly affect the composition of any fluid. The gneisses are approximately 400 Ma older than the intrusion (Sm-Nd model ages range 2467 to 2595 Ma; Cavell and Baadsgaard, 1986). Rb-Sr data for four samples of gneiss (Table 21) shows them to be Sr-poor (Sr = 50 to 150 ppm) and Rb-rich (Rb = 100-200 ppm). The Rb/Sr ratio of the gneisses varies from 2 to 11, much higher than that of most of the intrusive silicates (0.03 to 1.0). Alkali-rich fluids derived from gneisses would be most likely to increase the Rb/Sr ratio of metasomatised intrusive rocks.

Model ages calculated for gneisses using the mean whole earth parameters discussed earlier ($^{87}\text{Rb}/^{86}\text{Sr} = 0.030$, $^{87}\text{Sr}/^{86}\text{Sr} = 0.7050$) are shown in Table 21. The basic agreement among these model ages, three of which are 50-130 Ma younger than the Sm-Nd model (CHUR) ages is further evidence that disruption of the Rb-Sr system at about 1800 Ma was mild.

Table 21. Rb-Sr analytical results for gneissic host rock.

Sample	Rb ¹ ppm	Sr ¹ ppm	⁸⁷ Rb/ ⁸⁶ Sr	⁸⁷ Sr/ ⁸⁶ Sr ¹	(⁸⁷ Sr/ ⁸⁶ Sr) _{2188 Ma} (model)	Model age Ma ²
1025	123.9	86.2	4.1465	0.84652	0.7157	2412
1483	105.2	108.0	2.7989	0.80707	0.7187	2600
2074	201.0	51.8	11.4782	1.099	0.7477	2460
2281	117.5	149.2	2.2573	0.78250	0.7113	2468

¹Error estimated for ppm Rb, Sr = ±0.1%, ⁸⁷Sr/⁸⁶Sr = ±0.00010.

²Calculated using present whole earth parameters of ⁸⁷Rb/⁸⁶Sr = 0.030, ⁸⁷Sr/⁸⁶Sr = 0.7050.

Possible contamination of two sövites by gneissic host rock was inferred earlier on the basis of the REE distribution patterns (Chapter 3). These two samples (PC-81-185 and PC-82-088) also have initial Sr ratios higher than those of other sövites at 0.70321 and 0.70236 respectively. The lower Rb-corrected value (0.70236) is that of the sövite, mentioned earlier, which bears a relatively high Rb content (36 ppm). The Rb correction is less reliable and the initial ratio of this sample may be slightly higher than the 0.70236 determined. The Sr data are in agreement with gneissic contamination of these two sövites. In other samples original gneissic contamination is not distinguishable from metasomatic contamination on the basis of Sr data. Both processes increase radiogenic Sr.

The silicates as well as carbonatites must have had some initial magmatic contamination, most likely from the surrounding gneisses. Mixing of two components or contamination of a magma by wallrock is commonly shown as a mixing trend on a plot of initial $^{87}\text{Sr}/^{86}\text{Sr}$ vs ppm Sr. Such a plot (Figure 71) has been prepared from the data of Tables 18 and 20 but such a plot is not valid in the present study for two reasons:

- (1) The initial Sr ratios used in the plot have been shown to be disturbed by post-crystallisation movement of Rb and Sr.

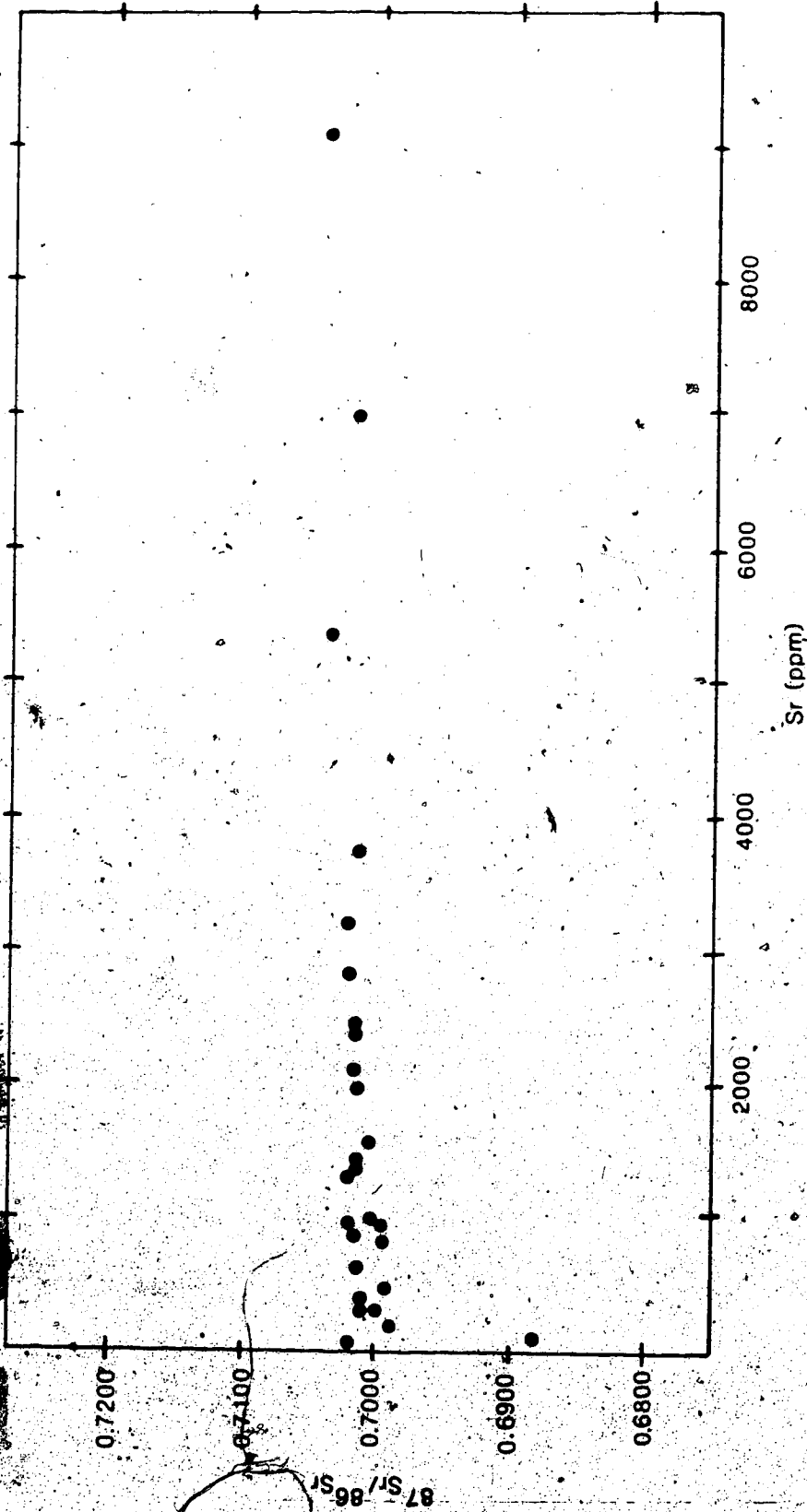


Figure 71. Model initial $^{87}\text{Sr}/^{86}\text{Sr}$ ratios vs ppm Sr for silicates and carbonates of the Big Spruce Lake alkaline intrusion. This plot is not valid to indicate mixing lines for reasons discussed in the text.

(2) Because of the variability of parent magma types, and differentiation within each series no single parent magma with a defined Sr concentration exists for the intrusive series, the data for contaminated samples plot on a "family of mixing lines" and hence appear as scattered on the plot of Figure 71.

No single trend can be discerned. A better demonstration of contamination would be one which is independent of element compositions (differentiation and differing magma types) dependent only on isotopic compositions. Such a plot (ϵ_{Sr} vs ϵ_{Nd}) is presented in the next section where Sr and Nd data are combined to evaluate possible assimilation effects.

Contamination by gneiss and post-crystallisation movement of Rb and Sr mean that the initial ratio of the parent magma(s) can only be approximated. A reasonable lower limit for the initial ratio of the carbonatites is 0.7016, the lowest of the sövite values in Table 20. It is inferred that this is the Sr isotopic composition of the parent magmas of both silicates and carbonatites and higher values have been created by gneissic contamination or by later metasomatism.

A magmatic initial ratio of 0.7016 for the melt that reached the upper crust is lower than that of the whole earth development at 2188 Ma (0.70233 calculated from

present whole earth parameters outlined above) and implies either that the source region had previously been Rb depleted (to decrease ^{87}Sr) or that magma from a mantle source with a whole earth $^{87}\text{Sr}/^{86}\text{Sr}$ ratio was contaminated by a depleted source during ascent and emplacement. The data from Big Spruce Lake alone are insufficient to distinguish between the two possibilities. Additional data from the literature are helpful in this regard. On Figure 72, taken from Bell et al (1982), the preferred initial Sr ratio of the Big Spruce Lake complex is plotted vs age to compare it with those of 13 other Canadian carbonatites. Bell et al found that the carbonatites of eastern Canada, fall into two separate groups. One group, labelled A in Figure 72, has initial Sr ratios close to or on the bulk earth development line; the other group (B) define a development line for a source region of much lower Rb/Sr which has behaved as a closed system for about 2700 Ma. The initial ratio of the Big Spruce Lake carbonatite places it in the second group, with a depleted mantle source. The Big Spruce Lake intrusion is much older than any other carbonatites shown in Figure 72 and the inferred initial ratio of 0.7016 plots very close to the development line of the Sr-depleted source determined by Bell et al. The agreement of data from Big Spruce Lake and other carbonatites of Group B (of widely divergent

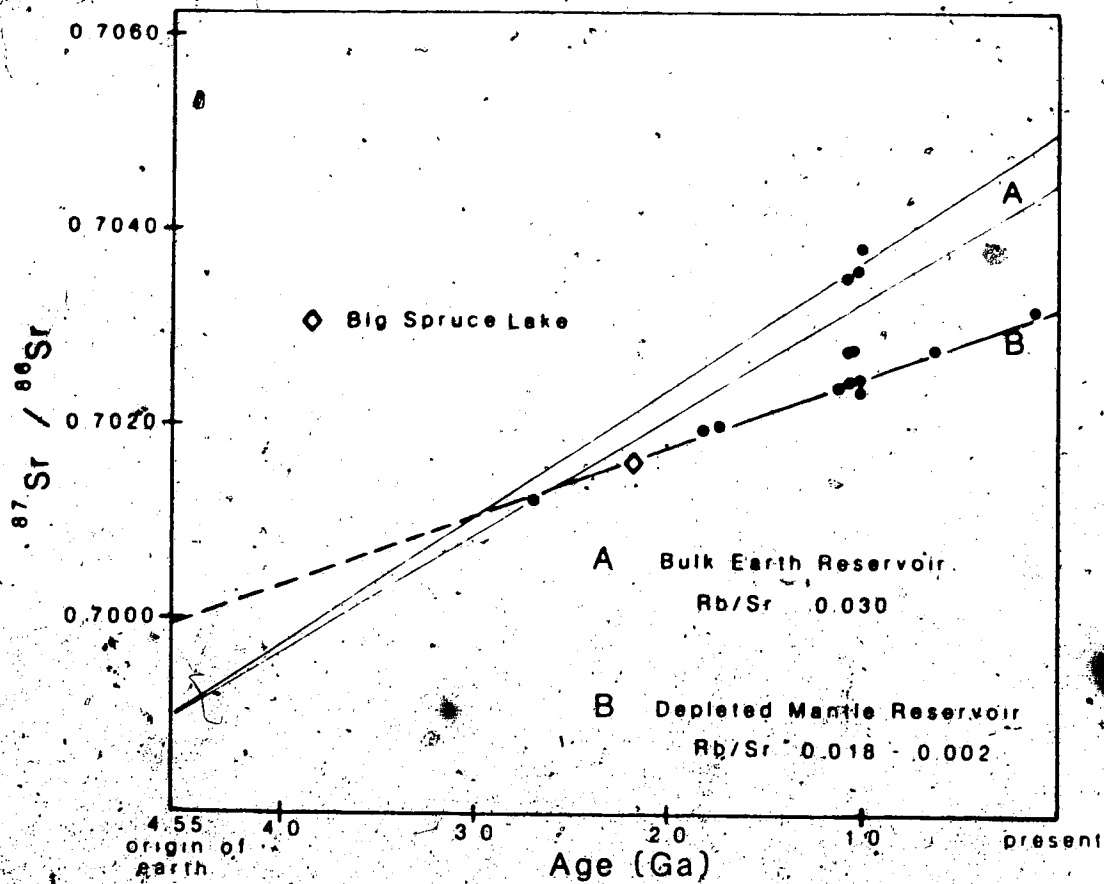


Figure 72. Plot of initial $^{87}\text{Sr}/^{86}\text{Sr}$ vs age of intrusion for carbonatites from the southern Canadian shield (based on Bell et al, 1982). One group (A) falls on the whole earth development line which is fan-shaped because of uncertainties in whole earth Rb-Sr parameters. The Big Spruce Lake initial ratio of 0.7016 falls in group B. This group defines an apparent mantle differentiation event at about 2700 Ma (resulting in a depleted mantle source for the carbonatites).

ages and locations) suggests that the source region was ^{87}Sr depleted mantle and that the low initial Sr ratios measured were not derived by contamination of magmas with original whole earth $^{87}\text{Sr}/^{86}\text{Sr}$ ratios by an upper level (upper mantle or lower crust) ^{87}Sr -depleted layer. Contamination of magmas from several different complexes would be expected to produce a more random variation of low Sr ratios and not the correlation evident in Figure 72.

One important implication of the data presented here is that, despite their high Sr contents and assumed rapid emplacement within or through the upper crust, carbonatites do not necessarily retain their original, magmatic Sr isotopic compositions. Initial Sr ratios cannot be obtained for a complex on the basis of a single sample by assuming that high Sr and low Rb contents are sufficient to buffer contamination effects.

E. Sm-Nd Systematics

Sm-Nd analytical results are presented in Appendix 4 and discussed there with regard to geochronologic interpretation. While individual Sm-Nd ages have not been obtained for the five centres of intrusive activity at Big Spruce Lake (geochronological application of the Sm-Nd is

limited by the long half-life of ^{147}Sm and short ranges of Sm/Nd information about the petrogenesis of the intrusion can be derived from initial $^{143}\text{Nd}/^{144}\text{Nd}$ ratios using the age of intrusion obtained in this study. The U-Pb zircon age is the preferred age of crystallisation (2188 \pm 16/-10 Ma, Cavell and Baadsgaard, 1986) but the Sm-Nd isochron age of 2183 Ma is used here in calculation of initial ratios for internal consistency.

Assessment of initial ratio variations is straightforward using the ϵ notation of De Paolo and Wasserburg (1976a), and parameters which refer to a bulk earth composition (CHUR).

ϵ_{Nd} is the fractional deviation of $^{143}\text{Nd}/^{144}\text{Nd}$ of the sample from that of the chondrite uniform reservoir (CHUR), assumed to be a bulk earth composition, in parts in 10^4 .

$$\epsilon_{\text{CHUR}} = \left[\frac{(^{143}\text{Nd}/^{144}\text{Nd})_{\text{sample}}}{(^{143}\text{Nd}/^{144}\text{Nd})_{\text{CHUR}}} - 1 \right] \times 10^4$$

The ϵ_{CHUR} of petrogenetic interest is $\epsilon_{\text{T}}^{\text{CHUR}}$ where T is the time of crystallisation. If $I_{\text{sample}}(T)$ is the $^{143}\text{Nd}/^{144}\text{Nd}$ initial ratio at time T, and $I_{\text{CHUR}}(T) = ^{143}\text{Nd}/^{144}\text{Nd}$ of the chondrite uniform reservoir (Jacobsen and Wasserburg, 1984 parameters) then

$$\epsilon_T^{\text{CHUR}} = \left(\frac{I_{\text{sample}}(T)}{I_{\text{CHUR}}(T)} - 1 \right) \times 10^4$$

A value of ϵ_T^{CHUR} near zero indicates a magma source which has had a time-integrated (averaged) chondritic Sm/Nd composition prior to time T. Deviation of ϵ_T^{CHUR} indicates a source enrichment or depletion of Sm relative to CHUR, at least once, prior to time T.

In this study the reference/bulk earth Sm-Nd parameters used in the calculations of ϵ^{CHUR} are the average chondritic composition determined by Jacobsen and Wasserburg (1980, 1984); this chondritic reservoir (CHUR) has $^{147}\text{Sm}/^{144}\text{Nd} = 0.1967$ and $^{143}\text{Nd}/^{144}\text{Nd} = 0.511847$ (normalised to $^{146}\text{Nd}/^{144}\text{Nd} = 0.7241$).

Regression of the Sm-Nd data for samples from all centres of intrusive activity (complete analytical results are included in Appendix 4) yielded the age of 2183 Ma discussed earlier and an initial $^{143}\text{Nd}/^{144}\text{Nd}$ ratio of 0.509093 ± 0.000056 (1 σ error) as a mean value for the entire group (Figure 73). This initial ratio corresponds to an ϵ^{CHUR} of $+1.8 \pm 1.1$, overlapping with zero within the conventional 2 σ error limit. $\epsilon^{\text{CHUR}} = 0$ implies that the source of these rocks, commonly agreed to be "primitive deep mantle" (e.g., Taylor et al, 1967; Le Bas, 1977; Wyllie, 1980) had a time-integrated chondritic Sm/Nd composition at the time of magma formation and emplacement

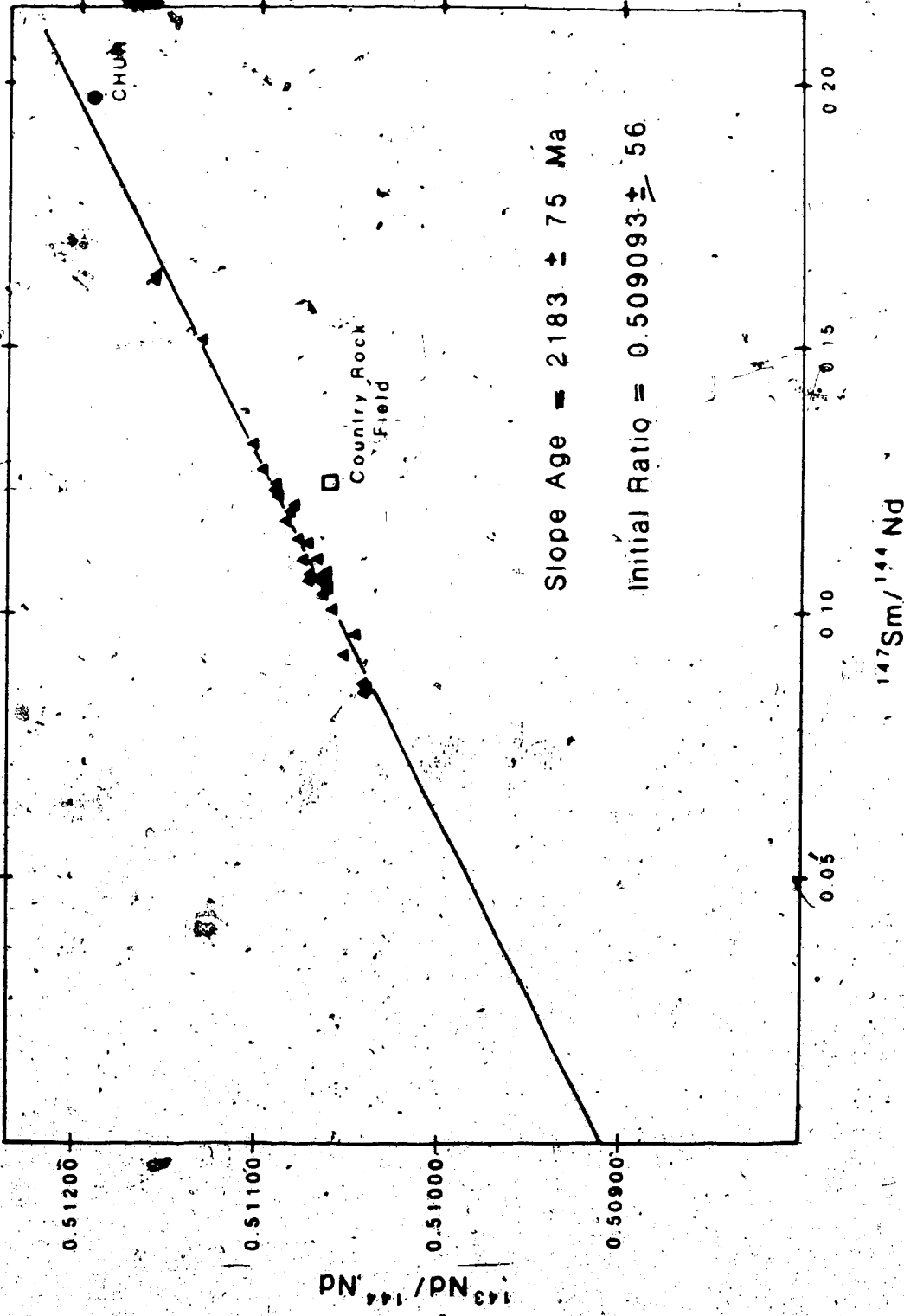


Figure 71. $^{143}\text{Sm}-\text{Nd}$ results for WR samples from all intrusive centres of the Big Spruce Lake intrusion.

at 2183 Ma; no prior enrichment or depletion of Sm relative to Nd had occurred.

However, detailed examination of the data indicates that ϵ_{Nd} is probably not zero for the source of the Big Spruce Lake series and overlap of ϵ_{Nd} with zero is a function of scattered data which produce a large error. An individual ϵ_{Nd}^{CHUR} for each sample has been calculated using the data from Appendix 4. These 32 values are presented in Table 22 and presented in histogram form in Figure 74. The histogram clearly shows that ϵ_{Nd} values for the intrusive rocks range from 0 up to +3.0, representing a range of initial ratios from 0.50902 to 0.50916. $^{143}Nd/^{144}Nd$ for CHUR at 2183 is 0.50902. Had the preferred U-Pb zircon age of 2188 Ma been used for the calculation of ϵ_{Nd} the difference would be negligible. A significant effect on the values of ϵ_{Nd} would be noted if the $^{143}Nd/^{144}Nd$ values for individual samples had been normalised to a value of 0.511860 for $^{143}Nd/^{144}Nd$ in the La Jolla standard solution used for interlaboratory checks. The mean value obtained for the La Jolla standard during this study was 0.511833 ± 9 (9 runs). Normalisation of all measured ratios by a factor of $0.511860/0.511833$ would increase the ϵ_{Nd} values by about 0.5 (the measured $^{143}Nd/^{144}Nd$ ratio of BCR-1 becomes 0.511847 ± 23 with such normalisation, in good agreement

Table 22. ϵ_{Nd} and ϵ_{Sr} for individual samples.

Sample	ϵ_{Sr}^1	ϵ_{Nd}^2	Sample	ϵ_{Sr}	ϵ_{Nd}
<u>Centre 1</u>			<u>Centre 4</u>		
PC-81-001	- 6.7	+2.7	PC-81-376	- 4.6	+1.7
PC-81-004		+2.8	PC-81-176	- 3.0	+2.3
PC-81-235		+1.5	PC-81-178	- 3.1	+0.9
PC-81-275	- 5.6	+1.6	PC-81-185	+12.5	+1.3
PC-81-363		+0.5	PC-81-383	+12.8	+2.8
PC-82-163		+0.9	PC-82-088	+ 0.4	+1.2
PC-82-173		+0.8	PC-82-412	-18	+2.3
			PC-82-506	-10.0	+2.4
<u>Centre 2</u>			<u>Centre 5</u>		
PC-81-012	- 0.7	+1.8	PC-81-061		+0.3
PC-81-285	-15.4	+2.0	PC-81-388	-49.3	+1.2
PC-81-332		+0.7	PC-82-260	-43.9	0
PC-82-096	-204	+0.2	PC-81-053	-29.1	
PC-82-099		+0.5	PC-81-057	-33.9	
PC-82-124		+1.2	PC-81-064	-12.5	
PC-82-358	-26	+1.8	PC-82-278	-17.1	
PC-82-151	-51	+0.2			
<u>Centre 3</u>					
PC-81-168		+2.0			
PC-81-194	-13.0	+1.6			
PC-81-287		+0.9			
PC-81-482	-12.0	+1.5			
PC-82-039	- 5.7	+1.8			
PC-82-525	- 8.1	+2.4			

¹Calculated using $t = 2188$ Ma, $(Rb/Sr)_{UR} = 0.030$, $(^{87}Sr/^{86}Sr)_{UR} = 0.7050$.

²Calculated using $t = 2183$ Ma, $(^{147}Sm/^{144}Nd)_{CHUR} = 0.1967$,
 $(^{143}Nd/^{144}Nd)_{CHUR} = 0.511847$.

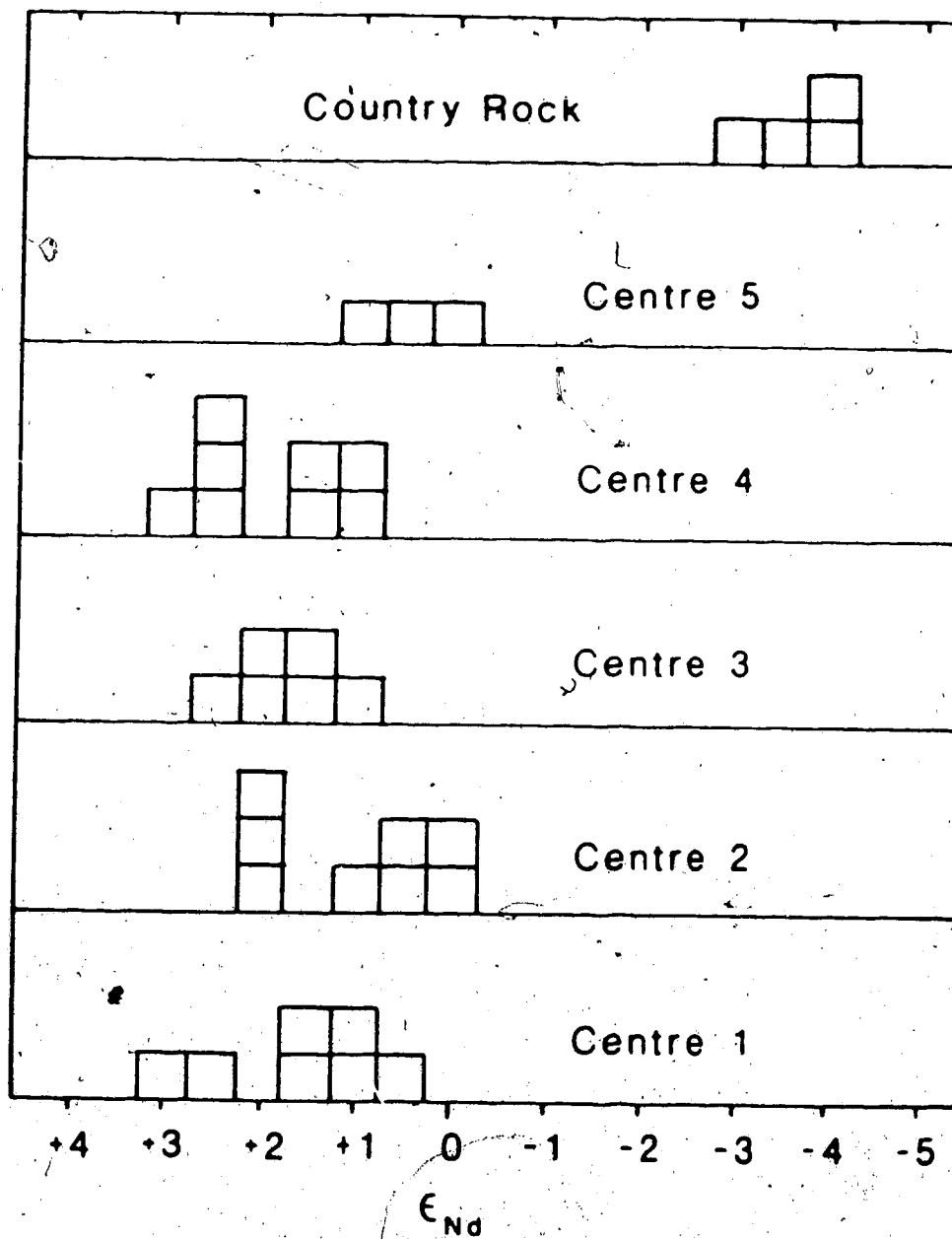


Figure 74. Histogram of individual ϵ_{Nd} for samples from each of the five intrusive centres and surrounding country rock. Each square represents a single sample.

with published values). Such normalisation of measured ratios has no effect on the slope ages determined but it does indicate that the ϵ_{Nd} values quoted here (not normalised to the La Jolla standard) are minimum values.

Initial ratios of all samples are at or above CHUR and the total range (0.00014) is greater than experimental error which is estimated at <0.00005 for the $^{143}Nd/^{144}Nd$ ratio. The age determined by regression of the Sm-Nd data is essentially equal to the U-Pb zircon age and very close to the WR Pb-Pb age of the main complex (2155 Ma; Cavell and Baadsgaard, 1986) indicating that the variation in ϵ_{Nd} is random with respect to the Sm/Nd ratio.

In this respect the results differ from those of a recent study by Catell et al (1984) of komatiitic and tholeiitic lavas from the Abitibi Belt, Ontario, Canada. They found that WR Sm/Nd data produced a poorly-constrained isochron yielding an age (2826 ± 64 Ma) about 130 Ma older than the U-Pb zircon age (2697 ± 1 Ma), and an ϵ_{Nd} of +2.65. In that study scatter of the data points was attributed to mixing between isotopically distinct mantle sources followed by fractional crystallisation. The 130 Ma discrepancy in ages was interpreted as reflecting the complex mixing and fractionation processes involved. Variations in initial ratios and Sm/Nd ratios within the Big Spruce Lake intrusive rocks can best be

explained by mixing of parent magma(s) of a depleted mantle composition (positive ϵ_{Nd}) with a crustal component (which is ^{143}Nd depleted relative to the magma) during ascent and fractionation, followed by metasomatism.

The most depleted or primitive Nd isotopic composition, inferred to be closest to that of parent magma(s), is carried by two rock types of widely different character, one silicate at the high end of the Sm/Nd range (magnetite pyroxenite) and the other carbonate (sövites) at the low end of the Sm/Nd range. Within error the ϵ_{Nd} of each of these rock types is the same $\epsilon_{Nd} = +2.7$ to $+2.8$ and $+2.3$ to $+2.8$ respectively. Each is equally enriched in radiogenic ^{143}Nd and each of these high ϵ_{Nd} values is represented by analyses of two or more separate samples. A line connecting the data points for these samples would be subparallel to the regression line which produces the 2183 Ma Sm-Nd age; these two divergent groups appear to represent an upper limit of ϵ_{Nd} value, i.e., the most primitive or uncontaminated isotopic composition. Other evidence of the probable uncontaminated character of the magnetite pyroxenites (PC-81-001 and 004), the lack of Eu anomalies in the REE distribution plots and early cumulate character, has been discussed earlier. Crustal involvement must have been minimal for these pyroxenites. A third pyroxenite (PC-82-163) has a small

positive Eu anomaly ($\text{Eu}/\text{Eu}^* = 1.2$), a lower $^{147}\text{Sm}/^{144}\text{Nd}$ (0.151) than the other two and $\epsilon_{\text{Nd}} = +0.9$, much lower than the limiting value of +2.7 for the other two pyroxenites. This sample is from a small body lying within the main diorite unit, which itself has $\text{Eu}/\text{Eu}^* = 2.2$ and a relatively low ϵ_{Nd} of +0.5 to +0.9, and the pyroxenite has probably assimilated diorite which is slightly contaminated.

The carbonatites which carry the depleted, magmatic Nd isotopic composition are inferred to be largely uncontaminated because they have very high REE abundances (3000 to 7000 ppm), and all three have almost identical $^{143}\text{Nd}/^{144}\text{Nd}$ ratios. ϵ_{Nd} ranges from +2.3 to +2.7 for these three sövites, all of which have almost identical $^{147}\text{Sm}/^{144}\text{Nd}$ ratios as well (0.086). A fourth carbonatite has a slightly higher $^{147}\text{Sm}/^{144}\text{Nd}$ ratio (0.092) and the same high ϵ_{Nd} , +2.8. It is important to note that a high REE abundance alone is not a sufficient basis on which to assume that the $^{143}\text{Nd}/^{144}\text{Nd}$ ratio has not been altered by contamination. Two sövite dykes that either cut gneiss or are associated with the margin of the complex (PC-81-185 and PC-82-088), were discussed earlier in connection with gneissic contamination affecting Sr initial ratios. These same two samples have 1000 to 2000 total REE, strong negative Eu anomalies and ϵ_{Nd} of +1.5 and +1.7.

respectively, somewhat lower than the limiting value of +2.8; the Nd isotopic composition appears to have been altered by assimilation of a component of low $^{143}\text{Nd}/^{144}\text{Nd}$, probably granodioritic gneiss.

There is thus some evidence that the primitive magma had $\epsilon_{\text{Nd}} \sim +2.7$ and that the observed scatter results, at least in part, from contamination by a crustal component which had a much lower $^{143}\text{Nd}/^{144}\text{Nd}$ ratio. Before discussing the petrogenetic implications of such an ϵ_{Nd} value and comparing it to those of other studies the effects of assimilation and open-system behaviour will be evaluated here to strengthen the evidence in support of $\epsilon_{\text{Nd}} = +2.7$.

In the earlier discussion of Sr initial ratios (model values) it was pointed out that assimilation of older crustal material by ascending magma would increase the radiogenic Sr component and that this effect is not separable from those of later metasomatism on the basis of Sr data only. Isotopic compositions of Sr and Nd, which are independent of variable abundances due to diversity of rock types in the complex, can be used to distinguish assimilation and open-system effects and allow inferences to be made about an original magmatic Sr and Nd isotopic composition.

Nd and Sr initial ratios can be correlated by plotting ϵ_{Nd} vs ϵ_{Sr} . ϵ_{Sr} is calculated in a manner similar to that of ϵ_{Nd} . There is no clearly defined and commonly accepted reference reservoir (UR) for the Rb-Sr system comparable to the chondritic uniform reservoir (CHUR) commonly used for the Sm-Nd system. Values for whole earth Rb/Sr range from 0.029 to 0.031; for present day $^{87}Sr/^{86}Sr$ in a whole earth reservoir the range is 0.7045 to 0.7052 (De Paolo and Wasserburg, 1976b; Allegre et al, 1979; Zindler et al, 1982). Values of 0.030 and 0.7050 have been chosen for use in this study as the mean value of those in the literature. The ϵ_{Sr} and ϵ_{Nd} values are presented in Table 22 and ϵ_{Sr} is plotted vs ϵ_{Nd} in Figure 75. The Nd and Sr isotopic compositions of the four granodioritic gneisses analysed in this study have been calculated for $t = 2188$ Ma using the present whole earth parameters outlined for calculation of ϵ_{Nd} and ϵ_{Sr} values. The resulting country rock compositions, expressed as ϵ_{Nd} and ϵ_{Sr} , are shown as a field in Figure 75.

In Figure 75 effects due to original contamination and to highly localised later disturbance (~1800 Ma) can be discerned. The majority of intrusive rock isotopic compositions plot in an elongate field with positive ϵ_{Nd} and negative ϵ_{Sr} , extending from about $\epsilon_{Nd} = +2.8$ and ϵ_{Sr}

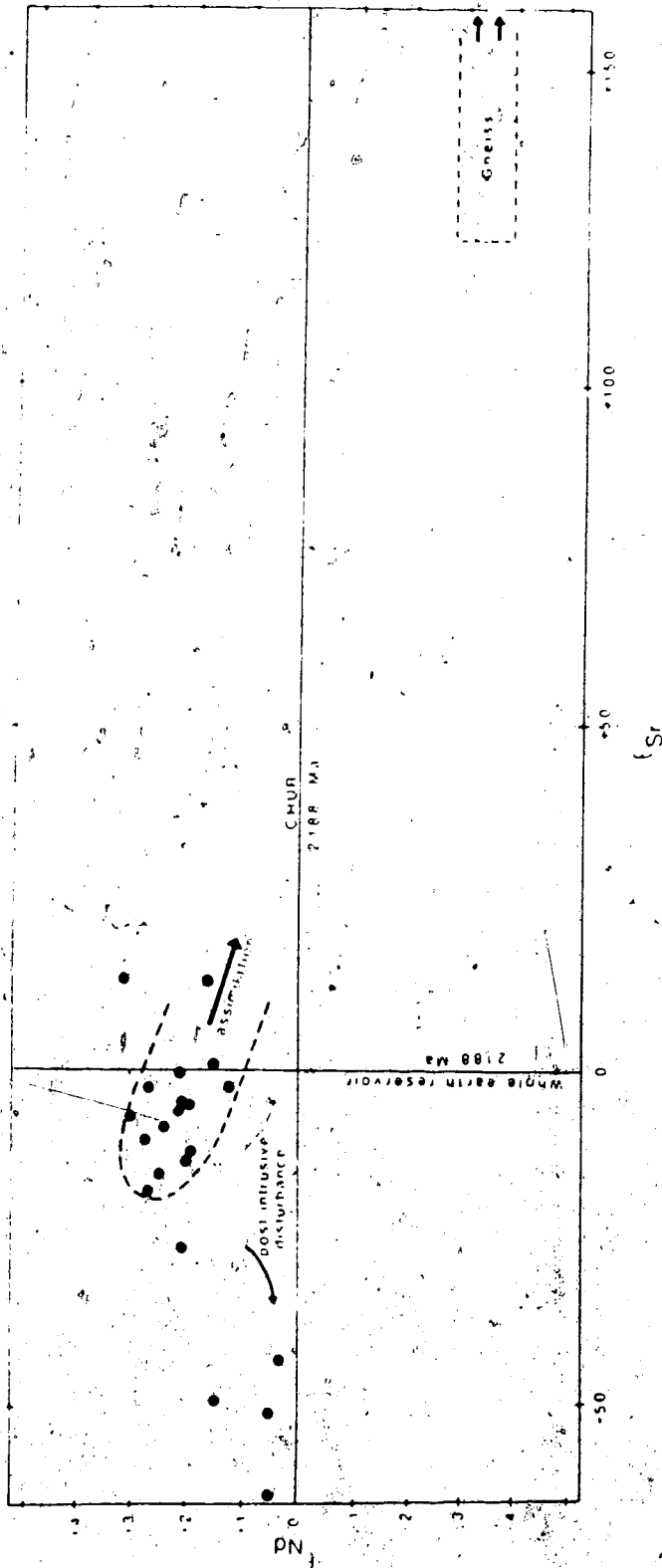


Figure 75. ϵ_{Sr} vs ϵ_{Nd} for samples from all intrusive centres of the Big Spruce Lake complex. The majority of intrusive rock compositions plot in an elongate field extending from primitive $\epsilon_{Nd} = +2.8$ and $\epsilon_{Sr} = -10$ to -12 towards gneissic compositions (assimilation trend). A few samples show widely variable ϵ_{Sr} and slightly variable ϵ_{Nd} in a post-crystallisation disturbance trend.

= -10 to -12 directly towards the field of gneissic country rock at negative ϵ_{Nd} (~ -3.5) and very positive ϵ_{Sr} (+125 to +600). At one end of this main trend of intrusive compositions are samples of the two rock types, carbonatite and magnetite pyroxenite, for which evidence has previously been presented indicating a "primitive" or probably least contaminated character. The magnetite pyroxenite (PC-81-001) is interpreted as a cumulate which formed very early in the crystallisation of alkali basalt magma of Centre 1 with little opportunity for prior assimilation of host gneiss. It is not sheared and the presence of unaltered pyroxene (and sometimes olivine) is evidence that this pyroxenite was largely unaffected by any disturbance after emplacement. The carbonatite which plots at the upper end of the intrusive field (PC-82-506) has high total REE and Sr contents, no indication of gneissic contamination (no Eu anomaly) and is relatively fresh. Whole rock Pb data described later also indicate minimal post-intrusive disturbance of this carbonatite. At the other end of the main intrusive trend, closest to the gneissic field, are the two carbonatites (PC-81-185 and PC-82-088) which have low total REE and strong negative Eu anomalies indicative of assimilation of host gneiss. This main field thus lies along a mixing line with magmatic isotopic compositions at one end ($\epsilon_{Nd} \sim$

+2.8, $\epsilon_{\text{Sr}} \sim -10$ to -12) and gneissic at the other ($\epsilon_{\text{Nd}} \sim -3.5$, $\epsilon_{\text{Sr}} > 125$). The amount of mixing is dependent upon the actual gneissic composition but a maximum of 20% is evident in Figure 75.

Some samples plot at much lower ϵ_{Sr} values, in a direction almost directly away from the assimilation trend. Most are samples which have had Rb/Sr increased by post-intrusive disturbance to the extent that the model or calculated initial $^{87}\text{Sr}/^{86}\text{Sr}$ ratio is decreased to near or below BABI. This is an open system trend, in which effects are highly localised (specific) and variable. The Sm-Nd system has suffered less disturbance than has the Rb-Sr system. This results in part from the geochemical coherence of Sm and Nd compared to Rb and Sr and in part from the fact that Sm/Nd ratios of intrusive and host rocks are similar while Rb/Sr ratios are not. A similar disturbance of Sr but not Nd isotopic compositions can be observed in ocean floor basalts (McCulloch, et al, 1980).

The correlation of Nd and Sr isotopic compositions evident in Figure 75 indicates that the mantle-derived magmas which reached the gneissic crust to form the intrusive complex originally had a depleted mantle isotopic composition with $\epsilon_{\text{Nd}} \sim +2.7$ and $\epsilon_{\text{Sr}} \sim -10$ to -12 , and that presently observed variations are due to

subsequent crustal contamination, fractional crystallisation and post-crystallisation disturbance (and normal radiogenic growth). The data for all five intrusive centres fall in the same main intrusive field, apart from the obvious effects of open system behaviour. The similar initial isotopic compositions indistinguishable from present data, are evidence for an isotopically homogeneous source region for the entire complex.

The Nd isotopic data do not distinguish between the least contaminated (most primitive) samples from the three petrographic groups of the main complex: they all have minimum ϵ_{Nd} in the range +2.5 to +3.0. Saturated silicates, undersaturated silicates and carbonatites are isotopically indistinguishable based on the present data. The satellite intrusion does have a lower ϵ_{Nd} , which is most simply explained by gneissic contamination. If this intrusion were indeed younger, e.g., 1900 Ma as Rb-Sr and Pb-Pb data suggest (with very large errors), then the calculated initial ratios would range from 0.509241 to 0.509307 and with CHUR for 1900 Ma at 0.509388 the ϵ_{1900}^{CHUR} values would be -2.9 to -1.6 indicating a major crustal component in the magma. Assimilation of gneissic crust in amounts sufficient to produce such ϵ_{1900}^{CHUR} values is precluded by the absence of

negative Eu anomalies in the K-rich rocks, and by alkali enrichment to values above gneissic abundances, both of which are discussed in Chapter 3. The Nd data thus suggest that the satellite intrusion is essentially coeval with the main complex and has suffered only minor gneissic contamination.

There are three possible explanations for the positive ϵ_{Nd} value inferred for the magma(s) which reached the upper crust. One possibility is that the currently accepted CHUR values (Jacobsen and Wasserburg, 1980, 1984) are not accurate. The second is that the original source region had $\epsilon_{Nd} = 0$ but, during ascent of the magma, contamination with a depleted upper mantle layer raised the $^{143}Nd/^{144}Nd$ ratio to positive values prior to emplacement in the crust. The third possibility is that the source region itself was depleted relative to the primitive whole earth composition represented by CHUR.

The CHUR values have recently been re-evaluated (Jacobsen and Wasserburg, 1984) by further analyses of chondritic meteorites. A change in the $^{143}Nd/^{144}Nd$ reference value from 0.51186 to 0.511847 was required due to an earlier revision of the oxygen isotope correction factor (Wasserburg *et al*, 1981), but apart from this minor revision this recent study warranted no change in the commonly accepted CHUR parameters. Assuming that the

whole earth does indeed have a chondritic Sm-Nd composition (the basic assumption of the ϵ_{Nd} notation) then the mantle source region of the carbonatite-alkaline silicate magmas had its Sm/Nd increased at some time prior to the 2183 Ma magma formation.

The second explanation of positive ϵ_{Nd} for this series of mantle-derived rocks is mixing of magma formed in a deep mantle source, previously undifferentiated with respect to Sm and Nd so that $\epsilon_{Nd} = 0$, with an upper ^{143}Nd -enriched layer. There is abundant evidence of a depleted mantle component in current literature (e.g., De Paolo, 1981; Goldstein et al, 1984; Menzies and Murthy, 1980). This model corresponds to the two-layer mantle model proposed by Wasserburg and De Paolo (1979) and more recently used by Basu et al (1984) to explain positive ϵ_{Nd} values of kimberlites. The continental crust into which the Big Spruce Lake complex was intruded, the Slave craton, has a minimum Nd model (CHUR) age of 2450 Ma (Appendix 4) and could be older than 3000 Ma (Frith et al, 1976; Krogh and Gibbins, 1978), hence a depleted mantle layer beneath this crust is at least 2450 Ma as well. At present there is no independent assessment of the mantle composition beneath the Slave craton at about 2200 Ma; isotopic characterisation of this mantle is one of the objectives of the present study. We have no way of

estimating the degree of depletion that might have existed. One model which might be compared is that of Goldstein et al (1984) who postulated the existence of a depleted mantle (DM) layer which had developed linearly from $\epsilon_{Nd}^{CHUR} = 0$ at 4.57 Ma to $\epsilon_{Nd}^{CHUR} = +10$ at the present, +10 being the ϵ_{Nd} of present day mid-ocean ridge basalts (MORB). At the time of intrusion of the Big Spruce Lake complex such a linearly developed DM would have had $\epsilon_{Nd}^{CHUR} \approx +5.3$ and assimilation of such a component would readily increase the ϵ_{Nd} value of magma(s) from a chondritic value of zero. Linear development of DM throughout the history of the earth is unlikely. If the depleted layer is formed episodically, and the mantle under the Slave craton was depleted at about 3.1 Ga to the same degree as the present MORB source ($^{147}Sm/^{144}Nd \sim 0.214$) then at 2200 Ma the depleted layer would have had $\epsilon_{Nd}^{CHUR} \approx 2$, slightly less than the ϵ_{Nd} found in this study.

The third possibility requires a deep mantle source which was itself LIL element depleted prior to magma formation, possibly as a result of an earlier partial melting episode. Deep mantle heterogeneity, implicit in this model, has been suggested previously by other workers. The suggestion by Bell et al (1982) that the mantle source region of carbonatites in the southern Canadian shield has been depleted since 2700 Ma has been

discussed in connection with the Sr data, and the correlation of initial Sr ratios between the Big Spruce Lake complex and the other carbonatites shown (Figure 72). The required depleted deep mantle source could have been formed beneath the Slave craton by a partial melting episode similar to that outlined above. The degree of depletion must be increased however, to $^{147}\text{Sm}/^{144}\text{Nd} \approx 0.224$ to create $\epsilon_{\text{Nd}}^{\text{CHUR}} \approx +3$ by 2200 Ma and if this reservoir existed until present as a closed system it would have $\epsilon_{\text{Nd}} \approx 11$.

Literature reports of Sm-Nd from carbonatite complexes are sparse; none have yet been reported in the detail of the present work, making assessment of possible contamination difficult in most cases. Basu and Puustinen (1982) reported $\epsilon_{\text{Nd}} = -6.7 \pm -1.4$ for the 2100 Ma Siilinjärvi carbonatite complex of Eastern Finland. They interpreted the low initial ratio as indicating differentiation of the mantle source region, leading to Sm depletion, long before the 2100 Ma melting episode. Results of the present study suggest that crustal contamination could have contributed to the unusually low initial ratios of the Finnish carbonatites. Roden et al (1984) reported small positive ϵ_{Nd} values (+0.6 to +1.6) for carbonates of the 130 Ma Jacupiranga, Brazil complex. This ϵ_{Nd} range is slightly lower than that of

the Big Spruce Lake series, but the original magmatic ϵ_{Nd} may actually have been slightly higher. These authors also reported high initial Sr ratios ($\epsilon_{Sr} = +1.5$ to $+10.6$) which they attribute to contamination by late Precambrian silicic crustal rocks, a process which should have decreased initial Nd isotopic ratios slightly as well. In an early Sm-Nd survey De Paolo and Wasserburg (1976b) reported an ϵ_{Nd} value of $+0.1 \pm 0.9$ for the (presently active) Oldoinyo Lengai natrocarbonatite. The carbonatite with this $\epsilon_{Nd} = 0$ value was, of course, inferred to be derived from an undifferentiated, chondritic mantle reservoir. However, initial Sr ratios of 0.7059 and 0.7061 for the Oldoinyo Lengai carbonatites (Bell, Dawson and Farquahar, 1973) are higher than any of the current estimates of whole earth Sr composition which range from 0.7045 (De Paolo and Wasserburg, 1976b) to 0.7052 (Zindler et al, 1982). Crustal contamination must be inferred from the Sr data and hence the original magmatic $^{143}Nd/^{144}Nd$ ratio may have been higher than that presently measured; a small positive ϵ_{Nd} may be the primitive magmatic value of the Oldoinyo Lengai carbonatite. Positive ϵ_{Nd} values of +5.9 and +7.8 were reported by Basu and Tatsumoto (1980) for the McClure Mountains, Colorado carbonatite and the Magnet Cove, Arkansas carbonatite, respectively. These authors assumed that the mantle source beneath the

continent was depleted similar to the suboceanic source of alkali basalts.

Variation of initial Sr ratios within and between individual carbonatite complexes has been reported by many authors (e.g., Rock's 1976 review of earlier data; Bell et al, 1982; Roden et al, 1984) and it is now apparent that Nd initial ratios of carbonatites and associated alkaline rocks also vary within and between individual complexes. For this reason model ages or petrogenetic interpretations based on single carbonatite samples cannot be considered reliable.

The presently available Sm-Nd data of this study and in the literature do not permit an unequivocal distinction between two possible models leading to depleted parent magmas: essentially isotopically homogeneous depleted deep mantle sources for carbonatites and silicates or magmas from an undifferentiated (CHUR) source region contaminated during ascent by an upper depleted mantle layer.

F. U-Th-Pb Systematics

The WR Pb analytical results for 42 intrusive rocks are presented in Appendix 4, while those for four granodioritic host gneisses are presented in Table 23.

Table 23. Whole rock lead analytical data for granodioritic gneisses.

Sample	$^{206}\text{Pb}/^{204}\text{Pb}$	$^{207}\text{Pb}/^{204}\text{Pb}$	$^{208}\text{Pb}/^{204}\text{Pb}$	Pb ¹ ppm
PC-81-025	18.309	15.603	37.336	24
PC-81-483	20.110	15.930	41.447	24
PC-82-074	27.079	17.094	40.719	25
PC-82-281	19.482	15.771	41.540	23

¹XRF analysis.

Plots of $^{207}\text{Pb}/^{204}\text{Pb}$ vs $^{206}\text{Pb}/^{204}\text{Pb}$ data for each individual centre of intrusive activity, also presented in Appendix 4, clearly show the Pb-isotopic data points to be scattered from isochron lines beyond analytical error. For this reason it was possible to obtain a reasonably well-constrained age only for Centre 3 in which the latest differentiates have U contents over 30 ppm (this produces a $^{206}\text{Pb}/^{204}\text{Pb}$ ratio over 100 in the most radiogenic samples). Even for this sample group the data points are scattered and regression yields an error of ± 22 Ma (error quoted is $2\sigma/\text{MSWD}$) on a $^{207}\text{Pb}/^{206}\text{Pb}$ slope age of 2165 Ma and an MSWD of 97.3. Data for all centres is combined in a single $^{207}\text{Pb}/^{204}\text{Pb}$ vs $^{206}\text{Pb}/^{204}\text{Pb}$ plot in Figure 76. The regression line for all samples is strongly controlled by the U-rich undersaturated samples and the age of 2155 Ma agrees within error with the U-Pb zircon age of 2188 $\pm 16/-10$ Ma as well as the WR Sm-Nd age of 2183 ± 75 Ma. Agreement of the Pb-Pb slope age with the zircon and Sm-Nd ages indicates that data scatter about the regression line shows no trend with U content.

The excess variation of Pb-isotopic compositions (as a result of contamination and metasomatism) may be evaluated in a manner similar to that employed to evaluate and interpret Sr and Nd initial ratios, and a time-integrated $^{238}\text{U}/^{204}\text{Pb}$ (μ) composition of the source region

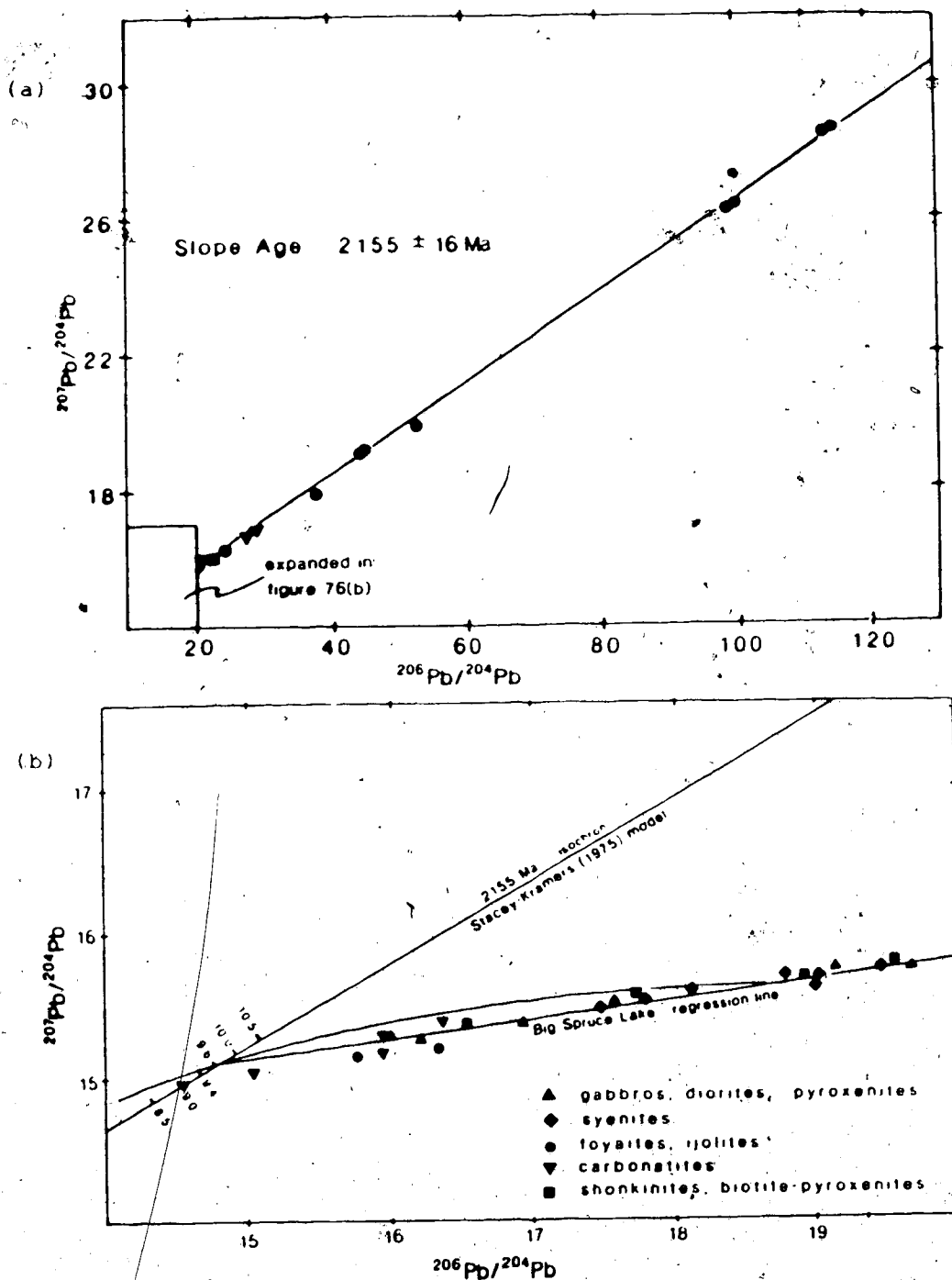


Figure 76. $^{207}\text{Pb}/^{204}\text{Pb}$ vs $^{206}\text{Pb}/^{204}\text{Pb}$ for whole rock samples from all intrusive centres.

(a) The most radiogenic samples with $^{206}\text{Pb}/^{204}\text{Pb}$ ratios from 20 to 120.

(b) Expanded version of the plot for less radiogenic samples showing intersection of the Big Spruce Lake regression line (slope age = 2155 Ma) with the Stacey-Kramers (1975) growth curve and with a 2155 Ma (S&K) isochron. Source μ values from 8.5 to 10.5 are shown on the 2155 Ma isochron line.

of the Big Spruce Lake magma(s), broadly equivalent to initial ratios of the other radioisotope systems, can be approximated by comparison of the data obtained here to a whole earth model. Values reported for source μ 's derived from measured Pb isotope ratios are strictly model dependent and none of the models currently in use has the general acceptance accorded to the chondritic reservoir hypothesis for Nd (CHUR; De Paolo and Wasserburg, 1976a and b): A source μ value will be determined first in terms of the Stacey and Kramers (1975) two-stage Pb evolution model, and then in terms of the single-stage model (Holmes, 1946; Houterman, 1946). The single-stage model postulates Pb evolution from a primordial meteoritic isotopic composition (Tatsumoto et al, 1973) beginning at 4.56 Ga (Tatsumoto et al, 1973). The Stacey and Kramers (1975) model postulates that terrestrial Pb developed in a reservoir of $\mu = 7.19$ from a primordial meteoritic composition beginning at 4.57 Ga (Tatsumoto et al, 1973) but at 3.7 Ga a major differentiation event of unspecified nature occurred giving rise to a major reservoir (the mantle) which now has $\mu = 9.74$. This major reservoir is the source of present day average Pb. Fitting of the second-stage growth line is based on data obtained from conformable Pb ore deposits of known ages.

The regression line for all samples intersects the Stacey-Kramers conformable Pb growth curve at $2190 \pm 90/-85$ Ma and at -8 Ma $-44/+148$ (errors quoted are $2\sigma/\text{MSWD}$). Intersection at the approximate age of the intrusion and at $T = 0$ indicates a mainly mantle derivation for these rocks and a two-stage Pb history for the source region, correlating directly with evolution of the $\mu = 9.74$ reservoir of the model. Figure 76 shows the regression line of all data to intersect a 2155 Ma Stacey-Kramers isochron at about $\mu = 9.65$. In discussion of Pb data the $^{207}\text{Pb}/^{206}\text{Pb}$ slope age of the intrusion is used in preference to the zircon age of 2188 Ma for internal consistency. The regression line-isochron intersection value indicates that the mean initial isotopic composition of the intrusive rocks at 2155 Ma was equivalent to derivation from a source which had a time-integrated μ of 9.65 over the interval from 3.7 Ga to 2155 Ma. For petrogenetic interpretation of WR Pb isotopic data a source μ has the same significance as initial ratios or ϵ values for the Rb-Sr and Sm-Nd systems. Interpretation of μ values is subject to the same conditions and assumptions as ϵ values, namely that

- (1) The age of intrusive activity (magma formation) is known so that the initial isotopic composition can be calculated from the present measured composition.

(2) The system has remained closed (on a hand specimen scale at least) to movement of parent and daughter elements since crystallisation.

An apparent source μ (μ_S) has been calculated for each individual sample by extrapolating the measured Pb- isotopic composition along a line of $^{207}\text{Pb}/^{204}\text{Pb}$ vs $^{206}\text{Pb}/^{204}\text{Pb} = 0.13430$ (slope age = 2155 Ma) to intersect with 2155 Ma isochron. The accuracy of the μ_S values derived in this manner, from the Stacey-Kramers model, is estimated to be about ± 0.03 and the values range from 8.8 to 10.3.

Both metasomatism and gneissic contamination have already been identified from the Rb-Sr and Sm-Nd results. To examine the possible effects of these two processes on the U-Pb system a simple leaching experiment was carried out on a group of carbonate samples, the rock type most sensitive to solution and recrystallisation with concomitant gain or loss of Pb and U. Seven sövites and two dolomite carbonatites, for which WR Pb isotopic composition were already available were selected. Each sample powder was leached with cold dilute (1:10) HCl or HNO_3 , the resulting solution was removed to a clean vessel and then the residue was decomposed following the procedure for WR samples. The Pb in each portion was purified by co-precipitation with $\text{Ba}(\text{NO}_3)_2$ followed by

anion exchange purification in the usual manner. The Pb isotopic compositions determined in this experiment are reported in Table 24, and plotted in Figures 77 and 78.

In two sövites (PC-81-185 and PC-82-088) the leachable and residual Pb have very similar compositions; the Pb is very resistant to solution and it may be readily inferred that effects of metasomatism on the Pb-isotopic compositions of these two sövites is minimal so the high apparent μ_S values for these samples, 10.1 and 9.9 respectively, represent original contamination. The REE distribution patterns ϵ_{Sr} and ϵ_{Nd} of these sövites, discussed earlier, indicate gneissic contamination of these samples, which would be consistent with slightly high μ_S values.

In four sövites (PC-81-176, PC-81-178, PC-81-383 and PC-82-506) the compositions of leachable, residual and WR Pb form lines on the $^{207}Pb/^{204}Pb$ vs $^{206}Pb/^{204}Pb$ plot equivalent to slope ages of 1670 to 1920 Ma. These four "ages" are very approximate but close to the 1800 Ma age of biotite K-Ar resetting (Leech et al, 1963; Martineau and Lambert, 1974) and Rb-Sr disturbance (Easton, 1983). In each of these samples the leachable or resettable Pb is the least radiogenic portion. This Pb component is in a readily soluble U-poor phase, possibly a carbonate such as cerussite. The most likely explanation for the

Table 24. Pb isotopic composition of leachable and residual Pb in carbonatites of the Big Spruce Lake intrusion.

204 Pb: 206 Pb: 207 Pb: 208 Pb

Sample	Leachable	Residual	Whole rock
<u>Sövites</u>			
PC-81-176	1:14.743:15.023:36.583	1:18.750:15.491:47.083	1:15.048:15.072:37.135
PC-81-178	1:15.743:15.139:38.722	1:17.363:15.298:51.648	1:15.929:15.178:40.032
PC-81-185	1:16.454:15.414:42.795	1:16.355:15.392:40.293	1:16.377:15.398:40.780
PC-81-376	1:18.409:15.724:43.509	1:15.046:15.031:42.116	1:14.478:14.931:35.091
PC-81-383	1:18.307:15.710:42.467	1:33.786:17.543:141.98	1:20.458:15.968:56.259
PC-82-088	1:15.899:15.313:42.195	1:16.027:15.315:47.228	1:15.949:15.297:44.508
PC-82-506	1:19.695:15.831:37.700	1:21.337:16.005:41.446	1:19.723:15.837:37.939
<u>Dolomite-Carbonatite</u>			
PC-82-408	1:24.496:16.604:45.644	1:31.440:17.112:43.516	1:27.152:16.754:45.067
PC-82-412	1:27.792:16.851:50.576	1:32.219:17.166:64.427	1:28.816:16.945:53.776

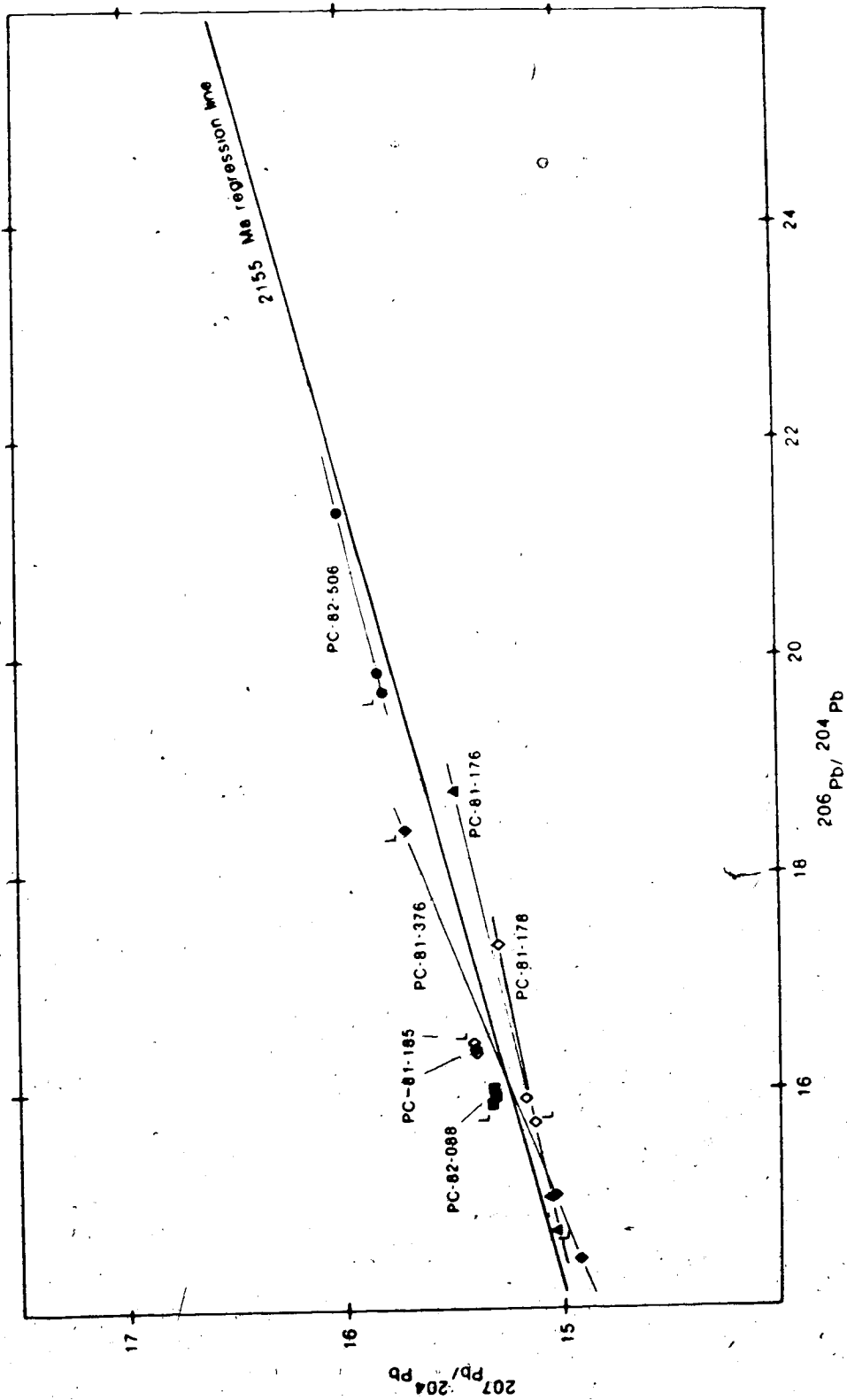


Figure 77. Isotopic compositions of leachable, residual and WR Pb in low-U sövites. Leachable Pb is indicated for each sample by L. Approximate slope "ages" are PC-81-176 = 1860 Ma, PC-81-178 = 1670 Ma, PC-82-506 = 1800 Ma, PC-81-376 = 2850 Ma.

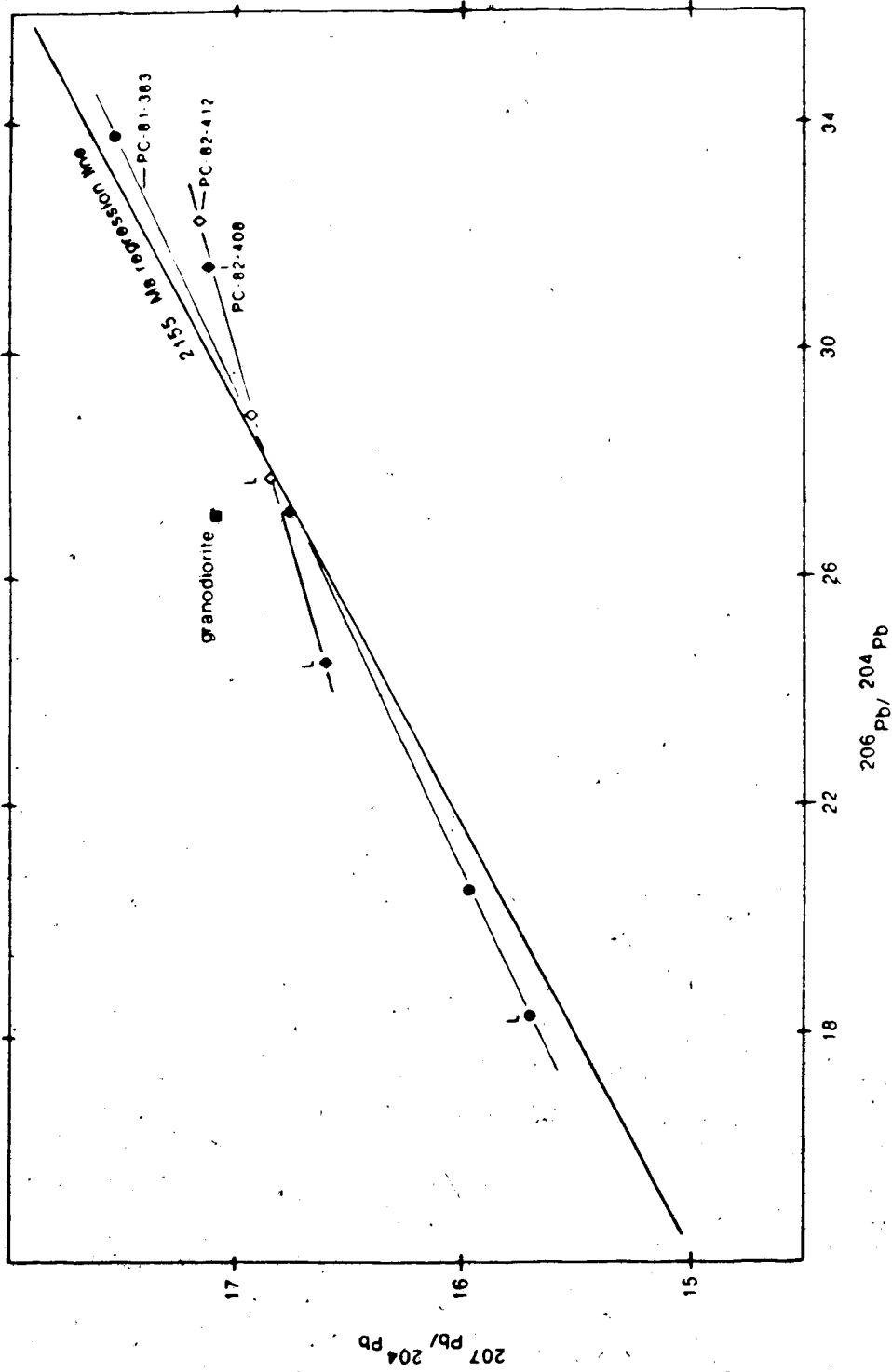


Figure 78. Isotopic compositions of leachable, residual and WR Pb in dolomite carbonatites and a high-U sövite. Leachable Pb is indicated by L. The present measured Pb-isotopic composition of granodiorite PC-82-074 is also shown. The approximate slope "age" of PC-81-383 is 1920 Ma, that of the dolomite carbonatites is 1000 Ma.

coincidence of these four "ages" is a simple WR recrystallisation or rehomogenisation at about 1800 Ma, at the same time as the biotite K-Ar was reset. Had significant movement of Pb occurred at any time between crystallisation and the present the composition of easily leached Pb would be expected to have altered to a different extent in each of these separate dykes (which have very different WR Pb compositions) producing more variable leach-residue slope "ages". Assuming then that metasomatic effects are minimal in these four dykes the apparent source μ 's represent variable initial Pb compositions due to contamination. The apparent source μ 's are 9.4, 9.4, 10.2 and 10.0 respectively.

In one sövite (PC-81-376) the easily leached Pb is more radiogenic than the residual Pb; it is especially enriched in ^{207}Pb so that the slope "age" of the leach-residue line is over 2800 Ma. The Pb of this carbonatite has been enriched at some time in the past by a very radiogenic Pb component. This dyke cuts mafic foyaites of Centre 3. Rocks of this particular unit have present μ values up to 280, sufficiently high to provide a source of radiogenic Pb at about 1800 (^{207}Pb -enriched). The apparent source μ of this sample has thus been metasomatically altered to its present value of 9.1.

Two dolomitic carbonatite samples from separate pipes cutting gneisses to the east of the main complex have leachable Pb less radiogenic than the WR compositions and the leach-residue slope "ages" are about 1000 Ma. There is no evidence for a regional metamorphic event at this time. Recent movement of Pb derived from a gneiss similar to PC-82-074, for which the present composition is plotted in Figure 78 for easy comparison with the leach-residue compositions, would enrich the leachable Pb component of the dolomite carbonatites in radiogenic Pb along a mixing line towards the gneissic composition and reduce the leach-residue slope "age" in the manner observed. If recent enrichment of dolomite carbonatite Pb by a gneissic Pb component has occurred then the apparent source μ values of these two samples, 9.65 and 9.5, have been increased from lower original values.

The original Pb isotopic composition of 3 of the 9 carbonatites tested appears to have been significantly altered by Pb movement, one enriched by highly radiogenic Pb at some time in the past (perhaps ~1800 Ma) and the other two most probably by recent movement from the host gneisses. In both cases metasomatism has increased the ^{207}Pb component of the carbonatite, thus increasing the apparent source μ . The WR Pb isotopic composition of the other 6 carbonatites is inferred, from this leaching

experiment, not to have been significantly altered from original values.

Only three events can be identified in the geologic history of this portion of the Slave craton which could have caused the variation of apparent source μ 's presently observed. These are:

- (1) Recent movement of Pb, during the present erosion cycle.
- (2) Movement of Pb and U during a very low-grade metamorphic event which reset biotite K-Ar systems at about 1800 Ma.
- (3) Contamination of magmas by upper mantle or crustal host rocks during ascent and crystallisation.

When the effects of these three processes on the Pb isotopic compositions of the various intrusive rocks are considered a probable parent magma Pb isotopic composition may be inferred.

Recent movement of U has no effect on the presently observed Pb ratios. Recent movement of Pb within the main complex alone (exchange between intrusive rocks) would result in final Pb compositions lying along mixing lines which themselves lie in a band parallel to the $^{207}\text{Pb}/^{206}\text{Pb}$ regression line (Figure 79a). Because of the wide range in $^{206}\text{Pb}/^{204}\text{Pb}$ in the intrusive rocks recent movement within the complex would be dominantly along the x axis of

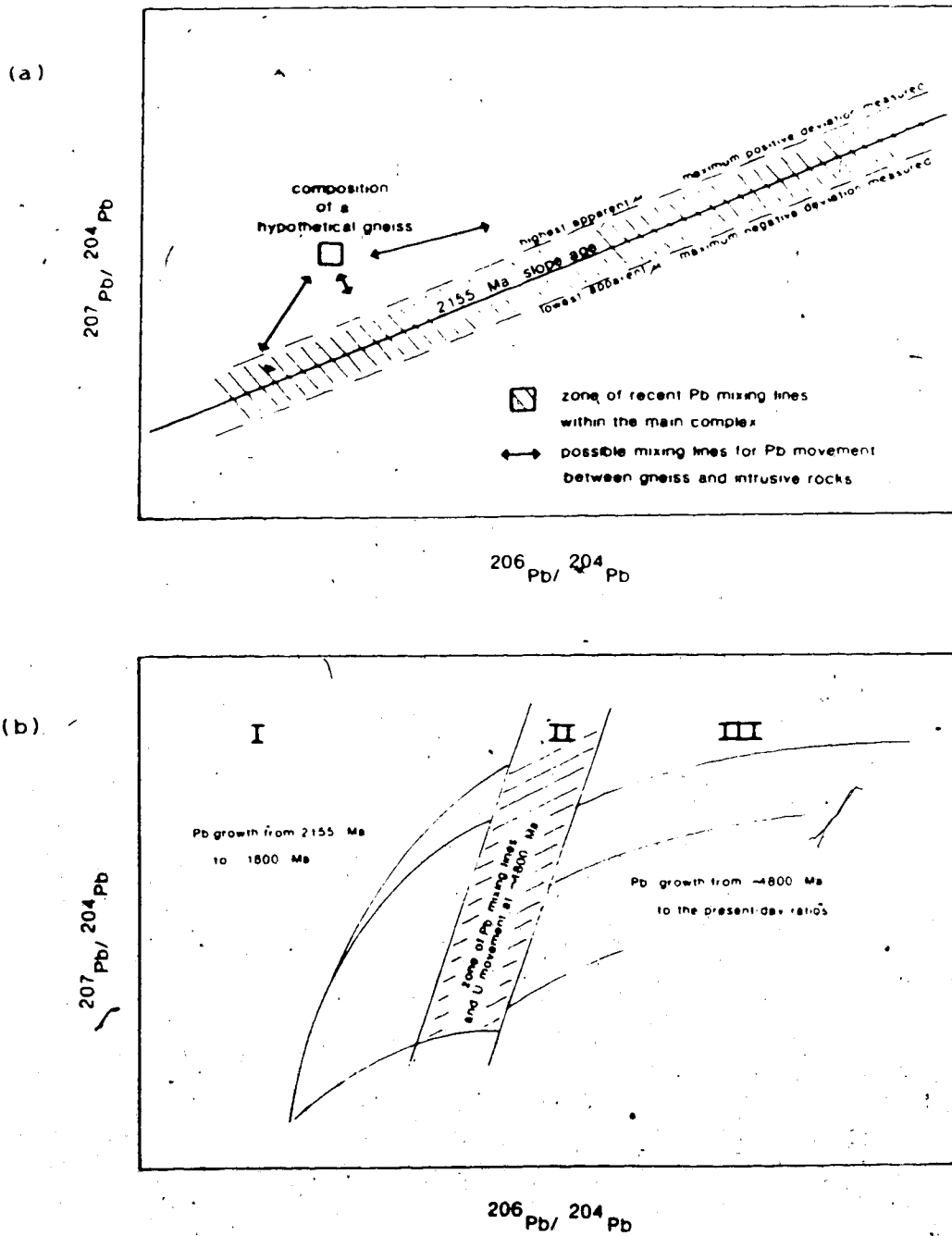


Figure 79. (a) Effects of recent movement of Pb on measured Pb-isotopic compositions. Major variations in $^{206}\text{Pb}/^{204}\text{Pb}$ result.
 (b) Effects of post-crystallisation (~ 1800 Ma) disturbance of U and Pb. The dominant effect is variation of $^{207}\text{Pb}/^{204}\text{Pb}$.

a $^{206}\text{Pb}/^{204}\text{Pb}$ plot, subparallel to the regression line. Recent addition of Pb from outside the complex, gneissic Pb, would result in mixing lines leading from any point within the band of scattered data points upwards (increasing the relative ^{207}Pb content) towards the gneissic composition. Recent gneissic contamination is expected to be greatest in the small isolated bodies of dolomite carbonatite of Centre 4 and the shonkinites and biotite pyroxenites of the satellite intrusion.

A U-Pb mixing event at about 1800 Ma, both within the complex and between gneiss and intrusive rocks, would have similar effects with two main differences. Old intra-complex Pb exchange had a larger relative ^{207}Pb component so that mixing between intrusives caused data points to scatter more widely on the y axis, Figure 79b. The second difference is that growth of Pb from the time of disturbance to the present, in rocks of widely variable U contents, retains and enhances variations caused by the earlier movement of both U and Pb. It is notable that the greatest deviations from the regression line, both negative and positive, are those in sample rocks from Centre 3 and from the closely associated sôvites, units with highest and lowest U contents. Small movements of U-Pb within the complex at about 1800 Ma could easily account for the observed data scatter although highly

localised movement of Pb from the host gneisses must also have occurred in conjunction with the Rb-Sr movement inferred from the Sr isotope compositions.

It follows from the foregoing discussion that the least radiogenic intrusive rocks are the most likely candidates from which to infer a limiting parent magma or source region Pb isotopic composition. Old addition of Pb from any source to a rock which itself has a very small U content is likely to have increased the ^{207}Pb component and hence the apparent source μ . Recent addition would have had little effect on the apparent source μ values. Of the ten least radiogenic samples analysed in this study five have apparent source μ values of 9.2 to 9.4, well below that of the regression line at 9.65 (Figure 76). Three non-radiogenic silicates, two from Centre 1 and one from Centre 3, have values very close to the mean, 9.55 to 9.85. The other two non-radiogenic samples are the sövites (PC-81-185 and PC-82-088) for which other evidence indicates significant gneissic contamination. The least radiogenic sample of all is sövite PC-81-376, and it has the lowest apparent μ of this group. The leaching experiment (outlined earlier) indicated that old soluble radiogenic Pb had been added to this sample and had raised the apparent source μ from some lower value to the present $\mu = 9.1$. A range of 9.2 to 9.4 is considered as a

reasonable approximation to the μ of the magma source region and μ could have been slightly lower still on the basis of PC-81-376. Internal consistency within this group of non-radiogenic samples suggests minimal crustal Pb contamination for them.

Assuming that a μ value of 9.2 to 9.4 is representative of the magma(s) which had least contamination by host gneiss Pb then the mantle source region from which the magmas were derived was depleted in U relative to the $\mu = 9.74$ source of conformable Pb (Stacey-Kramers model).

For the single-stage Pb evolutionary model described earlier a source μ can be derived in exactly the same manner as that outlined for the Stacey-Kramers model. The value obtained for μ is 7.9. Lambert (1985) has suggested that if any primitive mantle still exists then the μ of this reservoir would be about 8.0, indicating that the Big Spruce Lake magmas were derived from a reservoir which had previously been depleted in U relative to Pb. Other authors (Doe and Zartman, 1979; Zartman and Doe, 1981)^o have postulated a dynamically evolving earth in which a mantle (to 500 km depth) interacts with upper and lower crustal reservoirs to produce the observed pattern of Pb isotopic compositions. This model has no single differentiation event comparable to the 3.7 Ga

differentiation of the Stacey-Kramers model and hence is a variant of single-stage evolution. In this model the mantle, upper crust and lower crust reservoirs now have $\mu = 8.35, 13.23$ and 6.29 respectively, changed only slightly from 2.2 Ga (time of intrusion) when they were approximately $8.0, 12.6$ and 6.1 respectively. Again it is clear that the $\mu 7.9$ source of the Big Spruce Lake complex is slightly below that of the mantle, trending towards that of the lower crust.

No systematic difference in source μ is discernible between different rock types analysed in this study and it must be inferred that carbonatites and associated silicate rocks, silica saturated and undersaturated, were derived from Pb-isotopically similar source regions. The gabbro-syenite series which differentiated in chambers within the crust and the small satellite intrusive bodies have been contaminated to a greater extent by crustal Pb than have carbonatites and some of the leucocratic rocks of Centre 3. Lancelot and Allegre (1974) similarly found that the Pb-isotopic composition of carbonatites from the Cape Verde Islands, Canary Islands, Morocco and Uganda fall in the same field of $^{207}\text{Pb}/^{204}\text{Pb}$ vs $^{206}\text{Pb}/^{204}\text{Pb}$ as do alkali basalts and alkalic rocks from the same Atlantic islands. The depleted mantle source region for all Big Spruce Lake rock types inferred here from WR Pb data is in

agreement with WR Rb-Sr and Sm-Nd data for the same rocks. A subcontinental depleted mantle source is in agreement with a subcontinental LIL element depleted source region inferred by Bell et al (1982) and Grunenfelder et al (1982) from Rb-Sr data and WR Pb data respectively for the 120 Ma Oka Quebec carbonatite complex.

G. Summary and Conclusions

Minor contamination by gneissic country rock (affecting initial ratios) and later metasomatism contribute to variability in measured Sr, Nd and Pb ratios for WR samples. The two more coherent systems, Sm-Nd in which both parent and daughter are rare earth elements and $^{207}\text{Pb}/^{206}\text{Pb}$ in which parents and daughters are isotopes of the same elements, show variability which appears to be random about a mean value in such a manner that regression of WR data yields an age which correlates with those determined by other WR systems and by zircon U-Pb analyses. Only the Rb-Sr system in which parent and daughter elements are geochemically dissimilar yields a different age.

Pb data from carbonatites indicates two episodes of minor post-crystallisation movement of U and Pb, one about

1600 to 1900 Ma and the other recent. The severity of open-system disturbance of WR systems was in the order

Rb-Sr > Pb-Pb > Sm-Nd

correlating with the geochemical coherence of each system. An age of 1600 to 1900 Ma for the earlier metasomatic event (from Pb data) correlates with an age of 1800 Ma obtained earlier for resetting of biotite K-Ar (Leech et al, 1963, Martineau and Lambert, 1974). Sample to sample variation indicates that the effects of metasomatism on Sr, Nd and Pb isotopic compositions were highly localised.

Minor contamination by host granodioritic gneisses has affected element and isotopic compositions of carbonatites and associated alkaline intrusive silicate rocks.

Model ages and initial ratios calculated for an intrusive complex from analysis of a single sample by assuming negligible contamination on the basis of

- (a) rapid emplacement,
 - (b) high concentration of daughter element in the parent magma buffers contamination effects,
- are not valid. Assimilation of variable amounts of crustal rocks can affect Rb-Sr, Sm-Nd and U-Pb systems in

all rock types even when the rocks are very enriched in Sr, REE and/or Pb. Several samples from a complex must be analysed to obtain a valid initial ratio or model age.

The five separate stages of the Big Spruce Lake intrusion have not been separated in time by Sm-Nd, Pb-Pb or R-Sr methods. The maximum interval between emplacement of successive units is probably that between saturated and undersaturated units, Centres 2 and 3. Present zircon and WR Pb-Pb data indicate that these two units are coeval within error; however, the interval between them could be up to 30 million years when errors are considered. Similar intervals between emplacement of the other units would require a total of 90 to 100 million years for emplacement of the entire complex. Such a timespan is unlikely in view of the rapid emplacement of diverse alkaline magmas of the modern African Rift Valley. The main Big Spruce Lake complex was probably emplaced over an interval of less than 50 million years.

The age of crystallisation of the Big Spruce Lake intrusion is best defined by the zircon age of the syenites, $2188 \pm 16/-10$ Ma. Pb-Pb data for WR samples gives an age of 2155 ± 16 Ma, and Sm-Nd gives the age of 2183 ± 75 Ma.

No separate age can be assigned to the satellite complex on the basis of present data and it must be

assumed to be coeval with the main complex although it may be younger. Large errors on both the WR Rb-Sr age (1848 ± 90 Ma) and the $^{207}\text{Pb}/^{206}\text{Pb}$ age ($1915 \pm 165/-175$ Ma) (errors quoted in this study are $2\sigma/\text{MSWD}$) allow them to overlap with each other. The Pb-Pb date but not the Rb-Sr date overlaps with that of 1980 ± 40 Ma (error = 1σ) determined by Martineau and Lambert. If the true age of this centre is 1800 to 1900 Ma then the isotopic compositions indicate a significant crustal component to Sr, Nd and Pb, contrary to element composition results of Chapter 3.

The surrounding granodioritic gneisses have Sm-Nd model ages ranging from 2467 to 2595 Ma if calculated using chondritic parameters from Jacobsen and Wasserburg (1980, 1984) but 2866 to 2968 Ma if calculated using the depleted mantle parameters (DM) outlined by Goldstein et al (1984).

The variability of measured Sr, Nd and Pb isotopic compositions due to original contamination and later metasomatism precludes determination of separate initial ratios for each individual centre of intrusive activity. Both variability and the ratios measured are independent of rock type and composition, and no systematic difference between centres can be discerned in calculated initial Sr, Nd or Pb compositions. The parent magmas (silica-saturated, silica-undersaturated and carbonate) which

reached the upper crust were isotopically very similar (with $\epsilon_{\text{Sr}} = -10$, $\epsilon_{\text{Nd}} = +3$ and $\mu = 9.2$ to 9.4), derived from an isotopically homogeneous source region.

Whole rock Sr, Nd and Pb data for all intrusive rocks in the Big Spruce Lake complex clearly indicate that a LIL element depleted source was present under the Slave craton at the time of magma formation, 2188 Ma. The depleted mantle component may have existed at upper mantle/lower crust levels and have been assimilated by ascending magma derived from a deeper source with chondritic isotopic character, or the depleted mantle component may lie at depth as the original non-chondritic source of parent magma. The present data do not allow an unequivocal distinction to be made between the two possibilities but are slightly in favour of the latter.

CHAPTER 5

PETROGENETIC RELATIONSHIPS: SUMMARY AND CONCLUSIONS

A. Relationship to the Surrounding Area

Sorensen (1974) defines a group of alkaline complexes which "lie in tectonically quiet regions" with "specific locations controlled by deep faulting". The Big Spruce Lake alkaline intrusion belongs to this group. The intrusion lies in a lobe of the Slave structural province composed of granitic to granodioritic gneiss surrounded largely by metamorphosed Yellowknife supracrustals. The age of the host gneisses has been set at 2500 to 2600 (Sm-Nd CHUR model age), although they could be older if the age is calculated on the basis of a depleted mantle composition (Goldstein et al, 1984). In that case the gneisses are up to 2900 Ma. Rb-Sr and U-Pb age determinations for sialic basement elsewhere in the Slave craton (Nikic et al, 1975; Frith, 1978; Krogh and Gibbins, 1978) have identified crust of about 2.9 to 3.1 Ga.

The boundary of the Slave structural province with the younger Bear province (~1800 to 1900 Ma) is placed just 30 km to the west (Fraser et al, 1972).

Both the main complex and the enclosing gneiss are cut by the Snare fault, whose strong north-south expression on aerial and Landsat photographs (Figure 80) suggests that it is deep and near vertical. The fault was mapped, in part, by Lord (1942) who considered it to be vertical with sinistral movement. An offset of about 0.7 to 1.0 km has occurred in metasediments of the Yellowknife Supergroup at a point 12 km north of Big Spruce Lake. The age of the Yellowknife metasediments has been placed at about 2400 to 2600 Ma (Leech, 1963) and movement on the fault is clearly later. The age of the intrusion has been placed at 2188 Ma (U-Pb zircons, this study). Major movement along the Snare fault to produce the lineament visible in Landsat photos and to form a conduit for deep magmatism must have occurred prior to emplacement of the complex where no significant post-intrusive lateral movement can be observed.

The Snare fault was active during at least part of the intrusive activity. Several items of field evidence in support of this statement have been cited by Martineau (1970). Although little post-intrusive lateral movement can be positively identified from field evidence, activity probably continued on the main fault system at least long enough to shear the units of the complex which span the fault zone. Lord (1942) in his observations of exposures

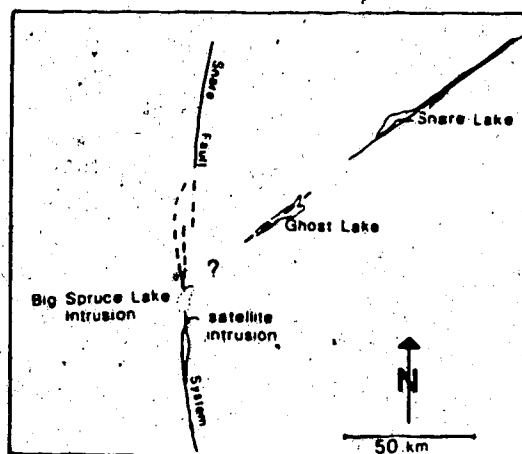
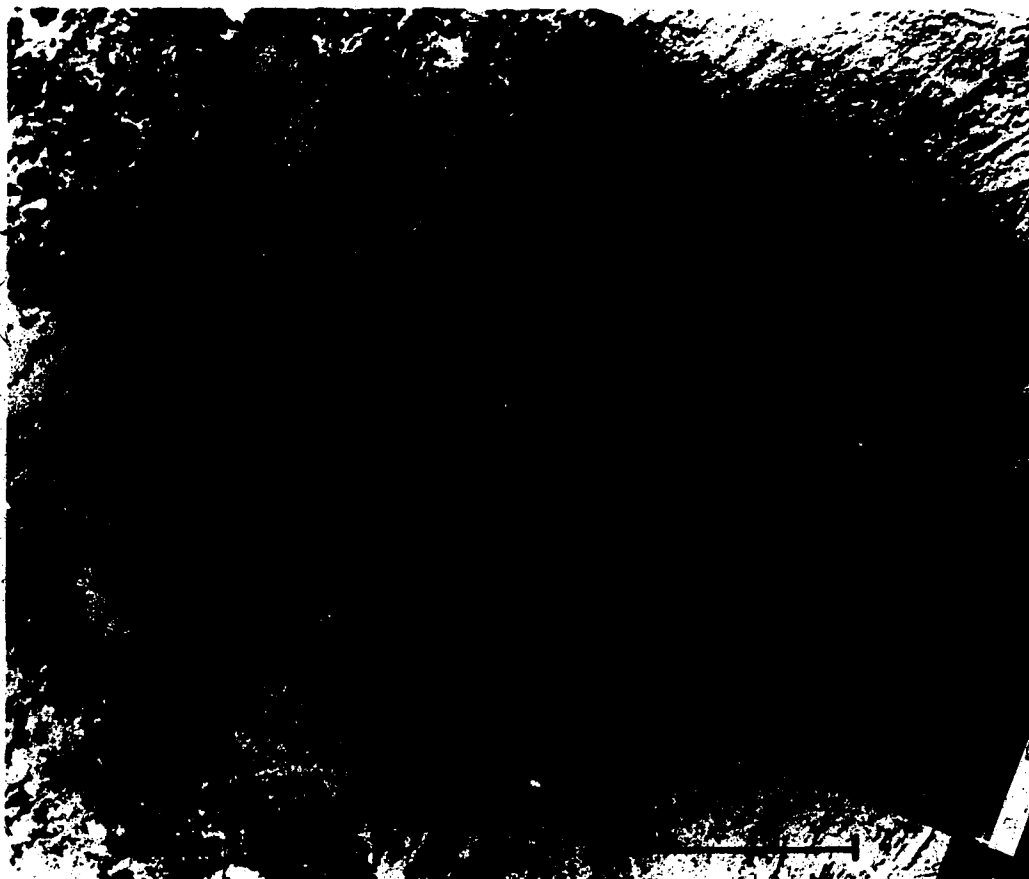


Figure 80. Composite Landsat photograph of the area around the Big Spruce Lake intrusion and legend showing the principal features. No expression of the major "Ghost Lake lineament" is visible around Big Spruce Lake.

now covered by a higher water level noted that crushed syenitic and granitic rocks occurred on a small island near the north end of the lake and he placed the fault zone through this island (Seagull Island, on the accompanying sample locations map). The presence and shape of the lake itself at the centre of the complex suggests a post-intrusive weakness in the rocks below. Cessation of movement along the Snare fault soon after emplacement of the complex may account for the lack of other nephelinitic bodies along this line.

Martineau (1970) suggests that the complex lies at the intersection of the Snare fault with a second major fault trending roughly north-east to south-west (Figure 81). While this may indeed be so, and a computer assisted analysis of the aeromagnetic data for the Big Spruce Lake area suggests (Samson, pers. comm., 1981) that an east-west structure of some kind played a part in the emplacement of the complex, there is at present no direct evidence for a second major fault of similar magnitude to the Snare. Examination of Landsat photographs which have become available since Martineau's work do show a very strong lineament trending north-east from Big Spruce Lake through Ghost Lake (40-50 km away). It continues along the Snare River channel where it was mapped by Lord (1942) as a fault at a distance of 80-100 km from Big Spruce

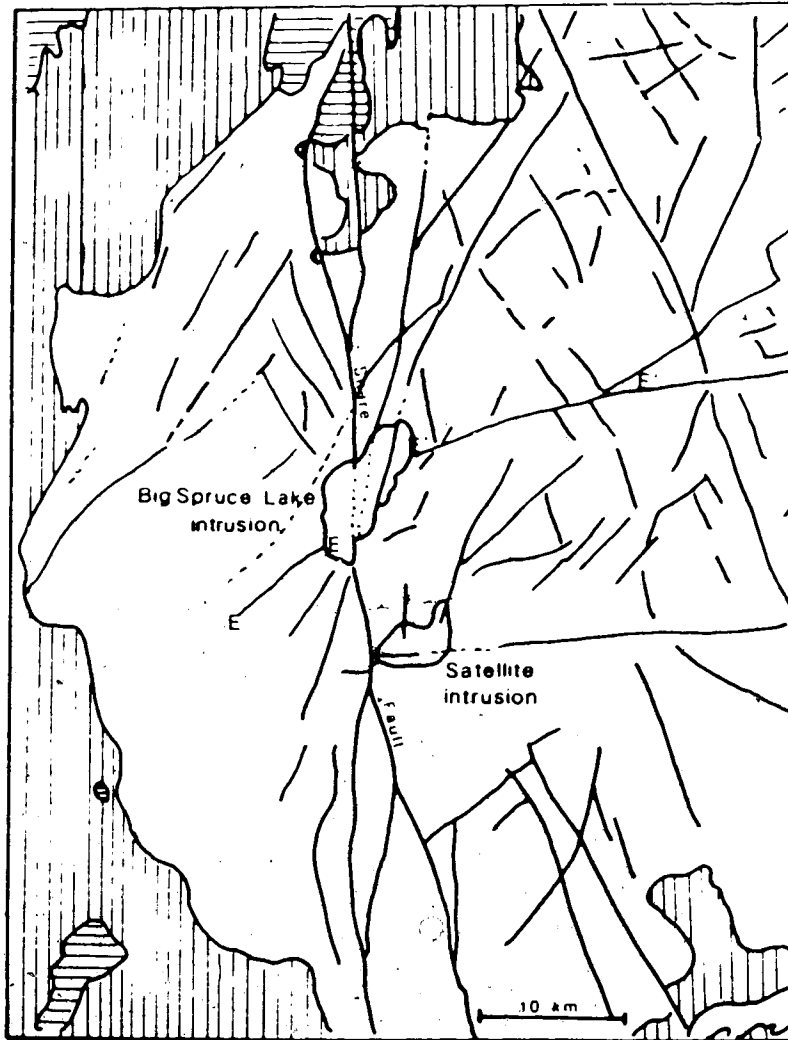


Figure 81. Fault lines around the Big Spruce Lake intrusion (redrawn from Martineau, 1970). The intrusion lies at the intersection of the Snare fault and a much smaller NE-SW fault, E-E'. Slave province metasediments are shown in vertical crosshatching, the younger Snare group by horizontal crosshatching.

Lake. However, no part of this fault has yet been mapped nearer than 80 km from Big Spruce Lake, (G.S.C. Open File Map #445, 1977) and perhaps more significantly, no expression of it around Big Spruce Lake is visible in the Landsat photographs. No northeast trending fault, comparable in size to the Snare fault, passes through the complex.

The fault actually outlined by Martineau (1970) is a smaller, more localised phenomenon which does indeed intersect the Snare fault at Big Spruce Lake and may have helped to control the location of the intrusion.

Field observations suggest a third possibility for structural control over emplacement location. The major or deep Snare fault appears to shift its position slightly as it passes through Big Spruce Lake, exiting at the south end somewhat to the east of the line on which it enters from the north. While this shift could be due to offset by a cross-cutting fault it is unnecessary to have a second fault present. Faults of all sizes can, due to inhomogeneities in the crust, divide into a series of smaller parallel fractures connected by local cross-cutting fractures. Such a development would form a zone of block faulted crust. Had this occurred on the major Snare fault, it alone could form a conduit or zone of weakness for emplacement at Big Spruce Lake.

The satellite intrusion lies away from the Snare fault along an east-west fault which is quite separate from any which might have influenced emplacement of the main complex.

The exact nature of structural control over the location of the Big Spruce Lake intrusive complex cannot be deduced from the present evidence and more detailed speculation is unwarranted at this time.

An age of $2188 \pm 16/-10$ Ma (U-Pb zircon of syenites) is considered the most reliable for the age of crystallisation of the main complex although the timespan required for emplacement of all units could have been as much as 50 million years. No separate age can be assigned to the satellite intrusion. It is inferred to be essentially coeval although it may be younger.

The presence of the intrusion and the Snare fault suggest that an episode of continental rifting may have begun about 2200 Ma and ended shortly after intrusive activity ended. The intrusion is closely correlated in age with the Hearne Channel Granite, the older alkaline phase of the Blachford Lake Intrusive suite which lies at the southern edge of the Slave province. A zircon age of 2175 ± 5 Ma was recently reported for this body (Bowring *et al.*, 1984). The Simpson Island dyke, an alkali gabbro body lying along the East Arm of Great Slave Lake, is also

apparently of the same age (Burwash and Baadsgaard, 1962; Leech et al, 1963) but any relationship among these three bodies is tenuous at best. A successful rift does appear to have developed, somewhat later, 30 km west of the Big Spruce intrusion and the Snare fault to form the present western edge of the Slave province (Hoffman, 1974, 1980). The age and timespan of the surprisingly brief Wilson cycle which followed, 1900 to 1885 Ma (Hoffman and Bowring, 1984; Bowring and Van Schmus, 1984) suggest that this rifting had little connection with the emplacement of the Big Spruce Lake intrusives 300 Ma earlier.

B. Magma Types and Sources

It can be concluded on the basis of field evidence and analytical results from this study (and from Martineau, 1970) that four discrete magma types, present at different times, formed the diversity of rock types presently exposed in the Big Spruce Lake complex. These were:

- (1) A Na-rich "wet" alkali basalt melt which formed intrusive Centres 1 and 2 in the northeastern corner of the complex.
- (2) A Na-rich, highly carbonated leucocratic melt (with low Fe^{2+}/Fe^{3+} , low Al/alkali, low Si/alkali) which

formed Centre 3, in the centre and southwestern portion of the complex.

- (3) Carbonatite melts, Ca-rich and Mg-rich varieties of which formed dykes and pipes within and adjacent to the nephelinitic rocks (intrusive Centre 4). Carbonatite and nephelinitic melts were interdependent, closely associated in space and time.
- (4) A mildly silica-undersaturated K_2O and LILE-enriched mafic melt which formed the potassic satellite intrusion, Centre 5.

Diversity of rock types was increased by cumulate formation and crystallisation of multiple batches of magma, each evolving along slightly different paths as a result of slight differences in original composition, degree of crustal contamination, rate of heat loss, pressure, etc.

None of these magmas was derived from crustal rocks. The Nd, Sr and Pb isotopic compositions of all rock types characterise a mantle source although minor crustal contamination and metasomatism obscure any possible small differences in isotopic compositions of the various parent melts. The source mantle material had a time-integrated LIL element depletion prior to magma formation with $\epsilon_{Nd} = +3$, $\epsilon_{Sr} = -10$, and $\mu = 9.2$ to 9.4 . The Nd isotopic composition of the mantle source of the

Big Spruce Lake magmas, $\epsilon_{Nd} = +3$, is not that of the depleted mantle component inferred by some workers to be the source of both ancient and young crustal rocks (Goldstein et al, 1984). This generalised depleted mantle component is postulated to have had a linear development from $\epsilon_{Nd} = 0$ at 4.5 Ga to $\epsilon_{Nd} = +10$ at present (MORB values) and would have had $\epsilon_{Nd} = +5$ at the time of Big Spruce Lake activity. Strictly linear development of the mantle isotopic composition is unlikely in view of the episodic nature of crustal development. An age of about 3100 Ma has been determined for parts of the Slave craton (Firth, 1978; Krogh and Gibbins, 1978). If an originally chondritic mantle reservoir (CHUR) was depleted at that time, and if this depletion was sufficient to create a reservoir of $\epsilon_{Nd} = +3$ at 2200 Ma, then such a reservoir would have a present day $\epsilon_{Nd} = +11$, i.e., near MORB values. The magnitude of the Sr depletion of the Big Spruce Lake source region is in agreement with Sr depletion in the source region of carbonatites of the southern Canadian Shield. Bell et al (1982) postulated that a major differentiation event may have occurred beneath that region at about 2700 Ma and is recorded by the Sr isotopic compositions of mantle-derived carbonatites. The initial $^{87}Sr/^{86}Sr$ composition of the Big Spruce Lake carbonatites of the Slave province plots

on the same evolution line as those for the younger southern carbonatites.

The isotopic evidence alone cannot discriminate between two possible mechanisms for magmas generated from the depleted mantle which reached the upper crust and were then variably contaminated. These two mechanisms, which were discussed in earlier sections are, derivation of all magmas from a source which was itself slightly depleted, or derivation from an undepleted mantle source region followed by assimilation of an upper depleted mantle layer during ascent prior to emplacement within the gneissic host rocks. Uniformity of isotopic compositions, in spite of wide differences in magma type and reactivity, suggest (but are not proof) that greater variability of initial ratios would be noted in the isotopic ratios if significant amounts of depleted mantle were assimilated during ascent. It is likely that silica-saturated or mildly undersaturated basaltic magma would react with a depleted mantle layer underlying continental crust (two-layer theory of Wasserburg and DePaolo, 1979) to a much different extent than would carbonated, alkalic, strongly silica-undersaturated melts or carbonate melts. The present evidence is thus slightly in favour of an original, deep source depletion, and relatively rapid ascent to the upper gneissic crust for final emplacement.

The enrichment of incompatible elements and the fractionation of more incompatible/less incompatible elements indicates that none of the parent magmas can be derived by direct partial melting of a mantle composition (spinel lherzolite or garnet peridotite) with chondritic abundances of the incompatible elements. All parent magma compositions require either an enriched source composition, which would be in conflict with the depleted source region defined by isotopic results, or source region metasomatism to enrich and to fractionate LIL elements immediately prior to or concurrent with magma formation. In addition, a separation of alkali elements, Na from K (plus Rb, Cs) is required by the parent composition of the satellite intrusion.

The alkali gabbro-syenite series of intrusive Centres 1 and 2 is not related to the foyaite-ijolite suite of Centre 3 through assimilation of granodioritic host rock by foyaitic-magma to form gabbros and syenites. This process is suggested for some alkalic complexes which begin with saturated and end with undersaturated units (e.g., Kanqerdluqssuaq, East Greenland, Pankhurst et al., 1977; Brooks and Gill, 1982). It is precluded for the Big Spruce Lake complex by isotopic systematics. The saturated and undersaturated series of the main complex might be related to each other as widely different

crystallisation series of similar but not identical primitive magmas. Amphibole fractionating from a "wet" alkali basalt would give rise to the syenite series whereas extensive crystallisation of olivine and aluminous clino-pyroxene (but not amphibole) from a dry, carbonated, highly oxidised alkali olivine basalt magma could produce the foyaite-ijolite suite. In this model different crystallisation paths resulting from widely different volatile contents could produce the two series from similar magmas. In an alternative model, widely different parent magmas could be produced from a single mantle source region by differing degrees of partial melting (Frey et al, 1978), alkali olivine basalt by 7-15% melting and a (carbonated) nephelinite by 5-7% melting. In this case the two series are related by variable partial melting processes.

The carbonatites are inferred to be related to the foyaite-ijolite suite by carbonate/silicate melt immiscibility following extensive fractional crystallisation of the carbonated silicate melt (alkali olivine basalt or nephelinite).

The origin of the satellite complex remains somewhat enigmatic. Its age relative to that of the main complex cannot be well constrained by any of the presently available radiometric systems. Rb-Sr and Pb-Pb WR data is

imprecise and uncorrelated. The dates obtained by Rb-Sr in this study and by Martineau and Lambert (1974) for the satellite complex differ by 100 Ma and are not considered reliable because of subsequent Rb-Sr disturbance.

Similarity of compositions of all bodies of this unit provide an inadequate range of Sm/Nd for an isochron. No zircons have been found from this intrusion. Either this unit is a part of the main intrusive activity at about 2188 Ma or it is a result of a recurrence just 5 km away but over 200 Ma later.

The petrogenesis of this satellite intrusion thus must be considered in terms of processes which could have produced the sodic and potassic intrusions concurrently as well as in terms of consecutive processes which could generate potassic magma at some time after the sodic series.

By direct analogy with studies of alkali basalt genesis, simple partial melting of spinel lherzolite or garnet peridotite mantle material with near chondritic REE abundances cannot produce a magma such as that of the satellite intrusion. The potassic magma is even more LILE-enriched and LILE-fractionated than the alkali basalt series (Kay and Gast, 1973; Sun and Hanson, 1975b; Frey et al, 1978). From an experimental study of a highly potassic magma, Edgar et al (1976) concluded that the

primary melt could not be a partial melt of average pyrolite (ol-opx-cpx-gar), but required the absence of orthopyroxene and garnet and the presence of mica in a source region. It could be derived by partial melting of an olivine-clinopyroxene-phlogopite-ilmenite assemblage (a mica peridotite). A later study (Edgar and Condliffe, 1978) indicated that K-rich ultramafic magmas could be generated by partial melting of peridotitic mantle; however, LILE-enrichment patterns largely preclude this mechanism for the Big Spruce Lake satellite intrusion. The existence of a heterogeneous mantle has been inferred to exist beneath Africa, which has a long history of igneous activity. The presence of mica pyroxenite xenoliths in potassic extrusive rocks is evidence that such assemblages exist within the mantle (Carmichael, 1970); Dawson et al, 1970). Discrete, atypical mantle source regions of mica peridotite could be established by partial melting or migration of minor melt or fluid phases within the mantle prior to generation of potassic melts. Alternatively, the necessary enrichment of the mantle source region could occur through migration of minor melt or fluid phases at the time of potassic magma generation.

The Big Spruce Lake complex is an isolated occurrence and not part of a larger igneous province whose development might have created mantle inhomogeneity.

Because the satellite intrusion is coeval or later than the main intrusion, it may be inferred that the mantle processes which created the enriched source for potassic magma were closely connected with intrusion of the main complex. Consecutive emplacement of main and satellite intrusions would have the potassic magma generated by partial melting of a mantle source previously enriched by fluids or partial melt formed during the main intrusive activity. Concurrent emplacement requires that mantle source region enrichment and magma generation, sodic and potassic, were coeval. Le Bas et al (1977) suggested, from fluid inclusion studies, that a potassium-rich silicate phase was present among early immiscible liquids during carbonatite formation. The Big Spruce Lake complex contains a typical nephelinite-carbonatite association, and the early separation of a potassic silicate phase during carbonatite formation could account for the source of the potassic suite. This is a reasonable explanation for the observed $\text{Na}_2\text{O}-\text{K}_2\text{O}$ separation and does not require a separate metasomatic event to produce the K_2O -rich mantle source.

C. Generalised Model

Compositional and isotopic constraints on the source

region are readily reconciled by a two-stage model in which isotopic compositions are altered by LILE depletion prior to 2188 Ma, and element compositions are altered by LILE-enrichment (and fractionation) at the time of magma formation. The LILE-depleted source which lay beneath the Slave craton at 2188 Ma could have been created by a differentiation episode at any earlier time. A likely time range during which differentiation may have occurred is 3100 Ma (age of old Slave craton crust, Nikic et al., 1975; Krogh and Gibbins, 1978; Frith, 1978) to about 2700 Ma (differentiation beneath the Southeastern Canadian Shield; Bell et al., 1982).

The isolation of the Big Spruce Lake complex from other intrusive events, its highly localised character with strong structural control over location, and derivation of diverse parent magmas from an isotopically homogeneous mantle source region all suggest that the intrusion is the result of a single mechanism which itself can generate a variety of magma types at a single location.

A possible generalised model is that proposed by Wyllie (1980) for the origin of kimberlites by diapiric action in the mantle. This model is based on an interpretation of peridotite-CO₂-H₂O melting relationships, much of which is summarised in Wyllie

(1979). In the diapiric model, CO_2 - and H_2O -rich volatiles rise from deep within the mantle, triggered by a minor thermal perturbation (Figure 82). When the rising volatiles meet the peridotite solidus at about 260 km depth (point A) they cause partial melting. This in turn produces a density inversion and light partial melt rises, adiabatically, to meet the solidus again, this time at point B. There it crystallises, with the evolution of CO_2 -rich vapours. These vapours explosively propagate fractures of the lithosphere to form a conduit to the surface. An initial episode of partial melting and crystallisation could be followed by one or more episodes in which partial melting could occur at any depth along A-B or C-surface and to any degree. Rising magma would not be impeded by the solidus at point B but could rise directly to the surface along the conduit already opened up. In his initial model Wyllie pointed out that kimberlitic magma would be formed by partial melting at depth and could rise explosively and sporadically directly to the surface. Adaptation of this model to the Big Spruce Lake intrusion would have the initial thermal perturbation (to trigger movement of deep mantle volatiles) related to action on the Snare Fault prior to magmatic activity. Rising mantle volatiles which are an integral part of this model readily account for LILE-

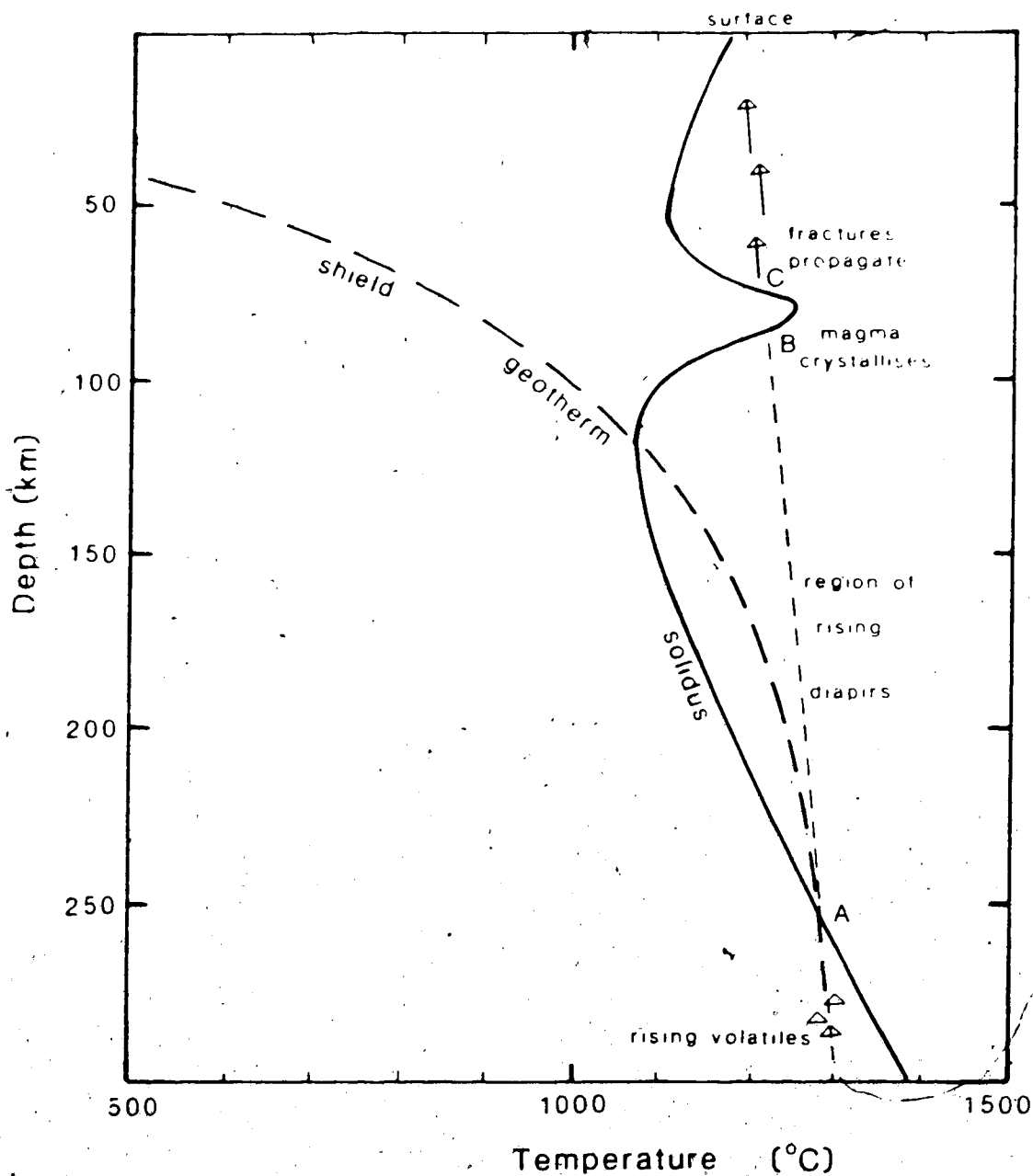


Figure 82. Sketch of a diapiric model for generation of the Big Spruce Lake complex, based on Wyllie (1980). The solidus shown is for periodotite with <5% CO_2 and <0.4% H_2O , in the proportions $\text{CO}_2/(\text{CO}_2+\text{H}_2\text{O}) = 0.8$. The shield geotherm is from Solomon (1976).

enrichment of the mantle within and around the diapiric column (mantle metasomatism) and for the LILE-enrichment and fractionation of magmas. This enrichment and fractionation must occur at or immediately prior to magma formation to produce the observed abundances yet maintain the Sr, Nd and Pb isotopic compositions derived from the original depleted mantle. From melting episodes at various depths a wide variety of magmas could form over a short timespan and at a single location. All components of the rising magmas are mantle-derived and hence isotopically homogeneous melts reach the upper crust. Some carbonatite melts could result directly from melting in this model (Wyllie, 1980), but some may also arise as a result of liquid immiscibility following fractional crystallisation of a CO₂-rich alkaline melt. This seems to be the case for the Big Spruce Lake intrusion. The potassic satellite intrusion would result from separation of K-rich fluids or melt as outlined above.

Wyllie's original model (1980) was based on interpretation of results from experimental petrology, but the same general model can be applied to the Big Spruce Lake natural system to account for field observations and analytical results.

REFERENCES

1. Allegre, C.J., Ben Othman, D., Polve, M. and Richard, P., 1979. The Nd-Sr isotopic correlation in mantle materials and geodynamic consequences. *Physics of the Earth and Planetary Interiors*, **19**, 293-306.
2. Allegre, C.J., Treuil, M., Minster, J.F., Minster, J.B. and Albarede, F., 1977. Systematic use of trace elements in igneous processes. I. Fractional crystallisation in volcanic suites. *Contributions to Mineralogy and Petrology*, **60**, 57-75.
3. Apps, M.J. and Apps, K.S., 1981. A simple to use neutron activation analysis computer program. *University of Alberta Slowpoke Facility Annual Report*, p. R4.
4. Azzouzi, M., Bougault, H., Maury, R.C. and Villemant, B., 1982. Application of the "extended" Coryell-Masuda diagram to the study of the fractionation of titanium and vanadium in the Chaine des Puys alkaline series. *Comptes Rendues Academie de Science, Paris, Series II*, **295**, 117-1120.
5. Baadsgaard, H. and Lerbekmo, J.F., 1983. Rb-Sr and U-Pb dating of bentonites. *Canadian Journal of Earth Sciences*, **20**, 1282-1290.

6. Bailey, D.K. and Schairer, J.F., 1966. The system $\text{Na}_2\text{O}-\text{Al}_2\text{O}_3-\text{Fe}_2\text{O}_3-\text{SiO}_2$ at 1 atmosphere, and the petrogenesis of alkaline rocks. *Journal of Petrology*, 7, 114-170.
7. Basu, A.R. and Tatsumoto, M., 1980. Nd isotopes in selected mantle-derived rocks and minerals and their implications for mantle evolution. *Contributions to Mineralogy and Petrology*, 75, 43-54.
8. Basu, A.R. and Puustinen, K., 1982. Nd-isotopic study of the Siilinjarvi carbonatite complex, Eastern Finland and evidence of early Proterozoic mantle enrichment. *Geological Society of America Abstracts with Program*, New Orleans, p. 440.
9. Basu, A.R., Rubury, E., Mehnert, H. and Tatsumoto, M., 1984. Sm-Nd, K-Ar and petrologic study of some kimberlites from eastern United States and their implication for mantle evolution. *Contributions to Mineralogy and Petrology*, 86, 35-44.
10. Bell, K., Dawson, J.B. and Farquhar, R.M., 1973. Strontium isotope studies of alkalic rocks: the active carbonatite volcano of Oldoinyo Lengai, Tanzania. *Geological Society of America Bulletin*, 84, 1019-1030.
11. Bell, K., Blenkinsop, J., Cole, T.J.S. and Menagh, D.P., 1982. Evidence from Sr isotopes for long-

- lived heterogeneities in the upper mantle. *Nature*, **298**, 251-253.
12. Bowring, S.A. and Van Schmus, W.R. 1984. U-Pb zircon constraints on evolution of the Wopmay Orogen, N.W.T. Geological Association of Canada/Mineralogical Association of Canada (GAC/MAC) Annual Meeting. Program with Abstracts, p 47.
 13. Bowring, S.A., Van Schmus, W.R. and Hoffman, P.F., 1984. U-Pb Zircon ages from Athapuscow aulacogen, East Arm of Great Slave Lake, N.W.T. Canada. *Canadian Journal of Earth Sciences*, **21**, 1315-1324.
 14. Brooks, C.K. and Gill, R.C.O., 1982. Compositional variation in the pyroxenes and amphiboles of the Kangerdlugssuaq intrusion, East Greenland: further evidence for the crustal contamination of syenite magma. *Mineralogical Magazine*, **45**, 1-9.
 15. Brown, E.H., 1971. Phase relations of biotite and stilpnomelane in the greenschist facies. *Contributions to Mineralogy and Petrology*, **31**, 275-299.
 16. Brueckner, H.K. and Rex, D.C., 1980. K-Ar and Rb-Sr geochronology and Sr isotopic study of the Alnö alkaline complex, northeastern Sweden. *Lithos*, **13**, 111-119.

17. Burwash R.A. and Baadsgaard H. 1962. Yellowknife-Nonacho age and structural relations. Royal Society of Canada Special Publication 4, pp 22-29.
18. Carmichael, I.S.E., 1967. The mineralogy and petrology of the volcanic rocks from the Leucite Hills, Wyoming. Contributions to Mineralogy and Petrology, **15**, 24-66.
19. Carlson, R.W., 1984. Isotopic constraints on Columbia River flood basalt genesis and the nature of the subcontinental mantle. Geochimica et Cosmochimica Acta, **48**, 2357-2372.
20. Cattell, A., Krogh, T.E. and Arndt, N.T., 1984. Conflicting Sm-Nd whole rock and U-Pb zircon ages for Archean lavas from Newton Township, Abitibi Belt, Ontario. Earth and Planetary Science Letters, **70**, 280-290.
21. Cavell, P.A. and Baadsgaard, H., 1986. The age of crystallisation of the Big Spruce Lake alkaline intrusion. Canadian Journal of Earth Sciences, in press.
22. Černý, P. and Černá, I., 1972. Bastnaesite after allanite from Rough Rock Lake, Ontario. Canadian Mineralogist, **11**, 541-543.
23. Chaplin, C.E., 1981. Isotope geology of the Gloserheia Granite Pegmatite, South Norway. University of Alberta M.Sc. Thesis., 120 pp.

24. Cox, K.G., Bell, J.D. and Pankhurst, R.J., 1979.
The Interpretation of Igneous Rocks, George Unwin,
London, 450 pp.
25. Cullers, R.L. and Graf, J.E., 1984. Rare earth
elements in igneous rocks of the continental
crust: predominantly basic and ultrabasic rocks.
in: Rare Earth Element Geochemistry, P. Henderson,
Ed., Elsevier, New York, 510 pp.
26. Cullers, R.L. and Medaris, G., 1977. Rare earth
elements in carbonatites and cogenetic alkaline
rocks: examples from Seabrook Lake and Callander
Bay, Ontario. Contributions to Mineralogy and
Petrology, **65**, 143-153.
27. Cullers, R.L., Mullenax, J., DiMarco, M.J. and
Nordeng, S., 1982. The trace element content and
petrogenesis of kimberlites in Riley County.
American Mineralogist, **67**, 223-233.
28. Cumming, G.L., 1969. A recalculation of the age of
the solar system. Canadian Journal of Earth
Sciences, **6**, 719-735.
29. Cumming, G.L., Rollett, J.S., Rossotti, E.J.C. and
Whewell, R.J., 1972. Statistical methods for the
computation of stability constants. Part I -
Straight line fitting of points with the correlated
errors. Journal of the Chemical Society, Dalton
Transactions, 2652-2658.

30. Currie, K.L., 1974. The alkaline rocks of Canada. Geological Survey of Canada Bulletin #239.
31. Daly, R.A., 1940. Origin of the alkaline rocks. Geological Society of America Bulletin, 21, 87-118.
32. Dawson, J.B., 1962. Sodium carbonate lavas from Oldoinyo Lengai, Tanganyika. Nature, 195, 1075-1076.
33. Dawson, J.B., 1966. The kimberlite-carbonatite relationship. International Mineralogical Association 4th General Meeting, 1964. New Delhi, India, p 1-4.
34. Dawson, J.B., Powell, D.G. and Reid, A.M., 1970. Ultrabasic xenoliths and lava from the Lashaine volcano, northern Tanzania. Journal of Petrology, 11, pt. 3, 519-548.
35. Deans, T. and Powell, J.L., 1968. Trace elements and strontium isotopes in carbonatites, fluorites and limestones from India and Pakistan. Nature, 218, 750-752.
36. Deer, W.A., Howie, R.A. and Zussman, J., 1966. An Introduction to the Rock-Forming Minerals, Longman, London, 528 pp.
37. Deer, W.A., Howie, R.A. and Zussman, J., 1978. Rock-Forming Minerals, Vol. 2A: Single-Chain Silicates, Longman, London, 668 pp.

38. Deines, P. and Gold, D.P., 1973. The isotopic composition of carbonatite and kimberlite carbonates and their bearing on the isotopic composition of deep-seated carbon. *Geochimica et Cosmochimica Acta*, **37**, 1709-1733.
39. De Paolo, D.J., 1981. Nd-isotopic studies: some new perspectives on earth structure and evolution. *Transactions American Geophysical Union*, **62**, 137-140.
40. De Paolo, D.J. and Wasserburg, G.J., 1976a. Nd-isotope variations and petrogenetic models. *Geophysical Research Letters*, **3**, 249-252.
41. De Paolo, D.J. and Wasserburg, G.J., 1976b. Inferences about magma sources and mantle structure from variations of $^{143}\text{Nd}/^{144}\text{Nd}$. *Geophysical Research Letters*, **3**, 743-746.
42. Doe, B.R. and Zartman, R.E., 1979. Plumbotectonics I, The Phanerozoic in: Geochemistry of Hydrothermal Ore Deposits, H.L. Barnes, Ed., 2nd ed., Wiley-Interscience, New York, pp. 22-70.
43. Dosso, L. and Murthy, V.R., 1980. An Nd isotopic study of the Kerguelen islands: inferences on enriched mantle sources. *Earth and Planetary Science Letters*, **48**, 268-276.

44. Drake, M.J., 1975. The oxidation state of europium as an indication of oxygen fugacity. *Geochimica et Cosmochimica Acta*, **39**, 55-64.
45. Duke, M.J.M., 1983. Geochemistry of the Exshaw Shale of Alberta. University of Alberta M.Sc. Thesis, 186 pp.
46. Easton, R.M., 1983. Regional resetting of Rb-Sr and K-Ar isotopic systems at 1770 Ma in the Bear and Western Slave provinces. GAC/MAC, Annual Meeting. Program with Abstracts, p. A19.
47. Eby, N.G., 1975. Abundance and distribution of the rare earth elements and yttrium in the rocks and minerals of the Oka carbonatite complex, Quebec. *Geochimica et Cosmochimica Acta*, **39**, 597-620.
48. Edgar, A.D., Green, D.H. and Hibberson, W.O., 1976. Experimental petrology of a highly potassic magma. *Journal of Petrology*, **17**, 339-356.
49. Edgar, A.D. and Condliffe, E., 1978. Derivation of K-rich ultramafic magmas from a peridotitic mantle source. *Nature*, 639-640.
50. Eriksson, S.C. 1984. Age of carbonatite and phoscorite magmatism of the Phalaborwa complex (South Africa). *Isotope Geoscience*, **2**, pp 291-299.
51. Evensen, N.M., Hamilton, P.J. and O'Nions, R.K., 1978. Rare earth abundances in chondritic

- meteorites. *Geochimica et Cosmochimica Acta*, **42**, 1199-1212.
52. Ewart, A. and Taylor, S.R., 1969. Trace element geochemistry of the rhyolitic volcanic rocks, Central North Island, New Zealand. Phenocryst data. *Contributions to Mineralogy and Petrology*, **22**, 127-146.
53. Faure, G., 1977. Principles of Isotope Geology, Wiley and Sons, New York, 440 pp.
54. Ferguson, J., 1970. The differentiation of agpaitic magmas; the Illimaussaq Intrusion, S. Greenland, *Canadian Mineralogist*, **10**, 335-349.
55. Fourcade, S. and Allegre, C.J., 1981. Trace element behavior in granite genesis: A case study of the calc-alkaline plutonic association from the Querigut Complex (Pyrenees, France). *Contributions to Mineralogy and Petrology*, **76**, 177-195.
56. Fraser, J.A., Hoffman, P.F., Irvine, T.N. and Mursky, G., 1972. The Bear Province in: Variations in Tectonic Styles, R.A. Price and R.J.W. Douglas, Eds. Geological Association of Canada Special Paper 11, pp. 453-504.
57. Freestone, I.C. and Hamilton, D.L., 1980. The role of liquid immiscibility in the genesis of carbonatites - an experimental study. *Contributions to Mineralogy and Petrology*, **73**, 105-117.

58. Frey, F.A., Green, D.H. and Roy, S.D., 1978. Integrated models of basalt petrogenesis: A study of quartz tholeites to olivine melilitites from South Eastern Australia utilizing geochemical and experimental petrological data. *Journal of Petrology*, **19**, 463-513.
59. Frith, R.A., 1978. Tectonics and metamorphism along the southern boundary between the Bear and Slave structural provinces in: Metamorphism in the Canadian Shield, J.A. Fraser and W.W. Heywood, Eds. Geological Survey of Canada Paper No. 78-10, pp. 103-113.
60. Fudali, R.F., 1963. Experimental studies bearing on the origin of pseudoleucite and associated problems of alkalic rock systems. *Geological Society of America Bulletin*, **74**, 1101-1126.
61. Ganapathy, R., Papia, G.M. and Grossman, L., 1976. The abundances of zirconium and hafnium in the solar system. *Earth and Planetary Science Letters*, **29**, 302-308.
62. Gast, P.W., 1968. Trace element fractionation and the origin of tholeitic and alkaline magma types. *Geochimica et Cosmochimica Acta*, **32**, 1057-1086.
63. Gerasimovsky, V.I., Volkov, V.P., Kogarko, L.N., Polyakov, A.I., Sabrykina, T.V. and Balashov, Yu.A.,

1966. The Geochemistry of the Lovozero Alkaline Massif.
64. Gerasimovsky, V.I., Volkov, V.P., Kogarko, L.N. and Polyakov, A.I., 1974. The Kola peninsula in: The Alkaline Rocks, H. Sorensen, Ed., Wiley and Sons, New York, 622 pp.
65. Gittins, J., 1979. The Feldspathoidal Alkaline Rocks in: The Evolution of the Igneous Rocks, H.S. Yoder, Ed., Princeton University Press, Princeton, N.J., pp. 351-390.
66. Gladney, E.S., Burns, C.E. and Roelandts, I., 1983. 1982 compilation of elemental concentrations in eleven United States Geological Survey Standards. Geostandards Newsletter, 7, 3-226.
67. Gold, D.P., 1966. Average and typical chemical composition of carbonatites. International Mineralogical Association 4th General Meeting, 1964. New Delhi, India, p. 83.
68. Goldstein, S., O'Nions, R.K. and Hamilton, P.J., 1984. A Sm-Nd isotopic study of atmospheric dusts and particulates from major river systems. Earth and Planetary Science Letters, 70, 221-236.
69. Green, D.H. and Ringwood, A.E., 1967. The genesis of basaltic magmas. Contributions to Mineralogy and Petrology, 15, 103-190.

70. Grunenfelder, M.H., Tilton, G.R. and Bell, K., 1982. Lead isotope relationships in the Oka carbonatite complex, Quebec. *EOS*, **63**, 1134.
71. Hamilton, E.I. and Deans, T., 1963. Isotopic composition of strontium in some African carbonatites and limestones and in strontium minerals. *Nature*, **198**, 776.
72. Hamilton, D.L. and Mackenzie, W.S., 1965. Phase equilibrium studies in the system $\text{NaAlSi}_3\text{O}_8$ (nepheline)- KAlSi_3O_8 (kalsilite)- SiO_2 - H_2O . *Mineralogical Magazine*, **34**, 214-223.
73. Hanson, G.N., 1977. Geochemical evolution of the sub-oceanic mantle. *Journal of the Geological Society, London*, **134**, 235-253.
74. Haskin, L.A., Haskin, M.A., Frey, F.A. and Wildeman, T.R., 1968. Relative and absolute terrestrial abundances of the rare earths in Origin and Distribution of the Elements, L.H. Ahrens, Ed., *International Series Monographs Earth Sciences*, **30**, 889-912.
75. Henderson, P., 1982. Inorganic Geochemistry, Pergamon Press, New York, 353 pp.
76. Henderson, P., 1984. General geochemical properties and abundances of the rare earth elements in Rare Earth Element Geochemistry, P. Henderson, Ed., Elsevier, New York, 510 pp.

77. Hoffman, P.F., 1974. Aulacogens and their genetic relation to geosynclines, with a Proterozoic example from Great Slave Lake, Canada in Modern and Ancient Geosynclinal Sedimentation. Society of Economic Paleontologists and Mineralogists Special Publication 19, pp. 38-55.
78. Hoffman, P.F., 1980. Wopmay Orogen: a Wilson cycle of early Proterozoic age in the northwest of the Canadian Shield in: The Continental Crust and its Mineral Deposits, D.W. Strangway, Ed. Geological Association of Canada, Special Paper #20, pp. 523-549.
79. Hoffman, P.F. and Bowring, S.A., 1984. Short-lived 1.9 Ga continental margin and its destruction, Wopmay orogen, northwest Canada. *Geology*, 12, 68-72.
80. Holmes, A., 1946. An estimate of the age of the earth. *Nature*, 157, 680-684.
81. Holmes, A., 1950. Petrogenesis of katungite and its associates. *American Mineralogist*, 35, 772-792.
82. Houtermans, F.G., 1946. Die Isotopenhäufigkeiten im natürlichen Blei und das Alter des Urans, *Naturwissenschaften*, 33, 185-186.
83. Hurlburt, C.S., Jr., 1939. Igneous rocks of the Highwood Mountains, Montana Part 1: The

- laccoliths. Bulletin of the Geological Society of America, 50, 1043-1112.
84. Iddings, J.P., 1909. Igneous Rocks, Vol. I, 1st Edition, J. Wiley and Sons, New York. 464 pp.
85. Irving, A.J., 1978. A review of experimental studies of crystal/liquid trace element partitioning. Geological Society of America, 42, 743-770.
86. Jacobsen, S.B. and Wasserburg, G.J., 1980. Sm-Nd isotopic evolution of chondrites. Earth and Planetary Science Letters, 50, 139-155.
87. Jacobsen, S.B. and Wasserburg, G.L., 1984. Sm-Nd isotopic evolution of chondrites and achondrites II. Earth and Planetary Science Letters, 67, 137-150.
88. Jaffey, A.H., Flynn, K.F., Glendenin, L.E., Bentley, W.C. and Essling, A.M., 1971. Precision measurement of half-lives and specific activities of U(235) and U(238). Physical Review, Section C: Nuclear Physics, C4, 1889-1906.
89. Kay, R.W. and Gast, P.W., 1973. The rare earth content and origin of alkali-rich basalts. Journal of Geology, 81, 653-682.
90. Kempe, D.R.C. and Deer, W.A., 1976. The petrogenesis of the Kangerdlugssuaq alkaline intrusion east Greenland. Lithos, 9, 111-123.

91. King, B.C., 1965. Petrogenesis of the alkaline igneous rock suites of the volcanic and intrusive centres of eastern Uganda. *Journal of Petrology*, 6, 67-100.
92. Korrington, M.K. and Noble, D.G., 1971. Distribution of Sr and Ba between natural feldspar and igneous melt. *Earth and Planetary Science Letters*, 11, 147-151.
93. Krogh, T.E., 1973. A low contamination method for hydrothermal decomposition of zircon and extraction of U and Pb for isotopic age determinations. *Geochimica et Cosmochimica Acta*, 37, 485-494.
94. Krogh, T.E. and Gibbins, W., 1978. U-Pb Isotopic ages of basement and supracrustal rocks in the Point Lake area, Slave Province, N.W.T. *Geological Association of Canada Abstracts with Program*, 3, 438.
95. Lambert, R.St.J., 1964. The Big Spruce Lake nepheline-syenite complex, Snare River, Northwest Territories. Unpublished preliminary report to the Boreal Institute. 8 pp.
96. Lambert, R.St.J., 1985. Lead isotopes in Archean rocks and the evolution of the mantle in: Evolution of Archean Supracrustal Sequences, L.D. Ayres, P.C. Thurston, K.D. Card and W. Weber, Eds., *Geological Association of Canada Special Paper*, 28.

97. Lambert, R.St.J. and Holland, J.G., 1974. Yttrium geochemistry applied to petrogenesis utilizing calcium-yttrium relationships in minerals and rocks. *Geochimica et Cosmochimica Acta*, **38**, 1393-1414.
98. Le Bas, M.J., 1977. Carbonatite-Nephelinite Volcanism, Wiley Interscience, New York. 347 pp.
99. Le Bas, M.J., 1981. Carbonatite magmas. *Mineralogical Magazine*, **44**, 133-140.
100. Le Bas, M.J., Aspden, J. and Wooley, A.R., 1977. Contrasting sodic and potassic glassy inclusions in apatite crystals from an ijolite. *Journal of Petrology*, **18**, 247.
101. Leech, G.B., Lowdon, J.A., Stockwell, C.H. and Wanless, R.K., 1963. Age determinations and geologic studies (including isotopic ages - report 4). Geological Survey of Canada Paper 63-17.
102. Littlejohn, A.L., 1981. Alteration products of accessory allanite in radioactive granites from the Canadian Shield. Geological Survey of Canada Paper 81-1B, 95-104.
103. Lord, C.S., 1942. Snare River and Ingray Lake map areas, Northwest Territories. Geological Survey of Canada Memoir #235.
104. Loubet, M., Bernat, M., Jayoy, M. and Allegre, C.J., 1972. Rare earth contents in carbonatites. *Earth and Planetary Science Letters*, **14**, 226-232.

105. Ludwig, K.R., 1980. Calculation of uncertainties of U-Pb isotope data. *Earth and Planetary Science Letters*, **46**, 212-220.
106. McCulloch, M.T., Gregory, R.T., Wasserburg, G.J. and Taylor, H.P., 1980. A neodymium, strontium and oxygen isotopic study of the Cretaceous Somaill Ophiolite and implications for the petrogenesis and seawater-hydrothermal alteration of oceanic crust. *Earth and Planetary Science Letters*, **46**, 201-211.
107. McGlynn, J.C. and Henderson, J.B., 1970. Archean volcanism and sedimentation in the Slave Structural Province. Geological Survey of Canada Paper 70-40.
108. Martineau, M.P., 1970. The Petrology of the Big Spruce Lake Complex. Ph.D. thesis, Oxford University, Oxford, England, 93 pp.
109. Martineau, M.P., Lambert, R., 1974. The Big Spruce Lake nepheline-syenite/carbonatite complex. GAC/MAC Annual Meeting. Program with Abstracts, p. 59.
110. Menzies, M. and Murthy, V.R., 1980. Enriched mantle: Nd and Sr isotopes in diopsides from kimberlite nodules. *Nature*, **283**, 634-636.
111. Metcalfe, P., (in preparation). Petrogenesis of alkali basalts in Wells Gray Provincial Park, B.C. Ph.D. Thesis, University of Alberta.
112. Middlemost, E.A., 1974. Petrogenetic model for the origin of carbonatites. *Lithos* **7**, 275-278.

113. Mitchell, R.H. and Brunfelt, A.O., 1974. Scandium, cobalt and iron geochemistry of the Fen alkaline complex, southern Norway. *Earth and Planetary Science Letters*, **23**, 189-192.
114. Mitchell, R.H. and Brunfelt, A.O., 1975. Rare earth element geochemistry of the Fen Alkaline Complex, Norway. *Contributions to Mineralogy and Petrology*, **52**; 247-259.
115. Möller, P. and Muecke, G.K., 1984. Significance of europium anomalies in silicate melts and crystal-melt equilibria: a re-evaluation. *Contributions to Mineralogy and Petrology*, **87**, 242-250.
116. Morris, R.V. and Haskin, L.A., 1974. EPR measurement of the effect of glass composition on the oxidation states of europium. *Geochimica et Cosmochimica Acta*, **38**, 1435-1445.
117. Nakamura, N., 1974. Determination of REE, Ba, Fe, Mg, Na and K in carbonaceous and ordinary chondrites. *Geochimica et Cosmochimica Acta*, **38**, 757-775.
118. Nash, W.P. and Wilkinson, J.F.G., 1970. Shonkin Sag Laccolith, Montana: I. Mafic minerals and estimates of temperature, pressure, oxygen fugacity and silica activity. *Contributions to Mineralogy and Petrology*, **25**, 241-269.

119. Nash, W.P. and Wilkinson, J.F.G., 1971. Shonkin Sag Laccolith, Montana: II. Bulk rock geochemistry. *Contributions to Mineralogy and Petrology*, 33, 162-170.
120. Nikic, Z., Baadsgard, H., Folinsbee, R.E. and Leech, A.P., 1975. Diatreme containing boulders of 3030 M.Y. old tonalite gneiss, Con Mine, Yellowknife, Slave craton. *Geological Society of America, Abstract with Program*, 7, 1213-1214.
121. Nolan, J., 1966. Melting relations in the system $\text{NaAlSi}_3\text{O}_8$ - NaAlSiO_4 - $\text{NaFeSi}_2\text{O}_6$ - $\text{CaMgSi}_2\text{O}_6$ - H_2O and their bearing on the genesis of alkaline undersaturated rocks. *Quarterly Journal of the Geological Society of London*, 122, 119-157.
122. O'Hara, M.J., 1975. Is there an Icelandic mantle plume? *Nature*, 253, 708-710.
123. Oversby, V.M., 1976. Isotopic ages and geochemistry of Archean acid rocks from the Pilbara, Western Australia. *Geochimica et Cosmochimica Acta*, 40, 817-829.
124. Pankhurst, R.J., 1977. Open system fractionation and incompatible element variation in basalts. *Nature*, 268, 36-88.
125. Pankhurst, R.J., Beckinsale, R.D. and Brooks, C.K., 1976. Strontium and oxygen isotope evidence relating to the petrogenesis of the Kangerdlugssuaq

- Alkaline Intrusion, East Greenland. Contributions to Mineralogy and Petrology, **54**, 17-42.
126. Philpotts, J.A., 1970. Redox estimation from a calculation of Eu^{2+} and Eu^{3+} concentrations in natural phases. Earth and Planetary Science Letters, **9**, 257-268.
127. Pineau, F., Javoy, M. and Allegre, C.J., 1973. Etude systematique des isotopes de l'oxygene du carbone et du strontium dans les carbonatites. Geochimica et Cosmochimica Acta, **37**, 2363-2377.
128. Piotrowski, J.M. and Edgar, A.D., 1970. Melting relations in undersaturated alkaline rocks from south Greenland compared to those of Africa and Canada. Meddlung om Grönland, **181**, (9).
129. Powell, J.L. and Bell, K., 1974. Isotopic composition of strontium in alkalic rocks in: The Alkaline Rocks, H. Sorensen, Ed., Wiley and Sons, London, 622 pp.
130. Presnall, D.C., 1966. The join forsterite-diopside-iron oxide and its bearing on the crystallisation of basaltic and ultramafic magmas. American Journal of Science, **264**, 753-809.
131. Ringwood, A.E., 1966. Chemical evolution of the terrestrial planets. Geochimica et Cosmochimica Acta, **30**, 41-104.

132. Rock, N.M.S., 1976. The comparative strontium isotopic composition of alkaline rocks: New data from Southern Portugal and East Africa. *Contributions to Mineralogy and Petrology*, **56**, 205-228.
133. Roden, M.R., Murthy, V.R. and Gaspar, J.C., 1985. Sr and Nd isotopic composition of the Jacupiranga carbonatite. *Journal of Geology*, **93**, 212-220.
134. Sahama, T.G., 1974. Potassium-rich alkaline rocks in: The Alkaline Rocks, H. Sorensen, Ed., John Wiley and Sons, London, 622 pp.
-
135. Schairer, J.F. and Bowen, N.L., 1935. Preliminary report on equilibrium relations between feldspars and silica. *Transactions American Geophysical Union*, 16th Annual Meeting, 325-328.
136. Schnetzler, C. and Philpotts, J.A., 1970. Partition coefficients of rare earth elements and barium between igneous matrix material and rock forming mineral phenocrysts. *Geochimica et Cosmochimica Acta*, **34**, 331.
137. Schwarzer, R.R. and Rogers, J.J.W., 1974. A worldwide comparison of alkali olivine basalts and their differentiation trends. *Earth and Planetary Science Letters*, **23**, 286-296.
138. Shannon, R.D., 1976. Revised effective ionic radii and systematic studies of interatomic distances in

- halides and chalcogenides. Acta Crystallographica, Section A, 32, 751-767.
139. Sheppard, S.M.F. and Dawson, J.B., 1973. $^{13}\text{C}/^{12}\text{C}$, $^{18}\text{O}/^{16}\text{O}$ and D/H isotope variations in primary igneous carbonatites. Fortschritt Mineralogie, 50, 128-129.
140. Solomon, S.C., 1976. Geophysical constraints on radial and lateral temperature variations in the upper mantle. American Mineralogist, 61, 788-803.
141. Sorensen, H., 1974. Alkali syenites, feldspathoidal syenites and related lavas in: The Alkaline Rocks, H. Sorensen, Ed., Wiley and Sons, London, 622 pp.
142. Sood, M.K. and Edgar, A.D., 1970. Melting relations of undersaturated alkaline rocks from the Illimaussaq intrusion and Grøntedal-ika complex, S. Greenland, under water vapor and controlled partial oxygen pressure. Meddlung om Grønland, 181, (12).
143. Stacey, J.S. and Kramers, J.D., 1975. Approximation of terrestrial lead isotope evolution by a two-stage model. Earth and Planetary Science Letters, 26, 207-221.
144. Streckeisen, A., 1980. Classification and nomenclature of volcanic rocks, lamprophyres, carbonatites and melilitic rocks: IUGS Subcommission of the systematics of igneous rocks. Geologische Rundschau 69, 191-207.

145. Sun, C., Williams, R.J. and Sun, S., 1974. Distribution coefficients of Eu and Sr for plagioclase-liquid and clinopyroxene-liquid equilibria in oceanic ridge basalt: An experimental study. *Geochimica et Cosmochimica Acta*, **38**, 1415-1433.
146. Sun, S.S. and Hanson, G.N., 1975a. Evolution of the mantle: geochemical evidence from alkali basalt. *Geology*, **3**, 297-302.
147. Sun, S.S. and Hanson, G.N., 1975b. Origin of Ross Island basanitoids and limitations upon the heterogeneity of mantle sources for } alkali basalts and nephelinites. *Contributions to Mineralogy and Petrology*, **52**, 77-106.
148. Sun, S.S. and Nesbitt, R.W., 1977. Chemical heterogeneity of the Archean mantle, composition of the earth and mantle evolution. *Earth and Planetary Science Letters*, **35**, 429-448.
149. Suzuki, K., 1981. Grain boundary concentration of rare earth elements in a hornblende cumulate. *Geochemical Journal (Japan)*, **15**, 295-303.
150. Tarney, J., Wood, D.A., Saunders, A.D., Cann, J.R. and Varet, J., 1980. Nature of mantle heterogeneity in the North Atlantic; evidence from deep sea drilling. *Philosophical Transactions of the Royal Society, London, A* **297**, 179-202.

151. Tatsumoto, M., Knight, R.J. and Allegre, C.J.,
1973. Time differences in the formation of
meteorites as determined from the ratio of lead 207
to lead 206. *Science*, **180**, 1279.
152. Taylor, H.P., Jr., Frechen, J. and Degens, E.T.,
1967. Oxygen and carbon isotope studies of
carbonatites from the Laacher See District, West
Germany and the Alnö District, Sweden. *Geochimica
et Cosmochimica Acta*, **31**, 407-430.
153. Tilley, C.E., 1958. Problems of alkali rock
genesis. *Quarterly Journal of the Geological
Society, London*, **113**, 323-359.
154. Treuil, M., and Varet, J., 1973. Critères
volcanologiques, pétrologiques et géochimiques de la
génése et de la différenciation des magmas
basaltiques: Exemple de l'Afar. *Bulletin Société
Géologique de France*, **7(XV)**, 506-540.
155. Upton, B.G.J., 1974. The alkaline province of
South-east Greenland in: The Alkaline Rocks, H.
Sorensen, Ed., Wiley and Sons, London, 622 pp.
156. Villemant, B., Jaffrezic, H., Joron, J-L., and
Treuil, M., 1981. Distribution coefficients of
major and trace elements; fractional crystallisation
in the alkali basalt series of Chaîne des Puys
(Massif Central, France). *Geochimica et
Cosmochimica Acta*, **45**, 1997-2016.

157. Von Eckermann, H., 1948. The alkaline district of Alnö. Sveriges Geologisches Undersökning, Ser. Ca. No. 36.
158. Wager, L.R., 1965. The form and internal structure of the alkaline Kangerdlugssuaq intrusion, East Greenland. Mineralogical Magazine, 34, 487-497.
159. Wager, L.R., Brown, G.M. and Wadsworth, W.J., 1960. Types of igneous cumulates. Journal of Petrology, 1, 73-85.
160. Wasserburg, G.J. and DePaolo, D.J., 1979. Models of earth structure inferred from neodymium and strontium isotopic abundances. Proceedings of the National Academy of Science, U.S.A., 76, 3594-3598.
161. Wasserburg, G.J., Jacobsen, S.B., DePaolo, D.J., McCulloch, M.T. and Wen, T., 1981. Precise determination of Sm/Nd ratios, Sm and Nd isotopic abundances in standard solutions. Geochimica et Cosmochimica Acta, 45, 2311-2323.
162. Watson, E.B., (1980). Some experimentally determined zircon/liquid partition coefficients for the rare earth elements. Geochimica et Cosmochimica Acta, 44, 895-897.
163. Weidner, J.R., 1982. Iron oxide magmas in the system Fe-C-O. Canadian Mineralogist, 20, 555-566.
164. Weill, D.F. and Drake, M.J., 1973. Europium anomaly in plagioclase feldspar: experimental results and

165. Winkler, H.G.F., 1974. Petrogenesis of Metamorphic Rocks, 3rd Ed., Springer-Verlag, New York, 320 pp.
166. Wood, D.A., Tarney, J., Varet, J., Saunders, A.D., Bougault, H., Joron, J.-L., Treuil, M. and Cann, J.R., 1979. *Earth and Planetary Science Letters*, **42**, 77-97.
167. Woolley, A.R., 1982. A discussion of carbonatite evolution and nomenclature, and the generation of sodic and potassic fenites. *Mineralogical Magazine*, **46**, 13-17.
168. Wyllie, P.J., 1965. Melting relationships in the system $\text{CaO-MgO-CO}_2\text{-H}_2\text{O}$ with petrological applications. *Journal of Petrology*, **6**, 101-123.
169. Wyllie, P.J., 1974. Limestone assimilation in: The Alkaline Rocks, H. Sorensen, Ed., Wiley and Sons, London, 622 pp.
170. Wyllie, P.J., 1979. Magmas and volatile components. *American Mineralogist*, **64**, 469-500.
171. Wyllie, P.J., 1980. The origin of kimberlite. *Journal of Geophysical Research*, **85**, 6902-6910.
172. Wyllie, P.J. and Tuttle, O.F., 1959. Effect of carbon dioxide on the melting of granite and feldspar. *American Journal of Science*, **257**, 648-655.
173. Wyllie, P.J. and Tuttle, O.F., 1960. The system $\text{CaO-CO}_2\text{-H}_2\text{O}$ and the origin of carbonatites. *Journal*

174. Wyllie, P.J. and Watkinson, D., 1970. Phase equilibrium studies bearing on genetic links between alkaline and subalkaline magmas with special reference to the limestone assimilation hypothesis. *Canadian Mineralogist*, **10**, 362-374.
175. York, D., 1966. Least-squares fitting of a straight line. *Canadian Journal of Physics*, **44**, 1079-1086.
176. Zartman, R.E. and Doe, B.R., 1981. Plumbotectonics - The model. *Tectonophysics*, **75**, 135-162.
177. Zindler, A., Jagoutz, E., and Goldstein, S., 1982. Nb-Sr-Pb isotopic systematics in a three-component mantle: a new perspective. *Nature*, **298**, 519-523.

APPENDIX 1

SAMPLE LOCATIONS AND DESCRIPTIONS

The locations of samples analysed in this study are shown on the Sample Locations Map (map pocket). Specific comments about locations, where necessary, are included in individual descriptions. Full descriptions of petrology and mineralogy of the complex are given in Martineau (1970). The following descriptions are of specific samples examined in thin section. Modal abundances cited are visual estimates.

Descriptions are arranged by sample number within each of the five centres of intrusive activity outlined in Chapter 2.

Centre 1: Gabbros, Diorites, Pyroxenites

PC-81-001: Magnetite Clinopyroxenite

Location: Outcrop on Island C, part of main pyroxenite body.

Coarse grained, equigranular, black weathering to a rusty stain. Compositional layering and grain orientation absent.

Rounded and embayed titanaukite, 1-5 mm, with inclusions of subhedral Fe-Ti oxide grains makes up 70-75% of the rock. Magnetite-serpentine pseudomorphs of rounded olivine grains occupy 5-10%. Fe-Ti oxides (20%) form an aggregate interstitial to olivine and pyroxene. Traces of iron sulfides accompany interstitial oxides. Minor patchy alteration of pyroxene to brown amphibole has occurred. There is no significant post-crystallisation shearing or alteration.

PC-81-004: Magnetite Olivine Clinopyroxenite

Location: East side of Island D, in main body 100 m from contact with ring syenite.

Very similar to PC-81-001 but with fresh olivine present. Exsolution of Fe-Ti oxides parallel to cleavages in titanaukite imparts a greyish colour in thin section.

PC-81-235: Big Feldspar Gabbro

Location: Within eastern ring of marginal gabbro. 100 m east of the inner margin/transition to LLG.

Mesocratic. No compositional layering but rough foliation with alignment of feldspar phenocrysts.

Subhedral-euhedral andesine (An_{45-48}), 1 cm, forms 50-55% in a matrix of titanaukite Fe-Ti oxides and late poikilitic amphibole. Feldspar shows no zoning, minor alteration to saussurite. Mafics show recrystallisation and alteration.

PC-81-275: Leucocratic Laminated Gabbro

Location: Outcrop on small inlet at southwest corner of Centre I.

Compositional layering (30°W, 30°N), with mafic bands of Fe-Ti oxides and pyroxene (1 cm wide) separated by leucocratic bands (feldspar and minor mafics) 4-5 cm wide. Alignment of feldspar and elongate mafics parallel to banding.

Tabular plagioclase (65%), An₄₃₋₁₅, plus minor titanite (<5%) are cumulate with orientation of elongate grains. The matrix consists of pyroxene poikilitic to euhedral Fe-Ti oxides, anhedral oxides, apatite and brown amphibole plus late anhedral feldspar. Minor chlorite is associated with the mafics.

PC-81-363: Diorite (altered and sheared)

Location: At the centre of the southwestern ring. A large sample from an inhomogeneous outcrop.

Leucocratic to melanocratic with no compositional layering or grain orientation. Weathers to a pale pink surface slightly pitted due to preferential weathering of mafics. Sheared in outcrop.

Plagioclase, 5-8 mm in size and subhedral in outline forms 50-60% of the rock. It is very altered to grey-brown clay/saussurite. Felted masses of green chlorite

(possibly pseudomorphs of earlier pyroxene) are associated with dark brown biotite and leucoxene, abundant apatite, Fe-Ti oxides and anhedral feldspar are interstitial to plagioclase. Chlorite forms about 25% of the rock, biotite 10-15%, oxides 5%, apatite 1%.

PC-82-163: Magnetite Clinopyroxenite

Location: Small exposure within alkali diorite in northeast sector of Centre 1. Offset by movement on fault X-X' (Figure 1).

Coarse-grained, equigranular with no compositional layering or grain orientation.

Titanaugite (75%), with exsolved acicular opaques along cleavages and inclusions of euhedral Fe-Ti oxides, is embayed and rounded, altered to patches of brown amphibole and chlorite. Both pyroxene and early euhedral Fe-Ti oxides are enveloped in an oxide/silicate (felted chlorite masses) matrix with traces of Fe sulphides. Total oxide content is about 20%, chlorite about 5-10%.

PC-82-173: Diorite

Location: Large outcrop in the northeast lobe of the outer ring.

Crude layering of feldspathic (aligned feldspar), and more mafic portions on a 1 cm scale.

Feldspathic bands are an interlocking network of crudely aligned plagioclase laths (An_{43-46}) with crude zoning and inclusions of euhedral oxides. Feldspar occupies 95%, oxides 4%, chlorite/pyroxene 1%.

Mafic-rich bands contain 50% feldspar, 20-25% pyroxene, 20% Fe-Ti oxide and 5-10% chlorite or amphibole. The feldspar is both subhedral laths of An_{20-25} and anhedral alkali feldspar. Pyroxene is anhedral titanite with exsolved acicular opaques on cleavages and Fe-Ti euhedral inclusions. Altered rims are green chlorite and brown amphibole transitional to green biotite. Oxides are present as euhedral grains and anhedral aggregates.

Centre 2: Syenites

PC-81-012: Mafic Syenite (Syenite 1)

Location: Centre of the south side of Island G.

Coarse-grained. Weathers to a very pale pink surface spotted with dark mafic aggregates.

Clear sodic feldspar (anorthoclase) in subhedral to euhedral tablets, 0.5 to 1.0 cm in length, shows no albite twinning and little perthitisation or zoning (~50% of the rock). Pyroxene, largely replaced by blue-green amphibole and green-brown biotite encloses euhedral Fe-Ti oxides.

grains and stubby apatite (~25% of the rock). Fe-Ti oxides in euhedral grains and anhedral masses (< 25%) has exsolution lamellae replaced by sphene. Stubby coarse apatite (about 1%) and traces of carbonate (in pyroxene pseudomorphs and mafic aggregates) are also present.

PC-81-078: Inner Quartz Syenite (Syenite 4)

Location: A small outcrop between Island H and the western mainland.

Sheared in outcrop, this syenite shows brick-red weathering surface with no compositional layering or grain orientation.

Large grains of feldspar (0.5 to 1 cm), subhedral to rounded euhedral tabular, show intricate exsolution patterns of ropey and patch perthite. Granulated and sutured inter-feldspar boundaries are formed with final alkali feldspar overgrowths. Myrmekitic (quartz-feldspar) intergrowths are common between grains. Cumulate feldspar forms 75%. Interstitial mafic aggregates form 20% of the rock. Green-brown anhedral to subhedral hornblende, ferrohastingsite, is commonly rimmed by alteration to biotite and is poikilitic to euhedral Fe-Ti oxides and abundant coarse (0.5 mm) apatite. The Fe-Ti oxides are rimmed with sphene. A few grains of coarse quartz (<3% of the rock) are present at the edges of mafic aggregates. Zircon is associated with mafic aggregates.

PC-81-285: Inner Quartz Syenite (Syenite 4)

Location: East shoreline of Big Spruce Lake about 200 m north of contact with foyaites.

Feldspar (70%) is bimodal similar to other quartz syenites. Subhedral to euhedral embayed rhombic grains (to about 1 cm) have core/rim structure, both parts strongly perthitised, and narrow alkali feldspar-sutured boundaries. Interstitial to large feldspar is anhedral perthitic feldspar (5%), quartz (0.5 to 1.0 mm and about 5%) and mafic aggregates consisting of subhedral to euhedral olive-brown hornblende (ferrohastingsite) which is poikilitic to euhedral oxide, anhedral Fe-Ti oxides poikilitic to prismatic apatite and rimmed by sphene, apatite, coarse zircon and carbonate. Granular Fe-Ti oxide plus serpentine may pseudomorph rare olivine in this sample. Hornblende is often altered to felted masses of biotite and euhedral Fe-Ti oxide inclusions.

PC-81-332: Mafic Syenite (Syenite 1)

Location: Large outcrop on the east side of the north tip of Island G.

Very similar to PC-81-012 but with more altered feldspar and inclusions of subhedral to euhedral early feldspar in coarse late anhedral feldspar.

PC-81-338: Inner Quartz Syenite (Syenite 4)

Location: 3 m inside the outer contact (pyroxenite screen) on the north-eastern side of the unit.

This rock is the chilled zone of inner quartz syenite and consists of about 70% feldspar, 30% mafic aggregates. Feldspar is a clear sodic anorthoclase in a mosaic of small anhedral grains (<5 mm). Complex patterns of patch perthite with visibly oriented albite twinning and variable proportions of alkali feldspar and plagioclase are present at the centres. Sutured boundaries between grains are formed by late alkali feldspar rims. Little subsequent alteration has occurred.

Subhedral pyroxene, rimmed with green amphibole is associated with anhedral (embayed) brown hornblende in mafic aggregates along with anhedral Fe-Ti oxides often rimmed with green biotite. Apatite, enclosed by mafics, is hollow crystals, possibly with fluid inclusions. Abundant zircon is associated with the edges of mafic aggregates.

PC-81-364: Outer Quartz Syenite (Syenite 3)

Location: Shoreline outcrop on the east side of the lake, an unknown distance from diorite (contact covered), part of the body earlier included with ring syenite dyke.

Feldspar (85-90%) occurs in well-defined tablets (1 cm) of ropey perthite in an anhedral mosaic of late sodic feldspar. A core-rim structure (both perthitic) is common but not always distinct and followed by narrow alkali-feldspar sutured rims. Interstitial mafic aggregates comprise 10-15%. Anhedral brown hornblende, euhedral Fe-Ti oxides, quartz, acicular apatite and coarse zircon are accompanied by traces of muscovite and carbonate.

PC-82-096: Outer Quartz Syenite (Syenite 3)

Location: 50 m from contact with gneiss at the western edge of Centre 2.

Coarse (8 to 10 mm) subhedral to euhedral rhombic tabular feldspar (80-85%) shows well-developed ropey perthite exsolution throughout the entire grain. Sutured boundaries have narrow albite rims. Interstitial to feldspar is quartz (5-10%, 0.5 to 1 mm) and aggregates of fine-grained mafics plus oxides (10%). The mafic/oxide aggregates do not appear to replace earlier coarse mafics and consist of fine-grained quartz/carbonate (40-50%), Fe-Ti oxides (40%) olive-green biotite (10%), apatite. Traces of stilpnomelane abut and vein feldspar.

PC-82-099: Outer Quartz Syenite (Syenite 3)

Location: 25 m from contact with gneiss at the western margin of the complex. 25 m east of PC-82-096 location.

Similar to PC-81-096 with 80% feldspar, 5-10% quartz, and about 10% mafic aggregates. The feldspar is smaller than in PC-82-096 and has poorly defined zoning. Mafic aggregates contain 80% brown biotite and 10-15% fine-grained quartz plus carbonate. Apatite, Fe-Ti oxides (euhedral) and allanite form the remaining 5%. Zircon is absent.

PC-82-124: Ring Syenite (Syenite 2)

Location: At the centre of the eastern ring dyke 200 m from southern end.

Subhedral to euhedral tabular feldspar (1 to 1.5 cm), shows rosey perthite exsolution and minor dusty alteration with traces of carbonate and has abundant inclusions of stubby apatite and minor euhedral oxides. Feldspar comprises 75% of the rock. Mafic aggregates interstitial to feldspar are similar to those in mafic syenite (PC-81-012 and 332) and include blue-green amphibole pseudomorphing pyroxene, primary olive-brown amphibole, subhedral oxides and abundant stubby apatite.

PC-82-129: Ring syenite (Syenite 2)

Location: At the centre of the eastern ring dyke 900 m from the southern end.

Similar to PC-82-124, an altered quartz-free ring syenite. Cumulate perthitic feldspar is fractured and contains patches of carbonate. Fine-grained quartz is

associated with mafic aggregates in which primary amphibole is absent. Blue-green amphibole, chlorite, fine-grained green biotite and carbonate are all fine-grained. Fe-Ti oxides are commonly altered to sphene on exsolution planes and at edges. Radiating aggregates of stilpnomelane occur in late cavities and veins with carbonate.

PC-82-151: Outer Quartz Syenite (Syenite 3)

Location: 50 m from contact with gneiss at the southeastern margin of Centre 2.

Similar to PC-81-364 but abundant coarse quartz (10%) is associated with cumulate perthitic feldspar (75-80%) and fine-grained mafic aggregates (10-15%) in which the major mineral is green biotite in felted masses. is abundant.

PC-82-358: Outer Quartz Syenite (Syenite 3)

Location: Within the lobe of syenite emplaced across the fault cutting Centre 1 (see Figure 8).

Early subhedral blocky/rhombic feldspar in large crystals (to 1 cm) shows no albite twinning, but a core-rim zoning structure is apparent in differing degrees of dusty alteration (greater in core), birefringence and texture of pervasive rosey perthite exsolution. Inclusions of euhedral Fe-Ti oxides are rare.

Interstitial to early feldspars are anhedral perthitic feldspar, quartz and mafic aggregates. The total feldspar content is 80% (50% early, subhedral, 30% late anhedral). Quartz (5-10%) occurs as individual grains and aggregates interstitial to feldspar. Mafic aggregates (10-15%) are slightly variable. In some, euhedral brown hornblende, poikilitic to euhedral Fe-Ti oxides and rare prismatic apatite, is fractured and altered to green biotite. Quartz and primary biotite are associated. Other aggregates are fine-grained masses of green biotite, euhedral oxides, traces of acicular to prismatic apatite and fine-grained quartz/albite. Zircon (to 0.5 mm) is associated with mafics.

There is no primary or pseudomorphed pyroxene.

Centre 3: Silica Undersaturated Series

PC-81-482: Southern Foyaite

Location: Massive outcrop at northwest tip of Island V.

"Typical" leucocratic foyaite.

Very coarse-grained, rubbly weathering, massive grey rock. Euhedral hexagonal nepheline (55%) up to 1 cm in length and euhedral but embayed sphene (2-3%) up to 2 mm in length are enclosed in a matrix of alkali feldspar laths (30%), subhedral prismatic aegirine-augite (5-10%) anhedral cancrinite (5-10%) and Fe-Ti oxides (<1%).

Nepheline is largely unaltered and carries zones of inclusions (aegirine and minor Fe-Ti oxides) near the rim. Strongly pleochroic aegirine to aegirine-augite is interstitial to nepheline; pyroxene cores are often rimmed with radiating clusters of acicular aegirine. Feldspar laths of cryptoperthite form an interlocking mass. Granular cancrinite often rims nepheline and feldspar and veins nepheline. Fe-Ti oxide grains show lamellar exsolution, sometimes with preferential replacement of ilmenite by sphene or a complex intergrowth with fluorite and calcite. Sparse apatite is associated with aegirine-augite.

PC-82-039: Southern Foyaite

Location: Massive outcrop on the northern tip of the main promontory at the south end of the area.

Coarse-grained, rubbly weathering, grey rock.

Subhedral to euhedral prismatic microperthitic alkali feldspar (microcline to 1 cm length) (70%) is enclosed by a fine-grained aggregate of biotite (10%), nepheline (15%), and euhedral sphene (10%). Feldspar is poikilitic to sphene and shows minor alteration to clay/sericite. Sphene is pale brown and, where enclosed by biotite/nepheline, has rims of granular sphene. Biotite is dark brown (pleochroic to pale brown) euhedral, and

clusters commonly form a boundary layer between early feldspar and granular nepheline which forms interstitial masses. Traces of microcrystalline opaques (Fe-Ti oxides) and anhedral cancrinite are associated with nepheline. Apatite is rare.

PC-81-168: Melteigite

Location: West side of Big Spruce Island, from a "reef" with indeterminate field relations, on the foreshore at the mouth of a radial fracture.

Euhedral prismatic (to 1 cm) aegirine-augite (80-85%), somewhat rounded and altered in patches to deep-brown biotite, is enclosed in a matrix of anhedral, hematized cancrinite and feldspar (15%), accompanied by fluorite and calcite. Abundant granular sphene (2-3%) is associated with aegirine and biotite. Traces of Fe-Ti oxides and monazite are also present.

PC-81-287: Mafic Foyaite

Location: Massive outcrop at the southwest corner of Little Spruce Island.

Euhedral hexagonal nepheline (up to 0.75 cm) is recrystallised to a mosaic of anhedral grains which often retain the original zones of aegirine inclusions (40%). These recrystallised forms are enclosed in a matrix of rounded aegirine-augite (50%), cancrinite/feldspar (5-

10%), and granular andradite garnet (2-3%). Fluorite occurs in the matrix along with flakes of brown biotite.

PC-81-165: Mafic Foyaite

Location: Northwest tip of Big Spruce Island.

Euhedral aegirine-augite (to 3 mm, 40%) is enclosed in a matrix of subhedral to rounded aegirine, nepheline/feldspar (40%) and brown biotite poikilitic to aegirine-augite, with traces of fluorite and carbonate. Sphene is absent.

PC-81-194: Mafic Foyaite

Location: From the centre of Big Spruce Island.

Hexagonal nepheline (to 0.5 cm, 50%) is recrystallised to an aggregate which retains zones of inclusions of aegirine-augite parallel to the original crystal faces. These pseudomorphs are enclosed in a matrix of subhedral aegirine-augite (25%) altered in patches to brown biotite accompanied by granular nepheline/cancrinite and K-feldspar (25%).

PC-81-2041: Melteigite

Location: A nepheline porphyry dyke (strike = 10°) on northeast tip of Island V, 1 m in width.

Nepheline phenocrysts (1 cm) in a matrix of subhedral-euhedral aegirine-augite (1-2 mm, 65%), euhedral

sphene (1 mm, 10%), anhedral interstitial perthitic feldspar (10%) and nepheline (15%). Minor euhedral Fe-Ti oxides are present. Aegirine-augite has reaction rims of radiating brown biotite against feldspar.

PC-82-525 Ijolite

Location: 200 m inland on the resistant ridge trending southeast from the northwest tip of Big Spruce Island.

Fresh, black, no compositional layering or orientation of grains. Euhedral nepheline (to 5 mm), is partly recrystallised to radiating clusters of cancrinite rimmed by granular aegirine-augite and fluorite. Euhedral aegirine-augite is interstitial to nepheline and associated with granular andradite garnet and subhedral brown biotite poikilitic to granular aegirine. Nepheline, aegirine-augite, biotite, and anhedral K-feldspar/cancrinite/nepheline 15%, biotite 2-3%, garnet 2%.

PC-82-526: Ijolite

Location: 100 m southeast of PC-82-525 location.

Similar to PC-82-525. Remnants of euhedral nepheline (25%) are altered at the rims to prismatic radiating cancrinite. Interstitial, rounded and embayed aegirine-augite (50%) is altered to granular andradite ~~garnet at~~ rims and in patches and is enclosed in a matrix (30%) of

sparse brown biotite and granular feldspar/nepheline with traces of fluorite.

An inclusion (2 cm) of medium-grained melteigite consists of euhedral aegirine-augite (80%), rims altered to andradite, enclosed in granular cancrinite and fluorite.

Centre 4: Carbonatites

PC-81-176: Sövite

Location: A lens (0.5 m) of resistant leucocratic carbonatite in ropey textured mafic carbonatite on islet west of Big Spruce Island.

A coarse, grey-green rock, appears equigranular in hand and unoriented. Large anhedral carbonate grains form a mosaic (70-75%) veined by fine-grained aggregates of euhedral-subhedral pleochroic yellow epidote (10%), microliths of albitic feldspar (15%), partly chloritised biotite (5%). Traces of allanite and riebeckite are present.

PC-81-178: Sövite

Location: Grey sövite dyke (0.5 m) between silico-carbonatites and gneiss, on islet west of Big Spruce Island.

Coarse white calcite with a slightly sugary texture. Slightly weathered in outcrop. Calcite (90%) contains interstitial aggregates and fine veins of riebeckite, allanite, sphene and alkali feldspar, which impart a grey colour to the outcrop.

PC-81-1185: Sövite

Location: Dyke (3 m in width) cutting gneiss west of Big Spruce Island. The dyke is rimmed with massive quartz.

Medium-grained red carbonatite with phenocrysts of pyrite up to 1 cm in size. The depth of red colour is variable, with sharp contacts and changes in mineralogy suggesting slightly different magma pulses. The sample analysed is a composite or average.

Pyrite (to 1 cm, 2-5%) and magnetite (<1 mm, 23%) are enclosed in a matrix of calcite (80%) and bastnaesite (10%) with quartz (5%) and barite (trace).

PC-81-376: Sövite

Location: Dyke (1 m in width) at the northeast tip of Little Spruce Island.

Coarse calcite (>95%) laminated, with aggregates of bastnaesite, allanite and traces of green biotite to produce a grey colour in outcrop. Similar to PC-81-178 and PC-82-506.

PC-81-383: Silico-carbonatite

Location: Southeast tip of Little Spruce Island. No field relations discernible.

Easily weathered, coarse, white calcite and resistant grey-green silicate vein each other irregularly. The thin section is 70% calcite veined with subhedral-euhedral yellow epidote, deep green biotite flakes (25%) and traces of brown allanite. Prismatic epidote sometimes has cores of allanite. Veinlets of granular quartz/feldspar (5%) also occur, not associated with epidote.

PC-82-088: Riebeckite-Sövite

Location: Dyke (2.5-3 m in width) associated with foyaite/syenite contact at the northwest corner of Big Spruce Lake.

Medium-grained, bluish-violet in hand specimen; laminated with alternating oriented layers of blue riebeckite-rich aggregates and pink carbonate. Euhedral riebeckite/arfvedsonite and brown biotite (15% and 10% respectively) with dark brown pleochroic allanite form oriented lamellar aggregates between coarse calcite (70%) carrying abundant fluorite (5%).

PC-82-408: Magnetite-Dolomite-Carbonatite

Location: Small pipe 200 m northwest of the main dolomite pipe, east of the main complex.

In outcrop, euhedral magnetite (1-2 cm) is weathered out from the typical dark-brown "spongy" dolomite surface. The pipe is brecciated and dolomite clasts dominate over gneissic clasts.

Phenocrysts of subhedral to euhedral magnetite are carried in a matrix of coarse anhedral carbonate grains with numerous inclusions of small magnetite and biotite, and aggregates of slightly chloritised green biotite. Magnetite forms 20-25% of the rock, biotite, 10%, dolomite, 65%.

PC-82-412: Magnetite-Dolomite-Carbonatite

Location: The centre of a small pipe cutting gneiss on the east side of Island P.

In outcrop grey dolomite is weathered to dark brown. Similar to PC-82-408. Coarse euhedral carbonate and rounded carbonate grains are enclosed in a network of chlorite and traces of brown biotite which is associated with granular aggregates of feldspar and fine carbonate as well as radiating clusters of prismatic feldspar. Euhedral magnetite appears throughout (<1 mm) but is sparse in coarse carbonate and abundant in the chlorite/feldspar/fine carbonate network. Carbonate forms about 50% of the rock, feldspar 5-10%, magnetite 10-15% and chlorite/biotite 35%.

PC-82-506: Sövite

Location: Dyke (1.5 m in width) on the east side of Little Spruce Island.

A grey dyke, with somewhat crumbly texture due to weathering. Very similar to PC-81-376. Coarse calcite carries fine veinlets of allanite and traces of granular bastnaesite.

Centre 5: Satellite Intrusion

All samples from this area are black, equigranular, and show no compositional zoning. Grain orientation is weak to absent.

PC-81-057: Olivine Shonkinite

Location: A small shoreline outcrop on the south side of the central area. Contacts with gneiss are sharp. There are no visible xenoliths.

Rounded grains of olivine (5-10%, to 1.5 mm in length) and prismatic augite (40-45%, 1.5-2.5 mm in length) are enclosed in a matrix of biotite (10%), alkali feldspar (35%), Fe-Ti oxides (5%), and late pyroxene. Olivine is fractured and heavily veined with hedenbergitic pyroxene. Pyroxene phenocrysts are sharply zoned with an augite core rimmed by a zone of inclusion-rich augite (biotite, oxides) and green pleochroic hedenbergite. Some

small late pyroxene is entirely hedenbergite. Biotite is strongly pleochroic (straw yellow to deep red-brown) subhedral to anhedral and poikilitic to euhedral Fe-Ti oxides, late pyroxene and apatite. Scattered anhedral grains of Fe-Ti oxides, rimmed by biotite or included in biotite are scattered throughout. Alkali feldspar is subhedral (long laths) to anhedral, very clear and unaltered. Albitic twinning is absent, Carlsbad is common. Sphene is absent.

PC-81-061: Biotite Pyroxenite

Location: Shoreline outcrop on the south side of the main intrusive area, adjacent to the outcrop from which PC-81-057 was taken.

Subhedral, rounded pyroxene grains (60%) with largely anhedral biotite (30-35%) and Fe-Ti oxides (5-10%) form an interlocking mosaic. Pyroxene is oscillatory zoned augite, with abundant inclusions of apatite (and sphene), and is fractured and altered in patches to brown biotite. Brown biotite contains exsolved rutile and inclusions of small euhedral pyroxene and Fe-Ti oxides. Fe-Ti oxides are largely anhedral masses, often rimmed with sphene. Pyrite is associated with the oxides. Sphene is abundant (2-3%) in interstitial granular aggregates. Short prismatic apatite is included in biotite, oxides and sphene.

PC-81-388: Biotite Shonkinite

Location: On the east side of a small island lying northwest of Moose Island. The island is almost entirely intrusive; gneiss appears only on the western side.

Very similar to PC-81-061 with less pyroxene.

Pyroxene is 40-45%, biotite is 40-45%, Fe-Ti oxides are 5-10% and apatite is 3-5% of the rock. Late granular sphene is present in traces along with carbonate.

A weak foliation (alignment of prismatic pyroxene) is visible in thin sections only.

PC-82-260: Olivine Shonkinite

Location: Outcrop on the northwest shore of Moose Island.

Similar to PC-81-056 but enriched in pyroxene (50-55% if 40-45%) and poorer in feldspar (20-25%). Olivine is completely altered to very fine talc/tremolite. Alkali feldspar is anhedral. Apatite (and sphene) is sparse/absent.

PC-82-278: Biotite Pyroxenite

Location: A small outcrop usually underwater, between Fish Island and Moose Island. No contacts visible. No xenoliths observed.

Similar to PC-81-061. Modal pyroxene (zoned augite/titanaugite) makes up 80% and biotite, with abundant

apatite inclusions makes up 15% of the rock. 3-5% of clear untwinned feldspar is very late interstitial. No post-crystallisation shearing and alteration is apparent.

Country Rock

PC-81-025: Granodioritic Gneiss

Location: Massive outcrop cleared by blasting immediately east of Snare Rapids hydroelectric dam.

A grey, porphyritic gneiss with sparse feldspar grains to 2 cm crudely aligned in an unoriented matrix. Plagioclase, with rounded and altered cores rimmed with albite (25%), and quartz aggregates (20-30%) are enclosed in anhedral microcline (40%) and vein and aggregates of bleached brown biotite with minor muscovite. Zircon and apatite are present in traces.

PC-81-483: Granodioritic Gneiss

Location: Large outcrop cleared by blasting, along the Snare River Channel, 1.5 km southwest of the main complex.

Grey, unoriented gneiss very similar to PC-81-025, but with chloritised biotite and more muscovite. Plagioclase makes up 20%, microcline 40%, quartz 25%, biotite (partly chloritised) 5% and muscovite 10%. Zoned zircon present.

PC-82-074: Felsic Gneiss

Location: Along the eastern side of the southeast outlet to Big Spruce Lake.

Leucocratic equigranular unoriented pink gneiss.

Altered plagioclase laths (20%) are enclosed in aggregates of quartz (25%) and anhedral microcline (40%) with aggregates and veins of bleached biotite (3-5%) and muscovite (7-10%).

PC-82-281: Granodioritic Gneiss

Location: Along the northern Snare River Channel, 100 m north of the complex.

Granular quartz and feldspar are crudely aligned with stringers of biotite between. The biotite (8%) is bleached and slightly chloritised along cleavages, associated with well-developed muscovite (3-5%).

Plagioclase (20%), microcline (30%) and quartz (40%) make up the remainder of the rock. Zoned zircon is present in traces.

APPENDIX 2

ANALYTICAL METHODS

A. Sample Preparation

1. Whole Rock Powders

Samples for whole rock analyses were selected to be the freshest representatives of the units from which they were taken and at the same time to produce the widest possible range of compositions for each intrusive centre to facilitate determination of separate isochrons (if possible, for each center). Sample size ranged from a minimum of about 1 kg to about 15 kg.

For powders a block weighing 0.75 to 1.0 kg (a minimum of 0.5 kg) was cut from the center of the field sample to avoid possible surface contamination or alteration. This block was cut into slices which would crush in the jaw crusher. A water-cooled diamond saw was used for this step. All cut surfaces were cleaned with garnet sandpaper to remove metal marks, and the blocks were washed with distilled water, covered with paper and allowed to dry in air. The bulk sample was crushed to less than 0.5 cm in a Sturtevant jaw crusher, then ground to less than 40 mesh in a Bico disc mill using mullite

plates. This coarse powder was thoroughly mixed and a split of about 50 g taken for the final grinding. Final grinding, to less than about 200 mesh, was performed in an agate swing mill. From this final powder a 10 g split was removed for XRF analysis, the remainder retained for other analyses.

2. Zircons

Zircons were separated from the minus 100 mesh fraction of six syenites of Centre 2. The non-magnetic fraction was settled in acetylene tetrabromide and then in methylene iodide to obtain a heavy fraction that was almost entirely zircon. The few grains of pyrite were removed by refluxing in 1:1 nitric acid, and a few dark impurities were removed by hand-picking. This produced a separate 99.9% pure which was cleaned in dilute HCl and water before analysis.

B. XRF Analysis

Whole rock XRF analyses were performed at Midland Earth Sciences Associates (MESA), Nottingham, England (Dr. B.P. Atkin). Ten major elements (Si, Al, Ti, Fe, Mg, Ca, Na, K, Mn and P) plus loss on ignition were determined by XRF fusion techniques. Eight trace elements (Nb, Sr, Y, Rb, Pb, Zr, Ta and Hf) were determined by pressed powder

methods. Limits of detection for the trace elements (2 σ) estimated by MESA are:

	<u>ppm</u>		<u>ppm</u>
Ta	2	Sr	1
Zr	3	Rb	1
Pb	2	Hf	not given
Y	2	Nb	1

Hf and Ta were found to be erratic at lower levels (<5 ppm) and instrumental neutron activation analysis (INAA) values are preferred for these elements. The accuracy of INAA for both Ta and Hf is about $\pm 10\%$ of the amount present. The detection limit for the sample size used is about 0.4 ppm by INAA.

Accuracy of major and minor element determinations by XRF was monitored by analysis of three USGS rock standards, W-2, DNC-1 and BHVO-1. The results are presented in Table 25. Precision was monitored by replicate analyses of 6 samples, 5 of which were analysed twice and one was analysed four times. The 1σ variances for various elements ($n = 4$) are:

SiO ₂	0.40	MnO	0.013
TiO ₂	0.013	CaO	0.013
Al ₂ O ₃	0.133	Na ₂ O	0.020

Table-25. US-GS standard samples analysed by MFSA (as blind standards).

	MFSA USGS-W-2 a	Consensus values Gladney et al (1983)	MFSA b	MFSA USGS-DNC-1 Gladney et al (1983)	MFSA Compiled values USGS-RHVC Gladney & Goode (1981)
SiO ₂	51.53	51.77	52.09	46.53 47.71 (47.29 ³)	49.67 49.9±0.8
Al ₂ O ₃	14.92	15.38±0.11	15.06	18.34 17.97±0.76 (18.39 ³)	13.34 13.8 ± 0.2
TiO ₂	1.05	1.03±0.03	1.05	0.48 0.48±0.3	2.72 2.65±0.09
Fe ₂ O ₃	10.96	10.68±0.56	11.03	10.10 9.94±0.37	12.28 12.2±0.3
MgO	6.56	6.37	6.71	10.51 (10.16 ³)	7.43 7.14±0.20
CaO	10.93	10.93±0.56	10.90	11.34 11.68±0.78	11.30 11.4±0.2
Na ₂ O	2.45	2.00±0.08	2.43	1.97 1.77±0.11	2.44 2.21±0.09
K ₂ O	0.64	0.61	0.62	0.23 0.23±0.01	0.53 0.55±0.08
MnO	0.17	0.17±0.02	0.16	0.15 0.15±0.02	0.16 0.166±0.005
P ₂ O ₅	0.14	0.15	0.12	0.09 0.16 (0.07 ³)	0.26 0.29±0.04*
LOI	0.20		0.00	0.34	0.00
Total	99.53		100.18	100.07	100.14

- (1) Gladney, E.S. and Goode, W.E. (1981): Elemental concentrations in eight new United States Geological Survey Rock Standards: A review. *Geostandards Newsletter*, 5, 31-64.
- (2) Gladney, E.S., Burns, C.E. and Roelandts, I. (1983): 1982 Compilation of elemental concentrations in eleven United States Geological Survey rock standards. *Geostandards Newsletter*, 7, 3-266.
- (3) Abbey, S. (1983): Studies in "Standard Samples" of silicate rocks and minerals 1969-1982. *Geological Survey of Canada Paper* 83-15.

$\Sigma \text{Fe}_2\text{O}_3$	0.037	K_2O	0.020
MgO	0.069	P_2O_5	0.013

C. Instrumental Neutron Activation Analysis (INAA)

Trace element analyses of whole rock powders were performed at the University of Alberta SLOWPOKE Facility (UASF) using INAA (Duke, 1983).

Two irradiation schemes were used to maximise the number of elements determined. The shorter-lived nuclides were determined by the comparator method following a four-minute irradiation at a thermal flux of 10^{11} n/cm²/s.

Subsequent to a one-week decay period, the longer-lived nuclides were determined by the semi-absolute method following a two-hour re-irradiation at a thermal flux of 10^{12} n/cm²/s. The γ -activity of samples was counted first for 1 to 3 h following a decay period of 6 days and then for 3-10 h following a total decay time of about 21 days. The counting time depended upon the rare earth element content of each sample. A full description of the method and instrumentation is presented in Duke (1983).

Analyses of selected USGS rock standards (AGV-1, andesite; GSP-1, granodiorite; G-2, granite; W-1 diabase; BCR-1, basalt) were used to check the accuracy of both the short and long irradiation methods (consensus values;

Gladney et al, 1983).

A summary of the elements determined by INAA in this study and the irradiation-decay-count scheme used for each is provided in Table 26. Several elements (e.g. Ba, Eu, Sn) may be determined by more than one scheme, however, only the scheme found to be most accurate and precise was used in this study. In addition, several major and minor elements such as Na, K, Al, Ti, Mn and Fe were determined in some samples. For internal consistency only the XRF data are reported for these elements although good agreement between XRF and INAA was generally found.

For most samples an aliquot of about 100 mg, carefully weighed to ± 0.1 mg and sealed in acid-washed polyethylene irradiation vials, was an optimum size. However, some of the samples are enriched in Mn, which activates to ^{56}Mn , with a half-life of 2.576 h, and interferes with precise determination of other short-lived nuclides. For these samples the aliquot used was reduced to about 60-75 mg, and three separate aliquots analysed for the short-lived nuclides. The value reported is the arithmetic mean of the three determinations in these cases. Following a one-week decay period the three aliquots were combined, thoroughly mixed, and a 100 mg portion removed for re-irradiation and determination of the longer-lived nuclides. The effects of the smaller

Table 26. γ energies and irradiation schemes used for INAA.

Nuclide	Energy keV	Irradiation-decay-count Scheme and Comments
^{131}Ba	496.2	(4)
^{141}Ce	145.4	(4) check interference of ^{59}Fe at 142.7 keV
^{60}Co	1173.2 1332.5	(3, 4) use weighted mean of 4 values
^{51}Cr	320.1	(4)
^{134}Cs	795.8	(4)
^{165}Dy	94.7	(2)
^{181}Hf	482.0	(4)
^{86}Rb	1077.2	(4)
^{122}Sb	564	(3)
^{124}Sb	1691	(4) } use weighted mean of two values
^{46}Sc	889.3 (1120.5)	(3, 4) weighted mean including 1120.5 keV if no significant Ta interference at 1121.3 keV
^{182}Ta	152.4	(4)
$^{233}\text{Pa}(\text{Th})$	311.9	(3, 4) use weighted mean
$^{239}\text{Np}(\text{U})$	277.9	(3)
^{140}La	1596.2 487.0 815.0 328.7	(3) use weighted mean of four values
^{147}Nd	531.0	(4) unreliable, MSID preferred method
^{153}Sm	103.2	(3)
^{152}Eu	1407.9	(4)
^{160}Tb	298.6	(4) correct for $^{233}\text{Pa}(\text{Th})$ line at 300.1 keV ⁽⁵⁾
^{52}V	1434.4	(1)
^{169}Yb	198.0	(4) correct for ^{182}Ta at 198.3 keV and ^{160}Tb at 197.0 keV ^(5,6)
^{175}Yb	396.3	(3) correct for $^{233}\text{Pa}(\text{Th})$ at 398.5 keV. ⁽⁵⁾ Unreliable at high rare earth element contents.
^{177}Lu	208.4	(3, 4) correct 6 day value for $^{239}\text{Np}(\text{U})$ at 209.7 keV then take weighted mean.

(1) 4 m irradiation at 10^{11} n/cm²/s, 12 m decay, 5 m count.

(2) 4 m irradiation at 10^{11} n/cm²/s, 30 m decay, 10 m count.

(Continued)

Table 26. (Continued)

- (3) 2 h irradiation at 10^{12} n/cm²/s, ~6d decay, 1-3 h count dependent upon REE content.
- (4) 2 h irradiation at 10^{12} n/cm²/s, ~21d decay, 3-10 h count dependent upon REE content.
- (5) Example of general correction method. ²³³Pa(Th) at 300.1 keV interferes with ¹⁶⁰Tb at 298.5 keV. Hence:

$$\frac{\text{ppm Th found at 311.9 keV}}{\text{ppm Th found at 300.1 keV}} \times \text{counts in 298.5 keV peak}$$

= net counts at 298.5 keV due to Th

and net Tb counts = Total counts at 298.5 keV - net counts due to Th.

$$\text{net ppm Tb} = \frac{\text{net Tb counts at 298.5 keV}}{\text{total counts at 298.5 keV}} \times \text{ppm } ^{160}\text{Tb found at 298.5 keV.}$$

- (6) The correction for ¹⁸²Ta at 198.3 keV includes an empirically determined correction factor for interference of ¹⁸²Ta onto ¹⁶⁹Yb, i.e., counts due to ¹⁸²Ta at 198.3 keV = 0.1888 x counts for ¹⁸²Tb at 152.4 keV.

sample size on precision were checked by replicate analyses of a single sample using aliquots of 100, 75, and 50 mg. Reduction of the size of the aliquot used increases the statistical uncertainty but in all cases the mean of triplicate analyses of smaller aliquots agrees within error with the results obtained using a 100 mg. aliquot.

The errors quoted in tables of results for INAA determinations are statistical uncertainties only and do not include uncertainties in weighing, timing and flux variations, which are negligible (Duke, 1983) in comparison to the statistical uncertainties.

D. Whole Rock Rb-Sr Analysis

Rb and Sr concentrations and Sr isotopic ratios were determined by methods outlined in Chaplin (1981).

E. U-Pb of Zircons

Concentrations of U and Pb and Pb isotopic compositions were determined by techniques outlined in Chaplin (1981) which is based on Krogh (1973).

F. Whole Rock Th-U-Pb

Concentrations of U, Th and Pb in selected whole rock samples were determined by an adaptation of the isotope dilution (ID)/isotope ratio (IR) method of Krogh (1973). Pb isotope ratios were determined following the procedures outlined below for dissolution and separation of Pb.

For whole rock IR determinations a sample estimated to contain about 10 μg Pb, usually 0.15 to 1.5 g, was decomposed overnight at 100°C using a 3:10 mixture of HNO_3 :HF. The solution was then uncovered and evaporated to dryness. Fluoride was removed by repeated evaporation with HNO_3 . The sample was then dissolved in 20 mL 1:1 HNO_3 : H_2O by refluxing covered for at least one hour. The resulting solution was evaporated to 10-11 mL volume and cooled before transfer (solution plus any precipitate) to a 15 mL Teflon centrifuge tube. The mixture was centrifuged and the supernatant liquid transferred to a silica centrifuge tube containing a few drops of Pb-free $\text{Ba}(\text{NO}_3)_2$ solution (approximately 10 mg $\text{Ba}(\text{NO}_3)_2$). Stirring with a Teflon rod usually produced a copious precipitate of $\text{Ba}(\text{NO}_3)_2$ which carries Pb as co-precipitate. If no precipitate formed then concentrated HNO_3 was added slowly, with stirring, until a precipitate formed. The centrifuge tube was covered and left overnight to allow complete precipitation of Ba and Pb nitrates.

Samples larger than 0.75 g often required a larger volume of 1:1 $\text{HNO}_3:\text{H}_2\text{O}$ to dissolve all or almost all of the decomposition residue. Up to 50 mL were used in some instances and this was evaporated to about 25-27 mL before cooling, centrifuging and precipitation of Ba and Pb nitrates.

The solution plus Ba + Pb precipitate was centrifuged and the supernatant discarded. The nitrate precipitate was dissolved in a minimum of water and the solution transferred to a 3 mL silica centrifuge tube. Barium nitrate was reprecipitated by addition of HNO_3 . Following centrifuging the supernatant liquid was discarded and the precipitate redissolved and reprecipitated at least twice in the small tube. The precipitate was then dried and dissolved in 1.0 mL 1.5 N HCl (vapour distilled). This solution was loaded onto a previously calibrated chloride anion exchange column to separate the Pb. The Pb-eluate was evaporated to dryness for the determination of Pb isotope ratios.

The purified Pb was loaded as a phosphoric acid-silica gel mixture onto a single filament of rhenium ribbon (0.75 x 0.025 mm). The 206/204, 207/206 and 208/206 ratios were measured at a temperature of 1200-1280°C on a VG Micromass 30 spectrometer using a nine-step peak jumping procedure. Mass normalisation factors of 206/204 = 1.002752, 207/204 = 1.004267 and 208/204 =

1.006420, determined by repeat runs of the NBS 981 standard, were applied to normalise the sample data to the NBS 981 standard.

For U-Th-Pb whole rock determinations both Pb IR and U-Th-Pb ID's were determined from a single sample dissolution. A sample sufficient to contain about 10 μ g Pb was weighed into a Teflon beaker. The sample was decomposed and dissolved in 1:1 HNO₃ and cooled as outlined above. At this stage the sealed beaker was weighed. Half the solution was poured into a clean weighed Teflon beaker and weighed. An aliquot of mixed ²³⁸U + ²³⁰Th spike was weighed in followed by an aliquot of either ²⁰⁸Pb or ²⁰⁶Pb spike (depending upon whether the sample was rich in U or Th). This portion was used for isotope dilution of U, Th and Pb concentrations. The second half of the sample solution was used for IR determination and was processed following the method outlined above.

The ID determinations required a modification of the Pb-IR method. The spiked solution was evaporated to a volume approximately equal to one-half of the ID sample aliquot, to make the HNO₃ almost concentrated. This solution was cooled, centrifuged and Ba(NO₃)₂ precipitated as before but the first supernatant liquid which contained U and Th was retained. The Pb was separated as outlined

above. The supernatant solution was transferred to a Teflon beaker and evaporated to a volume of about 1 mL HNO_3 . One mL H_2O was added and this solution added to a pre-calibrated nitrate anion exchange column to separate U and Th. The sample was passed twice through the column to purify Th and U. The final U-Th eluate was evaporated to dryness then loaded in a drop of HNO_3 onto the side filament of an outgassed double rhenium filament.

The purified Pb separate was loaded in the usual phosphoric acid-silica gel mixture onto the centre filament of the same assembly and ratios measured as outlined above.

U ($^{238}/^{235}$) and Th ($^{232}/^{230}$) ratios were measured on the VG Micromass 30 spectrometer using a 3-step peak-jumping procedure.

G. Whole Rock Sm-Nd Analyses

A sample containing at least 15 μg Nd (0.2 to 1.0 g usually) was weighed into a 25 mL screw-top Teflon vessel and mixed $^{145}\text{Nd} + ^{149}\text{Sm}$ spike solution added for isotope dilution analysis. A like amount of sample powder was placed in a second vessel for determination of the $^{143}\text{Nd}/^{144}\text{Nd}$ ratio. Use of separate dissolutions for ratio and concentration determinations was justified by repeat

analyses of several samples. Even for carbonatites containing over 1500 ppm Nd no significant difference in either $^{143}\text{Nd}/^{144}\text{Nd}$ or $^{147}\text{Sm}/^{144}\text{Nd}$ was found. Samples were decomposed overnight in 3 mL HNO_3 + 10 mL HF at $\sim 100^\circ\text{C}$. After centrifuging, the supernatant liquid was discarded, the fluoride residue was washed by digestion with 4% HF:4% HCl solution (centrifuge and discard wash liquid) then the fluoride was removed by repeated evaporation with HNO_3 . The final residue was dissolved in dilute HCl and R_2O_3 elements precipitated by addition of ammonia. If there was insufficient Fe or Al present to act as a carrier for Nd and Sm then the solution was re-acidified, a trace of pure Fe solution added and the R_2O_3 reprecipitated. If excessive amounts of Al or Fe were present at this stage then the following steps were repeated until the R_2O_3 precipitate reached an amount which would be soluble in less than 2 mL 6N HCl. To the hydroxide precipitate concentrated HF was added dropwise to dissolution. The resulting fluoride residue was baked to incipient dryness to remove excess HF then it was digested with 5% HF:4% HCl solution for 20 minutes to solubilise the Al and Fe as fluoride complexes. The solution was removed following centrifuging and the digestion procedure repeated twice more with fresh acid solution. Then the residue was treated with HNO_3 as before, to remove fluoride, taken up

in dilute HCl and the R_2O_3 group precipitated by the addition of ammonia. All steps were carried out in the original Teflon vessel. A second procedure, which could not be used for samples with a low Nd content, was sometimes employed to remove excessive amounts of aluminum. The ammonia precipitation was carried out in a 50 mL silica centrifuge tube. Following removal of the supernatant solution, pellets of pure NaOH were added to the hydroxide residue to dissolve the aluminum but not the iron or rare-earth hydroxides. The resulting solution was removed by centrifuging and decanting. To remove excess sodium the precipitate was again taken up in dilute HCl and hydroxides reprecipitated with ammonia.

In all cases the final hydroxide precipitate was dissolved in a minimum of 6N HCl and water such that the final volume of solution was less than 2 mL and less than 2N in HCl for addition to the first cation exchange column. Subsequent procedures for the separation of Nd (and Sm) are essentially those outlined by Dösso and Murthy (1980). The dilute HCl sample solution was added to a cation exchange column (Dowex 50W-X8, 100-200 mesh) 6.0 mm diameter, 21.4 cm length of resin previously cleaned with 6N HCl and equilibrated to 2.3N HCl. The major elements were removed by elution with 80 mL 2.3N HCl, then the REE (rare earth elements) were collected in

55 mL 2.3N HCl. The sample solution was evaporated to dryness and the residue taken up in 2 drops 1.5N HCl for addition to the second column. This column is 3 mm in diameter and contains a length of 34.3 cm Dowex 50W-X8, 100-200 mesh cation exchange resin cleaned with 6N HCl, rinsed with water and then equilibrated to 0.2 M 2-methylactic acid (MLA) adjusted to a pH = 4.43 ± 0.01 with ammonia. After the sample was loaded onto the resin the column was connected to a fraction collector and eluted with continuous stream of 0.2 M MLA. When elution of Nd was complete, the beakers containing the central portion of the Nd (or Sm) peak (as determined by a calibration run using mixed Sm and Nd) were combined in a Teflon beaker and the solution evaporated to dryness. For Nd the volume collected was about 25 mL, for Sm about 12-13 mL. Calibration of this column was monitored throughout the study. The remaining MLA was removed on a third column, 3 mm diameter with 8.0 cm of Dowex-X8, 100-200 mesh resin cleaned with 6N HCl and water then equilibrated to 0.1 M HCl. The sample was added to the column in about 0.5 mL 1.5N HCl then the MLA and ammonium salts were removed by elution with two 1 mL portions of 0.1 M HCl followed by 3 mL 0.1 M HCl, then 8 mL 2.3N HCl. Nd or Sm was then collected in 20 mL 6N HCl and the solution evaporated to dryness. At this stage, for

isotope dilution the sample was heated with a drop of HNO_3 to convert it to nitrate form and was now ready for loading onto the mass spectrometer filament. For measurement of the $^{143}\text{Nd}/^{144}\text{Nd}$ ratio two further steps were added for purification. The Nd sample, dissolved in 1 drop 2.3N HCl, was added to a fourth column containing a resin bed of 1 mm diameter, 12.3 cm length below a loading reservoir. The resin employed was Dowex 50W-X8, 100-200 mesh cleaned with 6N HCl and equilibrated to 2.3N HCl. The sample was washed in with 2 sequential drops of 2.3N HCl from a measured volume of 0.8 mL, then eluted with the remainder to remove soluble alkali. Nd was then collected in a Teflon beaker using 1.6 mL 6N HCl and this solution was evaporated. Because the isotope ratios of these samples were being measured in a chloride form on the mass spectrometer it was necessary to remove the organic matter to improve stability. The sample was transferred in three successive drops of HNO_3 to a special platinum vessel, dried on a hotplate, and carefully ignited to a red glow over a burner. The organic-free Nd sample was transferred to a round-bottomed Teflon vessel using 2 sequential drops of 6N HCl, ready for loading onto the mass spectrometer filament in a chloride form.

The total blank on the procedure was less than 0.3 ng Sm and 7 ng Nd. In all cases in this study, the

sample:blank ratio was significantly greater than 1000:1.

For determination of the $^{143}\text{Nd}/^{144}\text{Nd}$ ratio the sample was loaded from 6N HCl onto the side filament of a double filament assembly and dried in air at a low current. For determinations of ratios in spiked samples either Nd or Sm was loaded as the nitrate from dilute HNO_3 solution onto the side of a double filament, dried and heated to a dull red glow to convert to the oxide. Ratios were determined on a VG Micromass 30 spectrometer. Accuracy and precision were monitored throughout the study using four standards. Whole rock powders of USGS BCR-1 and an "in-house" gneiss standard were repeatedly carried through the entire procedure. The mean of 4 runs on BCR-1 was 0.511820 ± 23 . Repeat runs on the in-house standard gave a run-to-run reproducibility of $\pm .00003$ for the entire procedure. Two solutions of Nd were employed for mass spectrometer reproducibility and inter-laboratory checks. The Nd in each of these solutions was converted to the chloride form by evaporation of an HCl solution before loading onto the filament for measurement. The in-house standard solution gave run-to-run reproducibility of $\pm .00002$ indicating that for the samples most of the imprecision or error lies in the ratio determinations themselves and not in the chemistry. For the La Jolla Nd solution the mean of 9 runs was $0.511833 \pm 9 (1\sigma)$. This

value compares with that of 0.511837 ± 4 reported by Carlson (1984) but is lower than the La Jolla value of 0.511858.

APPENDIX 3

DETAILED ANALYTICAL RESULTS FOR WHOLE ROCK SAMPLES

The following abbreviations are used in the tables of results.

ND Not detected/below detection limits.

NA Not analysed/not determined.

XRF X-ray fluorescence analysis.

INAA Instrumental neutron activation analysis.

MSID Mass spectrometric isotope dilution analysis.

DNC Delayed neutron counting

Errors listed on INAA analysis are statistical (1 σ) errors.

Table 27. Analytical Results: Centre One, - Gabbros and Diorites

	Sample Number				Method
	PC-81-235	PC-81-275	PC-81-363	PC-82-173	
<u>Major and Minor Element Oxides (%)</u>					
SiO ₂	48.62	49.19	51.31	46.69	XRF
Al ₂ O ₃	18.57	21.27	19.23	16.24	XRF
TiO ₂	2.98	2.68	1.93	4.22	XRF
Fe ₂ O ₃	10.36	7.60	8.01	13.33	XRF
MgO	3.55	2.46	2.31	4.23	XRF
CaO	9.59	9.91	6.31	8.84	XRF
MnO	0.12	0.08	0.12	0.14	XRF
Na ₂ O	4.29	4.10	5.78	3.94	XRF
K ₂ O	0.90	1.36	1.79	1.23	XRF
P ₂ O ₅	0.22	0.10	0.77	0.16	XRF
LOI	1.19	1.39	2.19	0.98	
<u>Trace Elements (ppm)</u>					
Ba	432	507	1629	562	XRF
Ce	38.1±0.4	26.7±0.4	77.9±0.5	43.6±0.5	INAA
Co	32.9±0.2	26.5±0.2	15.3±0.1	42.2±0.2	INAA
Cr	38.2±1.9	10.4±1.8	9.4±1.7	28.9±2.3	INAA
Cs	ND	ND	0.47±0.12	ND	INAA
Dy	2.29±0.29	1.16±0.23	3.55±0.40	2.85±0.33	INAA
Eu	2.55±0.06	2.01±0.06	4.07±0.07	2.54±0.07	INAA
Hf	1.90±0.06	1.22±0.06	2.58±0.06	2.27±0.08	INAA
La	17.2±0.2	11.3±0.2	35.1±0.3	20.2±0.2	INAA
Lu	0.09±0.01	0.07±0.02	0.12±0.02	0.12±0.02	INAA
Mo	ND	ND	1	2	XRF
Nb	19	16	24	28	XRF
Nd	22.85	13.76	42.41	22.06	MSID
Pb	8	4	11	6	XRF
Rb	23	†22.0	40	25	XRF, †MSID
Sb	ND	ND	ND	ND	INAA
Sc	13.7±0.1	10.5±0.1	7.90±0.1	17.9±0.1	INAA
Sm	4.64	2.89	7.94	4.52	MSID
Sr	1713	†235.7	1861	1243	XRF, †MSID
Ta	1.44±0.07	1.08±0.07	1.70±0.07	2.21±0.07	INAA
Tb	0.64±0.09	0.28±0.09	0.63±0.09	0.46±0.01	INAA
Th	3.0±0.1	0.9±0.1	4.6±0.1	1.3±0.1	INAA
U	0.49±0.03	0.16±0.02	0.58±0.04	0.36±0.03	DNC
V	158±9	152±10	58±7	287±12	INAA
Y	11	8	19	12	XRF
Yb	0.68±0.06	0.50±0.06	1.08±0.06	0.74±0.07	INAA
Zr	93	70	117	111	XRF

Table 28. Analytical Results: Centre Two - Quartz Free Syenites

	Sample Number				Method
	PC-81-012	PC-81-332	PC-82-124	PC-82-129	
<u>Major and Minor Element Oxides (%)</u>					
SiO ₂	53.36	55.23	59.07	60.17	XRF
Al ₂ O ₃	16.01	16.59	16.66	16.63	XRF
TiO ₂	1.97	1.47	1.34	1.08	XRF
Fe ₂ O ₃	11.85	10.27	6.25	6.25	XRF
MgO	1.89	1.36	1.18	0.91	XRF
CaO	4.43	3.90	2.46	2.20	XRF
MnO	0.23	0.20	0.11	0.13	XRF
Na ₂ O	6.09	6.26	5.97	6.08	XRF
K ₂ O	2.56	3.18	5.13	5.35	XRF
P ₂ O ₅	0.56	0.38	0.29	0.24	XRF
LOI	1.10	1.05	1.57	1.22	
<u>Trace Elements (ppm)</u>					
Ba	397	3128	3335	2097	XRF
Ce	86.7±0.6	121±1	65.5±0.7	68.3±0.9	INAA
Co	10.1±0.1	7.6±0.1	4.9±0.1	4.0±0.1	INAA
Cr	ND	6.5±1.9	22.8±2.3	ND	INAA
Cs	0.64±0.12	ND	ND	1.07±0.15	INAA
Dy	5.17±0.53	6.78±0.60	3.30±0.36	3.85±0.40	INAA
Eu	7.42±0.08	7.44±0.10	5.70±0.09	4.87±0.09	INAA
Hf	3.13±0.06	5.40±0.13	2.71±0.07	4.5±0.1	INAA
La	41.2±0.3	55.3±0.3	29.7±0.3	34.2±0.2	INAA
Lu	0.18±0.02	0.26±0.02	0.14±0.03	0.17±0.02	INAA
Mo	3	2	1	-	XRF
Nb	40	58	23	28	XRF
Nd	†58.60	†68.20	†36.73	†43±7	†MSID, *INAA
Pb	7	10	10	9	XRF
Rb	†38.1	*40	*53	*72	*XRF, †MSID
Sb	0.35±0.09	0.31±0.10	0.89±0.09	ND	INAA
Sc	6.60±0.03	7.14±0.02	3.71±0.02	2.40±0.01	INAA
Sm	†11.35	†13.41	†6.94	*8.02±0.02	
Sr	†1353	1003	648	512	XRF
Ta	2.35±0.08	3.56±0.08	1.49±0.09	1.74±0.07	INAA
Tb	1.05±0.04	1.44±0.04	0.72±0.10	0.80±0.03	INAA
Th	1.9±0.1	4.6±0.1	4.6±0.1	6.2±0.1	INAA
U	0.63±0.04	0.67±0.04	1.10±0.05	*1.92±0.38	DNC, *INAA
V	ND	NA	NA	NA	
Y	27	35	16	20	XRF
Yb	1.53±0.07	2.13±0.08	0.99±0.08	1.17±0.06	INAA
Zr	146	212	127	130	XRF

Table 29. Analytical Results: Centre Two - Quartz Syenites¹

	Sample Number					
	PC-82-096	PC-82-099	PC-82-151	PC-82-358	PC-81-364	PC-81-285
Major and Minor Element Oxides (%)						
SiO ₂	63.96	61.95	63.61	64.88	63.39	59.63
Al ₂ O ₃	14.75	14.94	15.20	15.82	15.91	15.66
TiO ₂	0.47	0.43	0.76	0.60	0.69	1.27
Fe ₂ O ₃	6.40	4.84	5.82	4.76	5.23	7.46
MgO	0.60	1.13	0.78	0.59	0.60	1.72
CaO	1.02	2.75	1.74	1.46	1.70	2.45
MnO	0.09	0.22	0.13	0.09	0.08	0.11
Na ₂ O	5.56	5.76	5.04	5.58	6.04	5.61
K ₂ O	5.62	4.91	5.03	5.28	4.95	4.25
P ₂ O ₅	0.06	0.06	0.15	0.11	0.13	0.28
LOI	1.69	3.14	1.70	1.26	1.35	1.78
Trace Elements (ppm)						
Ba	309	405	657	836	804	963
Ce	190±1	341±1	192±1	199±1	154±1	166±1
Co	1.6±0.1	1.5±0.1	5.1±0.1	4.3±0.1	4.6±0.1	10.7±0.1
Cr	2.5±1.8	7.5±1.7	15.3±1.8	14.5±2.9	5.6±1.9	9.1±1.8
Cs	ND	1.66±0.11	0.96±0.11	ND	1.19±0.13	1.46±0.09
Dy	7.56±0.68	10.9±1.0	9.50±0.84	8.47±0.73	8.13±0.73	8.85±0.79
Eu	3.25±0.06	3.83±0.08	2.80±0.07	3.19±0.08	3.35±0.08	3.79±0.08
Hf	8.7±0.1	8.4±0.1	13.7±0.1	12.6±0.1	12.0±0.1	8.2±0.1
La	93.0±0.3	184.9±0.5	87.5±0.4	90.0±0.4	65.8±0.3	84.8±0.1
Lu	0.38±0.01	0.43±0.02	0.45±0.02	0.42±0.03	0.41±0.03	0.38±0.01
Mo	4	6	4	3	3	4
Nb	65	58	82	72	77	67
Nd	†87.7	†133.5	†95.7	†81.1	*82.5	†84.9
Pb	9	36	10	18	16	13
Rb	†92.6	*115	†114.2	†126.3	†128.6	†107.4
Sb	ND	0.33±0.08	0.26±0.09	0.57±0.08	ND	ND
Sc	1.88±0.02	1.61±0.02	2.97±0.02	2.31±0.02	2.89±0.02	5.31±0.03
Sm	†15.58	†21.15	†17.45	†14.39	14.60±0.03	†15.43
Sr	†87.4	242	†220.1	†289.5	†404.3	613.8
Ta	3.76±0.07	2.1±0.1	5.54±0.08	4.96±0.11	5.34±0.11	3.95±0.08
Tb	1.64±0.08	2.11±0.08	1.81±0.08	1.58±0.11	1.54±0.13	1.60±0.08
Th	14.5±0.1	17.7±0.1	18.0±0.1	20.9±0.1	16.1±0.1	12.4±0.1
U	2.68±0.08	2.39±0.08	3.01±0.08	3.34±0.09	2.48±0.08	2.23±0.07
V	ND	ND	12.0±6	ND	ND	48±8
Y	40	50	47	43	42	42
Yb	2.71±0.05	3.14±0.07	3.49±0.07	2.94±0.07	3.26±0.07	2.69±0.06
Zr	311	348	618	495	503	398

¹For methods used see Table 28.

Table 30. Analytical Results: Gneisses

	Sample Number				Method
	PC-81-025	PC-81-483	PC-82-074	PC-82-281	
<u>Major and Minor Element Oxides (%)</u>					
SiO ₂	71.20	72.39	74.58	71.92	XRF
Al ₂ O ₃	14.70	14.08	13.68	13.85	XRF
TiO ₂	0.26	0.29	0.14	0.28	XRF
Fe ₂ O ₃	2.26	2.52	1.22	2.54	XRF
MgO	1.56	1.09	0.45	0.84	XRF
CaO	0.47	0.57	0.51	0.75	XRF
MnO	0.01	0.01	0.02	0.03	XRF
Na ₂ O	3.57	3.49	3.21	3.41	XRF
K ₂ O	4.89	4.64	4.98	4.87	XRF
P ₂ O ₅	0.09	0.09	0.21	0.08	XRF
LOI	1.29	1.22	1.12	1.26	
<u>Trace Elements (ppm)</u>					
Ba	660	494	209	779	XRF
Ce	96.2±0.8	67.6±0.4	41.4±0.4	79.2±0.5	INAA
Co	3.2±0.1	3.8±0.1	2.0±0.1	4.3±0.1	INAA
Cr	5.0±0.8	3.3±0.1	6.8±0.1	5.2±0.7	INAA
Cs	1.29±0.13	0.84±0.10	2.04±0.10	1.06±0.11	INAA
Dy	5.76±0.51	3.97±0.36	1.42±0.18	4.49±0.41	INAA
Eu	0.99±0.04	0.70±0.04	0.28±0.03	0.94±0.04	INAA
Hf	585±0.09	4.74±0.08	2.45±0.06	5.60±0.08	INAA
La	46.0±0.3	39.2±0.2	17.9±0.2	39.9±0.3	INAA
Lu	0.49±0.03	0.27±0.01	0.08±0.01	0.24±0.01	INAA
Mo	NA	NA	NA	NA	
Nb	14	14	11	13	XRF
Nd	41.03	39.28	19.31	36.12	MSID
Pb	24	24	25	23	XRF
Rb	123.9	105.2	201.0	117.5	MSID
Sb	NA	NA	NA	NA	
Sc	5.16±0.02	4.38±0.02	1.49±0.01	5.16±0.02	INAA
Sm	8.37	8.00	3.96	7.52	MSID
Sr	86.2	108.0	51.8	149.1	MSID
Ta	0.76±0.05	0.54±0.05	0.59±0.04	0.64±0.05	INAA
Tb	1.17±0.07	1.00±0.05	0.39±0.04	0.99±0.02	INAA
Th	25.9±0.6	19.2±0.1	20.3±0.1	22.1±0.1	INAA
U	5.30±0.25	3.32±0.23	5.06±0.23	2.75±0.21	INAA
V	NA	NA	NNA	NA	INAA
Y	40	29	8	27	XRF
Yb	2.99±0.23	1.38±0.04	0.48±0.04	2.03±0.02	INAA
Zr	184	148	85	164	XRF

Table 31. Analytical Results: Centre One - Pyroxenites

	Sample Number				Method
	PC-81-001	PC-81-004	PC-82-163	PC-81-001 (pyroxene) (separate)	
<u>Major and Minor Element Oxides (%)</u>					
SiO ₂	29.77	36.42	34.38	NA	XRF
Al ₂ O ₃	2.36	3.36	4.37	NA	XRF
TiO ₂	10.19	5.14	7.34	NA	XRF
Fe ₂ O ₃	32.80	26.78	29.96	NA	XRF
MgO	12.31	14.63	10.88	NA	XRF
CaO	10.31	12.11	10.57	NA	XRF
MnO	0.24	0.27	0.23	NA	XRF
Na ₂ O	0.47	0.26	0.14	NA	XRF
K ₂ O	0.01	0.03	0.07	NA	XRF
P ₂ O ₅	0.01	0.02	0.14	NA	XRF
LOI	1.02	1.27	1.75		
<u>Trace Elements (ppm)</u>					
Ba	102	69	89	ND	XRF
Ce	14.1±0.6	10.5±0.6	30.2±0.6	21.5±0.6	INAA
Co	154±1	138±1	126±1	77.7±0.4	INAA
Cr	746±2	2679±5	706±5	100±3	INAA
Cs	ND	ND	ND	ND	INAA
Dy	2.30±0.33	1.37±0.23	3.39±0.39	3.86±0.43	INAA
Eu	1.01±0.09	0.74±0.07	2.14±0.09	1.71±0.11	INAA
Hf	1.74±0.10	1.34±0.11	2.98±0.13	2.2±0.2	INAA
La	4.6±0.1	3.1±0.1	10.4±0.1	6.7±0.2	INAA
Lu	ND	ND	ND	0.12±0.04	INAA
Mo	1	NA	NA	NA	XRF
Nb	16	9	20	NA	XRF
Nd	14.23	10.25	26.83	ND	MSID
Pb	7	9	4	NA	XRF
Rb	†0.79	3	3	ND	XRF, †MSID
Sb	ND	ND	2.4±0.1	ND	INAA
Sc	48.3±0.1	47.9±0.1	42.2±0.1	65.6±0.1	INAA
Sm	†3.84	†2.76	†6.73	*6.16±0.02	†MSID, *INAA
Sr	103	62	66	ND	XRF
Ta	1.22±0.09	0.30±0.08	1.38±0.09	ND	INAA
Tb	0.44±0.06	0.29±0.06	0.72±0.06	0.62±0.07	INAA
Th	ND	ND	0.71±0.11	ND	INAA
U	0.14±0.02	ND	ND	ND	INAA
V	1240±30	NA	NA	NA	INAA
Y	11	7	18	NA	XRF
Yb	0.49±0.11	ND	0.79±0.09	1.22±0.12	INAA
Zr	74	54	105	NA	XRF

Table 32. Analytical Results: Centre Three - Fovaites.

	Sample Number					Method
	PC-81-482	PC-82-039	PC-81-165	PC-81-194	PC-81-287	
<u>Major and Minor Element Oxides (%)</u>						
SiO ₂	53.31	50.80	41.29	42.54	44.89	XRF
Al ₂ O ₃	23.49	20.47	12.09	20.89	14.68	XRF
TiO ₂	0.26	2.20	0.22	0.17	0.30	XRF
Fe ₂ O ₃	2.21	7.83	14.42	8.86	13.92	XRF
MnO	0.02	0.19	1.99	0.82	1.90	XRF
CaO	0.78	1.41	9.86	4.26	8.02	XRF
MgO	0.06	0.26	0.48	0.26	0.47	XRF
Na ₂ O	11.23	7.43	11.38	14.14	10.10	XRF
K ₂ O	6.62	7.52	0.67	2.90	1.26	XRF
P ₂ O ₅	0.06	0.02	0.22	0.08	0.09	XRF
LOI	2.11	2.02	5.89	5.37	4.47	
<u>Trace Elements (ppm)</u>						
Ba	1914	2448	693	628	553	XRF
Ce	112±1	116±1	352±1	191±1	265±1	INAA
Co	ND	6.3±0.1	8.9±0.1	3.8±0.1	8.6±0.1	INAA
Cr	2.6±1.3	9.7±1.4	28.7±2.0	ND	28.0±2.0	INAA
Cs	1.14±0.09	2.65±0.18	0.57±0.15	ND	4.48±0.22	INAA
Dy	3.92±0.42	6.43±0.63	15.32±0.82	7.32±0.46	11.17±0.63	INAA
Eu	2.58±0.05	4.03±0.08	9.33±0.08	4.54±0.09	6.55±0.09	INAA
Hf	1.2±0.1	7.6±0.1	17.6±0.1	10.8±0.1	23.0±0.1	INAA
La	68.7±0.4	45.8±0.6	144.7±0.3	81.6±0.4	114.0±0.3	INAA
Lu	0.08±0.01	0.19±0.03	1.03±0.03	0.55±0.02	0.89±0.02	INAA
Mo	4	ND	5	3	4	XRF
Nb	21	194	65	38	153	XRF
Nd	†43.83	†67.61	*188±9	87.48	126.4	†MSID, *INAA
Pb	8	†3.2	†17.6	†10.4	†18.8	†MSID, *XRF
Rb	†158	†229	*38	†117	*73	†MSID, *XRF
Sb	ND	0.72±0.07	ND	0.29±0.08	ND	INAA
Sc	0.05	0.20±0.02	2.7±0.03	1.4±0.03	2.1±0.1	INAA
Sm	†7129	†13.10	*28.7±0.1	15.00	22.07	†MSID, *XRF
Sr	†1922	†977	*1876	†2097	1784	†MSID, *XRF
Ta	0.65±0.09	24.31±0.12	6.21±0.17	1.13±0.21	15.9±0.2	INAA
Tb	0.81±0.05	1.00±0.09	2.89±0.06	1.31±0.05	2.18±0.10	INAA
Th	*5.54±0.06	†3.60±0.08	†10.55±.78	†7.53±0.14	†12.01±.10	†MSID, *INAA
U	*0.28±0.03	†2.51	†6.10	†0.66	†14.70	†MSID, *DNC
V	ND	ND	32±5	ND	32±3	INAA
Y	24	26	61	34	48	XRF
Yb	1.07±0.05	2.11±0.3	4.71±0.15	2.64±0.08	3.55±0.21	INAA
Zr	79	417	1289	779	1362	XRF

Table 33. Analytical Results: Centre Three - Trolites, Meltegranites

	Sample Number				Method
	PC-82-525	PC-82-526	PC-81-168	PC-82-021	
<u>Major and Minor Element Oxides (%)</u>					
SiO ₂	43.52	43.25	46.38	48.32	XRF
Al ₂ O ₃	14.84	16.33	6.69	7.68	XRF
TiO ₂	0.21	0.20	1.45	2.50	XRF
Fe ₂ O ₃	13.22	12.49	22.14	18.52	XRF
MgO	1.76	1.55	2.89	1.17	XRF
CaO	7.93	7.26	9.83	12.90	XRF
MnO	0.42	0.38	0.69	0.58	XRF
Na ₂ O	12.76	12.12	6.16	5.19	XRF
K ₂ O	0.38	1.41	1.70	2.37	XRF
P ₂ O ₅	0.09	0.07	0.06	0.09	XRF
LOI	5.01	4.71	2.22	0.78	
<u>Trace Elements (ppm)</u>					
Ba	343	466	697	572	XRF
Ce	242±1	247±1	217±1	289±1	INAA
Co	8.0±0.2	7.9±0.2	15.4±0.2	13.3±0.2	INAA
Cr	ND	ND	ND	1.6±0.2	INAA
Cs	1.54±0.26	1.03±0.27	2.54±0.21	0.61±0.14	INAA
Dy	9.72±0.49	8.69±0.53	7.96±0.53	15.89±0.86	INAA
Eu	6.04±0.11	5.57±0.12	5.16±0.11	11.83±0.12	INAA
Hf	14.6±0.1	13.7±0.1	23.2±0.2	24.1±0.2	INAA
La	110.2±0.4	111.4±0.4	97.3±0.3	96.0±0.4	INAA
Lu	1.02±0.04	0.92±0.05	1.17±0.05	0.98±0.02	INAA
Mo	5	5	4	4	XRF
Nb	123	237	359	197	XRF
Nd	†112.6	*145±14	†93.9	*221±9	†MSID, *INAA
Pb	*20	†26.7	*19	*8	†MSID, *XRF
Rh	†23.2	39	75	56	†MSID
Sb	ND	ND	ND	ND	INAA
Sc	1.41±0.04	1.52±0.04	1.91±0.03	1.59±0.03	INAA
Sm	†19.72	*23.1±0.1	†16.52	*42.4±0.1	†MSID, *INAA
Sr	†1309	1534	974	1502	†MSID, *XRF
Ta	22.16±0.24	41.99±0.22	52.64±0.48	35.93±0.22	INAA
Tb	2.06±0.06	2.21±0.20	1.66±0.08	3.41±0.07	INAA
Th	*9.8±0.2	†10.90	*12.0±0.2	*34.6±0.7	†MSID, *INAA
U	*18.99±0.23	†39.48	*33.83±.29	*0.55±0.03	†MSID, *DNC
V	22±1	ND	29±2	ND	INAA
Y	45	37	32	57	XRF
Yb	3.40±0.05	3.11±0.05	2.35±0.05	3.72±0.04	INAA
Zr	991	982	1215	967	XRF

Table 34. Analytical Results: Centre Four - Carbonatites (a)

	Sample Number					Method
	PC-81-178	PC-81-376	PC-82-506	PC-81-176	PC-81-383	
<u>Major and Minor Element Oxides (%)</u>						
SiO ₂	1.41	0.79	0.83	25.51	9.33	XRF
Al ₂ O ₃	0.35	0.32	0.29	8.78	3.92	XRF
TiO ₂	0.09	0.03	0.06	0.10	0.02	XRF
Fe ₂ O ₃	1.16	0.78	0.98	2.26	3.62	XRF
MgO	0.18	0.17	0.14	0.41	0.07	XRF
CaO	53.82	53.72	53.12	33.56	45.20	XRF
MnO	0.87	1.58	2.08	0.24	0.32	XRF
Na ₂ O	0.0	0.0	0.0	3.34	0.24	XRF
K ₂ O	0.02	0.0	0.02	0.28	0.26	XRF
P ₂ O ₅	0.02	0.0	0.15	0.02	0.02	XRF
LOI	41.62	42.11	41.60	25.90	35.01	
<u>Trace Elements (ppm)</u>						
Ba	109	70	97	275	223	XRF
Ce	2921±3	4593±5	3303±1	1780±4	2963±6	INAA
Co	3.0±0.2	ND	1.3±0.2	1.8±0.2	ND	INAA
Cr	34±3	62±3	14 ±3	49±3	21±6	INAA
Cs	ND	ND	ND	ND	ND	INAA
Dy	48.31±4.31	23.40±2.93	41.99±4.20	14.45±0.73	47.95±2.35	INAA
Eu	75.11±0.36	90.84±0.35	63.05±0.33	24.96±0.20	58.8±0.41	INAA
Hf	ND	ND	ND	ND	ND	INAA
La	1058±1	1540±1	1204±1	985±1	1369±2	INAA
Lu	1.25±0.09	0.83±0.05	1.09±0.09	1.62±0.03	0.52±0.07	INAA
Mo	NA	NA	NA	7	1	XRF
Nb	20	19	182	14	10	XRF
Nd	1940	2277	1890	693	1692	MSID
Pb	†23.2	†132	*131	†87.7	†25	†MSID, *XRF
Rb	3	5	6	12	14	XRF
Sb	ND	ND	0.6±0.1	0.5±0.1	ND	INAA
Sm	339	342	270	98.4	243	MSID
Sr	2760	2414	3717	6980	9029	XRF
Ta	ND	ND	3.9±0.2	0.75±0.15	ND	INAA
Tb	13.87±0.14	9.16±0.14	9.44±0.09	4.30±0.11	10.03±0.20	INAA
Th	†38.1	†28.67	*48±1	†34.60	†63.4	†MSID, *INAA
U	†1.03	†0.19	*2.7±0.7	†1.39	†2.06	†MSID, *DNC
V	NA	NA	NA	NA	NA	INAA
Y	156	68	187	71	162	XRF
Yb	8.41±0.17	3.79±0.11	8.56±0.17	6.11±0.20	5.16±0.15	INAA
Zr	30	23	36	18	23	XRF

Table 35. Analytical Results: Centre Four - Carbonatites (b)

	Sample Number				Method
	PC-81-185	PC-82-088	PC-82-408	PC-82-412	
<u>Major and Minor Element Oxides (%)</u>					
SiO ₂	14.07	3.38	11.13	23.61	XRF
Al ₂ O ₃	0.56	0.34	4.59	4.79	XRF
TiO ₂	0.19	0.02	3.04	3.36	XRF
Fe ₂ O ₃	6.46	2.61	23.26	22.02	XRF
MgO	0.64	0.86	12.18	12.17	XRF
CaO	43.38	49.51	18.24	12.87	XRF
MnO	1.25	1.38	0.63	0.47	XRF
Na ₂ O	0.06	0.31	0.0	0.19	XRF
K ₂ O	0.0	0.36	1.43	1.51	XRF
P ₂ O ₅	0.15	0.0	1.87	2.59	XRF
LOI	34.66	39.91	23.94	16.68	
<u>Trace Elements (ppm)</u>					
Ba	1725	73	399	467	XRF
Ce	793±2	333±2	589±2	1242±2	INAA
Co	1.7±0.2	1.7±0.1	50.6±0.4	46.4±0.2	INAA
Cr	32±4	17±2	447±4	864±5	INAA
Cs	ND	1.13±0.17	1.99±0.32	0.67±0.22	INAA
Dy	25.02±1.63	28.61±1.48	12.84±0.72	24.20±2.04	INAA
Eu	13.25±0.18	12.48±0.14	13.16±0.15	21.00±0.19	INAA
Hf	ND	ND	6.24±0.20	5.87±0.12	INAA
La	438±1	145±0.4	283±1	680±1	INAA
Lu	2.37±0.05	1.24±0.04	0.31±0.05	0.28±0.03	INAA
Mo	1	NA	7	7	XRF
Nb	36	9	105	100	XRF
Nd	†470	†230	*319±18	†619	†MSID, *INAA
Pb	*35	†32.4	*7	*12	†MSID, *XRF
Rh	6	36	74	56	XRF
Sb	0.5±0.2	0.2±0.1	ND	0.5±0.1	INAA
Sc	1.45±0.03	ND	14.6±0.1	18.39±0.05	INAA
Sm	†81.4	†50.2	*47.9±0.1	†87.9	†MSID, *INAA
Sr	5373	3199	1580	1389	XRF
Ta	ND	ND	5.29±0.17	5.13±0.11	INAA
Tb	5.65±0.06	7.01±0.14	3.26±0.09	5.39±0.11	INAA
Th	*49.3±0.3	†73.8	*8.5±0.5	*31.6±0.2	†MSID, *INAA
U	*2.19±0.07	†1.0	*4.09±0.10	*5.91±0.12	†MSID, *DNC
V	ND	ND	ND	213±10	INAA
Y	123	161	48	89	XRF
Yb	8.16±0.16	5.27±0.11	1.52±0.08	1.61±0.05	INAA
Zr	26	23	251	316	XRF

Table 36. Analytical Results: Centre Five - Shonkinites and Biotite-Pyroxenites

	Sample Number					Method
	PC-81-057	PC-81-061	PC-81-388	PC-82-260	PC-82-278	
<u>Major and Minor Element Oxides (%)</u>						
SiO ₂	48.78	41.28	41.01	51.44	40.66	XRF
Al ₂ O ₃	9.93	4.12	4.30	11.65	3.47	XRF
TiO ₂	2.30	2.87	2.92	2.14	3.84	XRF
Fe ₂ O ₃	13.30	18.96	17.87	12.25	21.75	XRF
MgO	7.92	11.61	13.41	6.30	10.70	XRF
CaO	8.85	14.98	14.27	7.56	15.77	XRF
MnO	0.16	0.22	0.19	0.16	0.26	XRF
Na ₂ O	2.47	0.68	0.34	3.22	0.77	XRF
K ₂ O	4.28	2.78	2.45	4.32	1.09	XRF
P ₂ O ₅	0.70	2.19	1.55	0.63	1.36	XRF
LOI	0.60	0.60	1.31	0.74	0.26	
<u>Trace Elements (ppm)</u>						
Ba	1392	2466	2131	1128	471	XRF
Ce	104±1	223±1	123±1	96±1	110±4	INAA
Co	46.4±0.3	76.6±0.3	74.0±0.4	36.2±0.2	74.4±0.5	INAA
Cr	345±2	182±2	873±7	389±1	267±2	INAA
Cs	9.5±0.3	5.4±0.3	3.9±0.4	7.2±0.2	2.2±0.3	INAA
Dy	4.57±0.46	7.12±0.62	4.49±0.46	5.14±0.51	5.94±0.58	INAA
Eu	3.17±0.08	5.76±0.12	3.81±0.14	2.84±0.09	3.87±0.12	INAA
Hf	5.5±0.2	2.8±0.2	1.8±0.3	4.4±0.1	2.8±0.2	INAA
La	46.6±0.3	93.3±0.4	51.3±0.3	44.6±0.3	43.1±0.3	INAA
Lu	0.19±0.03	0.21±0.02	0.18±0.03	0.27±0.03	0.37±0.03	INAA
Mo	2	0	2	3	2	XRF
Nb	25	13	10	26	13	XRF
Nd	*60±11	†132.7	†82.20	†54.72	†75.40	†MSID, *INAA
Pb	19	14	8	21	7	XRF
Rb	†231	*175	†177	†234	†60.3	†MSID, *XRF
Sb	0.34	ND	0.28±0.1	0.39±0.1	ND	INAA
Sc	29.21±0.06	43.56±0.05	47.58±0.06	25.76±0.05	50.01±0.07	INAA
Sm	*12.6±0.1	†25.36	†16.58	†10.87	†16.26	†MSID, *INAA
Sr	†997	*978	†519	†843	†388	†MSID, *INAA
Ta	1.38±0.08	0.61±0.10	ND	1.40±0.10	0.45±0.10	INAA
Tb	1.16±0.09	1.69±0.07	1.09±0.08	1.0±0.10	1.28±0.06	INAA
Th	13.8±0.2	8.0±0.1	4.2±0.2	12.2±0.1	4.5±0.2	INAA
U	3.22±0.09	0.84±0.04	0.64±0.04	3.21±0.09	1.10±0.05	DNC
V	NA	NA	386±12	ND	NA	INAA
Y	28	32	24	27	29	XRF
Yb	1.49±0.11	1.95±0.16	1.01±0.20	1.39±0.08	1.54±0.03	INAA
Zr	213	82	67	205	106	XRF

Table 37. Analytical results for samples analysed by XRF only - satellite complex.

	PC-81-053	PC-81-063	PC-81-064	PC-82-535
<u>Major and Minor Element Oxides (%)</u>				
SiO ₂	43.12	39.89	40.68	48.53
Al ₂ O ₃	6.42	4.09	4.10	8.66
TiO ₂	3.17	4.15	3.32	2.60
Fe ₂ O ₃	17.36	20.72	19.20	13.37
MgO	9.54	12.13	11.09	7.87
CaO	12.99	13.56	15.51	10.26
MnO	0.21	0.26	0.24	0.19
Na ₂ O	1.31	0.36	0.89	2.01
K ₂ O	3.36	1.69	2.30	4.45
P ₂ O ₅	1.77	1.75	1.82	0.97
LOI	0.64	1.34	0.86	0.69
<u>Trace Elements (ppm)</u>				
Ba	2528	2148	2356	2311
Nb	28	12	19	30
Pb	8	8	6	21
Rb	198	108	143	238
Sr	991	511	815	787
Y	31	29	35	27
Zr	203	84	118	233

APPENDIX 4

GEOCHRONOLOGY OF THE BIG SPRUCE LAKE ALKALINE INTRUSION

Abstract

A zircon age of $2188 \pm 16/-10$ Ma has been determined for the silica-saturated syenites of the Big Spruce Lake alkaline complex. A whole-rock Pb-Pb age of $2165 \pm 21/-22$ Ma was obtained for the silica-undersaturated rocks of the complex, and 2155 ± 16 for the complex as a whole. The Sm-Nd whole-rock data yield an age of 2183 ± 75 Ma for the complex as a whole. Weighting the ages by the inverse square of the standard deviations, an average for the complex of 2174 ± 20 Ma is determined. However, it is felt the zircon age is the most reliable for the time of crystallization of the complex. Minor contamination by country rock (Sm-Nd model ages of 2467 to 2595 Ma) and metasomatism contribute to scattered Sm-Nd data points and large errors in the ages obtained for the five individual units. The Pb-Pb data enable a limiting estimate of about 50 Ma for the maximum timespan for the intrusion of centres 1 to 4.

Introduction

The Big Spruce Lake intrusive complex, centered at $63^{\circ} 33'N$, $115^{\circ} 55'W$, about 150 km northwest of

Yellowknife, N.W.T., (Figure 1) intrudes granodioritic gneiss of the Slave Province. The complex was mapped and described in detail by Martineau (1970) and Martineau and Lambert (1974). The intrusive rocks consist of a main complex, about 3.5×9 km, and a satellite complex of potassium-rich mafic rocks outcropping about 5 km to the southeast. Within the main complex the rock types range from silica-saturated to oversaturated gabbros, diorites and syenites through undersaturated foyaites and ijolites to carbonatites. Field relations indicate a time sequence of emplacement of the various units.

A Rb-Sr whole-rock age of 2170 ± 40 Ma for the main Big Spruce Lake intrusion was obtained by Martineau and Lambert (1974). They also reported an age of 1980 ± 40 Ma for the satellite complex, suggesting prolonged or repeated intrusive activity. However, the data points were scattered (R.St.J. Lambert, pers. comm. 1980). The scatter may have been due, in part, to the high strontium and low rubidium concentrations which are common in these rocks, but it may also have been due to post-intrusive metasomatic activity or to variability in initial $^{87}\text{Sr}/^{86}\text{Sr}$ ratios. Evidence for the existence of a low-grade metamorphic event which could have affected the Rb-Sr system lies in the K-Ar dates which have been reported. K-Ar data obtained from biotites from the main

complex have given dates of 1820 Ma (Martineau and Lambert, 1974) and 1785 Ma (Leech et al, 1963), significantly younger than the Rb-Sr dates.

The Big Spruce Lake intrusion lies on the Snare fault, a major N-S lineament almost parallel to the Wopmay fault which lies about 30 km west (Hoffman, 1980; Geol. Surv. Can. Open File Map 445, 1977). Because of its alkaline character and the location of the complex it was earlier suggested that this intrusion represents an early continental rifting phase of the Wopmay Orogen (e.g. Hoffman 1974, 1980), but recent work (Bowring and Van Schmus, 1984; Hoffman and Bowring, 1984) constrains successful rifting of the orogen to about 1.9 Ma making correlation between the Big Spruce Lake intrusion and the Wopmay rifting tenuous.

In the present study the ^{206}Pb - ^{207}Pb and Sm-Nd systems have been employed on whole-rock samples from Big Spruce Lake and a U-Pb isochron has been obtained from zircons from syenites, in an attempt to constrain the age of crystallization of the complex as a whole, if possible to quantify the time interval over which emplacement occurred, and to state unambiguously whether or not the satellite intrusion is associated in time with the main complex.

Outline of Geology

Martineau's (1970) detailed description of the complex was used as the basis for field work and sample collection. An outline map of the geology is shown in Figure 1. The intrusion consists of over 18 individual units but these separate readily into five major petrographic groups. Within the main complex four groups are discernible, three silicate and one carbonate. A sequence of intrusion of the three silicate groups or centers of activity is given by field relationships. There is very little geographical overlap between the silicate centers.

Intrusive activity began with the formation of a layered ring complex in the northeast (Center 1). An outer ring diorite, chilled against gneiss, was followed by central gabbro units. A generally massive gabbro with coarse feldspar is chilled against the diorite and grades transitionally into a more leucocratic laminated unit. This in turn grades rapidly into a rhythmically-banded gabbro which forms the center of the ring. The present erosion surface cuts a relatively slowly cooled and quiescent magma chamber. After solidification the gabbros were intruded by magnetite olivine pyroxenite and cut by a NNE-trending fault, a splay of the main Snare fault which

cuts the complex (Figure 1). The main fault line crosses Big Spruce Lake from NNW to SSE. The main portion of the pyroxenite lies in the northwest corner of the gabbros and diorite with smaller bodies scattered throughout.

Pyroxenite magmatic activity may have continued over a period of time as pyroxenite is cut by a fault (X-X' Figure 1) and in turn the pyroxenite fills the space between splays of this fault.

Following emplacement of the ring complex and pyroxenite an abrupt change in magma composition to syenitic, silica-saturated to oversaturated, was accompanied by movement of the center of activity about 2.5 km southwest. The postdating of intermediate/mafic units of Center 1 by the syenites of Center 2 is defined by massive syenite, itself unfractured, emplaced across the fault X-X. Individual syenites were emplaced as a ring around the gabbros, a small island of mafic (pyroxene-rich) syenite lying between Center 1 and the main portion of Center 2, and possibly two concentric units within the main arcuate mass centered on the north end of the lake. The exact number of individual syenite units is not clear at present because variations within the units originally defined by Martineau (1970) are sometimes as great as between units, and contacts in the field are often obscured. The exact number of syenites

is, however, immaterial to the overall sequence.

Emplacement of silica-undersaturated magmas (Center 3) to the southwest of the syenites followed. Grey to black foyaites are chilled against coarse red-brown syenite. Leucocratic foyaites occupy the southern portion of the area and were followed by mafic foyaite and ijolite to the northwest corner. Brecciation of foyaites near the contact with gneiss in some locations, fine-grained foyaite apparently chilled against coarse within the main body and a series of small N-S foyaite dykes indicate that the intrusion of undersaturated magmas was periodic and that the Snare fault system was still active to some degree.

The foyaites are surrounded by an aureole of fenitized gneiss. This band is of variable width and is particularly prominent across the southern contact.

— Carbonatite emplacement (Center 4), apparently the last phase of the main complex, had two foci. Calcitic carbonatite was intruded in and around the mafic undersaturated units. Exposed carbonatites are scattered sovite dykes, with widths up to 3 m and exposed lengths up to 75 m, cutting foyaites and adjacent gneiss. Flow patterns are visible in some of the dykes. Within mafic foyaites there are also coarse-grained silico-carbonatites which exhibit no clear field relations and may be primary

in origin or hybrid as a result of interaction of host foyaite or ijolite with later carbonates. Calcitic magmatic activity is also shown in a carbonated minette breccia pipe (10 m diameter), carrying sub-rounded clasts of gneiss and foyaite, cutting the gneiss immediately west of the main complex. Dolomitic carbonatite bodies occur within the gneiss to the east of the main complex, but have not been found within the intrusion. Dykes and pipes of dolomite (up to 15 m diameter) carry phenocrysts of magnetite and xenoliths of gneiss and may themselves be brecciated. Calcitic and dolomitic magmatic activity do not overlap geographically.

The fifth major rock type (Center 5) is restricted largely to an area about 2.5 km by 3 km lying 5 km to the southwest of the main complex. Within this area numerous small bodies of shonkinite and biotite pyroxenite are exposed. Aeromagnetic data (Geol. Surv. Can. Geophys. Paper 2966G, 1963) suggested a single elongate body lying at depth. No carbonatite is exposed at the surface in this area but the gneiss is fenitized adjacent to several bodies and carbonate has been identified in drill core from one of the more central bodies. The position of this intrusion (Center 5) within the time sequence of the main complex cannot be determined from field relations.

Porphyry dykes, up to 4 m in width and carrying

nepheline and sanidine as phenocryst phases, cut Centers 1 and 2 but not 3 to 5.

Samples

(a) Samples for whole-rock analyses were selected to be the least altered or weathered representatives of the units from which they were taken and at the same time to produce the widest possible range of compositions for each intrusive center to facilitate determination of separate isochrons (if possible, for each center). Sample size ranged from a minimum of about 1 kg to about 15 kg.

(b) Zircons were separated from the minus 100 mesh fraction of six syenites of Center 2. A separate (>99% pure) was produced by settling the non-magnetic fraction in heavy liquids (acetylene tetrabromide and methylene iodide), treating the heavy fraction with 1:1 nitric acid and hand-picking the final sample.

Whole Rock Lead

A powder sample sufficient to contain about 10 μ g total Pb was used wherever possible to maximize the sample:blank ratio as well as to minimize errors due to sample inhomogeneity. Sample size varied from 150 mg to 1.5 g. Samples were decomposed in a mixture of HF:HNO₃

and Pb was separated by coprecipitation with $\text{Ba}(\text{NO}_3)_2$ followed by chloride anion exchange separation of the Pb. The total blank was less than 5 ng Pb. Separate dissolutions of the same rock powder did not always produce the same measured Pb isotope ratios (outside of measurement error). This was more common for samples with a high proportion of radiogenic Pb and is probably the result of sample inhomogeneity with respect to uranium-rich sample grains. This inhomogeneity, similar to that reported in whole rock studies of other authors (e.g. Oversby, 1976) has no significant effect on the $^{207}\text{Pb}/^{206}\text{Pb}$ slope ages determined, as the repeat runs produced measured ratios lying on the same regression line (see Table 38).

For measurement of isotope ratios the purified Pb was loaded as a phosphoric acid-silica gel mixture onto a single filament of rhenium ribbon. The $^{206}/^{204}$, $^{207}/^{206}$ and $^{208}/^{206}$ ratios were measured at a temperature of 1200-1280°C, on a VG MM 30 mass spectrometer using a 9-step peak-jumping procedure. Mass fractionation corrections of $^{206}/^{204} = 1.002752$, $^{207}/^{204} = 1.004267$ and $^{208}/^{204} = 1.006420$, (determined by repeat runs of the NBS 981 standard) were applied to sample data.

Ratios were measured for a total of 47 whole rock samples, at least six from each center of intrusive

Table 38. Whole rock lead analytical data.

Sample		$\frac{206}{204} \text{Pb}$	$\frac{207}{204} \text{Pb}$	$\frac{208}{204} \text{Pb}$	Pb (ppm)
		Pb	Pb	Pb	
PC-81-001	pyroxenite	15.992	15.280	36.108	7
PC-81-235	gabbro	19.662	15.740	43.199	8
PC-81-275	gabbro	16.928	15.387	39.971	4
PC-81-363	diorite	17.576	15.502	40.514	11
PC-82-163	pyroxenite	19.131	15.743	39.784	4
PC-82-173	diorite	16.219	15.268	36.676	6
PC-81-012	syenite	17.477	15.465	38.256	7
PC-81-285	syenite	18.107	15.587	38.620	13
PC-81-364	syenite	19.029	15.677	39.845	16
PC-82-096	syenite	18.998	15.610	41.388	9
PC-82-099	syenite	19.459	15.751	41.967	36
PC-82-124	syenite	17.779	15.530	38.585	10
PC-82-151	syenite	20.447	15.888	41.674	10
PC-82-358	syenite	18.722	15.692	40.746	18
PC-81-161	ijolite	16.555	15.372	40.373	13
PC-81-165	foyaite	24.354	16.311	39.284	16
PC-81-168	melteigite	114.92	28.686	44.584	19
PC-81-194	foyaite	16.329	15.200	39.499	11
PC-81-287	foyaite	43.794	19.067	41.422	16
PC-81-482	foyaite	15.776	15.158	42.153	8
PC-82-039	foyaite	37.358	17.902	42.675	5
PC-82-041	melteigite	20.334	15.861	42.304	8
PC-82-525	ijolite	52.023	19.901	40.727	20
PC-82-526	ijolite	99.896	26.467	41.410	27
PC-82-526	rerun	98.425	26.281	41.696	27
PC-81-168	rerun	113.51	28.489	44.394	19
PC-81-287	rerun	44.561	19.127	41.582	16

(Continued)

Table 38. (Continued)

PC-81-176	carbonatite	14.937	15.046	37.041	73
PC-81-178	carbonatite	15.900	15.120	39.944	20
PC-81-185	carbonatite	16.377	15.398	40.780	35
PC-81-376	carbonatite	14.478	14.931	35.091	94
PC-81-383	carbonatite	20.587	15.999	56.771	24
PC-82-088	carbonatite	15.593	15.315	44.451	31
PC-82-412	carbonatite	28.816	16.945	53.776	12
PC-82-506	carbonatite	19.903	15.884	37.992	131
PC-81-176	rerun	14.921	15.029	37.023	73
PC-81-053	shonkinite	22.504	16.069	48.789	8
PC-81-057	shonkinite	18.906	15.675	39.455	19
PC-81-961	shonkinite	17.720	15.564	39.824	14
PC-81-063	biotite pyroxenite	18.753	15.657	39.754	8
PC-81-064	biotite pyroxenite	20.405	15.841	44.267	6
PC-81-388	shonkinite	19.532	15.784	41.740	8
PC-82-260	biotite pyroxenite	17.918	15.530	38.031	21
PC-82-278	shonkinite	19.458	15.748	40.483	7
PC-82-535	biotite pyroxenite	19.158	15.757	40.732	21
PC-81-392	shonkinite	20.585	15.888	40.175	10

activity in the main complex (as defined earlier) and 10 from the satellite center. Concentrations of Pb were measured by XRF analysis of pressed pellets (Midland Earth Science Associates, Nottingham, England). The results are listed in Table 38 and the ratios plotted in Figures 83 - 86. Regression analysis for isochrons, straight line fitting with correlated errors, was based on Cumming (1969) and Cumming et al (1972). An error of 0.5 per mil was used for 206/204 and 207/204 ratios, 0.6 per mil for the 208/204 ratios except where the individual precision errors exceeded these values. In those cases the individual error was substituted. The decay constants used to calculate slope ages are $\lambda_{238} = 0.155125 \times 10^{-9} \text{yr}^{-1}$ and $\lambda_{235} = 9.8485 \times 10^{-10} \text{yr}^{-1}$ (Jaffey et al, 1971). Regression lines and slope ages were calculated for the main complex as a whole and for various separate groups to see if the time sequence interpreted from field relations could be resolved. These results are presented in Table 39. Data scatter beyond experimental error is evident in the plots and in the high mean square of weighted deviates (MSWD; Table 39). Based on the whole-rock data no distinction can be made between scatter caused by post-intrusive movement of U and/or Pb and that caused by magma assimilation of varying amounts of contaminant during emplacement. Probably both effects are present to varying

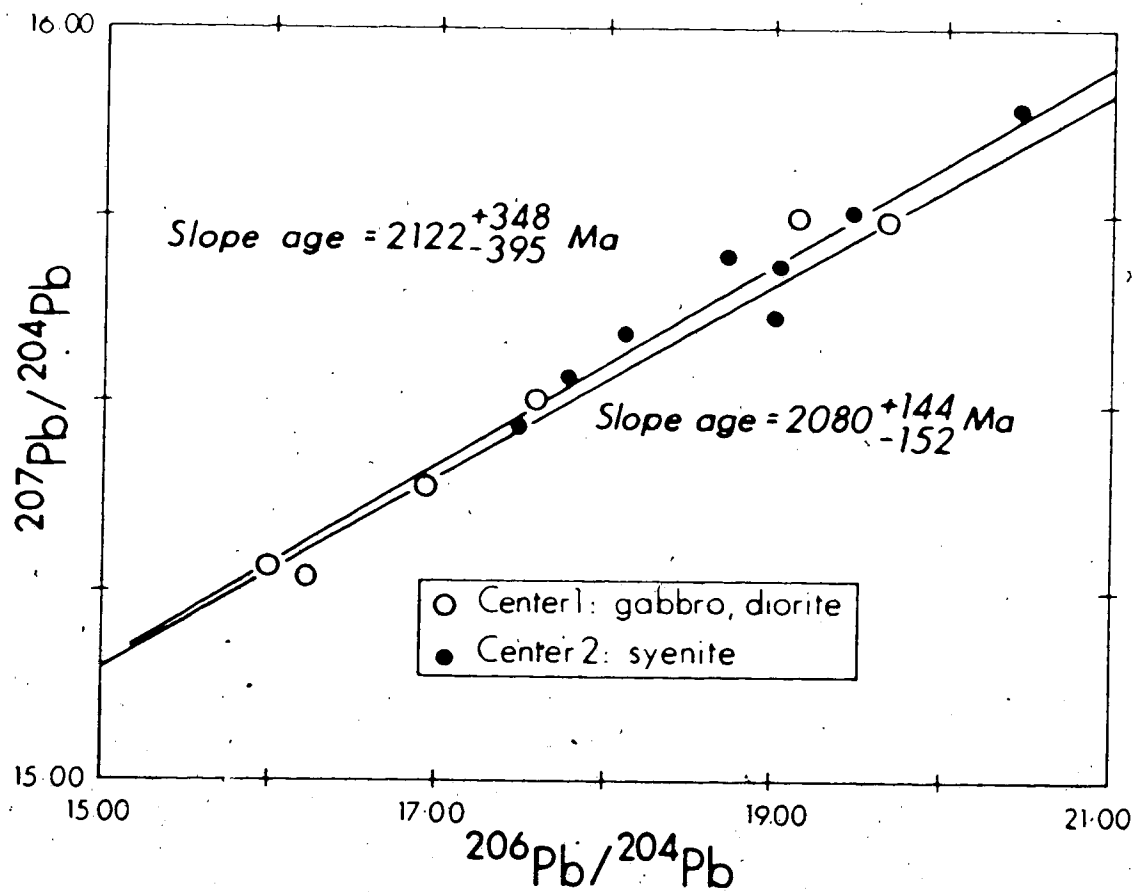


Figure 83. Whole-rock lead isotope ratios for samples from Centers 1 and 2 of the Big Spruce Lake complex. Combining data for Center 1 (2080 Ma) with that of Center 2 (2122 Ma) produces a single age of 2138^{+170}_{-181} Ma.

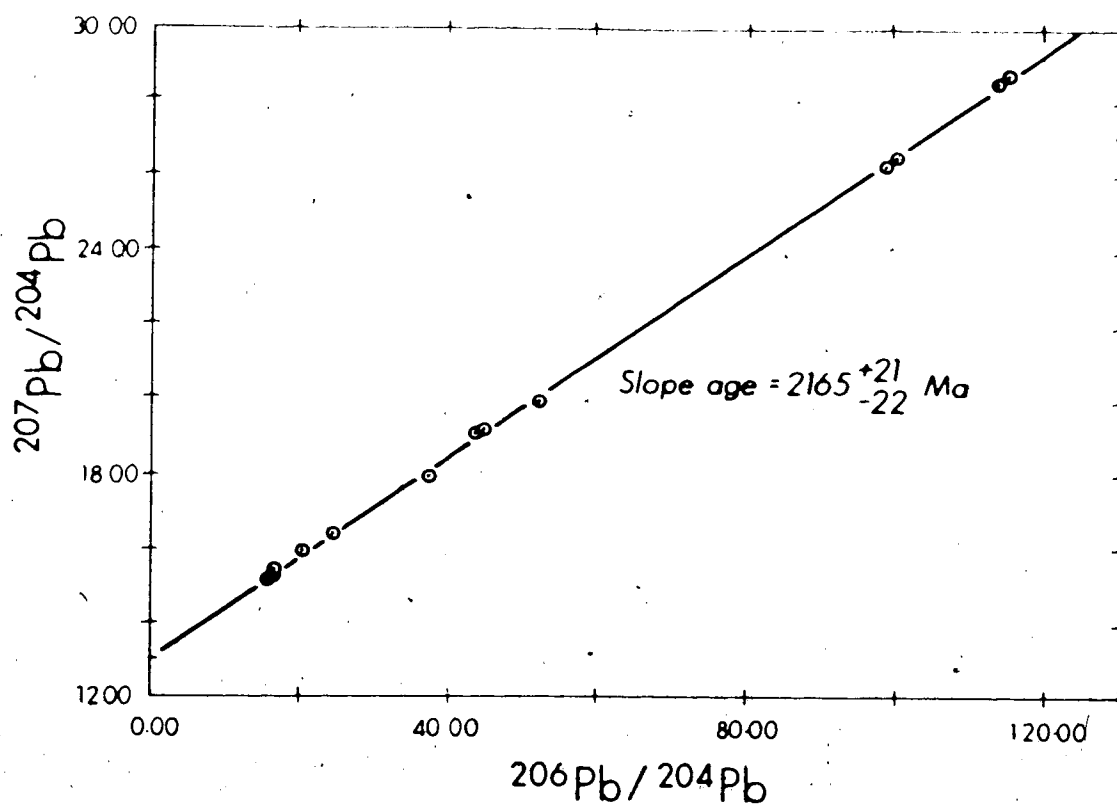


Figure 84. Whole-rock lead isotope ratios for samples from Center 3, foyaites and ijolites of the Big Spruce Lake complex.

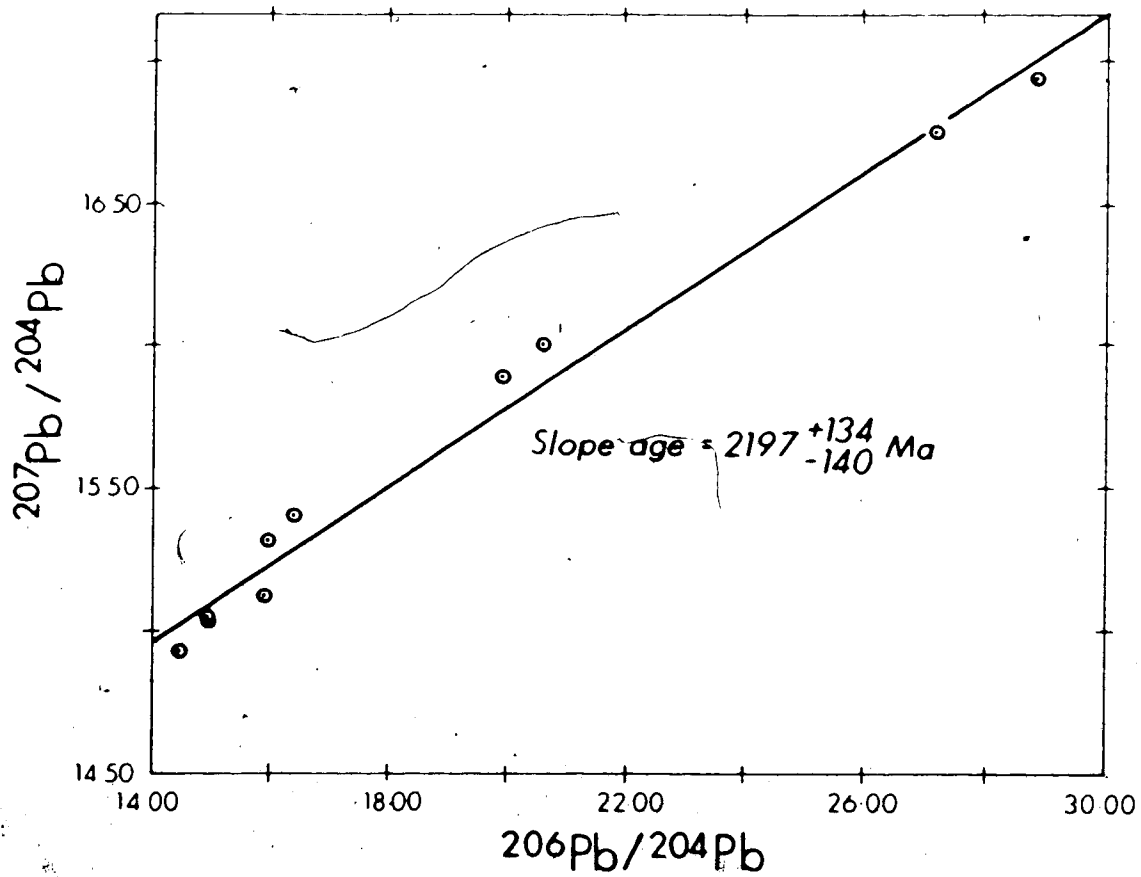


Figure 85. Whole-rock lead isotope ratios for samples from Center 4, carbonatites, of the Big Spruce Lake complex.

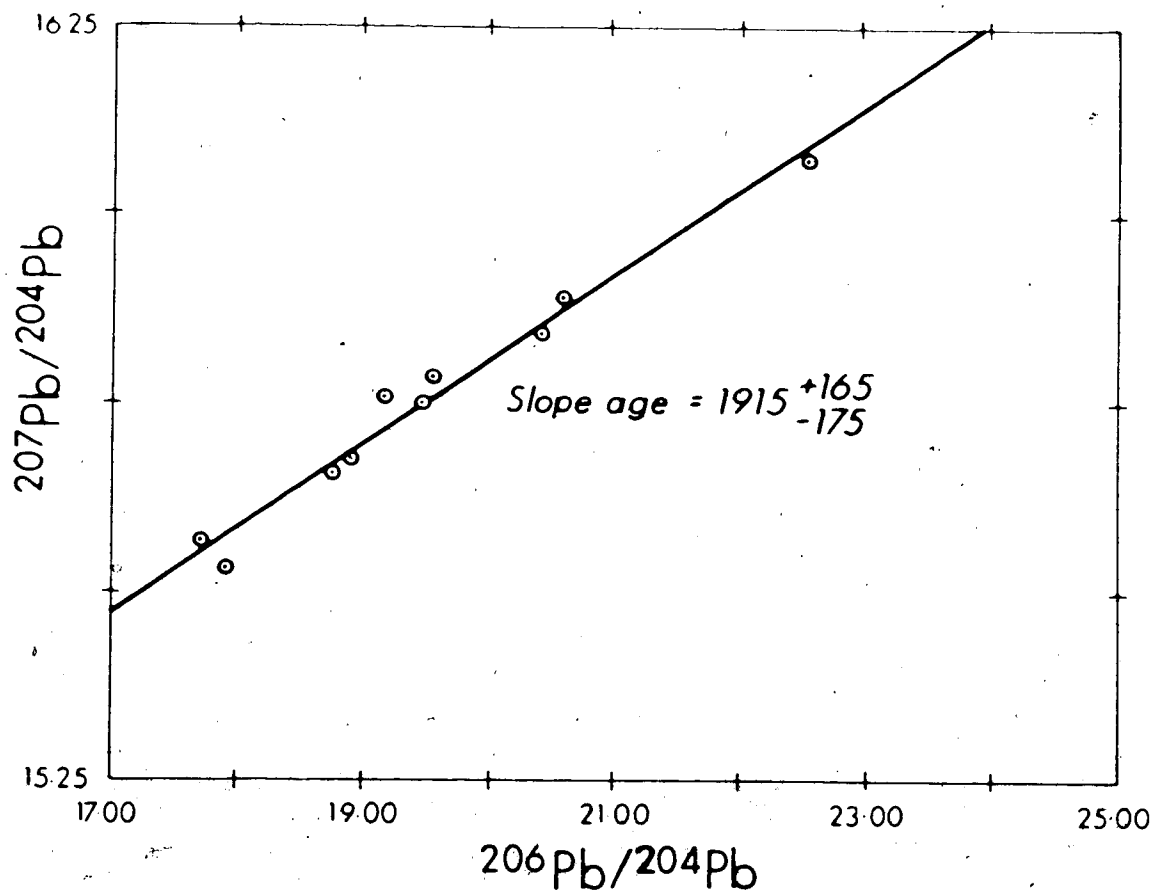


Figure 86. Whole-rock lead isotope ratios for samples from Center 5, shonkinites and biotite pyroxenites, from the satellite intrusion of the Big Spruce Lake complex.

Table 39. ^{207}Pb vs ^{206}Pb regression and slope age results.

Sample Group	No. of Samples	Slope	Sigma	MSWD	Age/Ma ¹
1. All centres, all samples	47	0.13424	7	63.7	2154 ± 15
2. Main complex Centres 1, 2, 3, 4	37	0.13431	7	75.5	2155 ± 16
3. Centre 1 (pyroxenite, gabbros & diorite)	6	0.12869	253	4.6	2080 +144 -152
4. Centre 2 (syenites)	8	0.13184	310	20.1	2122 +348 -395
5. Centre 3 (foyalites & ijolites)	13	0.13508	8	97.3	2165 +21 -22
6. Centre 4 (carbonatites)	10	0.13762	47	132.4	2197 +134 -141
7. Centre 5 (shonkinite & biotite pyroxenite)	10	0.11209	196	9.3	1915 +165 -175
8. Centres 1 & 2 (saturated silicates of main complex)	14	0.13303	188	12.5	2138 +170 -181
9. Centre 5 minus #1053	9	0.12386	320	8.1	2012 +250 -273

¹Error on age is $2\sigma/\text{MSWD}$.

degrees depending upon the rock type. For example, the individual small bodies of shonkinite/biotite pyroxenite of the satellite intrusive area commonly carry sub-angular to rounded clasts of gneiss, assimilation of which would affect the initial ratios; the carbonatites are easily recrystallized with concomitant gain or loss of material and may have been affected by a mild metamorphic event such as that which apparently reset the K-Ar system at 1800 Ma (Martineau and Lambert, 1974; Leach et al, 1963).

Assuming first that the satellite intrusion is related to the main complex, regressing all data produced an age of 2154 ± 15 Ma (Group 1, Table 39). Removing the data for the satellite intrusion has no real effect on the age of the main complex, 2155 ± 16 Ma (Group 2, Table 39), which is controlled by the radiogenic Pb in the mafic foyaites and ijolites of Center 3. Regression of any sample set which includes one or more of the most radiogenic silica-undersaturated rocks produces a slope age of 2155-2169 Ma, indicating the degree of control these samples exercise. To ensure that the values measured for these samples were correct, three of them were selected for repeat determinations on separate dissolutions of the sample powder. It is these reruns which were mentioned earlier as indicating a slight sample inhomogeneity. The results are included in Table 38 and

show that the two runs for a single radiogenic sample produce short lines essentially parallel (within measurement error) to the regression line. Hence, the inhomogeneity does not significantly affect the slope age.

For the individual centers of activity or rock types, the age of Center 3 (Group 5, Table 39) is the one best defined by the Pb-Pb data at $2165 \pm 21/-22$ Ma. This result is reasonable, in spite of its high MSWD, because of the highly radiogenic samples. For the other three rock types (Groups 3, 4 and 6, Table 39) the ages are not well constrained, although the large errors allow each to overlap easily with the Pb-Pb age of the complex as a whole. Combining the gabbroic and syenitic samples produces a regression line (Group 8, Table 39) somewhat more tightly constrained than the individual lines. Not only is the MSWD lower, but it is not possible from field relations for the syenites to have preceded the gabbros as the individual slope ages might indicate. These two must be considered coeval from the present data. In the same way, the carbonatites could not be older than their host rocks and the age determined by whole rock Pb-Pb, 2197 Ma, is too high. Isotope ratios in carbonatites are extremely susceptible to alteration at all stages from magma emplacement to the present exposure and further work is necessary to constrain the age of these rocks more

closely.

The data from the satellite center are also imprecise. Each sample was taken from a different outcrop, separated from the others by gneiss, surface water or both. Clasts of host-rock gneiss are common, especially near the margins, and this area is interpreted as many individual upward projections from a single deeper body, each one contaminated with a variable amount of country rock. The scattered data points bear this out, and the true age is not evident. Regression of all ten samples gives an age of $1915 \pm 165/-175$ Ma, younger than the main complex and the age of 1980 Ma determined for this intrusion by Martineau and Lambert using Rb-Sr. This Pb-Pb age is controlled by a single sample, PC-81-053 (Table 38) which has a higher radiogenic component than the others. Omission of this sample produces a slope age of $2012 \pm 250/-273$ Ma, almost coeval with the main complex. However the data are scattered appreciably, so that the age of the satellite intrusion cannot be ascertained with sufficient precision from the Pb-Pb data obtained.

U-Pb of Zircons

The zircon from all samples was largely fragments of coarser grains (up to 1 mm in cross-section in hand-specimens) with only a few complete euhedral grains present. The largely transparent grains varied from colorless to deep brown, indicating varying degrees of metamictization. A few grains (in samples 1078 and 1338, Table 40) had definite dark cores.

Samples of 8-20 mg zircon were decomposed in Teflon bombs (Krogh, 1973). U and Pb were separated, and concentrations and isotope ratios determined as described in Baadsgaard and Lerbekmo (1983). The analytical results are given in Table 40. The blank in the procedure was less than 4.5 ng Pb and 2 ng U. The isotopic composition of the blank used in calculations was that of modern lead, calculated using the Stacey and Kramers (1975) model, with $206/204 = 18.700$, $207/204 = 15.628$ and $208/204 = 38.63$. The composition used for common lead correction was derived from the whole-rock lead data. An isochron for an age of 2155 Ma (the Pb-Pb slope age of the complex) was calculated using the Stacey and Kramers model. The intersection of this line with the whole-rock $^{207}\text{Pb}/^{206}\text{Pb}$ regression line defined the common lead composition, $206/204 = 14.826$, $207/204 = 15.108$ and $208/204 = 34.289$.

Table 40. U-Pb analytical data for svenite zircons.

Sample	Measured Isotopic Composition		238, (ppm)	206Pb (ppm)	Common Pb (ppm)	$\frac{206}{238}$	$\frac{207}{235}$	
	206/204	207/206						
PC-81-078	2248 ± 42	0.138248 ± 19	0.22651 ± 3	399.4	100.8	1.39	0.29144	5.3246
PC-81-285	2141 ± 277	0.14062 ± 21	0.18781 ± 39	226.8	70.7	1.02	0.36222	6.6007
PC-81-338	5317 ± 70	0.13767 ± 5	0.18848 ± 1	308.2	94.3	0.57	0.35333	6.5971
PC-81-364	4734 ± 172	0.137555 ± 13	0.21314 ± 3	348.1	103.4	0.55	0.34315	6.3863
PC-82-151	2809 ± 60	0.138817 ± 16	0.17107 ± 1	243.2	69.3	0.45	0.32943	6.1041
PC-82-358	6359 ± 245	0.13784 ± 8	0.20841 ± 1	265.5	82.4	0.37	0.35845	6.7226

¹Precision of ²⁰⁶Pb ratios is estimated at ±0.3% (Baadsgaard and Terhegmo, 1983).

Using the intersection of a 2200 Ma growth line with the regression line made no significant difference to the final results.

A best-fit regression line, calculated using a correlation coefficient of $r = 0.90$ (Ludwig, 1980) is plotted in Figure 87. The zircon samples have lost about 14-32% Pb (Faure, 1977, p. 209) and lie along a well-defined discordia line which intercepts the concordia at $2188 \pm 16/-10$ Ma and 299 ± 113 Ma. The MSWD is 6.68, due largely to samples 1285 and 2358, for which a slight instability during isotope ratio measurements (see Table 40) may be responsible. Omission of these two points produced a regression line with an MSWD of 0.27 but an upper intercept only 3 Ma greater. The lower intercept of 299 Ma does not represent episodic loss of Pb since no late metamorphic event of this age is known for the whole region.

Whole Rock Sm-Nd

The method used for sample dissolution and separation of Sm and Nd, based on that of Dosso and Murthy (1980), is outlined in the appendix.

The total blank on the procedure was less than 0.3 ng Sm and 7 ng Nd. In all cases in this study the sample:blank ratio was greater than 1000:1.

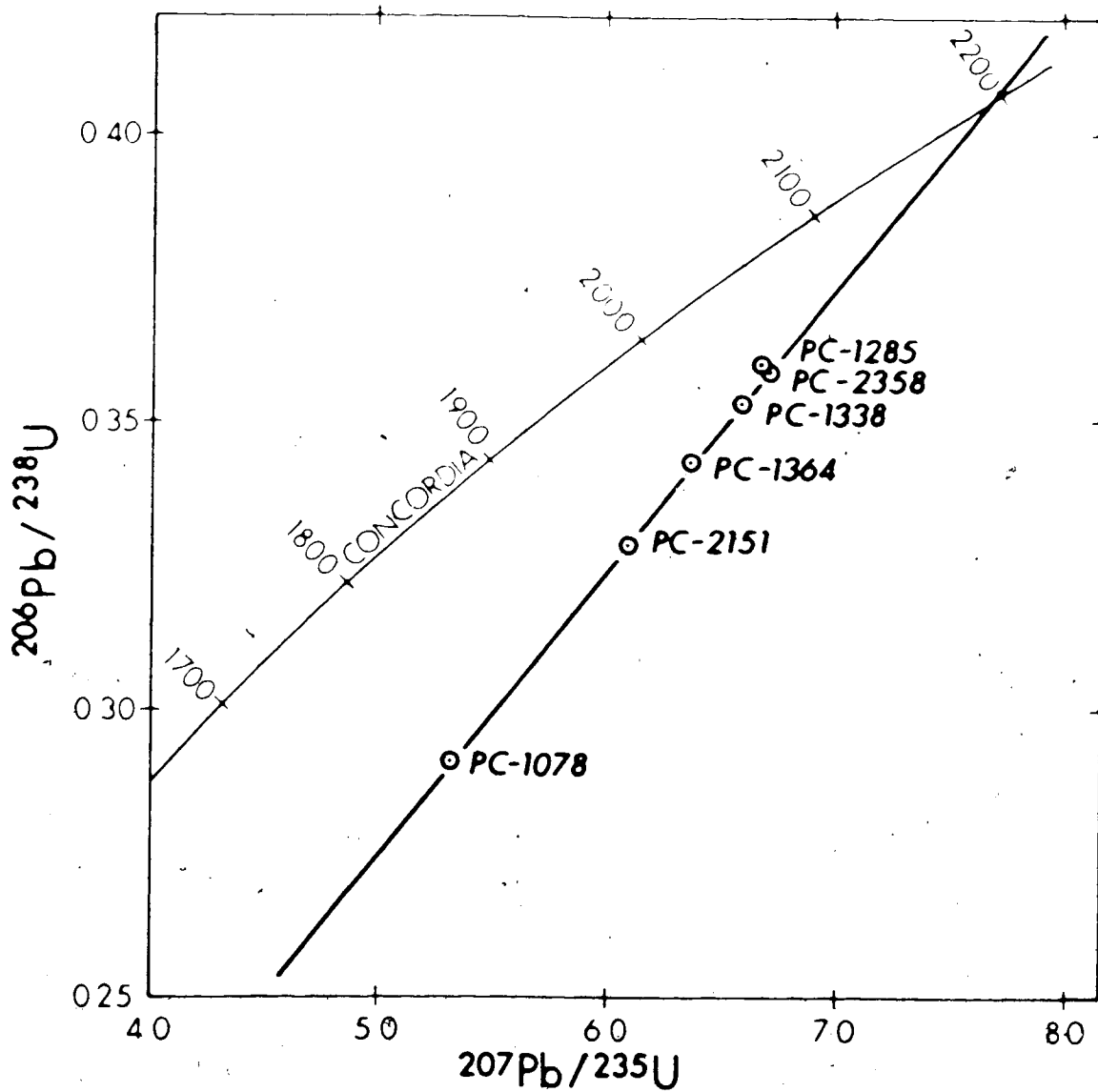


Figure 87. U-Pb results for zircons from syenites of Center 2 of the Big Spruce Lake complex. The upper intercept with the concordia is $2188 \pm 16/-10$ Ma (Error = 2σ MSWD).

For determination of the $^{143}\text{Nd}/^{144}\text{Nd}$ ratio the sample was loaded from 6N HCl onto the side filament of a double rhenium filament assembly and dried in air at a low current. For determinations of ratios in spiked samples either Nd or Sm was loaded as $\text{Nd}(\text{NO}_3)_3$ or $\text{Sm}(\text{NO}_3)_3$ nitrate, from dilute HNO_3 solution, onto the side of a double filament, dried and heated to a dull red glow to convert to the oxide. Ratios were determined on a VG MM 30 mass spectrometer. The mean of 4 runs on BCR-1 was 0.511820 ± 23 . For the La Jolla Nd-resolution the mean of 9 runs was 0.511833 ± 9 (1σ). An in-house standard solution gave run-to-run reproducibility of ± 0.00003 , indicating that for the samples most of the imprecision or error lies in the ratio determinations themselves and not in the chemistry.

The results for the 31 samples analysed in this study are listed in Table 41 and plotted in Figure 88. Four samples of gneissic country rock were also analysed and model ages calculated for each. The analytical results, model ages calculated and the parameters used are given in Table 42.

As with the Pb-Pb data, regression and isochron ages were calculated for the complex as a whole and for various groups. The program used was based on York (1966), using a ^{147}Sm decay constant of $6.54 \times 10^{-12}\text{yr}^{-1}$. The regression results are listed in Table 43. The two

Table 41. Sm/Nd whole rock analytical data.

Sample	Sm (ppm)	Nd (ppm)	$\frac{147\text{Sm}}{144\text{Nd}}$ 1	$\frac{143\text{Nd}}{144\text{Nd}}$ 2
PC-81-001 pyroxenite	3.842	14.232	0.16301	0.51150±3
PC-81-004 pyroxenite	2.759	10.251	0.16256	0.51150±2
PC-81-235 gabbro	4.644	22.845	0.12275	0.51085±2
PC-81-275 gabbro	2.886	13.759	0.12665	0.51092±3
PC-81-363 diorite	7.941	42.411	0.11307	0.51067±1
PC-82-163 pyroxenite	6.725	26.834	0.15133	0.51124±2
PC-82-173 diorite	4.523	22.059	0.12383	0.51084±3
PC-81-012 syenite	11.348	58.596	0.11695	0.51079±2
PC-81-285 syenite	15.434	84.860	0.10983	0.51070±1
PC-81-332 syenite	13.412	68.198	0.11876	0.51076±1
PC-82-096 syenite	15.575	87.745	0.10719	0.51057±1
PC-82-099 syenite	21.147	133.45	0.09568	0.51042±2
PC-82-124 syenite	6.944	36.732	0.11416	0.51072±1
PC-82-358 syenite	14.390	81.081	0.10717	0.51065±2
PC-82-151 syenite	17.453	95.713	0.11011	0.51061±1
PC-81-096 porphyry dyke	14.470	82.379	0.10607	0.51062±3
PC-81-168 melteigite	16.521	93.911	0.10624	0.51065±3
PC-81-494 foyaite	15.004	87.476	0.10358	0.51059±1
PC-81-287 foyaite	22.067	126.39	0.10543	0.51058±1
PC-81-482 foyaite	7.286	43.827	0.10039	0.51054±1
PC-82-039 foyaite	13.095	67.607	0.11696	0.51079±2
PC-82-525 ijolite	19.724	112.61	0.10577	0.51066±2
PC-81-176 carbonatite	98.421	693.05	0.08576	0.51037±2
PC-81-178 carbonatite	338.84	1940.3	0.10545	0.51058±1
PC-81-185 carbonatite	81.402	469.78	0.10464	0.51059±1
PC-81-383 carbonatite	241.00	1586.8	0.09168	0.51048±2
PC-81-383 rerun	245.4	1617.0	0.09165	0.51047±1
PC-82-088 carbonatite	50.176	230.19	0.13163	0.51097±1

(Continued)

Table 41. (Continued)

Sample	Sm (ppm)	Nd (ppm)	$\frac{147\text{Sm}^1}{144\text{Nd}}$	$\frac{143\text{Nd}^2}{144\text{Nd}}$
PC-82-088 rerun	50.766	230.41	0.13305	0.51099±1
PC-82-412 carbonatite	87.927	618.87	0.08580	0.51037±2
PC-82-506 carbonatite	269.82	1890.9	0.08617	0.51038±1
PC-81-388 shonkinite	16.582	82.196	0.12182	0.51083±1
PC-82-260 biotite pyroxenite	10.867	54.718	0.11993	0.51074±1

¹Estimated error is 0.1%.

²Ratios are normalized to $^{146}\text{Nd}/^{144}\text{Nd} = 0.724127$, precision listed is one sigma.

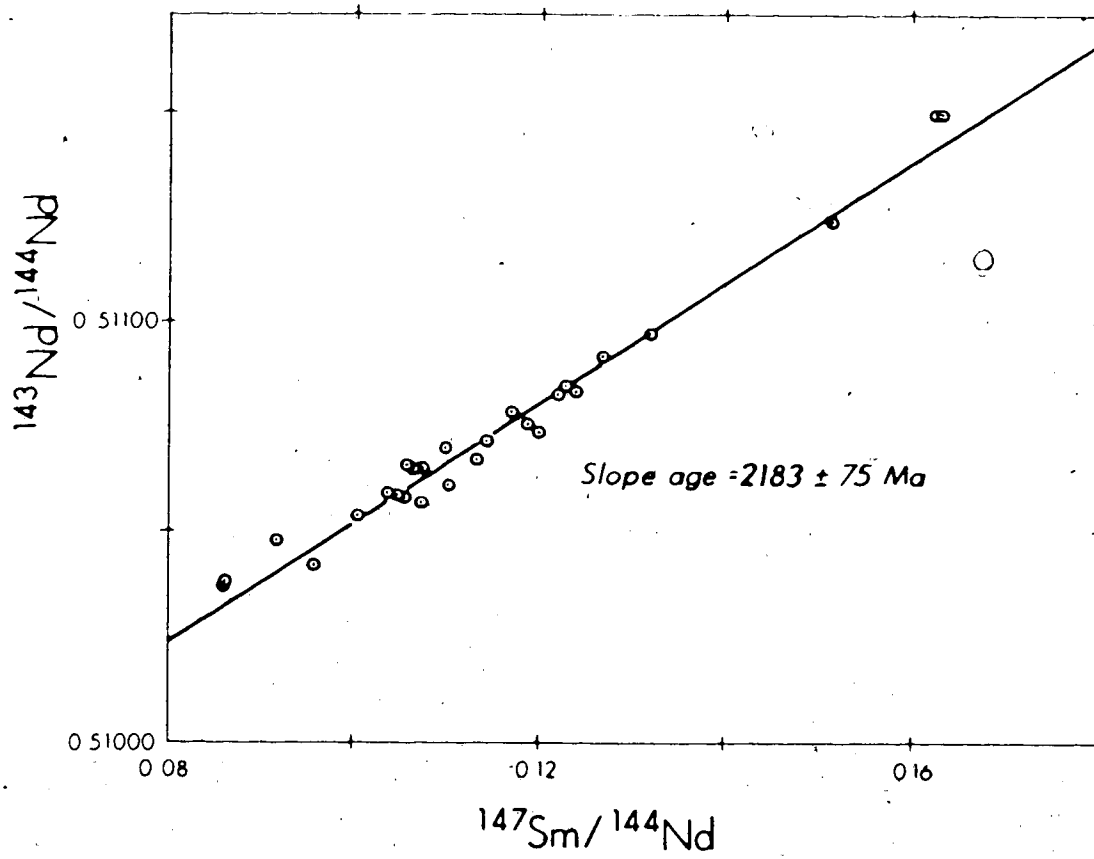


Figure 88. Sm-Nd results for whole-rock samples from all centers of the Big Spruce Lake complex.

Table 42. Sm/Nd analytical data and model ages for granodioritic country rock.

Sample	Sm (ppm)	Nd (ppm)	$\frac{^{147}\text{Sm}}{^{144}\text{Nd}}$	$\frac{^{143}\text{Nd}}{^{144}\text{Nd}}$	Model Age Ma ¹
1025	8.374	41.028	0.12325	0.51064	2467
1483	8.004	39.275	0.12306	0.51059	2559
2074	3.961	19.310	0.12386	0.51059	2595
2281	7.538	36.117	0.12571	0.51064	2557

¹ $\lambda_{\text{Sm}} = 6.54 \times 10^{-12} \text{ y}^{-1}$, $(^{147}\text{Sm}/^{144}\text{Nd})_{\text{CHUR}} = 0.1967$ and
 $(^{143}\text{Nd}/^{144}\text{Nd})_{\text{CHUR}} = 0.511836$ from Jacobsen and Wasserburg (1980).

Table 43. Sm/Nd whole rock regression and age results.

Sample Group	Number of Samples	Slope	1 σ	MSWD	Age ¹ (Ma)
(1) All centres, all samples	31	0.014376	488	0.65	2183 \pm 75
(2) Centre 1 (gabbro, diorite, pyroxenite)	7	0.016177	1006	0.34	2454 \pm 154
(3) Centre 2 (syenites)	8	0.015782	2680	0.60	2394 \pm 410
(4) Centre 3 (foyalites, ijolites)	6	0.015101	4079	0.30	2292 \pm 623
(5) Centre 4 (carbonatites)	7	0.012634	1237	0.27	1920 \pm 189

¹Calculated using $\lambda_{Sm} = 6.54 \times 10^{-12} \text{ year}^{-1}$; error listed is $2\sigma_{MSWD}$.

samples listed in Table 41 from the satellite intrusion were selected from XRF analyses of major and trace elements to provide the widest range of Sm/Nd for an isochron. However the very short range actually obtained precludes calculation of an individual Sm-Nd age for that group of samples.

From Tables 41 and 43 and Figure 88 it is clear that the Sm-Nd results cannot be used to resolve the sequence of emplacement of the various units. A small part of the observed scatter is due to experimental error in the ratio measurements, but most seems to arise from the samples themselves (see the Pb-Pb data). Because of the geochemical coherence of Sm and Nd it is likely that the major part of the scatter can be ascribed to variable amounts of contamination (initial ratios) rather than to later metasomatism. Individual data points which strongly control the various regression lines were repeated and reproduced either by a repeat dissolution of the same sample powder (carbonatites PC-81-383 and PC-82-088) or by analysis of a geographically adjacent, closely related sample. Data points for the two magnetite pyroxenites in Table 41, PC-81-001 and 004 are almost coincident. Three other samples, carbonatites, for which the data plot almost on top of each other in Figure 88 are the most Sm-depleted samples. These carbonatites are very light REE-

enriched and ^{143}Nd -enriched, and lie outside error limits above the regression line calculated for the complex as a whole. The Sm-Nd isochron age calculated for the complex using all data is 2183 ± 75 Ma and is strongly controlled by accurate data points significantly above the regression line at the high end of the Sm/Nd range (magnetite pyroxenites) as well as at the low end (carbonatites). Removal of only the Sm-enriched magnetite pyroxenites from the regression produces an age of 1999 ± 103 Ma. Removal of these same two samples from the regression of Center 1 (Group 2, Table 43) lowers the calculated age from 2454 ± 154 Ma to 2215 ± 275 Ma, the increased error resulting from a smaller $^{147}\text{Sm}/^{144}\text{Nd}$ range. Short ranges of Sm/Nd for the syenites and undersaturated silicates of the main complex (Groups 3 and 4, Table 43) combined with the scatter mentioned earlier lead to very poorly defined ages for these units, 2394 ± 410 Ma and 2292 ± 625 Ma respectively. The age calculated for the carbonatites alone, 1920 ± 189 Ma appears to be forced to this low value by the three most Nd-enriched samples mentioned earlier.

Discussion

Although the times of emplacement of three of the five individual phases of this complex cannot be closely defined by the present data, well constrained ages have been obtained for two centers (one silica-saturated and one silica-undersaturated), and for the complex as a whole.

The age of crystallisation of the entire complex is probably best defined by the zircon age of the syenites, $2138 \pm 16/-10$ Ma. The Sm-Nd age for the complex as a whole, 2183 ± 75 Ma, agrees well with the zircon age and the error allows it to overlap easily with the Pb-Pb age. The Pb-Pb age of 2155 ± 16 Ma for the main complex does not agree within error with the zircon age but the failure to do so may be due to a spuriously low error (considering the observed scatter in the data) caused by the radiogenic foyaites and ijolites which control the regression line. Regression of data for the undersaturated silicates only gives an age of $2165 \pm 21/-22$ for Center 3, which does agree within error with the zircon age of the syenites. If one speculates that the difference between the ages of the syenites and foyaites could be real then there are two possible explanations. One is that undersaturated intrusive activity followed the

saturated after an interval of 10-20 million years. The other is that the whole rock Pb-Pb system reached closure after the zircon U-Pb closure. Neither of these hypotheses has any supporting evidence, and it must be considered that these units are essentially coeval. The conclusion from the data that the carbonatites are coeval with their host foyaites is supported by a recent study of the Phalaborwa complex (Eriksson, 1984) which found that the time of emplacement of carbonatites and associated undersaturated rocks was the same within 10 million years.

No separate age can be defined for the satellite intrusion to confirm the age of 1980 ± 40 Ma reported by Martineau and Lambert (1974). Because the Rb-Sr data were scattered (Lambert pers. comm., 1980) as are the Pb-Pb data from this study, this unit must be considered associated in time with the main complex pending more definitive work.

The scatter noted in both whole rock systems appears to be due mainly to variable initial ratios accompanied by a smaller effect due to very low grade metamorphism. The zircon data produces a good regression line yet the whole rock Pb data for four of the same syenite samples is disparate. If the isotopic composition of Pb incorporated into these four samples was variable due to assimilation of country rock then it would have a significant effect on

the whole rock system but not on the zircon system where only small amounts of common Pb are incorporated during crystallisation. Similarly, post-intrusive low-grade metamorphism (which is petrographically difficult to separate from deuteritic action) appears not to have significantly affected the geochemically-coherent Sm-Nd system. The fact that the Sm-Nd isotopic data is scattered while the REE show smooth chondrite-normalized distribution patterns (in preparation) with no discontinuities suggests that original isotopic variations are responsible.

A well-constrained (zircon) age of emplacement of 2188 Ma for this alkaline intrusion and the presence of the Snare fault suggest that an episode of continental rifting began along the fault about 2200 Ma ago. Significant movement along the Snare fault to produce the lineament visible in Landsat photos must have occurred prior to the emplacement of the complex where no significant post-intrusive lateral movement can be observed. Movement on the Snare lineament apparently ended shortly after the Big Spruce Lake intrusion, a fact which may account for the lack of other nephelinitic bodies along this line. The Big Spruce Lake intrusion is closely correlated in age with the Hearne Channel Granite, the older alkaline phase of the Blachford Lake Intrusive

suite which lies at the southern edge of the Slave province. A zircon age of 2175 ± 5 Ma was recently reported for this body (Bowring et al., 1984). The Simpson Island dyke, an alkali gabbro body lying along the East Arm of Great Slave Lake, is also apparently of the same age (Burwash and Baadsgaard, 1962; Leech et al., 1963) but any relationship among these three bodies is tenuous at best. A successful rift does appear to have developed, somewhat later, 30 km west of the Big Spruce intrusion and the Snare fault to form the present western edge of the Slave province (Hoffman, 1974, 1980). The age and timespan of the surprisingly brief Wilson cycle which followed, 1900 to 1885 Ma (Hoffman and Bowring, 1984; Bowring and Van Schmus, 1984) suggest that this rifting had little connection with the emplacement of the Big Spruce Lake intrusives 300 my earlier.

Conclusions

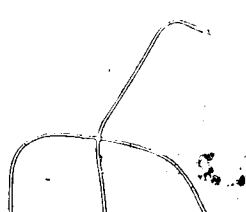
- (1) Minor contamination by gneissic country rock, affecting initial ratios, and later metasomatism contribute to variability in measured Nd and Pb ratios for whole-rock samples.
- (2) The five separate stages of the Big Spruce Lake intrusion have not been separated in time by Sm-Nd or

Pb-Pb methods. The maximum interval between emplacement of successive units is probably that between saturated and undersaturated units, Centers two and three. Present zircon and Pb-Pb data indicate that these two units are coeval within error; however, the interval between them could be up to 31 million years when errors are considered. Similar intervals between emplacement of the other units would require a total of 90-100 million years for emplacement of the entire complex. Such a timespan is unlikely in view of the rapid emplacement of diverse alkaline magmas of the modern African Rift Valley. The main Big Spruce Lake complex was probably emplaced over an interval of less than 50 million years.

(3) The age of crystallisation of the Big Spruce Lake intrusion is best defined by the zircon age of the syenites, $2188 \pm 16/-10$ Ma. Pb-Pb data for whole rock samples gives an age of 2155 ± 16 Ma, and Sm-Nd gives an age of 2183 ± 75 Ma.

(4) No separate age can be assigned to the satellite complex on the basis of present data although it may be younger.

(5) Four Sm-Nd model ages for granodioritic country rock range from 2467 to 2595 Ma.



Acknowledgements

This work was carried out with the aid of NSERC Grant (A-1158) to HB, during the tenure of an NSERC scholarship and a Steinhauer (Province of Alberta) award to PAC. Field work was facilitated by aid from the Yellowknife office of DIAND and a grant from the Boreal Institute for Northern Studies. Northern Canada Power Commission personnel at Yellowknife and the Snare Rapids damsite greatly facilitated sample collection and transportation.

References

References for this appendix have been integrated with the main list.

Appendix: Sm-Nd Separation Method

A sample containing at least 15 μg Nd (0.2 to 1.0 g usually) was weighed into a 25 ml screw-top Teflon vessel and a mixed ^{145}Nd plus ^{149}Sm spike solution added for isotope dilution analysis. A like amount of sample powder was placed in a second vessel for determination of the $^{143}\text{Nd}/^{144}\text{Nd}$ ratio. Use of separate dissolutions for ratio and concentration determinations was justified by repeat analyses of several samples. Even for carbonatites

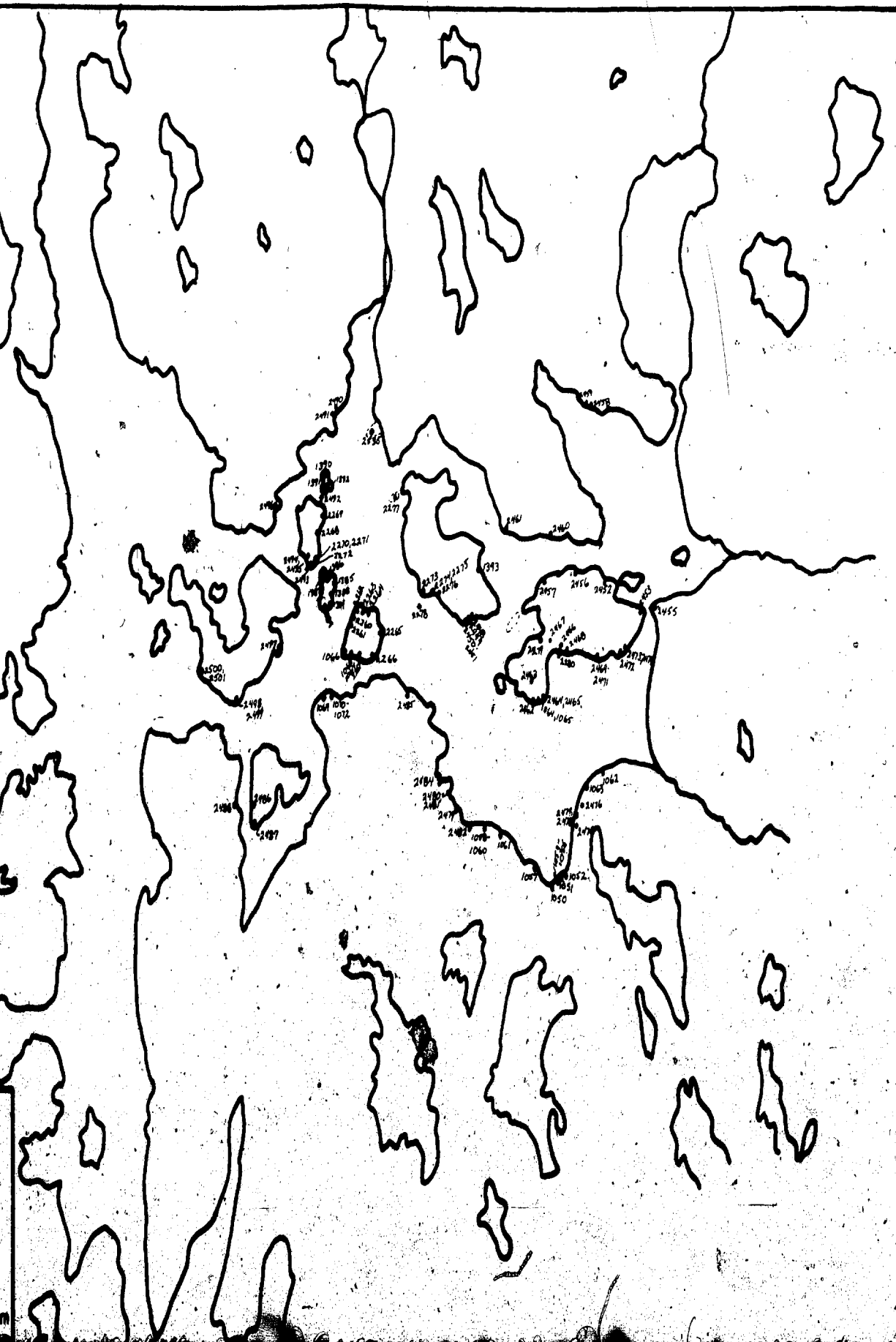
containing over 1500 ppm Nd no significant difference $^{143}\text{Nd}/^{144}\text{Nd}$ or $^{147}\text{Sm}/^{144}\text{Nd}$ was found. Samples were decomposed overnight, in 3 ml HNO_3 + 10 ml HF at 100°C . After centrifuging, the supernatant liquid was discarded, the fluoride residue was washed by digestion with 4% HF:4% HCl solution (centrifuge and discard supernatant wash liquid) then the fluoride was removed by repeated evaporation with HNO_3 . The final residue was dissolved in dilute HCl and R_2O_3 elements precipitated by addition of ammonia. If there was insufficient Fe or Al present to act as a carrier for Nd and Sm then the solution was re-acidified, a trace of pure Fe solution added and the R_2O_3 reprecipitated. If excessive amounts of Al or Fe were present at this stage then the following steps were repeated until the R_2O_3 precipitate reached an amount which would be soluble in less than 2 ml 6N HCl. To the hydroxide precipitate conc. HF was added dropwise to dissolution. The resulting fluoride residue was baked to incipient dryness to remove excess HF then it was digested with 4% HF:4% HCl solution for 20 minutes to solubilize Al and Fe as fluoride complexes. The solution was removed following centrifuging and the digestion procedure repeated twice more with fresh acid solution. Then the residue was treated with HNO_3 as before, to remove fluoride, taken up in dilute HCl and the R_2O_3 group

precipitated by the addition of ammonia. All steps were carried out in the original Teflon vessel. A second procedure, which could not be used for samples with a low Nd content, was sometimes employed to remove excessive amounts of aluminum. The ammonia precipitation was carried out in a 50 ml silica centrifuge tube. Following removal of the supernatant solution, pellets of pure NaOH were added to the hydroxide residue to dissolve the aluminum but not the iron or rare-earth hydroxides. The resulting solution was removed by centrifuging and decanting. To remove excess sodium the precipitate was again taken up in dilute HCl and hydroxides reprecipitated with ammonia. In all cases the final hydroxide precipitate was dissolved in a minimum of 6N HCl and water such that the final volume of solution was less than 2 ml and less than 2N in HCl for addition to the first cation exchange column. Subsequent procedures for the separation of Nd (and Sm) are largely based on those outlined by Dosso and Murthy (1980), employing three separate cation exchange columns. The first removes the rare earth elements from major elements and other trace elements. The second employs a fraction collector and a column eluted with a methylactic acid (MLA) solution. The third column provides Nd or Sm in a chloride form free of MLA residue. At this stage, for isotope dilution the sample was heated

with a drop of HNO_3 to convert it to a nitrate form and was now ready for loading onto the mass spectrometer filament. For measurement of the $^{143}\text{Nd}/^{144}\text{Nd}$ ratio, two further steps were added for purification. The Nd sample, dissolved in one drop 2.3N HCl, was added to a fourth column containing a resin bed of 1 mm diameter, 12.3 cm length below a loading reservoir. The resin employed was Dowex 50W-X8, 100-200 mesh cleaned with 6N HCl and equilibrated to 2.3N HCl. The sample was washed in with 2 sequential drops of 2.3N HCl from a measured volume of 0.1 ml, then eluted with the remainder to remove soluble alkali. Nd was then collected in a Teflon beaker using 1.6 ml 6N HCl and this solution was evaporated. Because the isotope ratios of these samples were being measured in a chloride form on the mass spectrometer organic matter was removed to improve stability. The sample was transferred in three successive drops of HNO_3 to a special platinum vessel, dried on a hotplate, and carefully ignited to a red glow over a burner. The organic-free Nd sample was transferred to a round-bottomed Teflon vessel using 2 sequential drops of 6N HCl, and dried ready for loading onto the mass spectrometer filament in a chloride form.

SAMPLE LOCATIONS, 1981-1982

MOOSE ISLAND COMPLEX, N.W.T.



KEY

 Aegirine Syenite
Fenite

 Shonkinite

 Minette

 Biotite Pyroxenite

 Contact Established

 Contact Inferred

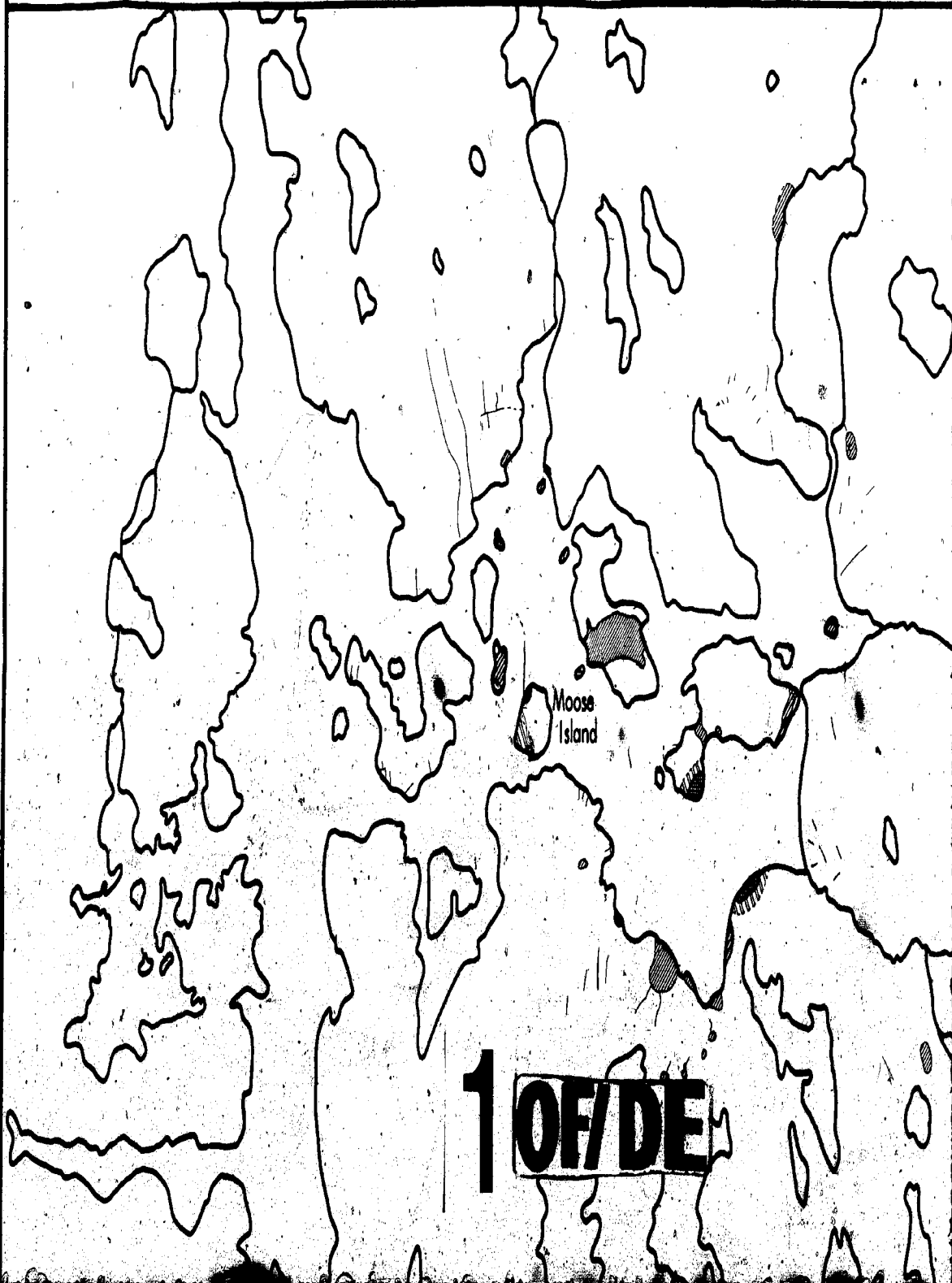
 Contact Arbitrary

Scale in kilometers



THE GEOLOGY OF THE MOOSE ISLAND COMPLEX

N. W. T., CANADA



Moose Island

1 OF/DE

Legend

Fenite

Shonkinite

Minette

Biotite Pyroxenite

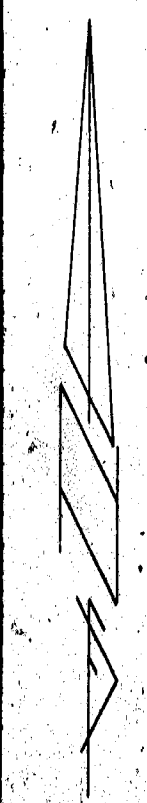
Contact Established

Contact Inferred

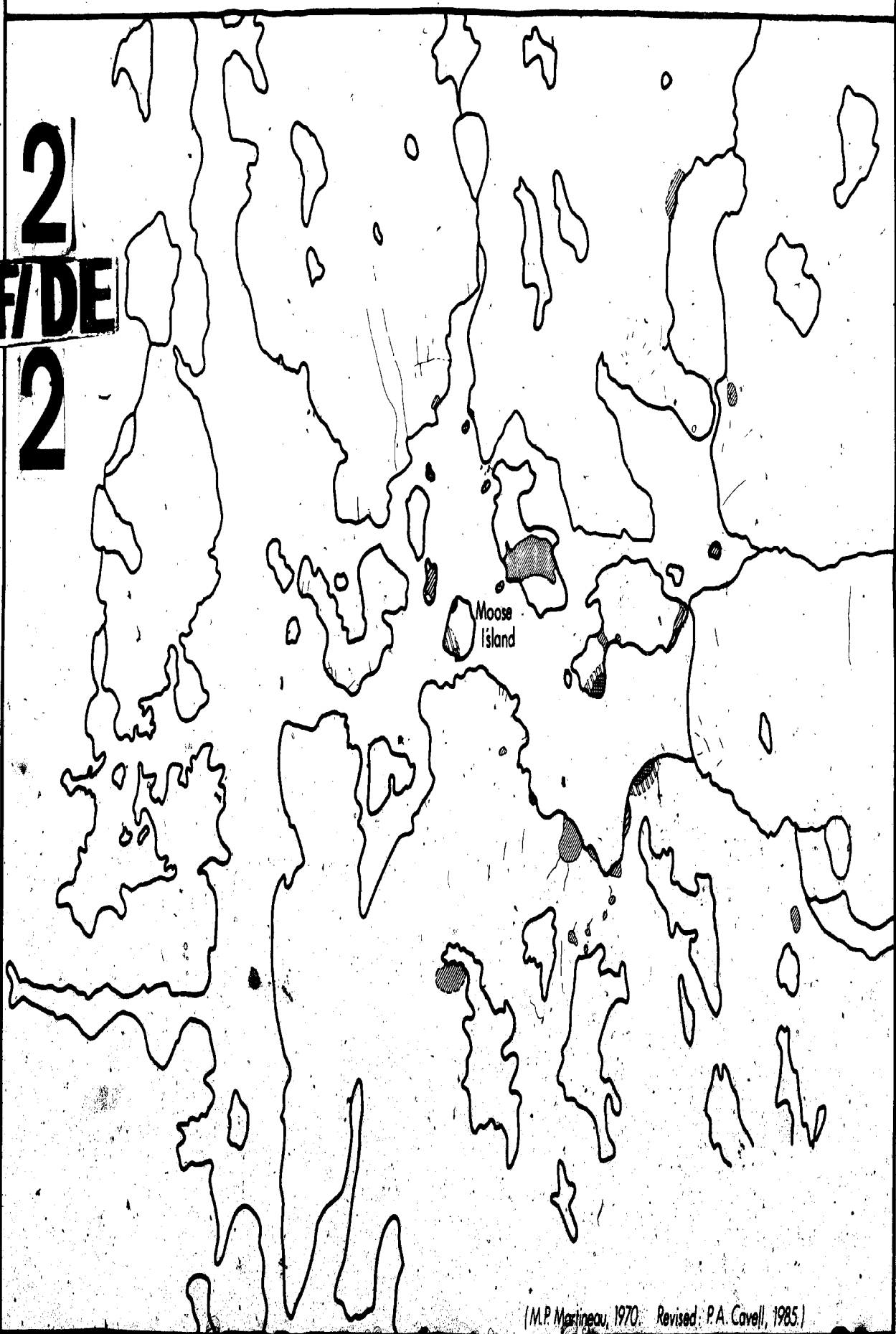
Contact Arbitrary

Scale in kilometers

0.5 1.0 1.5 2.0








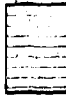
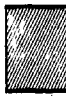



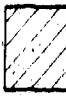
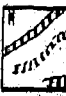



2
OF/DE
2

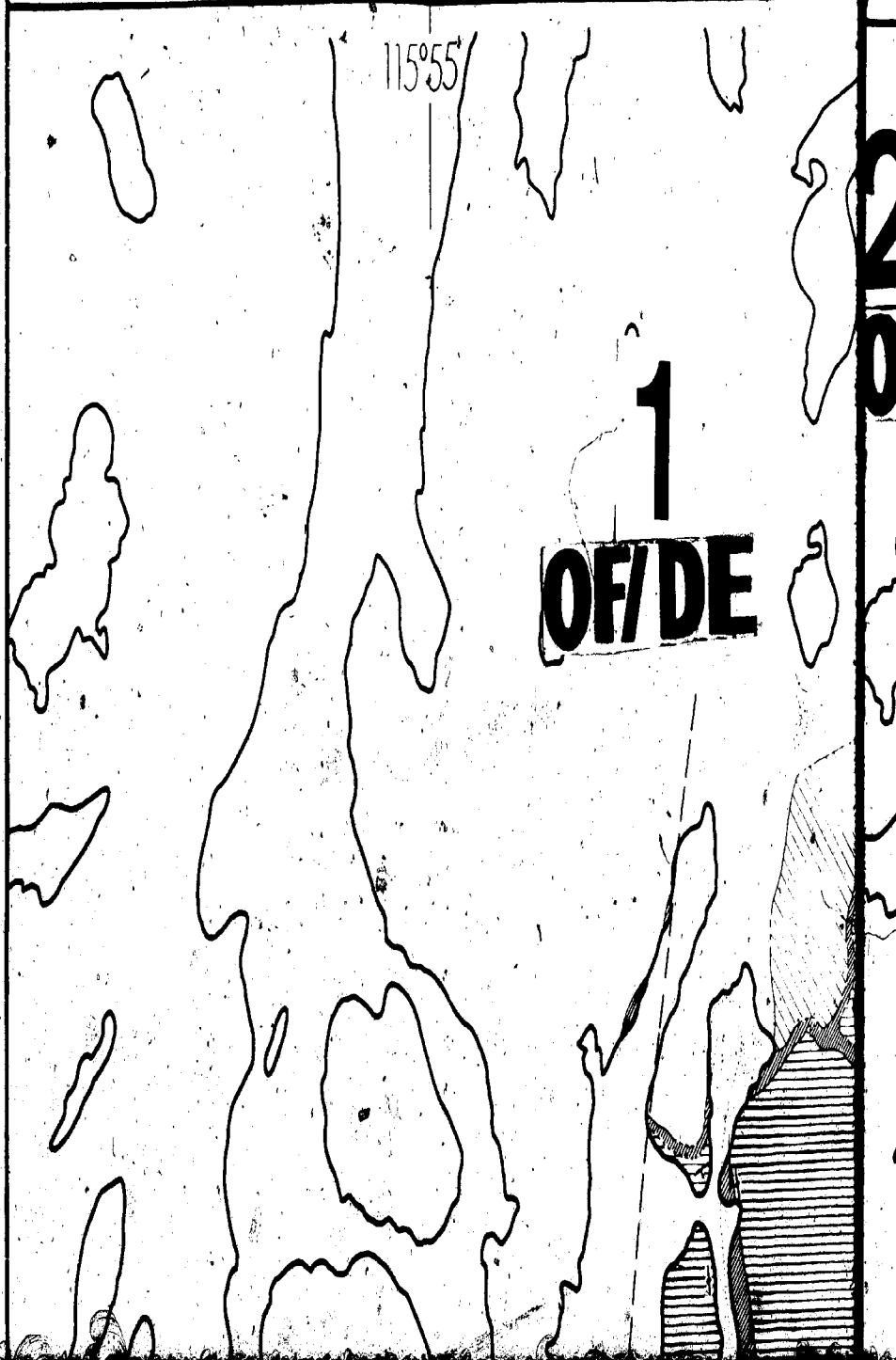


(M.P. Martineau, 1970. Revised: P.A. Covell, 1985.)

THE GEOLOGY OF THE BIGSPRUC

N. W. T., CANADA

-  Granodiorite
-  Alkali Diorite
-  Big Feldspar Gabbro
-  Leucocratic Laminated Gabbro
-  Rhythmic Banded Gabbro
-  Intrusive Magnetite Pyroxenites
-  Remobilized & Hybrid Rocks
-  Mafic Syenite S₁
-  Quartz Free Ring Syenite S₂
-  Outer Quartz Syenite S₃
-  Inner Quartz Syenite S₄
-  Comendite
-  Northern Mafic Foyaite
-  Aegirine Syenite Fenite
-  Southern Foyaite

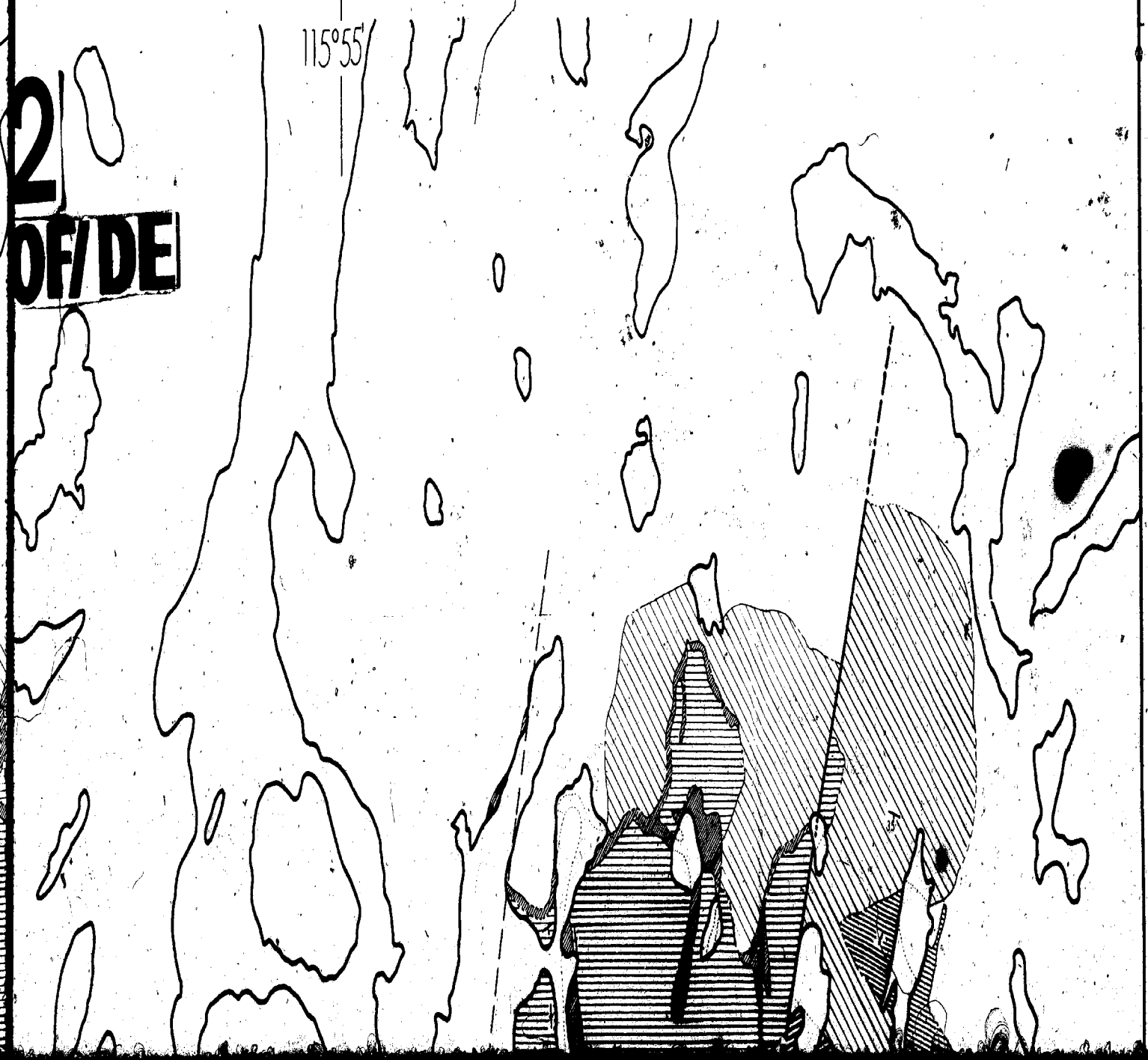


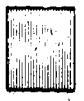
THE GEOLOGY OF THE BIGSPRUCE LAKE COMPLEX

N. W. T. , CANADA

2
OF/DE

115°55'





Laminated Chilled Foyaité



Ijolite



Dolomite Carbonatite

3
OF/DE

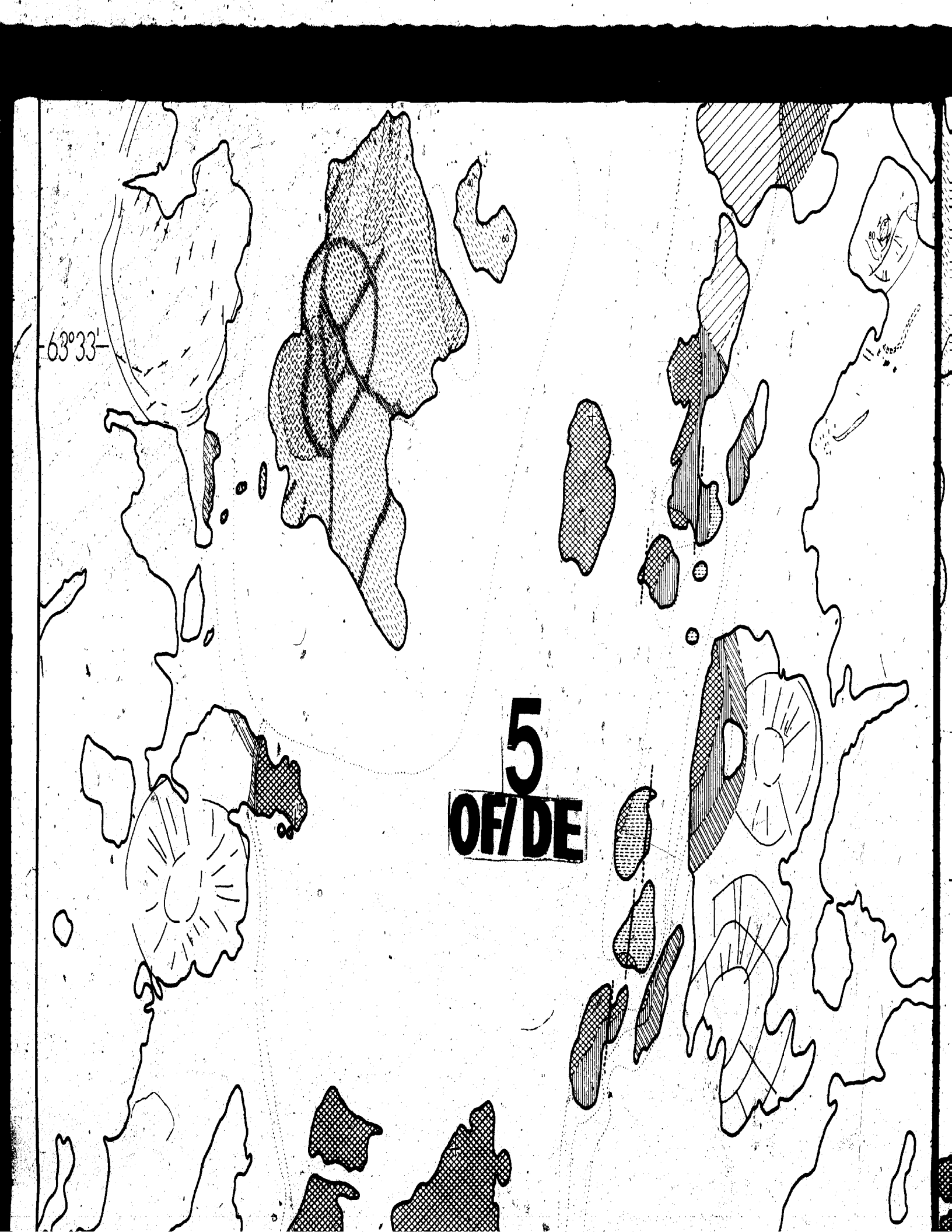




4
OF/DEI






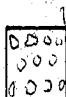
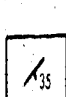



63°33'

5
OF/DE



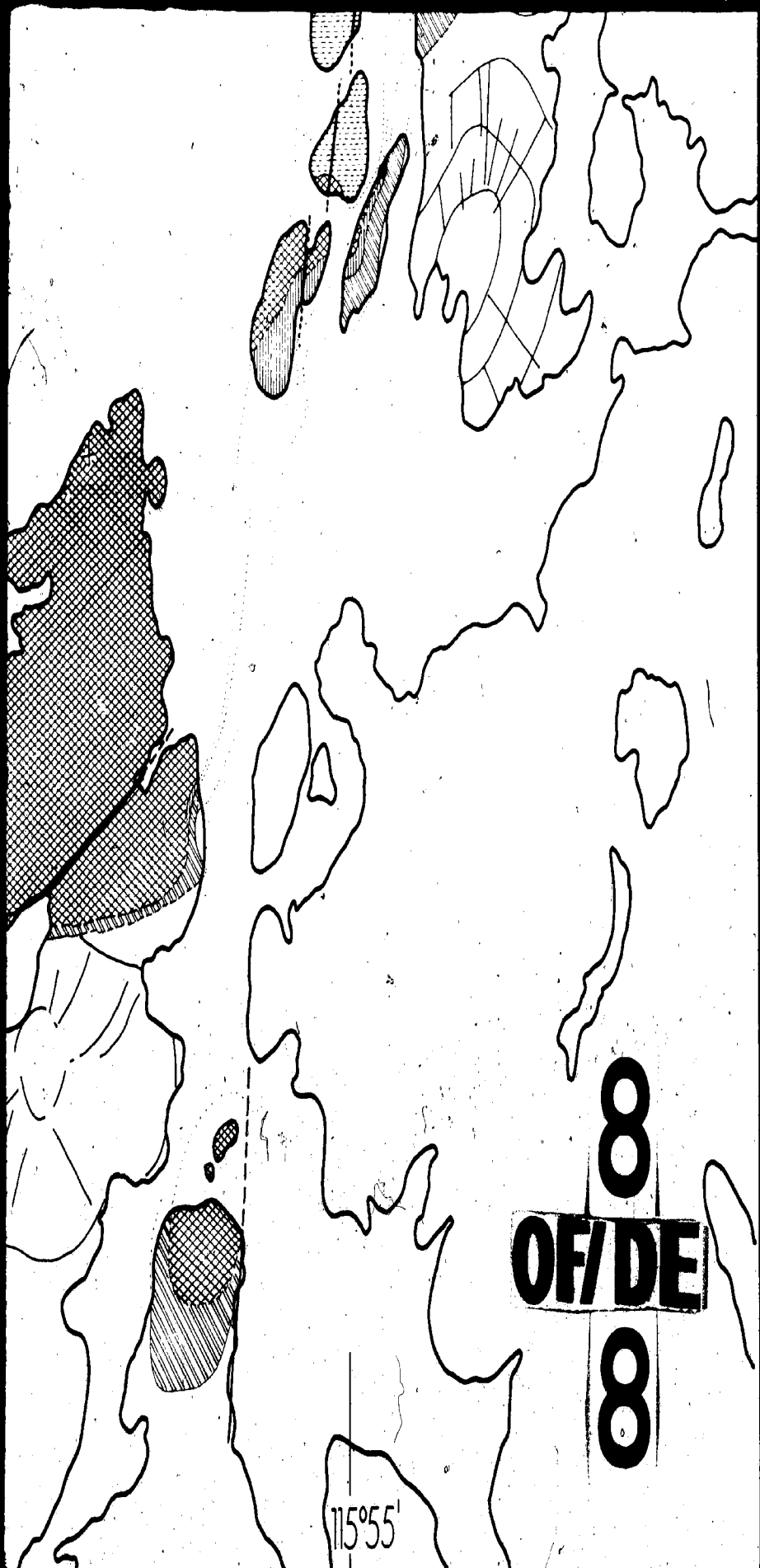
63°33'



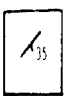





6
OF/DE

- 
-  Radial Fracture System
 -  Fenitized Cone Fractures
 -  Broad Basic Dykes
 -  Riebeckite Metasomatized Zone
 -  Breccia
 -  Attitude of Layered Rocks
 -  Faults and Crush Lines
 -  Contact Established
 -  Contact Approximate

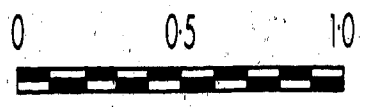
7
OF/DE



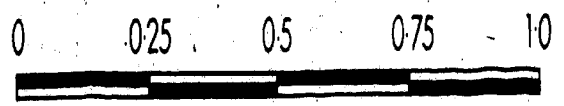


-  Riebeckite Metasomatized Zone
-  Breccia
-  Attitude of Layered Rocks
-  Faults and Crush Lines
-  Contact Established
-  Contact Approximate
-  Contact Inferred
-  Attitude of Foliated Microgranite

Kilometers



Miles



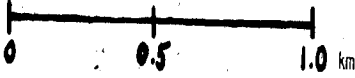
(M.P. Martineau, 1970. Revised: P.A. Cavell, 1985)

1 OF/DE

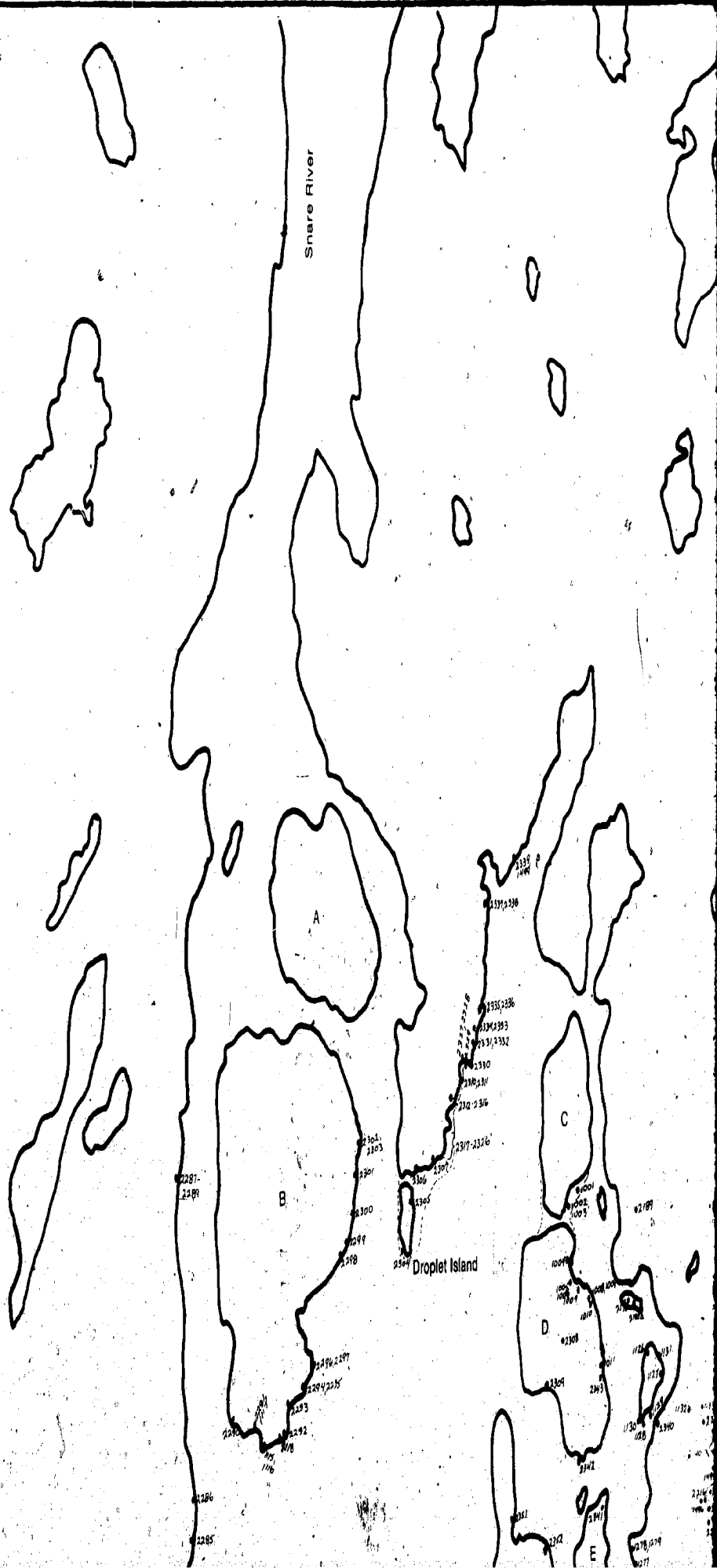
KEY

1000 series = 1981 samples
2000 series = 1982 samples

SCALE

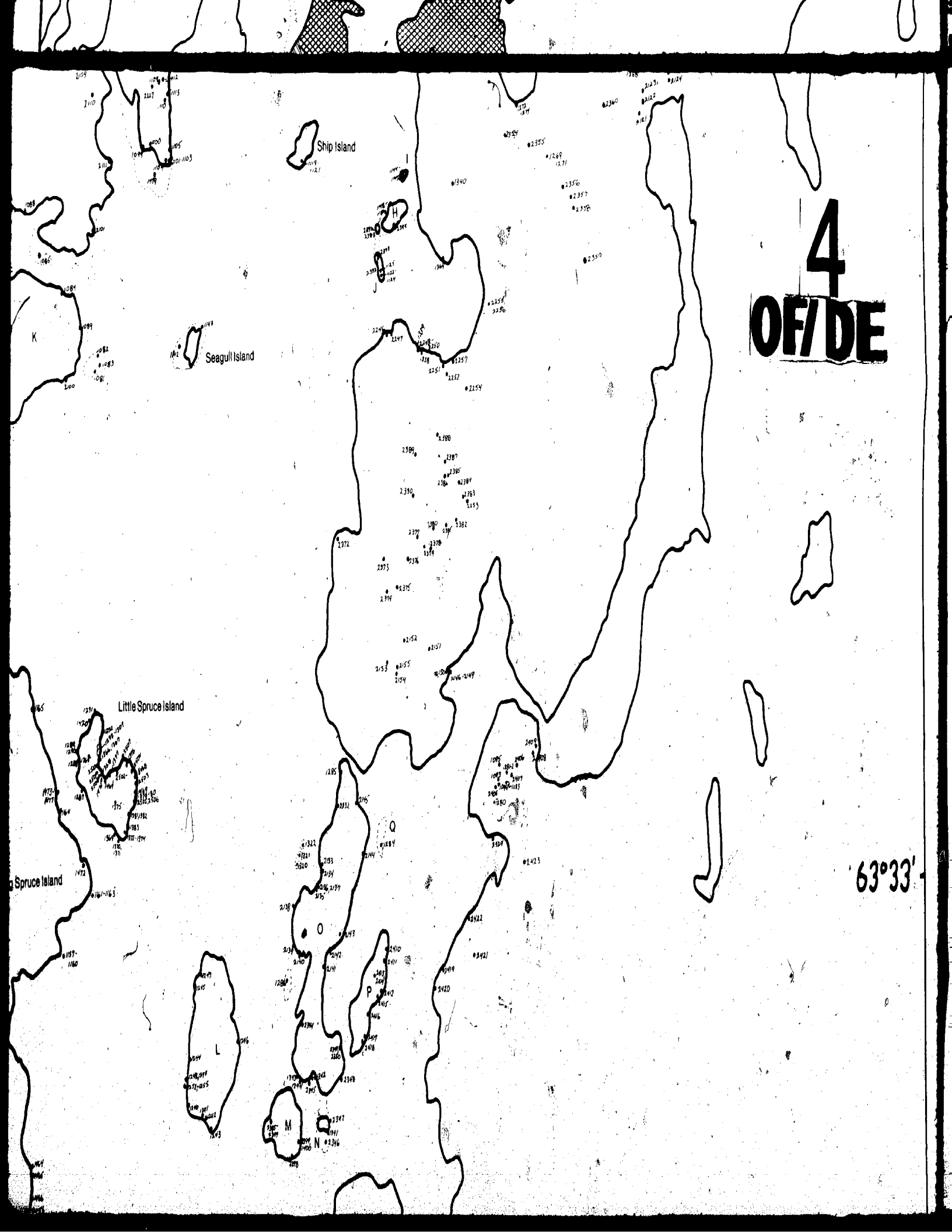


A horizontal scale bar with three segments. The first segment is labeled '0', the second '0.5', and the third '1.0 km'.



3
OF/DEI





Ship Island

Seagull Island

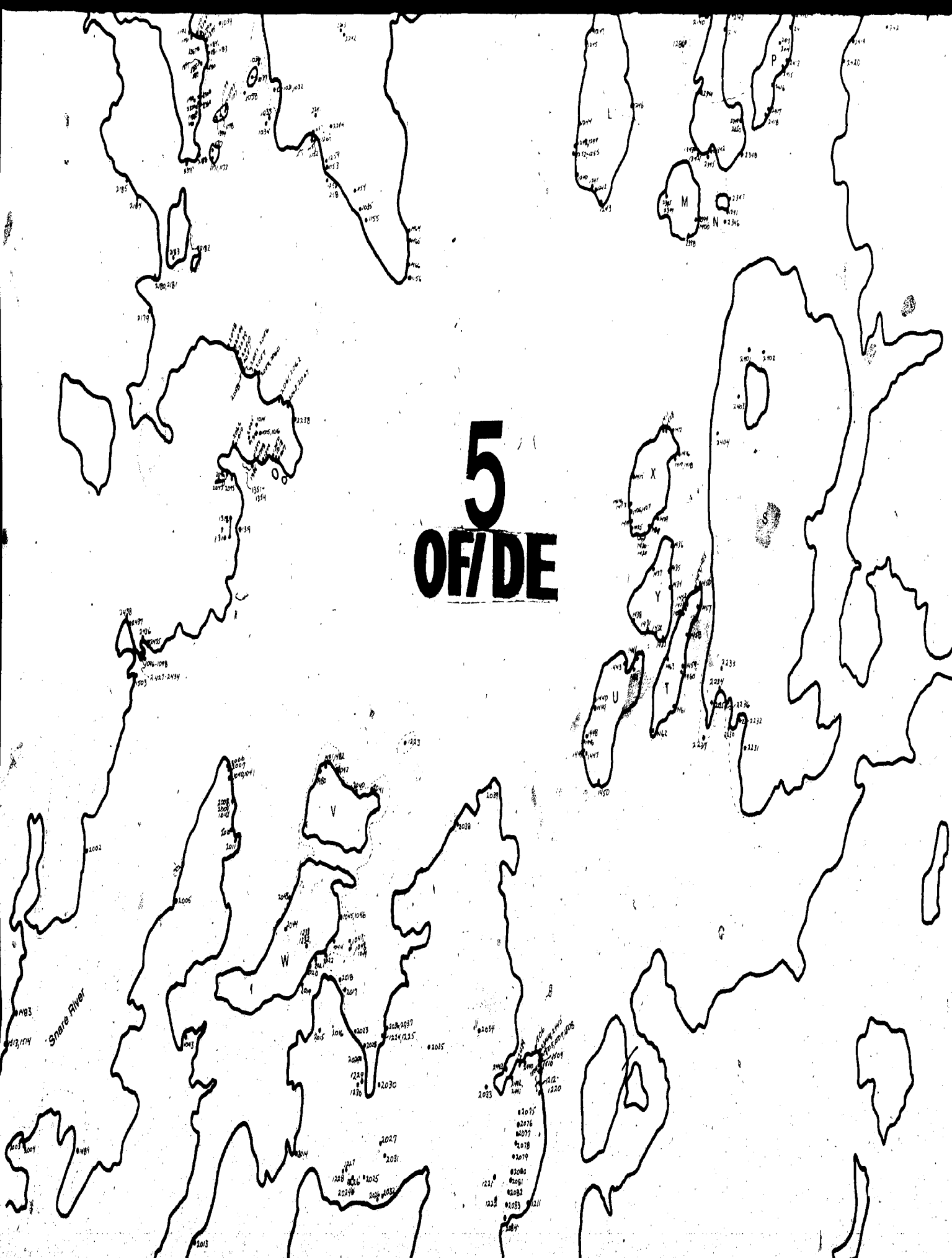
Little Spruce Island

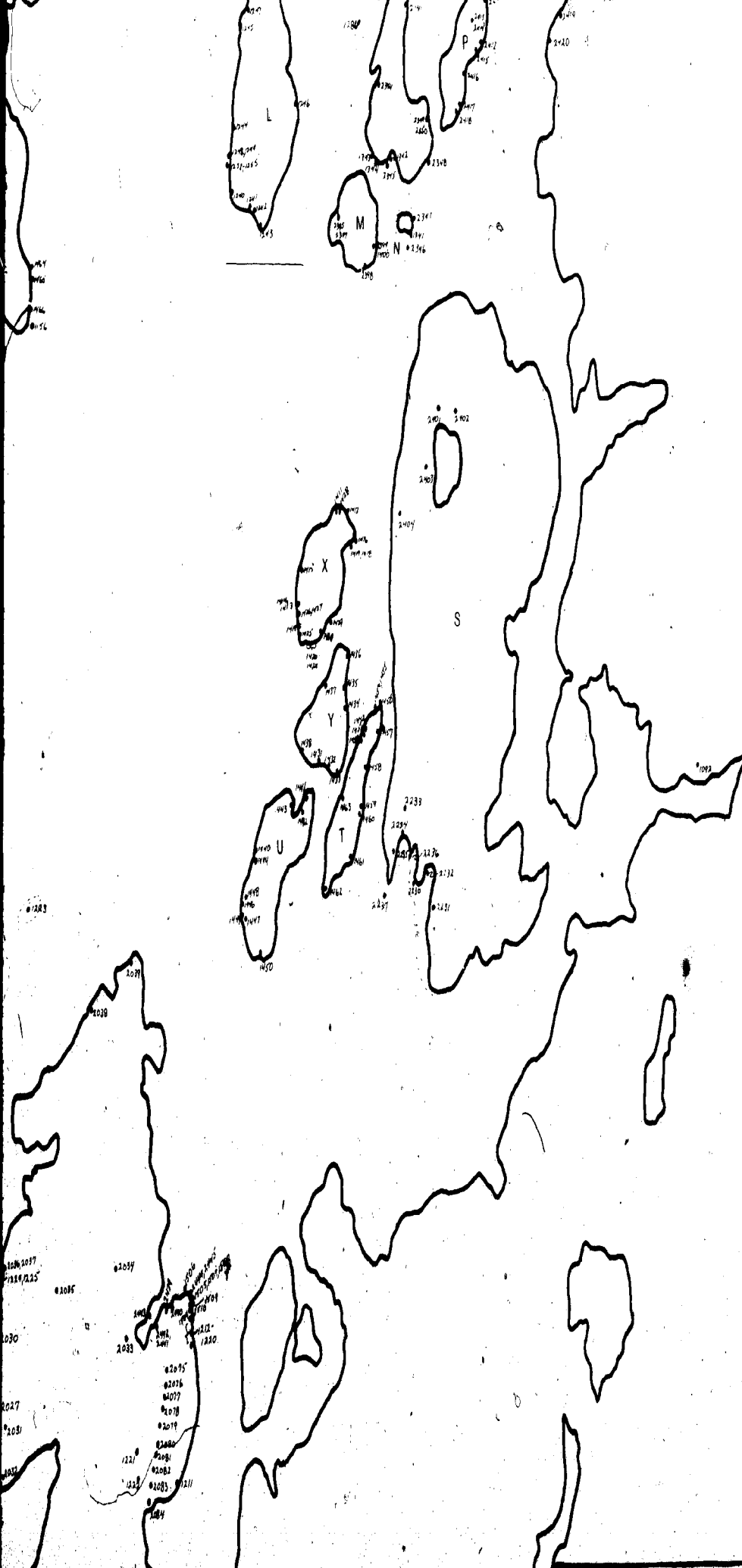
Spruce Island

4
OF/DE

63°33'

5
OF/DE

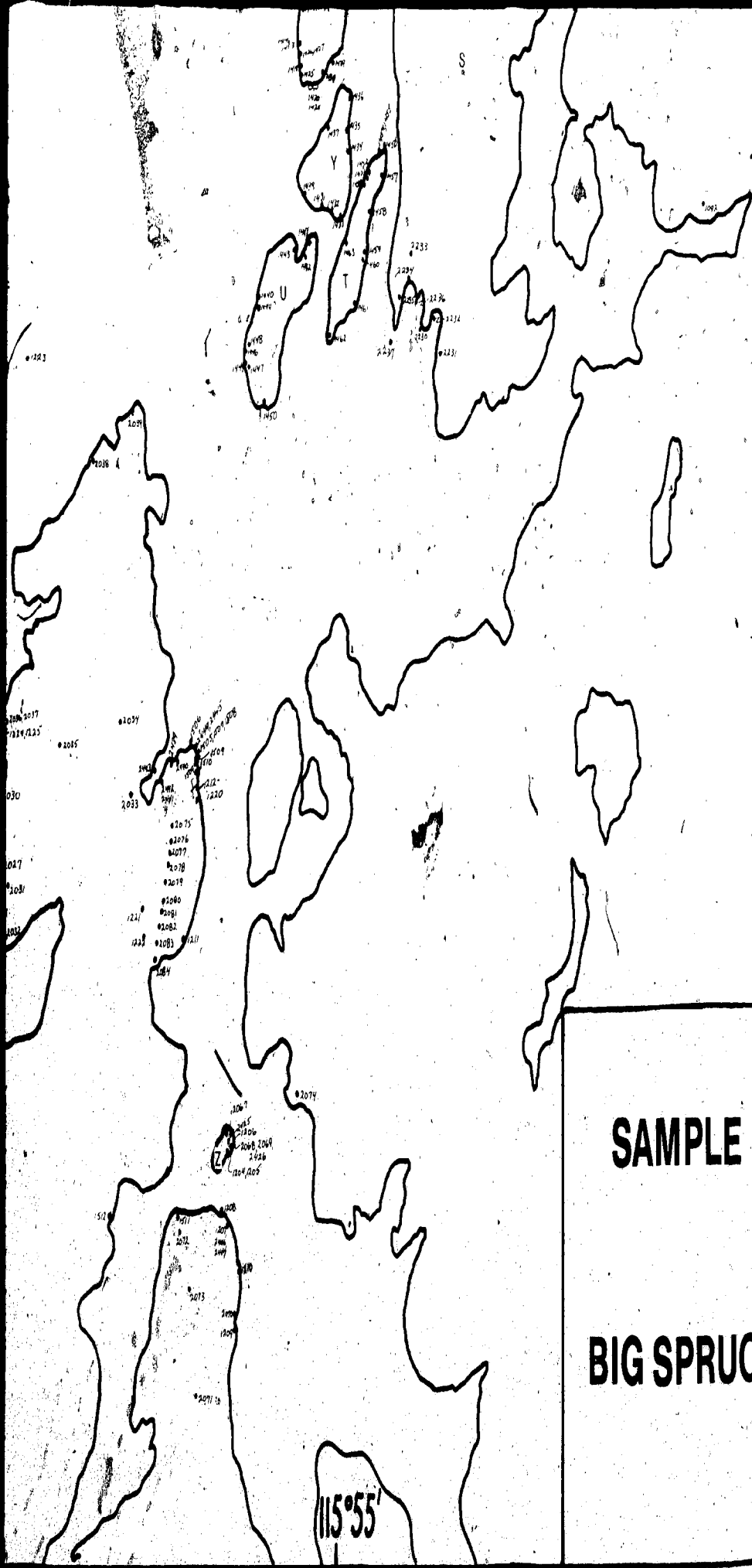




6
OF/DE

- 2097
- 2098
- 2099
- 2100
- 2101
- 2102
- 2103
- 2104
- 2105
- 2106
- 2107
- 2108
- 2109
- 2110
- 2111
- 2112
- 2113
- 2114
- 2115
- 2116
- 2117
- 2118
- 2119
- 2120
- 2121
- 2122
- 2123
- 2124
- 2125
- 2126
- 2127
- 2128
- 2129
- 2130
- 2131
- 2132
- 2133
- 2134
- 2135
- 2136
- 2137
- 2138
- 2139
- 2140
- 2141
- 2142
- 2143
- 2144
- 2145
- 2146
- 2147
- 2148
- 2149
- 2150
- 2151
- 2152
- 2153
- 2154
- 2155
- 2156
- 2157
- 2158
- 2159
- 2160
- 2161
- 2162
- 2163
- 2164
- 2165
- 2166
- 2167
- 2168
- 2169
- 2170
- 2171
- 2172
- 2173
- 2174
- 2175
- 2176
- 2177
- 2178
- 2179
- 2180
- 2181
- 2182
- 2183
- 2184
- 2185
- 2186
- 2187
- 2188
- 2189
- 2190
- 2191
- 2192
- 2193
- 2194
- 2195
- 2196
- 2197
- 2198
- 2199
- 2200
- 2201
- 2202
- 2203
- 2204
- 2205
- 2206
- 2207
- 2208
- 2209
- 2210
- 2211
- 2212
- 2213
- 2214
- 2215
- 2216
- 2217
- 2218
- 2219
- 2220
- 2221
- 2222
- 2223
- 2224
- 2225
- 2226
- 2227
- 2228
- 2229
- 2230
- 2231
- 2232
- 2233
- 2234
- 2235
- 2236
- 2237
- 2238
- 2239
- 2240
- 2241
- 2242
- 2243
- 2244
- 2245
- 2246
- 2247
- 2248
- 2249
- 2250
- 2251
- 2252
- 2253
- 2254
- 2255
- 2256
- 2257
- 2258
- 2259
- 2260
- 2261
- 2262
- 2263
- 2264
- 2265
- 2266
- 2267
- 2268
- 2269
- 2270
- 2271
- 2272
- 2273
- 2274
- 2275
- 2276
- 2277
- 2278
- 2279
- 2280
- 2281
- 2282
- 2283
- 2284
- 2285
- 2286
- 2287
- 2288
- 2289
- 2290
- 2291
- 2292
- 2293
- 2294
- 2295
- 2296
- 2297
- 2298
- 2299
- 2300
- 2301
- 2302
- 2303
- 2304
- 2305
- 2306
- 2307
- 2308
- 2309
- 2310
- 2311
- 2312
- 2313
- 2314
- 2315
- 2316
- 2317
- 2318
- 2319
- 2320
- 2321
- 2322
- 2323
- 2324
- 2325
- 2326
- 2327
- 2328
- 2329
- 2330
- 2331
- 2332
- 2333
- 2334
- 2335
- 2336
- 2337
- 2338
- 2339
- 2340
- 2341
- 2342
- 2343
- 2344
- 2345
- 2346
- 2347
- 2348
- 2349
- 2350
- 2351
- 2352
- 2353
- 2354
- 2355
- 2356
- 2357
- 2358
- 2359
- 2360
- 2361
- 2362
- 2363
- 2364
- 2365
- 2366
- 2367
- 2368
- 2369
- 2370
- 2371
- 2372
- 2373
- 2374
- 2375
- 2376
- 2377
- 2378
- 2379
- 2380
- 2381
- 2382
- 2383
- 2384
- 2385
- 2386
- 2387
- 2388
- 2389
- 2390
- 2391
- 2392
- 2393
- 2394
- 2395
- 2396
- 2397
- 2398
- 2399
- 2400
- 2401
- 2402
- 2403
- 2404
- 2405
- 2406
- 2407
- 2408
- 2409
- 2410
- 2411
- 2412
- 2413
- 2414
- 2415
- 2416
- 2417
- 2418
- 2419
- 2420
- 2421
- 2422
- 2423
- 2424
- 2425
- 2426
- 2427
- 2428
- 2429
- 2430
- 2431
- 2432
- 2433
- 2434
- 2435
- 2436
- 2437
- 2438
- 2439
- 2440
- 2441
- 2442
- 2443
- 2444
- 2445
- 2446
- 2447
- 2448
- 2449
- 2450
- 2451
- 2452
- 2453
- 2454
- 2455
- 2456
- 2457
- 2458
- 2459
- 2460
- 2461
- 2462
- 2463
- 2464
- 2465
- 2466
- 2467
- 2468
- 2469
- 2470
- 2471
- 2472
- 2473
- 2474
- 2475
- 2476
- 2477
- 2478
- 2479
- 2480
- 2481
- 2482
- 2483
- 2484
- 2485
- 2486
- 2487
- 2488
- 2489
- 2490
- 2491
- 2492
- 2493
- 2494
- 2495
- 2496
- 2497
- 2498
- 2499
- 2500

8
OF/DE
8



SAMPLE LOCATIONS, 1981-1982

BIG SPRUCE LAKE COMPLEX, N.W.T.